Processing and Characterization of Bulk Heterojunction Solar Cells Based on New Organic n-Type Semiconductors

Dissertation zur Erlangung des
naturwissenschaftlichen Doktorgrades
der Julius-Maximilians-Universität Würzburg

vorgelegt von
Reinhard Johannes Hecht, geb. Wagener
aus Papenburg

Würzburg 2018

‘‘The combined results of several people working together is often much more effective than could be that of an individual scientist working alone.‘‘

John Bardeen (1972)

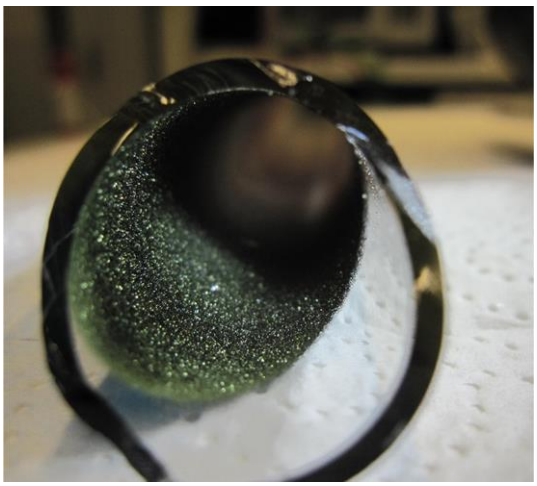

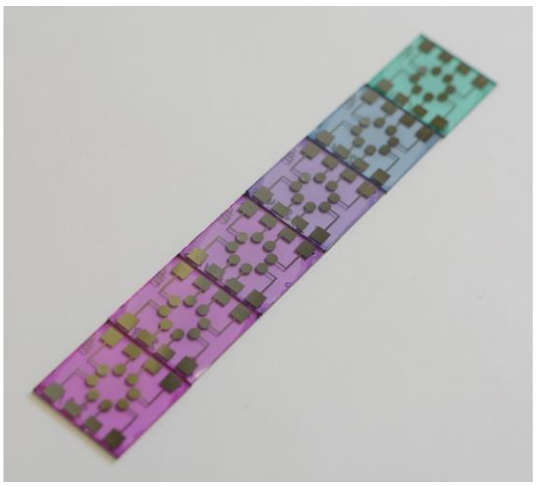

Eingereicht bei der Fakultät für Chemie und Pharmazie am:

_____

Gutachter der schriftlichen Arbeit:

1. Gutachter: Prof. Dr. Frank Würthner

2. Gutachter: _____

Prüfer des öffentlichen Promotionskolloquiums:

1. Prüfer: Prof. Dr. Frank Würthner

2. Prüfer: _____

3. Prüfer: _____

Datum des öffentlichen Promotionskolloquiums:

_____

Doktorurkunde ausgehändigt am:

_____

List of Abbreviations

Physical Constants

c	speed of light (299792458 m s^{-1})
e	elementary charge (1.602 × 10^{-19} C)
h	Planck's constant (6.626 × 10^{-34} J s)
k	Boltzmann constant (1.381 × 10^{-23} J K^{-1})
m_e	electron mass (9.109 × 10^{-31} kg)
N_A	Avogadro constant (6.022 × 10^{23} mol^{-1})
ε_0	permittivity of vacuum (8.854 × 10^{-12} A^2 s^4 $m^{-3}s^{-1}$)

Variables

A	absorbance
a, b, c	crystal lattice parameter, length of unit cell
BLA	bond length alternation
c	concentration
C_i	capacitance
χ_s	electron affinity
D	diffusion coefficient
d	thickness
ΔE_{HOMO}	HOMO offset
ΔE_{LUMO}	LUMO offset
$\Delta E_{HOMO\text{-}LUMO}$	offset between HOMO of donor and LUMO of acceptor
$\Delta\varepsilon_{max}$	difference in maximum molar extinction coefficient
E	electric field
E_{00}	adiabatic transition energy in vacuo
$E_{1/2}$	half wave potential
$E_{1/2}^{ox}$	oxidation half wave potential
$E_{1/2}^{red}$	reduction half wave potential
$E_{AM\ 1.5G}$	AM1.5G spectrum
E_b	exciton binding energy
E_g	band gap energy
E_{gap}^{CV}	electrochemical band gap
E_{gap}^{opt}	optical band gap
E_{HOMO}	HOMO energy level
$E_{HOMO}^{acceptor}$	HOMO energy level of acceptor
E_{HOMO}^{donor}	HOMO energy level of donor
E_{ion}^{H}	ionization energy of hydrogen
E_{light}	light energy
E_{LUMO}	LUMO energy level
$E_{LUMO}^{acceptor}$	LUMO energy level of acceptor
E_{LUMO}^{donor}	LUMO energy level of donor
EQE	external quantum efficiency

EQE_{max}	maximum of external quantum efficiency
E_{sim}	solar simulator spectrum
E_t	thermalization energy
E_V	voltage loss
f	oscillator strength
$F_{(000)}$	structure factor for Miller indices h = k = l = 0
FF	fill factor
$GooF(F^2)$	goodness of fit on F^2
$\bar{h}$	mean pixel height
h_{mn}	measured pixel height
I	current
I_0	reverse current
I_{abs}	integral of absorption band
I_d	diode current
I_{DS}	drain-source current
I_{MPP}	current at the maximum power point
I_{ph}	photocurrent
I_{SC}	short circuit current
I_{SH}	shunt current
J	coupling constant
$j_{diffusion}$	diffusion current
j_{drift}	drift current
J_{SC}	short circuit current density
j_{total}	total current
L	channel length of transistor
L_D	exciton diffusion length
M	molar mass
MM	mismatch factor
MPP	maximum power point
n	charge carrier concentration; ideality factor
∇n	charge carrier concentration gradient
N	number of conjugated double bonds; pixel number
N_{MCC}	maxium conducive chain length
P	power
p	pressure
PCE	power conversion efficiency
PCE_{max}	maximum power conversion efficiency
P_{in}	input power
P_{MPP}	power at the maximum power point
P_{out}	output power
r	sublimation rate
R(all data)	residual factor for refinement with all data
$R(I>2\sigma(I))$	redsidual factor for refinement with observed data
R_1	residual factor
R_{rms}	root mean square roughness
R_S	series resistance
R_{SH}	shunt resistance
SR	spectral response

SR_{ref}	spectral response of reference cell
SR_{test}	spectral response of test cell
T	temperature; transmission
T_K	crystallization temperature
T_M	melting temperature
T_s	substrate temperature
T_{sub}	sublimation temperature
U(eq)	equivalent isotropic displacement parameter
V	voltage; volume of unit cell
V_{bi}	build in potential
V_{DS}	drain-source voltage
V_{GS}	gate-source voltage
V_{MPP}	voltage at maximum power point
V_{OC}	open circuit voltage
V_T	thermal voltage; threshold voltage
W	channel width of transistor
wR^2	residual factor
x, y, z	atomic coordinates
Z	dimensionality; number of molecules in unit cell
α, β, γ	crystal lattice parameters; angles of unit cell
δ	chemical shift
$\Delta\tilde{\nu}$	stokes shift
ε	molar extinction coefficient
ε_{max}	maximum molar extinction coefficient
ε_r	relative permittivity
θ	dihedral angle; incident angle; contact angle
λ	wavelength; reorganization energy
λ_{em}	wavelength of emission maximum
λ_i	inner reorganization energy
λ_{max}	wavelength of absorption maximum
λ_{max}^{film}	wavelength of absorption maximum in thin film
λ_{max}^{sol}	wavelength of absorption maximum in solution
μ	charge carrier mobility; absorption coefficient
μ_e	electron mobility
μ_h	hole mobility
μ^2_{eg}	square transition dipole moment
μ_{eh}	effective mass of an exciton
μ_g	ground state dipole moment
ν	frequency
$\tilde{\nu}$	wave number
ρ	density
σ	conductivity
τ	exciton lifetime
Φ_{fl}	fluorescence quantum yield
ϕ_m	work function of metal
Φ_B	Schottky-barrier height

Chemical Compounds

Ac	acetate
Ac_2O	acetic anhydride
Ag	silver
AgCl	silver chloride
Al	aluminum
AlO_x	aluminum oxide
Alq_3	tris-(8-hydroxyquinoline)aluminum
DOCP	dioxocyano-pyridine
BFI	tetraazabenzodifluoranthene diimide
BINAP	2,2'-bis(diphenylphosphino)-1,1'-binaphthyl)
BTT	(3-boryl-2-thienyl)-2-thiazole
Bu	butyl
C_{60}	fullerene
Ca	calcium
CAR	carbazole
CB	chlorobenzene
CPDT	cyclopentadithiophene
Cu	copper
dba	dibenzylideneacetone
DCE	1,2-dichloroethane
DCIND	1,1-dicyanomethylene-3-indanone
DCM	dichloromethane
DCM	dichloromethane
DIO	1,8-diiodooctane
DMF	dimethylformamide
DPP	diketopyrrolopyrrole
DTP	dithienopyrrole
Et	ethyl
Et_2O	diethyl ether
EtHex	2-ethylhexyl
EtOAc	ethyl acetate
EtOH	ethanol
Fc	ferrocene
FL	fluorine
FOPA	pentadecylfluoroocadeclphosphonic acid
HMDS	hexamethyldisilazane
IND	1,3-indandione
*i*PrOH	*iso*-propanol
ITO	indium tin oxide
LDA	lithium diisopropylamide
LiF	lithium fluoride
MC	merocyanine
Me	methyl
MEH-PPV	poly[2-methoxy-5-(2-ethylhexyloxy)-1,4-phenylene vinylene]
MeOH	methanol
Mes	mesityl

Mes_2BF	dimesitylborane
Mo	molybdenum
MoO_3	molybdenum(VI)-oxide
NaOAc	sodium acetate
NaO*t*Bu	sodium *tert*-butoxide
NBS	*N*-bromosuccinimide
*n*Bu	*n*-butyl
*n*BuLi	*n*-butyllithium
OTES	*n*-octadecyltriethoxysilan
P3HT	poly(3-hexylthiophene-2,5-diyl)
PBI	perylene bisimide
$PC_{61}BM$	[6,6]-phenyl-C_{61}-butyric acid methyl ester
$PC_{71}BM$	[6,6]-phenyl-C_{71}-butyric acid methyl ester
PCC	pyridiniumchlorochromat
$Pd_2(dba)_3$	tris(dibenzylideneacetone)dipalladium(0)
PEDOT	poly(styrene-sulfonic acid)
PEDOT:PSS	poly(3,4-ethylenedioxythiophene):poly(styrene-sulfonic acid)
PPV	poly(*p*-phenylenevinylene)
PSS	poly(styrene-sulfonic acid)
Pt	platinum
PTFE	polytetrafluoroethylene
PVDF	polyvinylidene difluoride
Si	silicon
SiO_2	silicon oxide
TBAB	tetra-*n*-butylammonium bromide
THF	tetrahydrofuran
THZL	thiazole
TMS	tetramethylsilane
TPA	*n*-tetradecylphosphonic acid
TTF	tetrathiafulvalenes
Xe	xenon
ZnO	zinc oxide

Other Abbreviations

1D	one-dimensional
2D	two-dimensional
3D	three-dimensional
A	acceptor
AFM	atomic force microscopy
AM 1.5 G	air mass 1.5 global
bc	back contact
BHJ	bulk heterojunction
CCD	charge-coupled device
CELIV	charge carrier extraction by linearly increasing voltage
CMOS	complementary metal-oxide-semiconductor
CT	charge transfer
CV	cyclic voltammetry

D	donor
d	day; doublet
DFT	density functional theory
DSC	differential scanning calorimetry
ΔT	thermal annealing
ESI	electronspray ionization
ETL	electron transport layer
EXO	exothermic
FET	field-effect transistor
FMO	frontier molecular orbital
h	hour
HOMO	highest occupied molecular orbital
HPLC	high performance liquid chromatography
HTL	hole transport layer
ICT	intramolecular charge transfer
LUMO	lowest unoccupied molecular orbital
MALDI	matrix-assisted laser desorption/ionization
m	multiplet
min	minute
M.p.	melting point
n/n	mol/mol
NMR	nuclear magnetic resonance
OD	optical density
OFET	organic field-effect transistor
OLED	organic light emitting diode
OSC	organic solar cell
OTFT	organic thin-film transistor
PCM	polarizable continuum model
PHJ	planar heterojunction
PTC	phase-transfer catalysis
rpm	rounds per minute
RT	room temperature
s	second; singulet
S_0	singulet ground state
S_1	first singulet excited state
SAM	self-assembled mono layer
SCLC	space charge limited current
SVA	solvent vapor annealing
t	triplet
TD-DFT	time dependent density functional theory
ToF	time of flight
UV/vis	ultraviolet/visible
UVO	ultraviolet-ozone
vol%	volume percent
w/w	weight/weight
XRD	X-ray diffraction
Y	yield

Table of Contents

Chapter 1
Introduction and Aim of Thesis

If mankind does not reduce the consumption of natural resources according to the living planet report (WWF)[1] by the year 2030 we will need at least a second planet Earth to cover the worldwide demand. In 2050 already almost three planets like ours will be needed to cover all consumptions. Only considering the world energy consumption, in 2016 about 1.5×10^{14} kWh[2] of energy were used. Instead of decreasing, this number is steadily rising by about 1.9 % per year.[2] In the light of this development the United Nations declared 17 goals for a global sustainable future: affordable and clean energy as well as responsible consumption and production, amongst others.[3]

At the moment the huge amount of energy we rely on primarily stems from energy sources that are not renewable, as shown in the report of the World Energy Council in 2016 (Figure 1).[4] The main energy sources are oil, coal and gas with 33.0, 29.2 and 23.8 %, respectively. Renewable energy sources only contribute with 9.6 %, nuclear energies with 4.4 %. It is well known that fossil fuels (coal, gas and oil) as well as nuclear power have major drawbacks. If the former are continuously used for energy production, big amounts of carbon dioxide are released, which in turn leads to an increase in global temperature. Further consequences are among others extreme weather events, melting of glaciers and polar caps and water scarcity. In this regard, nuclear energy is a clean energy source, but the risk of long-lasting radioactive contamination is high, as can be

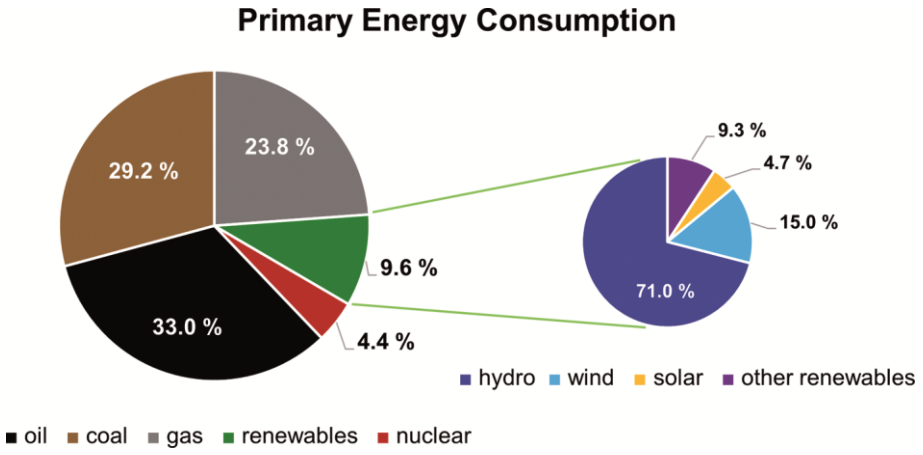

Figure 1. Primary energy consumptions in 2016 dependent on different energy sources, data from[5].

seen from serious accidents, like in Kyschtym (Soviet Union, 1957), Tschernobyl (Soviet Union, 1986) and Fukushima (Japan, 2011). Renewable energies all have less adverse effects for the environment than fossil fuels or nuclear energies. Thus, it is an important goal to increase their contribution to the world energy production. The renewable energy sources themselves can be divided into hydro (71.0 %), wind (15.0 %), solar (4.7 %) and other energy sources (9.3 %). Among these, solar energy is the one with the highest growth potential because the sun provides a constant energy flow of 1.5×10^{18} kWh/a on the earth's surface.[6] This is enough energy to cover all consumptions multiple times. The only problem is to harvest this energy effectively. A first way to do so was opened up by Becquerel, who discovered the photovoltaic effect in 1839.[7] However, a big jump in the direction of real application was only made in 1954 when D. M. Chapin *et al.* invented silicon p-n junction photocells with efficiencies of 5 – 6 %.[8]

Nowadays, inorganic silicon based solar panels are installed all over the world with a total capacity of 227 GW_p, which is about 1 % of the global energy demand.[4] Even though power conversion efficiencies for crystalline silicon solar cells are well above 25 % (laboratory efficiencies),[9,10] and have become much cheaper today (~1.8 US\$/W_p in 2015 compared to ~4 US\$/W_p in 2007),[4] they still have some major drawbacks. For example, they suffer from long energy payback times (1 to 2 years),[11] shading effects, high-weight and no mechanical flexibility. In this regard, organic solar cells outperform the inorganic ones, where energy payback times are only in the order of days.[12] Additionally, high throughput roll-to-roll processing and low material consumption bear the potential of very cheap modules.[13] Furthermore, organic solar cells show no major drop in power output, when the device is not completely illuminated and they can be processed on light-weight and flexible substrates. Thus, it is possible to utilize them where inorganic solar cells have their weaknesses, e.g. when integrated into house facades and windows, applied on curved surfaces or when used as portable power supplies with low weight and pack size. Nowadays, organic solar cells are already commercially available, e.g. from Heliatek® (Dresden, Germany) or OPVIUS GmbH (Kitzingen, Germany). As of now these companies only supply a niche market, however, further developments and increased photovoltaic efficiencies (~12 %)[14] will lead to a wider application of organic solar cells in the future.

To overcome the problems mentioned above, much effort has been spent on the development of organic photovoltaics since the late 1970s. The development towards

highly efficient organic solar cells began in 1995, with the discovery of the bulk heterojunction (BHJ) architecture.[15] Since then research activities have focused on optimization of the BHJ morphology as well as on material design through elegant and high yielding synthesis.[15] Especially the design of new donor materials with favorable absorption and hole transport properties as well as suitable HOMO and LUMO levels, has been promoted during the first decade of this century.[16] Thereby, fast progress was made and power conversion efficiencies (*PCE*) could be increased from less than 1 % to around 10 % for single layer BHJ devices.[17] Since their discovery, fullerene-based materials were the archetype electron acceptor materials in organic photovoltaics because they worked very well with almost any electron donor due to their high electron affinity, formation of a favorable morphology and ability for three dimensional charge transport.[18,19] As a result, the development of alternative electron acceptor materials has lagged far behind, although the fullerene-based acceptors have some major drawbacks, e.g. weak absorption and low electronic tunability. The rare attempts to utilize non-fullerene acceptors before 2011 resulted in power conversion efficiencies below 3.2 %.[20] However, supported by the fast development of high-performance n-type semiconductors for organic field-effect transistors (OFETs), many researcher started to explore non-fullerene acceptors for organic photovoltaics.[17] Today, the developments in the area of non-fullerene acceptors are highly promising,[17,21–25] with record efficiencies of already up to 12 %.[26]

The aim of this thesis was firstly to establish working procedures and to examine the newly installed characterization tools in our laboratory. To this end, a defined standard system was investigated under ambient conditions. On the basis of this system the interesting dyad concept, where the active layer components of a solar cell are covalently linked, was explored. The second aim was to design and investigate new molecules, in order to obtain promising substitutes for fullerene acceptors. This objective emerged from recent developments in the field of organic photovoltaics and more specifically in the area of non-fullerene acceptors. Exciting concepts like incorporation of an electron deficient boron atom into the molecular structure were applied to accomplish these goals (Figure 2).

Chapter 2 explores the design of organic solar cells, ranging from cell architectures (e.g. planar and bulk heterojunction) and interlayers to many aspects that are related to the light to energy conversion process in the devices. Furthermore, interesting tools for the

design of active layer components are introduced, before the characterization of organic solar cells is explained. Finally, the state of the art in the field of small molecular non-fullerene acceptors is shown by giving an overview of the best performing materials found in literature to date.

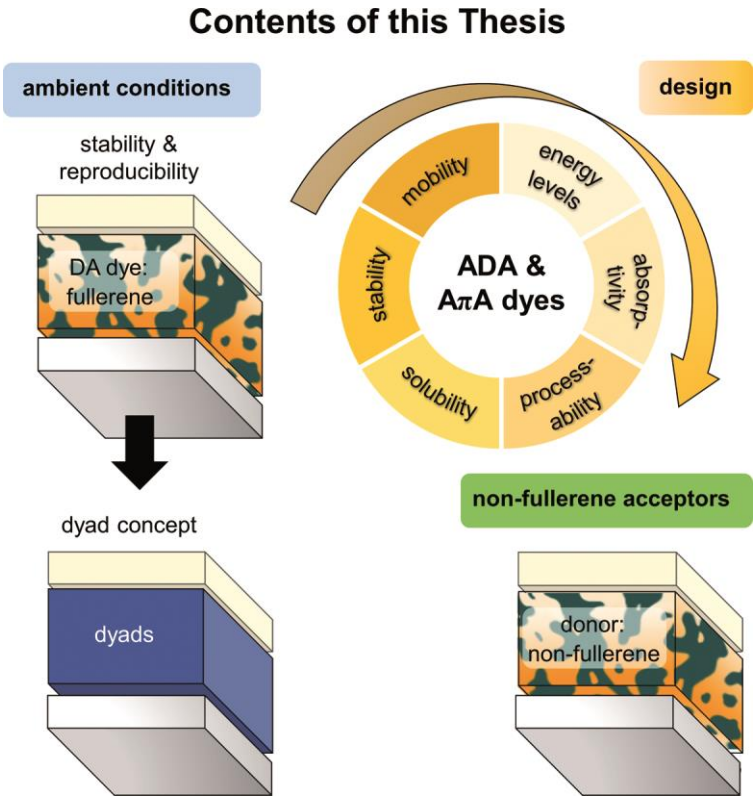

Figure 2. Illustration of the contents of this thesis. The effect of ambient conditions was studied on BHJ solar cells of DA dyes (donor) and fullerenes (acceptor). Furthermore, the dyad concept was applied by covalently linking these donor and acceptor compounds. Finally, ADA and AπA dyes with suitable properties were designed to obtain non-fullerene acceptors.

Chapter 3 describes and discusses the results obtained in this thesis. In **Chapter 3.1.1** the establishment of organic solar cell fabrication and characterization under ambient conditions is addressed. Moreover, the effect of ambient conditions on the device's stability and reproducibility is evaluated. **Chapter 3.1.2** introduces the interesting dyad concept: A series of three merocyanine-fullerene dyads was studied under ambient conditions and finally optimized under inert conditions, during a guest stay in the research group of Prof. Dr. K. Meerholz (Cologne). **Chapter 3.2** covers another major goal of this thesis: the design and investigation of new molecules in order to obtain promising substitutes for fullerene acceptors in organic solar cells. Therefore, a series of eight newly designed acceptor-donor-acceptor dyes (ADA dyes) is presented in **Chapter 3.2.1**. The syntheses of these compounds via Knoevenagel condensation are

described, along with their optical and electrochemical properties. Furthermore, the charge transport properties of the compounds are studied in organic thin film transistors. In **Chapter 3.2.2** the performance of the most promising n-type semiconducting ADA dye and one of its derivatives in organic solar cells are discussed. To this end, the molecules were combined with donor polymers and investigated in devices under inert conditions, during a guest stay in the research group of Prof. Dr. R. A. J. Janssen (Eindhoven). Furthermore, an interesting concept for the design of non-fullerene acceptors is introduced in chapter **Chapter 3.2.3**. A series of three acceptor-π-bridge-acceptor dyes (AπA dyes) is presented, where the electron accepting propensity was successfully increased, on account of an electron deficient boron atom incorporated in the center of the molecular scaffold. Finally, the charge transport behavior of these new dyes is discussed and rationalized with the help of single crystal structures.

Chapter 4 and **Chapter 5** summarize the achievements and findings of this thesis in English and in German, respectively.

Chapter 6 contains detailed information about the fabrication and characterization of transistor and solar cell devices as well as about the syntheses and characterization of the investigated new molecules.

Chapter 2

State of Knowledge

2.1 Design of Organic Solar Cells

2.1.1 Device Architectures

In the early days of organic photovoltaics, the largest improvements in device performance were not made by development of active layer materials, e.g. small molecules and polymers, but rather by advancement of the device architecture. This became very clear when Tang published the first planar heterojunction device (PHJ) in 1986, which performed better (*PCE* about 1 %) than the single layer devices fabricated beforehand (<<1 %).[27] In contrast to the single layer devices, where only one light absorbing material was sandwiched between electron and hole collecting contacts, Tang's PHJ solar cells consisted of a donor and an acceptor layer stacked on top of each other. In these kind of devices, the donor is responsible for hole transport to the anode, while the acceptor transports electrons to the cathode. At the donor-acceptor interface the strongly bound excitons are split, because of the energetic offset between donor and acceptor (see following sections). In single layer devices the excitons have to be split by the electrical field within these, which resulted in a strong field dependence of charge generation.[27,28] Utilizing the PHJ architecture, the solar cell efficiency of ~1 % in 1986[27] could be increased to around 4 %,[29] when nowadays conventional fullerene acceptors were applied. Another large improvement was made, when solution-processed bulk heterojunction solar cells (BHJ) were developed by Heeger and co-workers (Figure 3).[30] In these devices the donor and acceptor material are well intermixed forming microphase separated active layers. As a consequence, a huge donor-acceptor interface is formed, so that another limiting step in charge generation is overcome: the exciton diffusion. While this is an advantage over planar heterojunction devices and often results in better solar cell performance, the microphase separated structure of the BHJ devices is not thermodynamically stable and its formation is not easy to control. So both architectures have their right to exist, and both are applied frequently. After introduction of the BHJ concept in 1995, the power conversion efficiencies could be increased from ~3 %[30] to around 10 %,[31] using the common fullerene acceptors. However, the state of

the art power conversion efficiencies cannot be reached in devices based on fullerene acceptors, but for solar cells that utilize small molecular acceptor dyes. These non-fullerene based solar cells already yield efficiencies of around 9[32] and 12 %[26] in PHJ and BHJ architecture, respectively. Accordingly, the concept of non-fullerene based solar cells appears to be the next great breakthrough in organic photovoltaics (apart from perovskite solar cells),[33] after discovery of fullerene acceptors (1985),[34] invention of PHJ (1986) and BHJ (1995) solar cell architectures. However, it is worth to mentioning that plenty of other strategies are pursued to optimize other limiting factors in organic solar cells. For example, concentrator cells[35,36] or double[37] and even triple junction solar cells[38], as well as advanced photoconductive interlayers[39,40] or inverted solar cells are fabricated.[41,42]

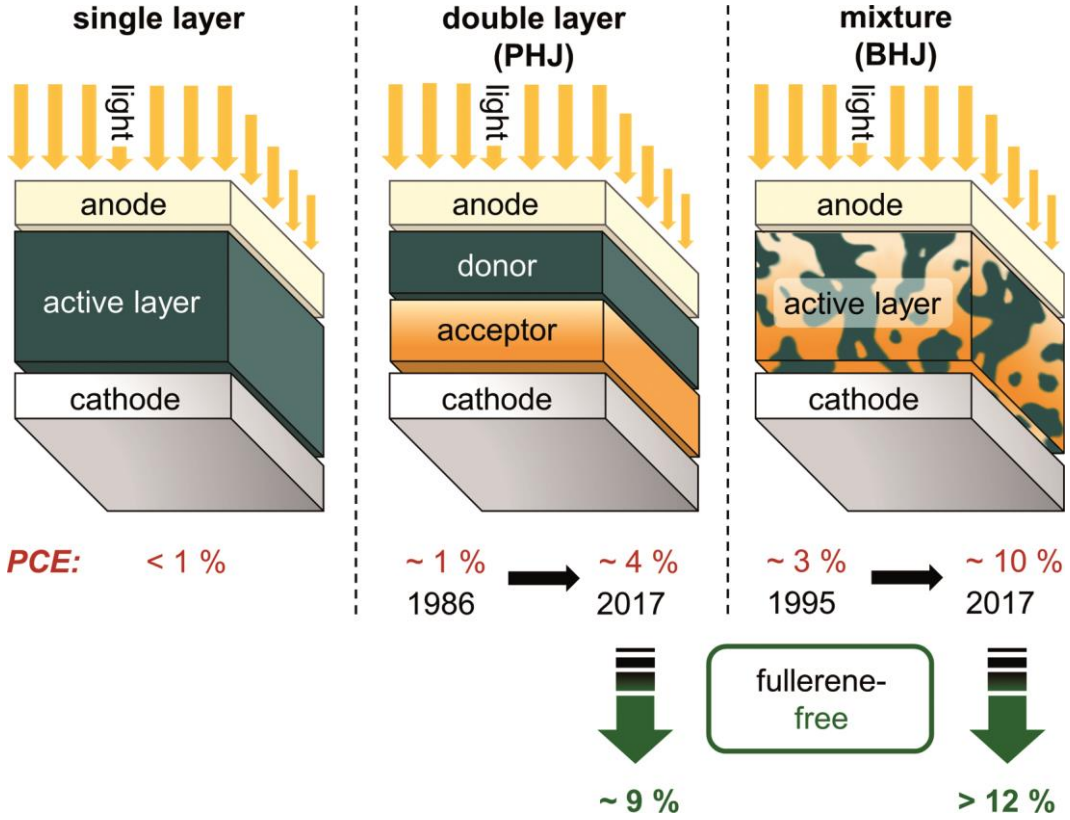

Figure 3. Organic solar cell device based on a single layer (left), a planar heterojunction layer (PHJ; middle) and on a bulk heterojunction architecture (BHJ; right) and corresponding power conversion efficiencies in fullerene-based (red) and fullerene-free devices (green).

2.1.2 Interlayers

Interlayers are indeed another important possibility to take influence on the device's performance. They consist of special materials that are either positioned between photoactive layer and anode (hole transport layer; HTL) or cathode (electron transport

layer; ETL). Their main functions are to adjust the energetic barrier height between electrode and active layer to give charge carrier selectivity, to determine the polarity of the device, to prevent reactions between active layer and electrode material and to function as optical spacer.[43] In the ideal case ohmic contacts are formed between the active layer and the electrodes, where the charges can flow easily from the active layer into the electrodes. If a difference between the metal work function ϕ_m and the semiconductor's electron affinity χ_s exists, a Schottky barrier is formed. In a most simple way the Schottky-barrier height Φ_B can be ascribed by $\Phi_B = \phi_m - \chi_s$.[44] This equation is often not valid because of another phenomenon, called Fermi-level pinning: The Fermi-level position of the semiconductor is independent of ϕ_m, due to the presence of surface-specific states.[43,44] In this case interlayers can help to reduce the barrier so that e.g. higher short circuit currents can be obtained.[44,45]

As can be seen in Figure 4, the polarity of the device is dependent on the position of electron and hole transport layer.[46] In conventional devices, the holes are collected at the transparent anode while the metal cathode collects the electrons. If a suitable electron

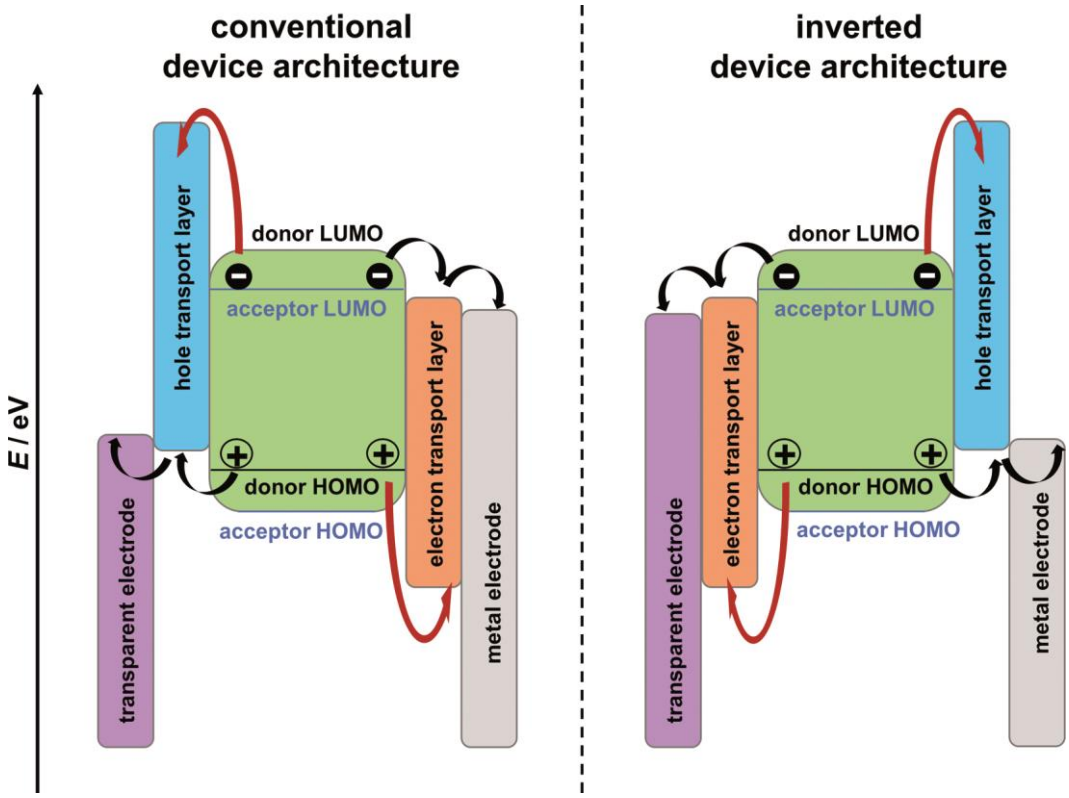

Figure 4. Schematic alignment of energy levels in BHJ solar cells with conventional (left) and inverted (right) device architecture. The polarity of the device is controlled by the interlayers. Black arrows indicate the desired path for charge carriers, while red arrows indicate pathways where the charges have to overcome high energy barriers (charge carrier selectivity). See reference[46] for more details.

transport layer is inserted between transparent electrode and semiconductor and a hole transport layer is positioned between semiconductor and metal electrode (inverted device architecture), the photo current flows though the device in reversed direction. In most cases the interlayer materials possess a large band gap. On the one hand this makes them transparent. However, on the other hand this leads to the fact that only their highest occupied molecular orbital (HOMO) or their lowest unoccupied molecular orbital (LUMO) fits well to one of the frontier molecular orbitals (FMO) of the small band gap active layer materials. Hole transport layers are in energetic alignment with the donor's HOMO level, while electron transport layers match the energy of the acceptor's LUMO level. As a consequence, interlayers collect only charge carriers of a specific type, when there is an energy level alignment with the active layer material, but they form a huge barrier for charges of the different type (red arrows, Figure 4). That is why the interlayers are often named hole or electron selective layers.

As stated earlier, interlayers can prevent chemical reactions or diffusion of material into the active layer, where recombination of excitons and charge carriers occurs. For example, during evaporation of Al for electrode preparation, some atoms can be embedded into the active layer of a solar cell, where they can react with one of the active layer components. Additionally, these Al atoms are able to react with the PCBM's carboxylic oxygen atom.[47] Consequently, the interlayer can shield the active layer and prevent the formation of traps. The light distribution inside of an organic solar cell, which is an interferential thin film system, can be most effectively optimized by adjusting the interlayer thickness. Adjustment via the active layer thickness is unfavorable, because this already has to match e.g. the exciton diffusion length. For example, S. B. Dkhil *et al.* showed by simulations that the variation of a ZnO interlayer thickness (0 to 70 nm) lead to a large variation in the number of photons absorbed by the solar cell (up to 35 %).[48] Therefore, control of active layer thickness can lead to a huge improvement in the performance of the device.

Interlayer engineering appears like a research field of its own. However, some frequently applied compounds that are also utilized in this work, are described below: PEDOT:PSS is the most widely used HTL, because it works well in organic solar cells (OSC) and organic light emitting diodes (OLED).[49] Its work function is at around −5.1 eV, but it highly depends on the segregation of PSS to the thin film surface after processing.[50] PEDOT:PSS films consist of ellipsoidal-shaped PEDOT particles that are separated by

insulating PSS layers.[51,52] In-plane the PSS layer thickness is 1 nm while perpendicular to the surface it amounts to 3 – 4 nm, yielding an anisotropic conductivity.[51,53,54] Advantages of PEDOT:PSS are its adjustable conductivity via the PEDOT to PSS ratio,[53,55] its good transparency,[56] and its high ductility.[57] Disadvantages of PEDOT:PSS include the etching of the commonly used ITO electrodes, due to the fact that PSS is highly acidic (release of In^{III+})[58,59] and the fact that PSS is very hygroscopic, which leads to an accumulation of PSS at the layer surface and consequently a reduced conductivity.[56] Furthermore, it is worth noticing that PEDOT:PSS is processed as aqueous suspension, typically via spin coating, and dried on a hot plate. While this enables the subsequent processing of the active layer through the orthogonal solvent approach, it is hard to say how much water will remain in the PEDOT:PSS, especially under ambient conditions, which is far from being ideal and in the end might lead to faster device degradation and weaker performance.

As alternative to PEDOT:PSS, metal oxides like molybdenum oxide are frequently used as HTL. Like PEDOT:PSS, MoO_3 has a good transparency and an improved environmental stability.[60] While the work function of PEDOT:PSS (~ −5.1 eV) can limit the charge injection into materials with deep lying HOMO levels,[61] the work function of MoO_3 is typically much lower, up to −6.9 eV. This would mean that MoO_3 works as n-type semiconductor. However, MoO_3 is often used successfully as hole transport layer. This is probably due to high variation in the work function of MoO_3, which depends on the amount of oxygen vacancies/MoO_3 stoichiometry,[62,63] on the processing procedure[61] or on the surface oxidation state. For example, in oxygen or air exposed MoO_3 layers the work function decreases to typically −5.3 to −5.7 eV, resulting in p-type semiconducting behavior.[64]

Even though it appears as if calcium is an interlayer, it functions as a low work function electrode material (−2.9 eV). Organic solar cells with Ca typically show a higher open circuit voltage compared to devices with Al or Ag electrodes.[30] Often thick layers of Al or Ag are evaporated on top of the calcium film, mainly to protect the Ca layer from oxygen and moisture.[65]

LiF in combination with an Al electrode is frequently used as ETL in organic solar cells, where it helps to increase fill factor and open-circuit voltage.[66] It is assumed to form a dipole layer, which lowers the metal's work function for better energy level alignment

between active layer and electrode.[67–69] This is in agreement with the fact that dipole layers at the interface are probably able to overcome the Fermi-level pinning effects.[44] Doping of the active layer is another proposed mechanism for LiF interlayers.[70,71]

2.1.3 Light to Energy Conversion in Organic Solar Cells

In organic photovoltaic devices six processes are of importance in converting incident light into electrical energy. A deep understanding of every single step is important, when e.g. active layer materials or new device architectures are to be designed. The different processes are shown in Figure 5 for the case of excitation at the donor molecule in a PHJ solar cell. Analogous, the six steps could be expressed for excitation of the acceptor and for BHJ solar cells, too.

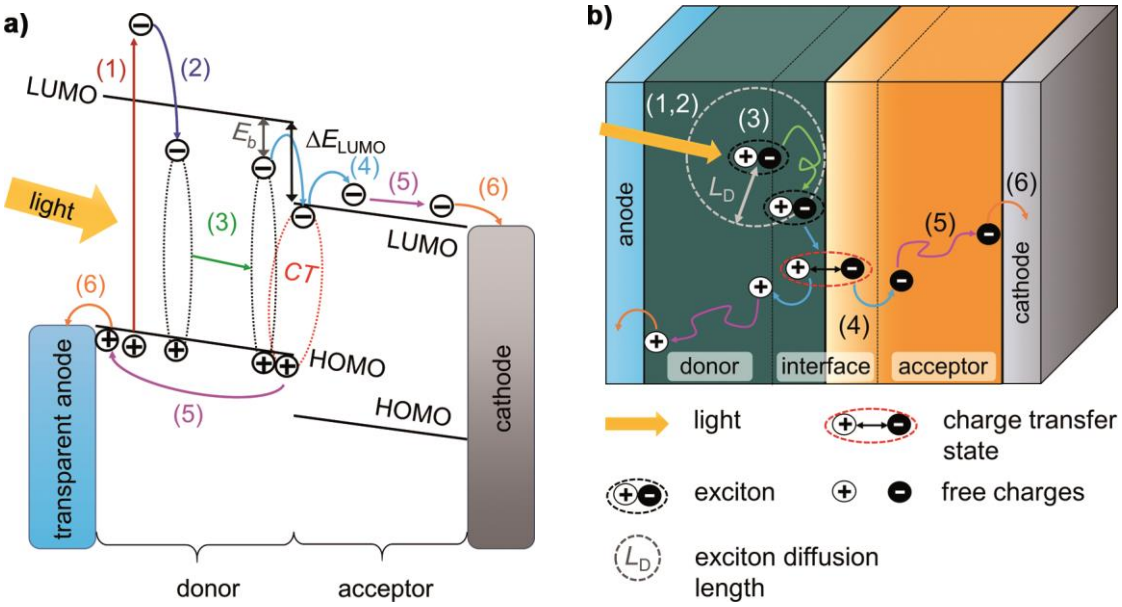

Figure 5. Important steps for light conversion in organic solar cells: (1) Light absorption, (2) exciton formation, (3) exciton diffusion, (4) exciton dissociation, (5) charge transport and (6) charge collection. a) Processes are shown in a band diagram of a PHJ solar cell (energetic picture). A forward bias is applied to the device, so that operation at the maximum power point is ensured. E_b is the exciton binding energy and ΔE_{LUMO} is the energy difference between donor and acceptor LUMO levels. b) Processes are shown in a schematic structure of a PHJ solar cell (spatial image).

During the first step light has to be absorbed (1), which leads to the formation of a bound electron hole pair (2). Further, the bound electron hole pair, also known as exciton, has to diffuse to the donor-acceptor interface (3), where enough driving force is present for exciton dissociation (4). The free charge carriers can be transported to the corresponding electrodes (5), where they are finally collected (6). The six processes are discussed in more detail as follows.

Light Absorption and Exciton Formation (steps 1 & 2)

During the first step light has to be absorbed by the active layer of the device. To reduce energy losses during this step, as much light as possible has to reach the active layer of the organic solar cell, so that substrate, electrode as well as a possible interlayer have to be as transparent as possible. Additionally, the reflectance at all interfaces should be minimized. One exception is the back contact, which functions as reflective mirror, so that all light that is not absorbed after passing through the active layer is reflected and has another chance to be absorbed (Figure 6). The light can only be absorbed by the active layer materials, if its energy is equal to the energy between two stationary states of one of these dyes.[72] Simplified, the energy of photons ($E_{photon} = h\nu$) has to be higher than a specific threshold, which is given by the active layer material. Photons with lower energies are transmitted or reflected. The amount of light absorbed by the active layer depends on the molar extinction coefficient of the molecules, their orientation with regard to the direction of the incident light and on the thickness of the active layer. It is worth mentioning that the absorption of organic solar cells cannot be described properly by the Beer-Lambert law because they are made of anisotropically aligned thin films.[72]

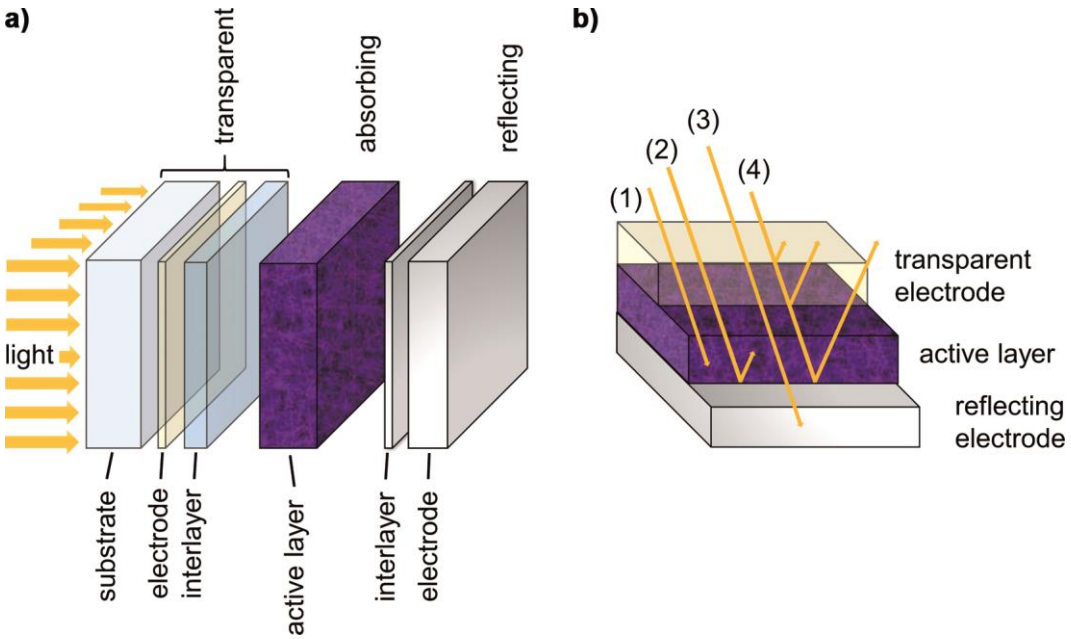

Figure 6. a) Structure of an organic solar cell consisting of transparent substrate, top electrode and interlayer, a strongly absorbing active layer and of another interlayer completed by a reflecting back electrode. b) Light shining onto a solar cell is (1) absorbed, (2) absorbed after reflection at the back contact, (3) parasitically absorbed by the top back contacts or (4) reflected out of the device at different interfaces.

Several hundred femtoseconds after light absorption, bound electron-hole pairs (excitons) form within the organic semiconductor/absorbing material.[73] Because of the

low dielectric constant ε_r of organic materials, Coulombic interactions are typically strong, thus, the excitons are strongly bound.[74] The exciton binding energy E_b (see Figure 5a) can be estimated according to Equation 2.1, where μ_{eh} is the effective mass of the exciton, m_e is the free electron mass, ε_r is the relative dielectric constant of the absorber and E_{ion}^{H} is the ionization energy of the hydrogen atom. Usually, values of 0.3 to 0.8 eV are obtained for E_b in organic semiconductors.[75] This corresponds well to the practically observed values for the exciton binding energy of 0.3 – 1.4 eV.[76]

$$E_b = \frac{\mu_{eh}}{m_e}\frac{1}{\varepsilon_r^2}E_{ion}^{H}. \tag{2.1}$$

Some trends for the exciton binding energy were observed by Djurovich *et al.* and Hummer *et al.*, who showed that E_b increases with increasing band gap and that E_b decreases with increased size of the molecule.[77]

Exciton Diffusion and Dissociation (steps 3 & 4)

Excitons are neutral quasi-particles that are formed e.g. after photoexcitation in organic semiconductors,[75] where they are strongly bound via the exciton binding energy E_b. To distinguish them from the weakly bound and delocalized Wannier-Mott excitons, formed in inorganic semiconductors, they are called Frenkel excitons. As mentioned earlier, the exciton binding energy has to be overcome in organic solar cells to generate free charge carriers. Therefore, it is favorable to use a combination of donor and acceptor molecules in the active layer. The energy of the FMO's of the acceptor molecules has to be lower than in the donor molecules, to create a driving force for exciton dissociation. For efficient exciton dissociation at the donor and acceptor interface, the energy difference between donor and acceptor has to be higher than E_b. Otherwise the exciton dissociation is not thermodynamically favored.[78] So if an exciton is created within the bulk material, it has to reach the donor-acceptor interface in order to undergo dissociation. Consequently, it has to move from the position where it was created to the interface. Because excitons are neutral in charge, their motion is not affected by the electrical field,[6] they move randomly from areas of high to areas of low concentration.[79] This type of movement is known as diffusion. The average displacement of the exciton from its initial position is known as exciton diffusion length L_D (see Figure 5b) and can be expressed as follows:

$$L_D = \sqrt{ZD\tau}, \tag{2.2}$$

where Z amounts to 1, 2 or 3 for diffusion in one-, two- or three-dimensions, D is a diffusion coefficient and τ is the exciton's lifetime.[80] In the ideal case L_D is very high, so that all generated excitons are able to reach the interface before they recombine. If this is not the case, the active layer thickness has to be optimized so that a donor-acceptor interface can always be reached within L_D. This is e.g. possible by either decreasing the thickness of donor or acceptor layer, which will also cause reduced light absorption, or by using the microphase-separated BHJ architecture (see above). Common values for exciton diffusion lengths in organic solar cells are $10 - 40$ nm.[81] In order to obtain a high L_D the lifetime τ of the excitons has to be high, but in most cases values below 1 ns are observed (conjugated polymer films).[82] Additionally, a fast exciton movement/high diffusion coefficient is desired. But the exciton dissociation depends on the time the exciton stays at the interface, too. So fast exciton migration might require very fast exciton dissociation at the interface, otherwise the device will not work well.[83] A high polarizability at the interface region helps in this case, because then the excitons are trapped at the interface, which is favorable for the dissociation process.[78] At the donor-acceptor interface electrons will be transferred from the donor to the acceptor. This process is very fast and efficient (several hundreds of femtoseconds) and leads to the formation of a charge transfer state.[84,85] Whether free charge carriers are formed directly from this state or if an intermediate 'charge transfer exciton' is formed, is still under debate.[86] It is worth mentioning that dissociation of excitons is also possible at trap sites within the active layer material, where one of the charge carriers is trapped, while the other one stays free.[87,88]

Charge Transport to the Electrodes (step 5)

After separation of the excitons, the free charge carriers have to be transported to the electrodes. The transport of the charges is driven by two factors. One is the potential gradient (V_{bi}) which is created by the different electrodes in the organic solar cell. As mentioned earlier, this potential gradient is not very high at the working point of an organic solar cell. So, as second driving force the diffusion current becomes more important, which is driven by the charge carrier concentration inside of the solar cell. Accordingly, the charges move away from the donor-acceptor interface, where they are

generated.[74] Both factors are included in Equation 2.3, which describes the total current density as function of drift and diffusion current density:

$$j_{\text{total}} = j_{\text{drift}} + j_{\text{diffusion}} = en\mu E + kT\mu\nabla n. \tag{2.3}$$

In this equation e is the elementary charge, n is the concentration of charge carriers, μ is the charge carrier mobility, E is the electric field, k is the Boltzmann constant, T the temperature and ∇n is the charge carrier concentration gradient.[89] As a consequence, the most important parameter for the charge transport is the charge carrier mobility inside of the active layer. It can be probed by different techniques: the time of flight (ToF) technique, the space charge limited current (SCLC) method, the characterization in field-effect transistors (FET), and a method where charge carriers are extracted by linearly increasing voltage (CELIV).[90] Charge carrier mobilities are typically low in organic materials, but nowadays they can exceed the mobility of amorphous silicon thin-film devices (0.5 – 1 $cm^2 V^{-1} s^{-1}$), which was considered limit for application.[91] Koster *et al.* showed that the slowest charge carrier dominates the recombination process.[92] Furthermore, space charges are built up within the device, if the charge carrier mobilities are unbalanced. This would limit the maximum photocurrent of the solar cell.[93] So a careful adjustment by e.g. synthesis or variation of donor to acceptor ratio of donor and acceptor mobilities is very important. The charge transport is in competition with recombination. The bimolecular recombination of the free carriers is a very important process, which depends on the charge carrier mobility, too.[94] In PHJ solar cells recombination should be low, because electrons and holes are spatially separated in the acceptor and donor layers. Due to the mircophase-separation in BHJ solar cells, charges are more likely to meet in these devices and therefore the charge recombination is typically more pronounced.

Charge Collection at the Electrodes (step 6)

For efficient charge collection at the electrodes, the formation of an ohmic contact is desired. If this is not the case, the charge carrier collection is hindered and charges can accumulate at the electrode, which would then affect a reduced charge dissociation and charge diffusion. Additionally, the electrodes should possess selectivity for one type of charge carrier, so that recombination at the electrode with charge carriers of the different type is excluded.[95] Important electrode parameters under investigation are e.g. the

metal's work function, the surface energy, the wetting properties, the stability as well as the selectivity of the contacts.[96]

2.1.4 Influence of Ambient Conditions

Once fabricated organic solar cells start to degrade, which means that the power conversion efficiency of the devices decreases over time. Many factors play a role in device degradation, which are not only related to external factors present under ambient conditions (e.g. air, moisture). Thus, degradation could be observed in devices that were encapsulated in sealed glass containers or even stored in a high vacuum chamber.[97,98] Some mechanisms and processes that lead to degradation of the device are given as follows:

Degradation by Diffusion

One example for degradation by diffusion are indium atoms that are released over time from transparent indium tin oxide (ITO) electrodes. This process is accelerated by moisture and acidic compounds like PEDOT:PSS, which is commonly used as interlayer on top of an ITO electrode.[99] For the indium ions it is possible to move through the whole device.[100] Lee *et al.* could show that indium ions that were released into the active layer of OLED devices, lead to luminescence quenching.[101]

Chemical and Photochemical Reactions

Chemical reactions are one possible degradation pathway in organic solar cells. For example, common electrode materials like aluminum can either be oxidized forming an insulating layer of aluminum oxide or they undergo chemical reactions with active layer components like poly(*p*-phenylenevinylene) (PPV), as suggested by calculations done in literature (Figure 7a).[102] Photochemical reactions like shown in Figure 7b,c for a common donor polymer poly[2-methoxy-5-(2-ethylhexyloxy)-1,4-phenylene vinylene] (MEH-PPV) are possible, too. By light absorption organic compounds become more oxidative as well as more reductive so that further chemical reactions can occur quite easily. Figure 7a shows an example: a dioxetane intermediate is formed in a [2+2] cycloaddition, which decomposes into two aldehyde species and by that cleave the MEH-PPV polymer chain.[103] Of course, this leads to a change of material properties and will affect the device's performance. Additionally, the generated aldehyde species bear further potential for subsequent reactions. Another example is the cleavage of a

solubilizing side chain of MEH-PPV upon irradiation and under presence of oxygen. The radical based reaction mechanism proposed by Chambon *et al.* is shown in Figure 7b. Not only the polymeric structure and properties are changed in this example, but also a variety of decomposition products are released into the active layer.

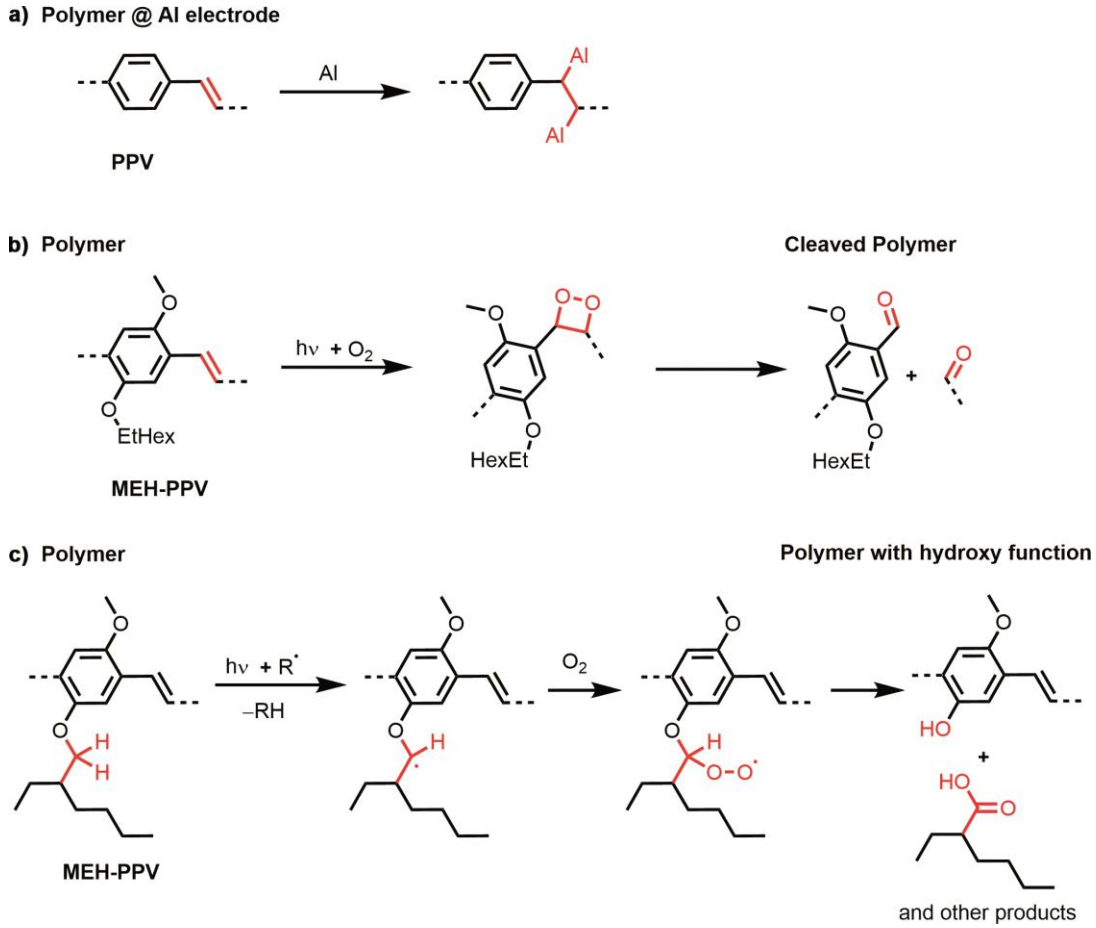

Figure 7. a) Possible reaction of poly(*p*-phenylenevinylene) with aluminum at the metal-polymer interface according to literature.[102] b) Cleavage of vinylene bond in a common donor polymer (MEH-PPV) by singlet oxygen. c) Photodegradation of MEH-PPV, induced by light absorption and in the presence of oxygen. Figure based on reference[104].

Morphology Degradation

Layer thicknesses, homogeneity and morphology especially of the BHJ active layer are crucial for a good performance of the device. In most cases a nano- to microphase separated microstructure is required. This structure, which is typically the best for solar cell operation, is not the most thermodynamically stable one, because the active layer components are still able to move slowly over time. This is especially true at higher temperatures (heating of device during operation by e.g. illumination), so that active layer components might completely separate.[104] In consequence, this would tremendously decrease the device's performance. Also, interlayers like PEDOT:PSS undergo

morphological changes over time. Due to the hygroscopic behavior of PSS, segregation of PEDOT and PSS can be observed in the presence of moisture. This decreases the electrical conductivity of the layer or even removes it, which is highly unfavorable for operation of the device.

To sum up, the degradation of solar cells is a complex process that depends on a variety of factors and cannot be stopped completely, not even by the best encapsulation available. Studying the degradation pathways of active layer and interlayer components in detail can help to design molecules with less 'weak points', e.g. labile or reactive bonds. It is also possible to change the device architecture in order to increase the stability of the solar cells, e.g. ITO can be substituted by silver nanowires or an inverted device architecture can be used, where the high work function metal protects the device.[105,106]

2.2 Characterization of Organic Solar Cells

2.2.1 Operation Regimes of a Bulk Heterojunction Solar Cell

For device characterization it is helpful to understand the operation regimes of a bulk heterojunction (BHJ) solar cell. A simple model is shown in Figure 8.

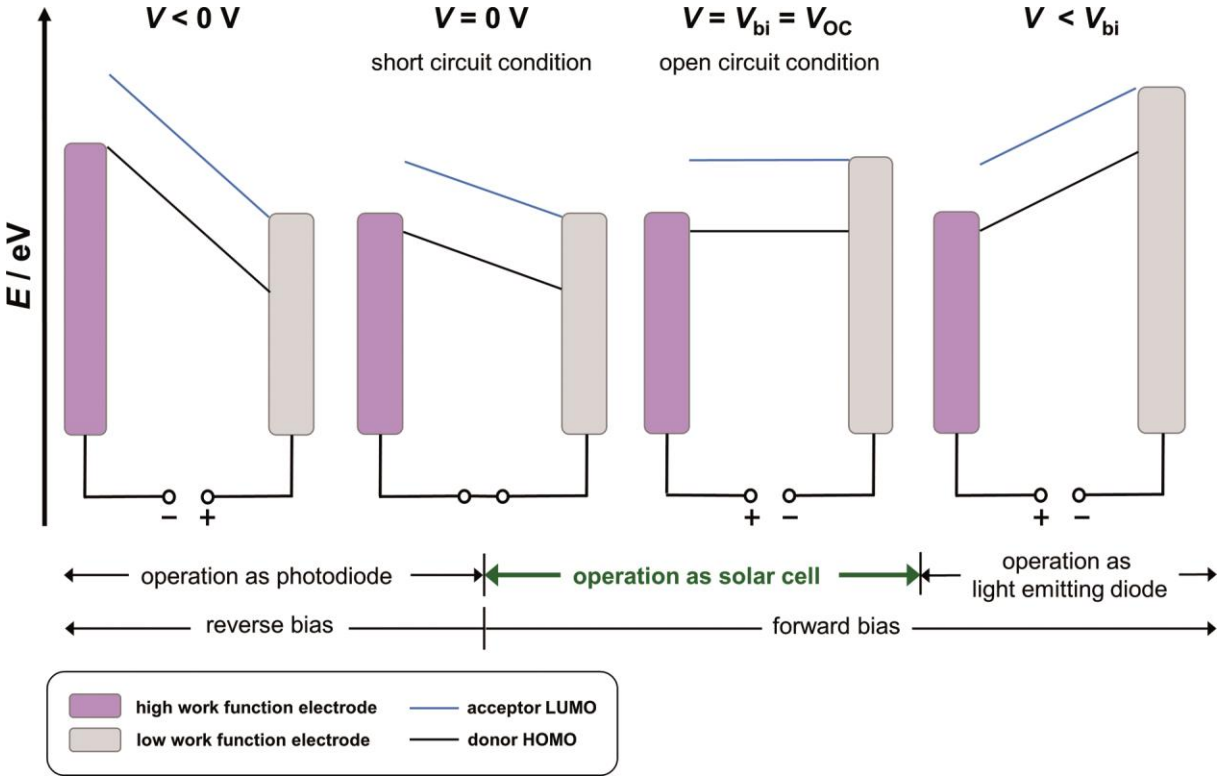

Figure 8. Schematic energy diagram of an organic BHJ solar cell, showing different bias conditions and operation regimes.

The active layer of a BHJ solar cell is represented by the energy levels that are important for the charge transport. These are the LUMO levels of the acceptor molecules (electron transport) and the HOMO levels of the donor molecules (hole transport). The active layer is sandwiched between two electrodes, one with a high work function and the other one with a low work function. A negative, a positive or no bias can be applied. When the voltage is zero the system is at equilibrium, where the fermi levels of the electrodes must be the same. This leads to a tilt of the bands in the organic semiconductor, which is in the size of the electrode work function difference. In general, the strength of the tilts is correlated to the electrical field within the organic layer, which drives the motion of the charges in the device. In this model the work function difference of the pristine electrodes is called build in potential V_{bi}. At V equals 0 V the short circuit current can be measured in organic solar cells. The tilt of the energy bands can be increased, when a reverse bias

is applied (V < 0 V). Then the device can operate as photodiode, because the initial current which flows through the device is very low and increases linearly upon illumination. When a forward voltage (V > 0 V) is applied, the tilt of the bands is reduced. Now the device can operate as solar cell, until the applied voltage matches V_{bi}. A situation where V equals V_{bi} leads to flat energy bands, the driving force for charges to move is not present. Accordingly, the open circuit voltage can be measured in this case. It is worth mentioning that the ideal operating point (maximum power point) of a solar cell is typically quite close to a situation where V is close to $V_{bi.}$ As a consequence, the charge carriers diffuse rather than drift,[107] which again verifies the importance of interlayers. If the applied voltage exceeds the build in voltage ($V > V_{bi}$) charges are injected into the device, where they recombine. Thus, in this region the device behaves as light emitting diode.

2.2.2 *I-V* Measurements

Organic solar cells are made for energy production by conversion of light into electrical energy. Therefore, it is important to know how efficient they can perform this conversion. This is described by the power conversion efficiency (*PCE*), which is the most important solar cell parameter. It is defined as the ratio between output power (P_{out}) to input power (P_{out}):

$$PCE = \frac{P_{out}}{P_{in}}. \tag{2.4}$$

To determine the *PCE* of a solar cell it is required to measure the power output, but according to Equation 2.4 it is also important to know how much power is shining onto the device. As consequence, a light source is needed which has a defined light spectrum and power output. Additionally, it should be similar to the sunlight, as this is the light source which is important for real application. Therefore, the AM 1.5G spectrum was defined, which is used with an intensity of 100 mW cm^{-2}. Detailed information can be found in the reference.[108] The AM 1.5G spectrum is shown in Figure 9. Exemplarily, the optical band gap E_g of an organic semiconductor is given (E_g ~ 1.5 eV). All light lower in energy is not absorbed, while light with higher energy than E_g is absorbed by the organic compound.

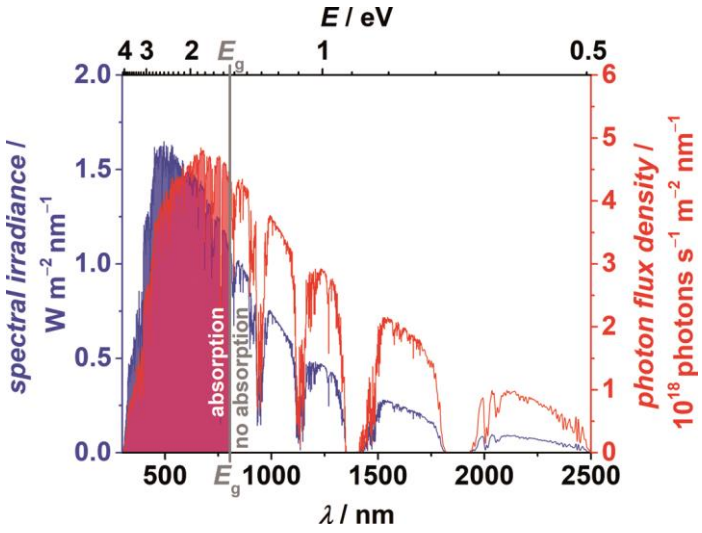

Figure 9. Spectral irradiance and photon flux density of the AM1.5 G spectrum. The band gap of an organic semiconductor E_g is given and the curves are filled where light is absorbed ($\lambda < 800$ nm).

In Figure 10a an example for a current voltage characteristic of an organic solar cell is displayed, which was measured under simulated AM1.5 G illumination with a light intensity of 100 mW cm^{-2}. Herein, important parameters are defined which are characteristic for each device. These are the maximum power point *MPP*, the short circuit current I_{SC}, the open circuit voltage V_{OC}, and the fill factor *FF*. The *MPP*, defined by V_{MPP} and I_{MPP}, is the point where the highest power output P_{MPP} (compare the green curve) is generated by the solar cell. Devices in application typically operate at this point. The highest photo current and photo voltage that can be produced by solar cells are given by I_{SC} and V_{OC} under short and open circuit conditions. How the present solar cell behaves in comparison to an ideal photovoltaic device with corresponding V_{OC} and I_{SC} is defined by the fill factor *FF*:

$$FF = \frac{V_{MPP} I_{MPP}}{V_{OC} I_{SC}}, \tag{2.5}$$

with the help of Equation 2.5 Equation 2.4 also can be expressed as follows:

$$PCE = \frac{V_{MPP} I_{MPP}}{P_{in}} = \frac{FF V_{OC} I_{SC}}{P_{in}}. \tag{2.6}$$

This means that in order to get high power conversion efficiencies *FF*, V_{OC} as well as I_{SC} have to be optimized, while the incoming light is fixed according to the standard AM 1.5G illumination, mentioned above.

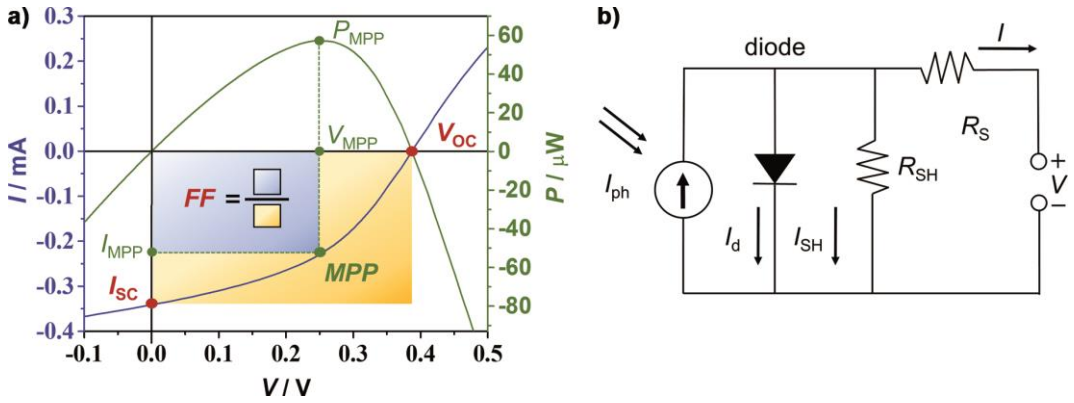

Figure 10. a) *I*–*V* characteristics of an organic solar cell and power plot, illustrating the important solar cell parameters: short circuit current I_{SC}, open circuit voltage V_{OC} and maximum power point *MPP* given by I_{MPP} and V_{MPP}. The blue area represents the maximum power of the present solar cell and the yellow area gives the maximum power of an ideal solar cell with given I_{SC} and V_{OC}. b) Simple but frequently used equivalent circuit, with current source, diode, shunt resistance R_{SH} and series resistance R_S, for modeling the current voltage characteristics of organic solar cells.

Without external illumination an organic solar cell behaves like a diode. In the ideal case the diode current I can be described by the Shockley Equation 2.7, where I_0 is the reverse current, V is the diode voltage, n is the ideality factor and V_T is the thermal voltage ($V_T = k_B T/e$).

$$I = I_0 \left[e^{\frac{V+IR_S}{nV_T}} - 1 \right]. \tag{2.7}$$

Under illumination a photocurrent I_{ph} is generated which is often described by the equivalent circuit given in Figure 10b.[109] It is worth mentioning that this equivalent circuit is based on the single-diode model and a variety of more complex models can be found in the literature, e.g. based on the double-diode model.[109,110] According to this model the current of the device I is given by photocurrent I_{ph}, the diode current I_d and the shunt current I_{SH}:

$$I = I_{ph} - I_d - I_{SH} = I_{ph} - I_0 \left[e^{\frac{V+IR_S}{nV_T}} - 1 \right] - \frac{V + IR_S}{R_{SH}}. \tag{2.8}$$

In this formula R_S is the series resistance, R_{SH} is the shunt resistance. As a result, it is necessary to obtain a very high shunt resistance, while the series resistance of the device should be as low as possible, for a good performance. Both resistances do have an effect on the shape of the *I*-*V* curve and so they influence the fill factor. For a better comparison of solar cells made in different geometry or with increased device area, the current density J [mA cm^{-2}] is frequently used instead of the current I [mA].

In 1961 W. Shockley and H. J. Queisser introduced a simple calculation to obtain an upper limit for the efficiency of a p-n junction solar cell. It was calculated to be around 30 % for single junction device under non-concentrated light.[111] Some fundamental phenomena that lead to a more limited power conversion efficiency are shown in Figure 11. 1) Only photons with energy exceeding the optical band gap ($E_{h\upsilon} < E_g$) can be collected and transformed into electrical energy; 2) Charge carriers that are created upon light absorption ($E_{h\upsilon} < E_{light}$) undergo thermalization E_t and relax down to the LUMO level energy; 3) To overcome the exciton binding energy E_b an energy offset between donor and acceptor LUMO levels is necessary, so less energy can be collected and 4) an additional voltage loss (E_v) of around 0.3 eV is often reported, which decreases the open circuit voltage V_{OC} in organic solar cells, given by Equation 2.9:[112,113]

$$V_{OC} = \frac{1}{e}\left(|E_{HOMO}^{donor}| - |E_{LUMO}^{acceptor}|\right) - 0.3. \tag{2.9}$$

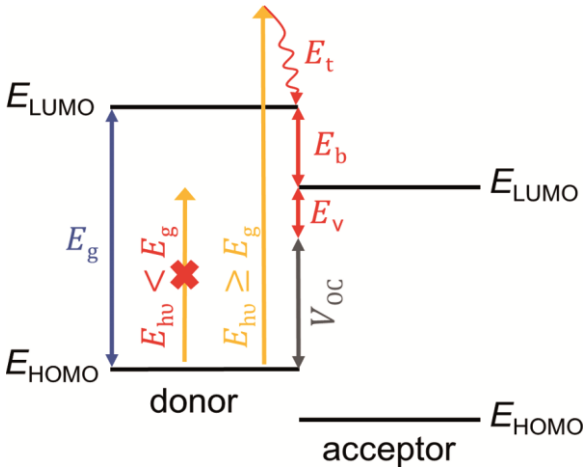

Figure 11. Fundamental phenomena limiting the performance of organic solar cells. Band gap of the donor E_g, light energy E_{light}, thermalization energy E_t, exciton binding energy E_b, empirical energy loss in open circuit voltage E_v and expected open circuit voltage V_{oc}. Energies that will be lost are marked in red.

If further losses are assumed, namely a *EQE* of 65 % for energies larger than the semiconductors band gap E_g, and a maximum fill factor of 65 %, a practical limit can be calculated that is around 11 %. In Figure 12 this calculation was performed for different HOMO or LUMO differences (ΔE_{HOMO} and ΔE_{LUMO}) between donor and acceptor molecules. Thereby, ΔE_{HOMO} and ΔE_{LUMO} ideally match E_b. These calculations show that a small exciton binding energy E_b and an optical band gap E_g of around 1.5 eV are ideal.[114] It is worth mentioning that the Shockley-Queisser calculation is valid for single junction solar cells, but it can be overcome by e.g. tandem solar cells. These consist of

two sub-cells which absorb complementarily, yielding a new *PCE* limit of around 42 %.[115]

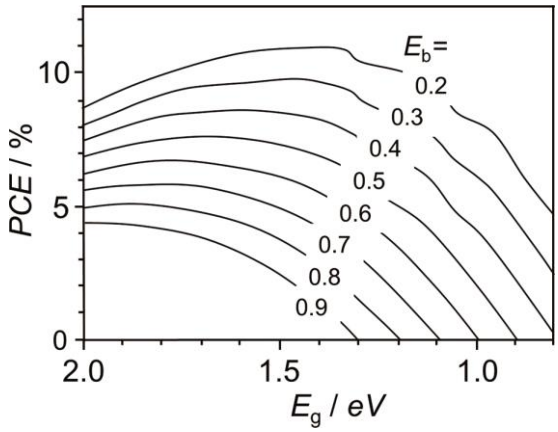

Figure 12. Energy conversion efficiency of bulk heterojunction solar cells under AM 1.5G illumination as a function of optical gap of donor or acceptor molecules. For calculation it was assumed that the *EQE* is at 65 % for energies larger than the optical gap, the fill factor is 65 % and an open circuit voltage is given by $|E_{\mathrm{HOMO}}^{\mathrm{donor}}| - |E_{\mathrm{LUMO}}^{\mathrm{acceptor}}|$ reduced by the exciton binding energy (0.4 eV). Reproduced from reference[114] with permission from Wiley-VCH Verlag GmbH, Copyright 2017.

2.2.3 External Quantum Efficiency Measurements (*EQE*)

The external quantum efficiency *EQE* is given by Equation 2.10. It gives information about the light absorption and the creation of charge carriers within the device. Typically, it is measured as a function of wavelength, resulting in an *EQE* spectrum.[116]

$$EQE(\lambda) = \frac{collected\ electrons}{incident\ photons}. \tag{2.10}$$

An example for a spectrally resolved external quantum efficiency is given in Figure 13. In the ideal case the external quantum efficiency is at 100 % for all wavelengths that are absorbed. This is determined by the optical band gap E_g. In reality the *EQE* is lower than 100 %, which is a result of e.g. reflection, absorption and recombination losses.[116] If the *EQE* is measured under short circuit current conditions (V = 0 V), it is possible to calculate the short circuit current of the solar cell using the *EQE* spectrum (see Equation 2.11).

$$I_{\mathrm{SC}} = \frac{hc}{e}\int \frac{E_{\mathrm{AM1.5G}}(\lambda)EQE(\lambda)}{\lambda} d\lambda, \tag{2.11}$$

where h is the Planck's quantum, c is the speed of light, e is the elementary charge, $E_{\mathrm{AM1.5G}}$ is the solar spectrum, *EQE* is the solar spectrum and λ is the wavelength. In the ideal case this calculated I_{SC} matches with the measured short circuit current

(*I-V* measurement) which can prove a good calibration of the solar simulator.[117] It is important to notice that this is only possible if the devices do not degrade during the measurement, which is often not guaranteed under ambient conditions. Furthermore, the measurement conditions during *EQE* determination should be comparable to those of *I-V* measurements. The incident light power is the largest difference between the two measurements, which can be overcome by application of additional light stress (bias light) during *EQE* measurement.

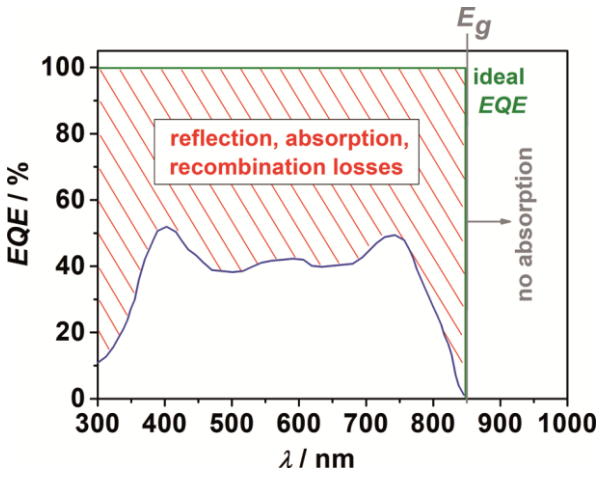

Figure 13. Spectrally resolved external quantum efficiency. Typical (blue) and ideal (green) *EQE* spectrum of an organic solar cell. Losses due to reflection, absorption or recombination processes are marked in red. A grey line indicates the smallest band gap E_g of utilized active layer components, intrinsically limiting the absorption to 'shorter' wavelength (< 850 nm).

Additionally, the *EQE* spectrum is necessary to perform a correction with the mismatch factor *MM*. This factor corrects for differences of the solar simulator spectrum E_{sim} to the ideal AM1.5 G spectrum $E_{AM1.5G}$ and for the difference in spectral response and therefore in *EQE*, of the calibrated reference cell and the measured cell under test. The spectral response *SR* is associated to the *EQE* by Equation 2.12.[118]

$$SR = \frac{e\lambda}{hc} EQE. \tag{2.12}$$

Accordingly, the spectral response of the calibrated silicon solar cell SR_{ref} and the spectral response of the organic solar cell under test SR_{test} can be determined. The mismatch factor itself is given by Equation 2.13:[119]

$$MM = \frac{\int E_{AM1.5G} SR_{ref} d\lambda}{\int E_{sim} SR_{ref} d\lambda} \frac{\int E_{sim} SR_{test} d\lambda}{\int E_{AM1.5G} SR_{test} d\lambda}. \tag{2.13}$$

A properly measured solar simulator spectrum E_{Sim} and an *EQE* of the organic solar cell are the most critical points for determination of the mismatch factor. The best way to minimize the mismatch factor is to use a reference cell whose *EQE* is as similar as possible to that of the organic solar cell under test.[118,120] It is worth mentioning that no absolute spectral responses are needed for the calculation which simplifies the mismatch correction.

2.3 Design of Active Layer Materials

2.3.1 General Design Rules

In addition to the design of organic solar cells, their functionality is described in Section 2.1. Device architectures ranging from single and PHJ to BHJ solar cell as well as the importance of interlayers were discussed. Furthermore, design rules related to the working principle were presented. However, another way to improve the solar cells function has not been mentioned so far and that is the design of new active layer components. This approach is powerful, versatile and very appealing especially for chemists. Most active layer materials that have been designed so far are either electron donor or acceptor components that belong to the class of polymers, oligomers and small molecules. Regardless of that, they have to fulfill several requirements in order to perform well in organic solar cells, which are discussed below.

The active layer materials in organic solar cells should be able to absorb light in the visible range of the sun's spectrum (400 – 700 nm), where the photon flux density is the maximized.[121] Light absorption of organic compounds is correlated to their band gap, which can be estimated by the simple Equation 2.14:

$$E_g = \frac{hc}{\lambda_{max}}, \tag{2.14}$$

where h is the Planck's quantum, c is the speed of light and λ_{max} is the absorption maximum of the organic semiconductor. Thus, by adjusting the band gap the absorption can be controlled, too. The ideal band gap for a single absorber was calculated to be quite low, around $1.2 - 1.6$ eV, which corresponds to a wavelength of 1000 – 800 nm.[111,113,122] If both components, donor and acceptor, are able to collect sunlight, a complementary absorption is able to enhance the photocurrent in the organic solar cell.[92,93] Consequently, two different band gaps are ideal for both active layer components, e.g. 1.9 and 1.0 eV.[113] The active layer thickness in organic solar cells is often around 100 nm.[123] In order to realize devices with lower active layer thickness with the same light harvesting capabilities, compounds with high extinction coefficients are desirable. Furthermore, reduced active layer thicknesses are good for exciton diffusion and charge carrier transport. Next to the absorption properties the position of the frontier molecular orbitals of the active layer components is important. As described in Section 2.1.3, the offset between the two active layer components' LUMO or HOMO

levels has to be as high as the exciton binding energy. If the offset is higher additional energy is lost unnecessarily. The energy difference between the donor's HOMO and the acceptor's LUMO levels should be as high as possible for high open circuit voltages. On the other hand, this is somewhat limited because the band gap (HOMO-LUMO distance) of donor and acceptor should be optimized for complementary light absorption, too.

There are several strategies available that allow to design new electron donor or acceptor materials, so that they can meet all or most of the criteria mentioned above. The strategies introduced below are valid for the design of both electron donor and electron acceptor materials.

Quinoid Approach[124]

In this approach the bond length alternation (*BLA*) is reduced by stabilizing the quinoid structure in a molecule or polymer. However, the aromatic form is usually lower in energy as the quinoidal form. To circumvent this problem two aromatic moieties can be fused. In doing so one unit has to possess a larger value of resonance energy than the second moiety, so that the second moiety starts to dearomatize, forming a more quinoidal structure. As an example benzene and thiophene can be fused (Figure 14), which have resonance energies of 150 and 122 kJ mol^{-1}, respectively.

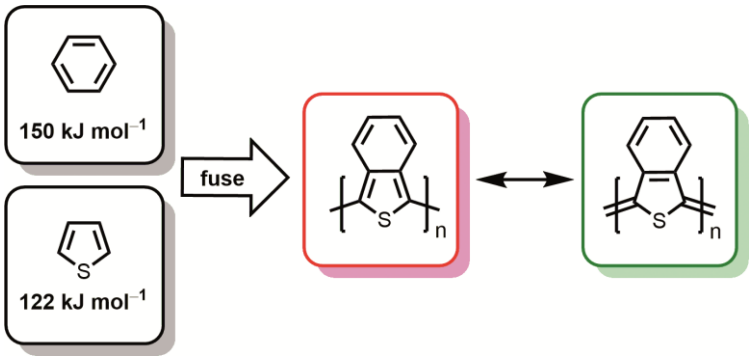

Figure 14. Quinoid approach. By fusing e.g. benzene (resonance energy of 150 kJ mol^{-1}) and thiophene (resonance energy of 122 kJ mol^{-1}) (left), systems can be generated where the quinoidal structure (green) is preferred over the aromatic structure (red) along the molecular/polymer backbone.

Donor-Acceptor Approach:

The donor-acceptor approach is frequently applied in the field of organic electronics. An electron-donating moiety is linked covalently to an electron-accepting unit, forming a quinoid resonance structure by intramolecular charge transfer (ICT).[125] The biggest advantage of this method is that it bears the possibility to take complete control over the

HOMO and LUMO level independently, which is a huge advantage with regard to molecular design.[124] However, apart from this ideal situation there are four more imaginable, if an electron donor is combined with an electron acceptor, forming a donor-acceptor compound (Figure 15).[126] Which situation is the case depends on the properties of the donor, acceptor moieties and how they are connected.

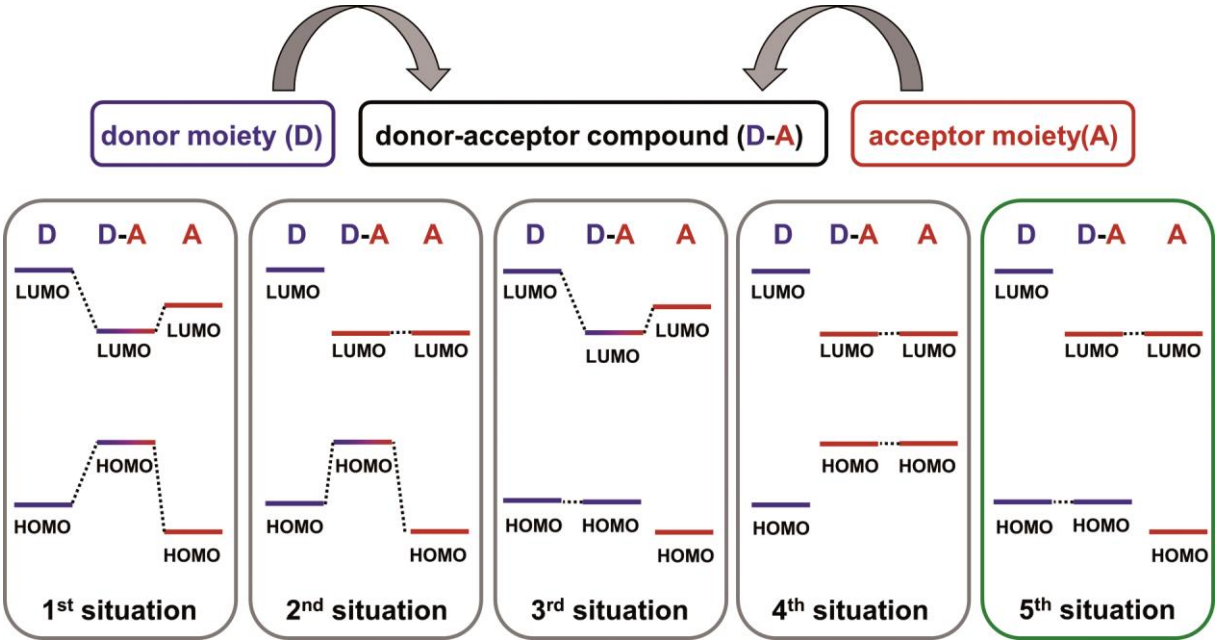

Figure 15. Donor (D, blue) and acceptor (A, red) moieties are combined to form donor-acceptor compounds (D-A). Five different situations for the behavior of the frontier molecular orbitals of the individual moieties and the donor-acceptor components are shown. The green frame (5th situation) highlights the most desired situation, where the HOMO and LUMO of the D-A compound are solely determined by utilized donor and acceptor moiety, respectively. Reproduced from reference[126] with permission from Wiley-VCH Verlag GmbH, Copyright 2017.

In the 1st situation the individual orbitals of donor and acceptor moieties are mixed in a way that the resulting frontier molecular orbitals of the donor-acceptor compound are delocalized over donor and acceptor units. In this situation, it is the most difficult to control the position of the frontier molecular orbitals of donor-acceptor compound. In the 2nd and 3rd situation either the HOMO or the LUMO level of the donor-acceptor compound can be completely controlled by utilization of a proper donor or acceptor moiety, respectively. This is already an improvement with regard to the first situation. In the 4th situation, the FMOs of the donor-acceptor compound are completely localized on the acceptor subunit and determined by its choice. However, this is not ideal because HOMO and LUMO, and therefore the band gap, cannot be controlled independently. The most ideal situation is the 5th one, because HOMO as well as LUMO level can be tuned separately, by choosing appropriate donor and acceptor moieties. Examples for all five

cases can be found in literature (1st situation,[127] 2nd situation,[128] 3rd situation,[129] 4th situation,[126] and 5th situation[130]).

Planarization Approach

The p_z orbitals of the carbon atoms are responsible for the formation of π-bonds. For delocalization of the π-electrons over the whole molecule a proper alignment of all neighboring p_z orbitals is required, e.g. between conjugated double bonds to give a fully conjugated π-scaffold. If the molecular backbone is twisted or bond rotation is possible, then the conjugation is hindered, which leads to higher band gaps and reduced charge carrier delocalization. Different strategies that can be followed in order to obtain more planar compounds are shown in Figure 16.

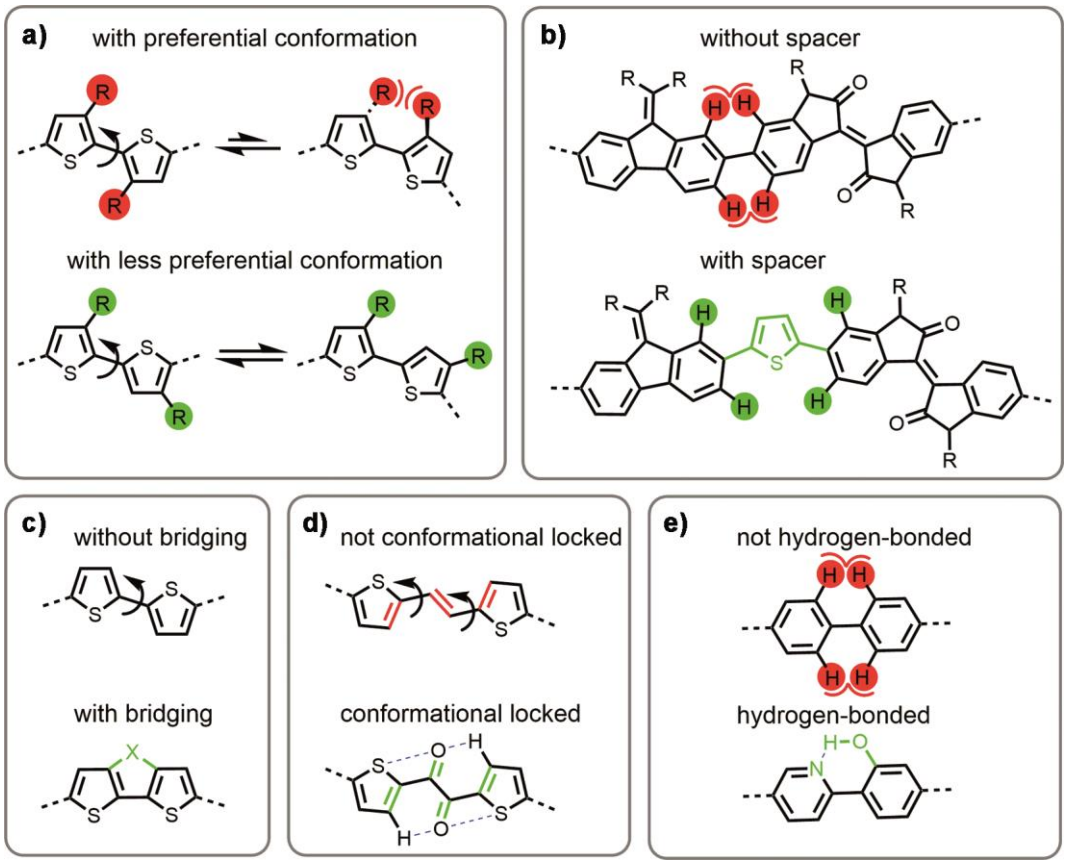

Figure 16. Approaches to planarize aromatic π-scaffolds by a) proper alignment of side chains, e.g. in regioregular fashion, b) utilization of spacer units, c) covalent bridging of neigboring moieties, d) locking the conformation over specific interactions and utilization of cross-conjugation and e) by introduction of hydrogen bonds.

Unfortunately, desired highly planar and rigid compounds are often not very soluble. Thus, the introduction of solubilizing side chains cannot be avoided. Unfortunately, these side chains can again reduce planarity of the molecules. A good example is poly(3-hexylthiophene-2,5-diyl) (P3HT), which can be synthesized with a region-

random or regio-regular orientation of the side chains. While the side chains can collide in the regio-random P3HT upon rotation of the thiophene subunits, this is not possible in the regio-regular derivative. Therefore, the latter component possesses a higher planarity, a smaller band gap as well as better packing properties in the solid state (Figure 16a).[131] Sometimes, neighboring moieties are twisted against each other, for steric reasons. One example are fluorene and isoindigo subunits that are covalently bound to each other (Figure 16b). By introducing a spacer unit, e.g. thiophene, the steric repulsion can be reduced, so that the planar conformation of the molecule is more favored.[132] It should be kept in mind that such changes will most likely affect the electronic properties of the molecule, too. Another possibility to really force two neighboring subunits into a planar arrangement is the introduction of another bridging atom, e.g. nitrogen or carbon, as shown in Figure 16c.[96] Conformational locking can further be achieved by putting the neighboring units in cross-conjugation so that with the help of specific interactions between oxygen and sulfur or hydrogen, the planar conformation can be stabilized (Figure 16d).[133] Similarly, classical hydrogen bonds can be used to hinder the rotation between two neighboring subunits (Figure 16e).[134]

Substituents and Heteroatoms

An efficient way to tune HOMO and LUMO levels is the introduction of chemical functionalities. These can be divided into electron-donating (e.g. $–NR_2$, –OR) and electron-withdrawing (e.g. –CN, –F) functionalities. If for example an electron-withdrawing substituent is used, electron density is drawn from the molecular backbone so that the LUMO level of the compound is lowered. Additionally, the band gap decreases, because the HOMO is less affected. If an electron-donating substituent is utilized, electron density is pushed into the molecular backbone and the HOMO level is raised. So in order to obtain electron accepting materials one should rather apply electron-withdrawing substituents. Furthermore, heteroatoms like nitrogen (N), oxygen (O) or sulfur (S) can be utilized to take influence on the HOMO and LUMO energies. Due to the higher electronegativity of the heteroatoms in comparison to carbon, many heterocyclic compounds are electron-deficient. For example, HOMO and LUMO levels of benzene can be lowered effectively by substitution of one (pyridine), two (pyrimidine) or three (triazine) carbon atoms by nitrogen.[135]

Oligomer-/Polymer-Approach

The semiconducting properties of organic molecules are the result of π-conjugated electrons. The more π-bonds are in conjugation with each other, the closer the HOMO and the LUMO levels are, defining the band gap. Additionally, conjugation leads to decreased bond length alternation *BLA*, so that the molecule does not exist out of alternating single and double bonds but rather out of equidistant atoms with delocalized π-bonds. The increased number of interacting states in highly conjugated molecules leads to a more band like character of their energy levels (Figure 17a).

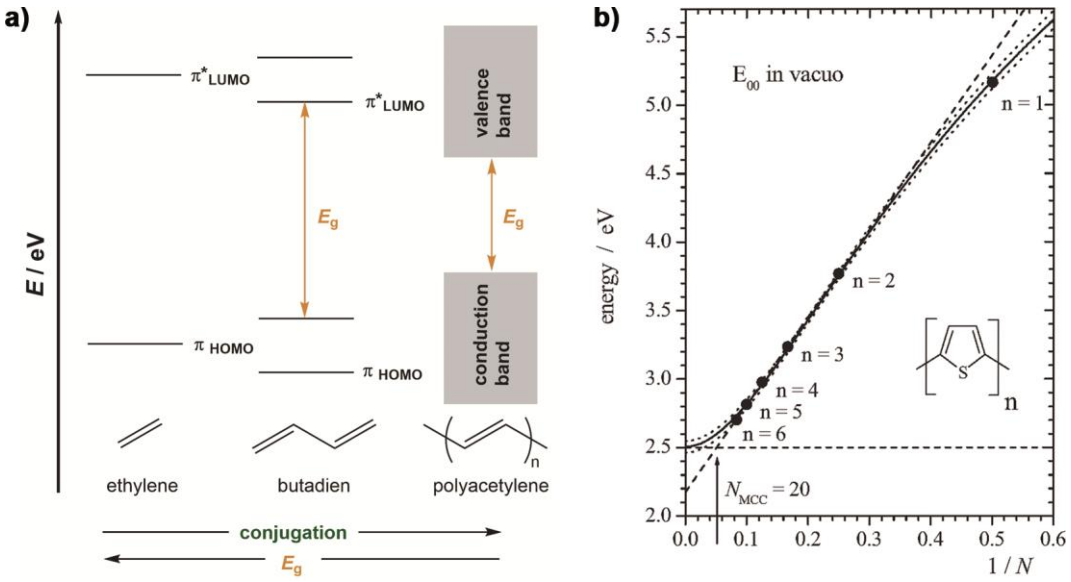

Figure 17. a) Band formation by increased conjugation length. b) Adiabatic transition energies (E_{00} in vacuo) of thiophene (n = 1) and oligothiophenes (n > 1) as function of the number of conjugated double bonds (N) and Kuhn fit (solid line). Linear fit (dashed line) used for determination of maximum conducive chain length (N_{MCC}). Reprinted from reference[136] with permission from Wiley-VCH Verlag GmbH, Copyright 2017.

One could assume that metallic behavior can be observed in organic compounds, if a very large conjugation length is realized (zero bond length alternation). However, this is not the case because of the Peierl's distortion.[137] It states that there will always be a distortion, and consequently a *BLA* in a molecular chain, which will lead to a splitting in energy levels. Thus, the lowered energy levels are filled with electrons while the raised ones stay empty, so that the net energy is minimized. As consequence, a one-dimensional metal, with regular chain structure will never be stable.[137] Nevertheless, it is important to reduce the bond length alternation in order to obtain desired small band gap materials. As just mentioned, the band gap and concomitantly the adiabatic transition energy E_{00} of a compound decreases, when the conjugation length/the number of conjugated double

bounds (N) is increased. Therefore, the synthesis of oligomers and polymers is a good approach in order to obtain small band gap materials. An example for this is shown in Figure 17b, where the experimentally observed adiabatic transition energies of thiophene monomer (n = 1) and oligomers (n > 1) are plotted against $1/N$.[136] A linear decrease in transition energy can be observed for smaller oligomers (n = 2 to 6). This trend is not followed by the monomer and by longer oligomers.[138] However, from the linear fit and the measured transition energy of the polymer (polymer limit) a maximum conducive chain length (N_{MCC}) can be deduced, which helps to quantify this effect. N_{MCC} is typically in the range of 18 to 20.[138] It is worth noticing that the transition energy decreases the most for small n values, so that an oligomer consisting of six thiophenes (transition energy ~ 2.7 eV) is already close to the polymer limit (2.5 eV).

As shown above, there are several techniques available to design active layer materials, by taking control over the HOMO and LUMO levels, the band gap and therefore the optical properties. However, suitable molecules should further be ambient stable and possess good charge transport properties, with charge carrier mobilities in the range of $0.01 - 1\,cm^2\,V^{-1}\,s^{-1}$.[94,139] In order to obtain air stable electron transport materials, the LUMO level energies should be at least as low as −4.3 eV, if the overpotential is 1.0 V.[140] Furthermore, the charge transport at the microscopic level depends on the electronic coupling between adjacent molecules. Thereby, the relative positions of the molecules as well as the nature of the frontier molecular orbitals are of importance (close π-π stacking distances and good orbital overlap).[140] So not only the molecular properties, but also the packing properties are very important to optimize the charge transport properties. And even though it is possible to take influence on the packing by molecular design, e.g. by utilizing bulky side chains, the outcome is extremely difficult to predict. Furthermore, the purity of the utilized compounds highly affects the charge transport behavior of the bulk material, because impurities might act as charge-carrier traps or exciton quenching sites.[141,142]

In conclusion, there are many different aspects to consider, when designing active layer materials. In addition to the absorption properties, the band gap, the position of HOMO and LUMO levels need to be controlled. In the ideal case the designed molecule is tailored to its donor or acceptor counterpart, so that solar cell performance is maximized. Furthermore, the molecules should be designed in a way that good charge transport is possible. The synthesis of the compound should be feasible and solubility good enough

to ensure easy purification. Apart from the molecular level, the compounds should further possess a good processability and favorable packing in the solid state. To achieve all this in an optimal fashion is almost impossible, precisely because many of these parameters affect each other. However, there are many strategies available that help to simplify the design of active layer acceptor materials and achievements have been made during the past years, leading to power conversion efficiencies of already 12 %.[26]

2.3.2 Dyads for Single Component Organic Solar Cells

Another concept, surpassing the design of separate donor and acceptor components, is the synthesis of dyad molecules. In these one electron donor and a suitable electron acceptor material are covalently linked together, often without being in conjugation. For example, fullerene-based donor-acceptor dyads were developed in which fullerenes were covalently linked to commonly used donor dyes, e.g. diketopyrrolopyrroles (DPP), oligo-/thiophenes or tetrathiafulvalenes (TTF).[143] The advantage of such systems is that the photochemical charge separation should take place easily, without the need of exciton migration which might be limiting in conventional organic solar cells. Furthermore, they are good model compounds to study e.g. rates and yields of photo induced electron transfer processes.[144,145] They bear the potential of controlling the orientation of donor and acceptor with respect to each other as well as to beneficially guide the active layer morphology.[146] And finally, they might stabilize the nanoscale separated microstructure in BHJ solar cells, which is typically not thermodynamically stable and starts to separate over time, leading to a decreased device performance.[147] The dyad molecules presented in Figure 18 all contain fullerene acceptor moieties, which are frequently used in this field, because of their intrinsic properties, like high electron affinity, small reorganization energy and their three dimensional electron transport properties.[143] Another big advantage of the fullerene based dyads is the possibility to separately tune the HOMO and LUMO level of the dyad molecule (5^{th} situation in the donor acceptor approach; Section 2.3.1). Unfortunately, the fullerene itself is not easily tunable and can hardly be tailored to a specific donor molecule. Therefore, it is the donor part of the dyads which has to be tailored, by following many general design principles as discussed in Section 2.3.1.

There are only a few cases where fullerene-based dyad molecules were investigated in organic solar cell devices and even less examples can be found where the dyads were

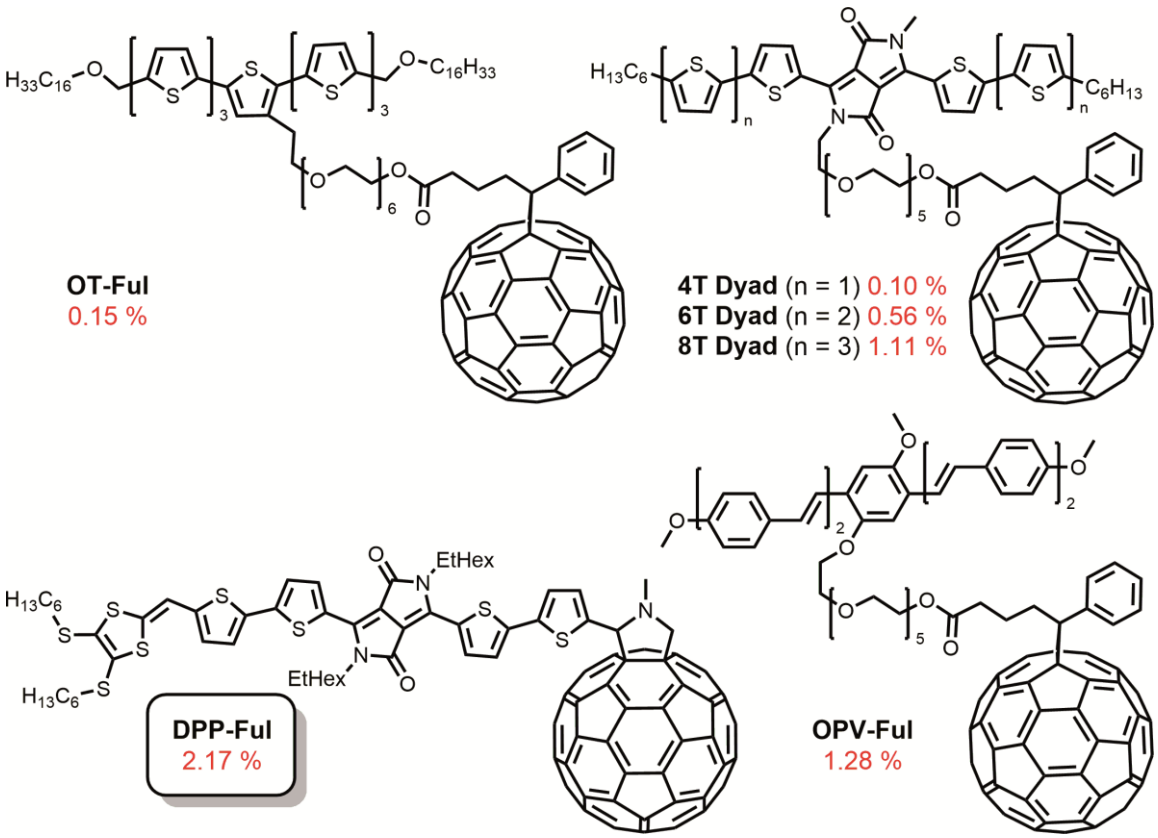

Figure 18. Chemical structures and their power conversion efficiencies of the best performing dyad molecules in single junction organic solar cells.[148–152]

used exclusively as active layer material. A dyad molecule that consists of an oligothiophene attached to a fullerene (**OT-Ful**) was investigated by Nishizawa *et al.*, giving a low *PCE* of 0.15 %.[148] A much higher power conversion efficiency of 1.28 % was found for an oligo(*p*-phenylenevinylene)-fullerene dyad (**OPV-Ful**), which utilized ethylene spacer units.[149] A series of dyad molecules was investigated in the group of Tajima *et al.*,[150] where a thiophene decorated diketopyrrolopyrrole was used as donor moiety and where the connection to the fullerene was realized by a long ethylene glycol chain (**4T Dyad**, **6T Dyad**, **8T Dyad**). The devices showed high fill factors (46 %) and power conversion efficiencies of up to 1.11 %. In this case the electron poor DPP core was inserted into the electron-rich thiopene chain, using the donor-acceptor approach to tune the donor moiety. Recently, an improved power conversion efficiency of around 2.20 % could be obtained by connecting a similar DPP dye to the fullerene moiety via a short thiophene bridge (**DPP-Ful**).[151] This molecule utilized 2-ethylhexyl chains at the DPP which will have an effect on the molecules solubility and solid state packing.

In conclusion, most of these molecules have three things is common: The electron donating moiety is quite large and designed to electronically match to the fullerene. High molar masses of around 1736 – 2895 g mol^{-1} can be found for the molecules and they possess a long and flexible spacer unit between fullerene and chromophore. The latter point is not valid for the best performing dyad **DPP-Ful**, where the conjugated π-system of the chromophore is in close proximity to the fullerene. Even though dyads have not been extensively studied in one component solar cells, it is worth mentioning that there are plenty of examples in the literature, where fullerenes were either slightly modified to fine tune their LUMO levels, or where they were covalently bound to metal complexes or even more complex arrangements, containing e.g. more than one electron donor.[28,143,153–155]

2.4 Small Molecular Electron Acceptors as Substitutes for Fullerenes

The first fullerene discovered in 1985 was the C_{60}-Buckminsterfullerene.[34] The synthesis of this carbon allotrope in reasonable amounts was developed by Krätschmer *et al.* in 1990,[156] and enabled the intense investigation and application of fullerenes and fullerene derivatives.[157–159] Since then fullerenes, especially C_{60}, C_{70} as well as their soluble derivatives $PC_{61}BM$ and $PC_{71}BM$, have become the fruit fly of organic photovoltaics,[117,160–163] due to their unique properties. For example they possess a high electron affinity,[164] good electron transport properties in all spatial directions[18,19] and a good processability.[155] Highly efficient organic solar cells have been produced based on fullerene acceptors. For example, small molecular donors resulted in power conversion efficiencies of ~10 % in combination with fullerenes[165] and single junction devices based on donor polymers exceed the ten percent mark as well.[166–168] Thus, lots of effort has been spent to modify fullerenes, to achieve optimized solar cell devices.[155,169] Nevertheless, it is well known that fullerenes have some major drawbacks: (1) The absorption in the visible region is low (Figure 19), [23] (2) the electronic modification of fullerenes is not easy and the conjugation between the fullerene and the covalently attached moieties is usually broken[170,23,171] and (3) fullerenes degrade upon photo or thermal stress.[172,173]

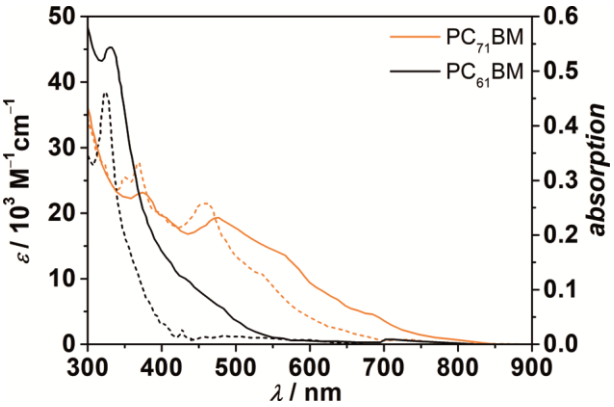

Figure 19. Absorption of $PC_{61}BM$ and $PC_{71}BM$ in solution (dashed; 10^{-5}M in $CHCl_3$) and in thin films (solid; spin coated from $CHCl_3$, thickness = 100 nm). Reproduced from reference[23] with permission from The Royal Society of Chemistry.

In contrast, non-fullerene acceptors can be tailored so that the absorption is complementary to the donor material and a broad range of the sunlight is collected. The HOMO and LUMO levels can be easily adjusted to fit to the ones of the corresponding

donor molecule or polymer. The difficulties are to maintain the advantages of fullerenes at the same time. A lot of effort has been spent on the design and synthesis of substitutes for fullerenes, not only covering small molecule acceptors, but polymer based acceptors as well. [16,17,24,174–176] The advantage of the small molecules over polymers is that they have a very defined structure and molecular weight. They can be also obtained very pure without batch to batch variations.[161,177,178] In 2013 the best performing acceptor molecule was a thiophene bridged PBI dimer (**Bis-PDI-T-EG**), described by X. Zhang *et al.* (Figure 20).[179,17] Organic solar cells based on this dye yielded efficiencies of about 4 %, in combination with the donor polymer **PBDTTT-C-T**. By that time, fullerene based solar cells showed much higher efficiencies of up to 7 – 9 %.[17]

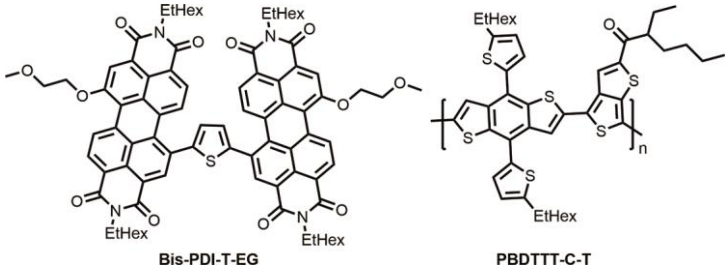

Figure 20. Best performing non-fullerene acceptor **Bis-PDI-T-EG** in 2013. Investigated in devices with PBDTTT-C-T donor of ITO/PEDOT:PSS/**active layer**/Ca/Al architecture.

Now, only 4 years later, power conversion efficiencies of 11 – 12 % were measured using a variety of non-fullerene acceptor molecules.[24,180] Thus, they are on the same level with the fullerene based devices. The best performing non-fullerene acceptor molecules (*PCE* >8 %), their corresponding donor polymers and the characteristic solar cell parameters (inert conditions) are concluded in Figure 21 and Table 1. When looking at record efficiencies of new molecules, it is important to keep in mind that the efficiency of the solar device strongly depends on the choice of donor polymer as well and that only the right donor acceptor combination will lead to high performance devices. Additionally, the utilized device architecture will have a huge impact. Some of the good performing molecules today look very similar to **Bis-PDI-T-EG**. For example, **SdiPBI-Se** and **SF-PDI$_2$** are still based on two perylene bisimide (PBI) units that are either linked directly at their bay-position or bridged via a spirofluorene moiety, giving rise to power conversion efficiencies of 8.4 and 9.5 %, respectively.[181,182] The device with **SF-PDI$_2$** in combination with **P3TEA** reveals another advantage of non-fullerene acceptors, as they can work well with only a minimal LUMO-LUMO offset ΔE_{LUMO} (E_{LUMO}(**P3TEA**) − E_{LUMO}(**SF-PDI$_2$**) = −3.57 eV − −3.62 eV = 0.05 eV).[182] Consequently, non-fullerene

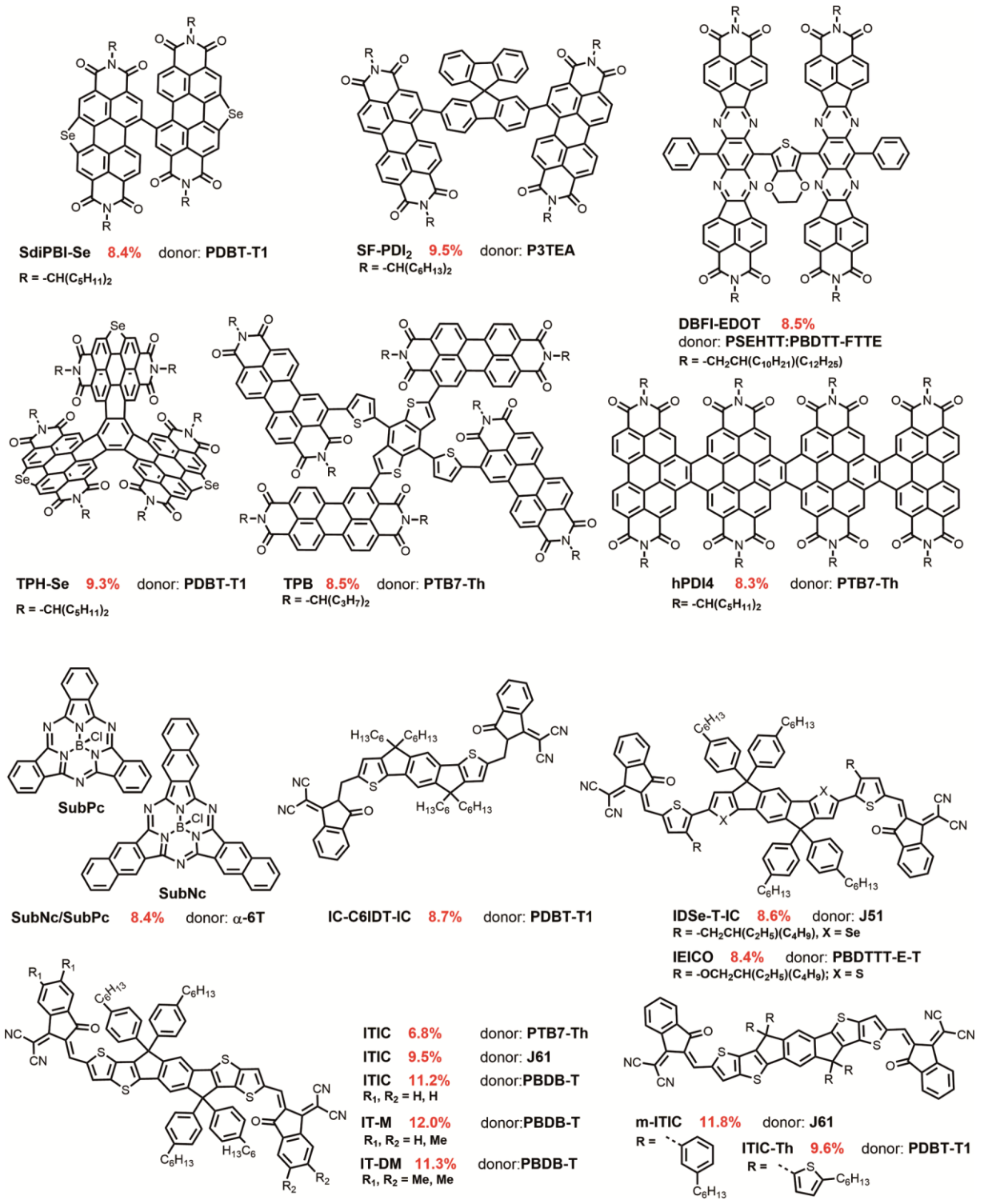

Figure 21. Best performing non-fullerene acceptors found in literature to date.[26,32,181–194]

based solar cells can generate higher open circuit voltages to yield higher *PCE*s. Tetraazabenzodifluoranthene diimide (**BFI**) based dimers can yield very good solar cell performance, too. For example, **DBFI-EDOT** yielded a power conversion efficiency of 8.5 %.[184] Another approach of D. Meng *et al.*, Q. Wu *et al.* and Y. Zhong *et al.* was to increase the number of electron accepting building blocks. Additionally,

three-dimensionality is present in these molecules, so that they mimic the round shape of fullerenes. For the propeller shaped selenium-annulated triperylene hexaimide (**TPH-Se**) a power conversion efficiency of 9.3 % was measured.[189] Somewhat lower efficiencies of 8.5 and 8.3 % were measured for the cross-like **TPB** and the fused tetra PBI **hPDI4**, respectively.[190,194] The boron subphthalocyanin **SubPc** and the boron subnaphthalocyanine **SubNc** acceptors, both combined simultaneously with a simple thiophene donor molecule, resulted in power conversion efficiencies of up to 8.40 %.[32] Interestingly, these two molecules were already investigated as donor molecules in 2009. Hereby, power conversion efficiencies of 2.5 % could be measured for **SubNc** in combination with C_{60}.[195] This shows again, how strongly the device performance depends on the right donor or acceptor choice.

Table 1. Device parameters of best performing non-fullerene acceptors found in literature to date.

acceptor	LUMO/HOMO [a] [eV]	E_g^{opt} [a] [eV]	donor	*PCE* [%]	J_{SC} [mA cm^{-2}]	*FF* [%]	V_{OC} [V]	ref.
SdiPBI-Se	−3.87/−6.09	2.22	**PDBT-T1**	8.42	12.5	70	0.95	[181]
SF-PDI$_2$	−3.62/−5.99	1.74	**P3TEA**	9.50	13.3	64	1.11	[182]
DBFI-EDOT	−3.65/−5.76	1.70	**PSEHTT: PBDTT-FTTE**	8.52	15.7	60	0.91	[184]
TPH-Se	−3.80/−5.97	2.17	**PDBT-T1**	9.28	12.5	72	1.00	[189]
TPB	−3.89/−5.71	1.82	**PTB7-Th**	8.47	17.9	58	0.79	[190]
hPDI4	−3.91/−6.26	2.35	**hPDI4**	8.30	15.2	68	0.80	[194]
SubPc/	−3.6/−5.6	2.10	**α-6T**	8.40	14.6	54	0.94	[32]
SubNc	−3.6/−5.3	1.70						
IC-C6IDT-IC	−3.91/−5.69	1.62	**PDBT-T1**	8.71	15.05	65	0.89	[186]
IDSe-T-IC	−3.79/−5.54	1.52	**J51**	8.21	15.2	62	0.91	[185]
IEICO	−3.95/−5.32	1.34	**PBDTTT-E-T**	8.4	17.7	58	0.82	[192]
ITIC	−3.83/−5.48	1.59	**PTB7-Th**	6.80	14.2	59	0.81	[187]
ITIC	−3.08/−5.32	1.93	**J61**	9.53	17.4	62	0.89	[183]
ITIC	−3.78/−5.51	1.59	**PBDB-T**	10.68	16.7	71	0.90	[193]
IT-M	−3.98/−5.58	1.60	**PBDB-T**	12.05	17.4	73	0.94	[26]
IT-DM	−3.93/−5.56	1.63	**PBDB-T**	11.29	16.5	70	0.97	[26]
m-ITIC	−3.82/−5.52	1.58	**J61**	11.77	18.3	71	0.91	[191]
ITIC-Th	−3.93/−5.66	1.60	**PDBT-T1**	9.6	16.2	67	0.88	[188]

[a] Values for acceptor.

The remaining high performance acceptor molecules all consist of an electron donor (D), which is flanked by two 1,1-dicyanomethylene-3-indanone (DCIND) electron acceptors (A) so that ADA compounds are formed. In all these ADA molecules the central core consists of a phenyl moiety which is fused symmetrically with several aromatic five membered rings. Heteroatoms, especially sulfur atoms are included in these flanking units, too. For good solubility at least four solubilizing side chains are attached

to the central core, which contain an aromatic ring quite often. The quality of the utilized sidechains will of course affect the solid state packing and the quality of the π-π stacking. **IEICO** seems to be the more soluble and less rigid version of compound **IC-C6IDT-IC** (*PCE* = 8.7 %)[186] due to the introduction of thiophene spacers and an increased number solubilizing side chains. However, its power conversion efficiency (8.4 %)[192] stays in the same range as for **IC-C6IDT-IC**. The substitution of sulfur by selenium does not have a strong effect, either (**IDSe-T-IC**).[185] The most promising electron accepting molecules are based on **ITIC**, first published by X. Zhan *et al.* in 2015.[187] Power conversion efficiencies of 6.8 % were obtained. The structure of this molecule is quite similar to the ones above. The central donor core consists of a phenyl unit which bears two thienothiophenes, which again are additionally bridged to the phenyl by a carbon atom, so that the system is planarized. Solubilizing side chains are attached to this bridging atom. By combining **ITIC** with better suitable donor polymers like **J61** or **PBDB-T** power conversion efficiencies were already increased to 9.5 % and 10.7 %, respectively. By introduction of one methyl group at the DCIND units, efficiencies could be improved up to 12 %.[26] Good solar cells were obtained, too, when smaller modifications were performed at the solubilizing side chains of the central core. [188,191]

To sum up, the field of non-fullerene acceptors evolved very fast. Within a few years the newly developed molecules were able to outperform the fullerene based devices that have been the 'gold standard' until now. One major advantage of these new acceptors over the fullerenes is the possibility to modify the compounds easily, which enables efficient tuning of optical band gaps as well as HOMO and LUMO levels. Therefore, a variation of around 1 eV can be found for E_g, HOMO and LUMO levels, respectively. The most successful acceptor molecules, yielding power conversion efficiencies above 8 %, belong to the class of rylene-based compounds or they are of the acceptor-donor-acceptor type (ADA). For molecules of the former class, three dimensionality seems to be favorable. However, the record values of up to 12 % (**IT-M**) were obtained in the class of ADA molecules.

2.5 Conclusion

Chapter 2 discussed the structural and molecular design of organic solar cells. PHJ/BHJ architectures, advantages and functions of interlayers, as well as processes of photocurrent generation and device degradation were presented (Section 2.1). In Section 2.2 the operation regimes of an organic solar cell were introduced, followed by two important methods for solar cell characterization, namely the measurement of *I-V* curves and *EQE* spectra. In Section 2.3 general rules for the design of active layer components were described, like the donor-acceptor, the planarization or the polymer approach. Furthermore, dyad molecules were presented as another interesting design concept. Finally, it was shown that the substitution of fullerene acceptors in organic photovoltaics enabled significant improvements (Section 2.4) and opens up a lot of opportunities for future research in this field.

Chapter 3

Results and Discussion

3.1 Fabricating and Characterizing Organic Solar Cells under Ambient Conditions

3.1.1 BHJ Solar Cells of DA Dyes

3.1.1.1 Ambient versus Inert Conditions

Inert conditions are the common standard in the field of organic solar cells, because typically not all utilized components of a solar cell are stable against oxygen and moisture[104,172] and degradation takes place under ambient conditions (see Section 2.1.4). However, the technical requirements to fabricate and characterize organic solar cells under inert conditions are high, i.e. a well-equipped glove box system with an integrated evaporation chamber is needed. Therefore, the fabrication of organic solar cells under ambient conditions should be established in our laboratory. Figure 22 defines what is meant with the terms inert and ambient conditions, when a simple device with glass/ITO/PEDOT:PSS/**BHJ**/top electrode architecture is fabricated. For manufacturing such a cell, several main steps have to be followed: a) cleaning of the substrates, b) interlayer preparation, c) active layer fabrication and d) electrode deposition. Finally,

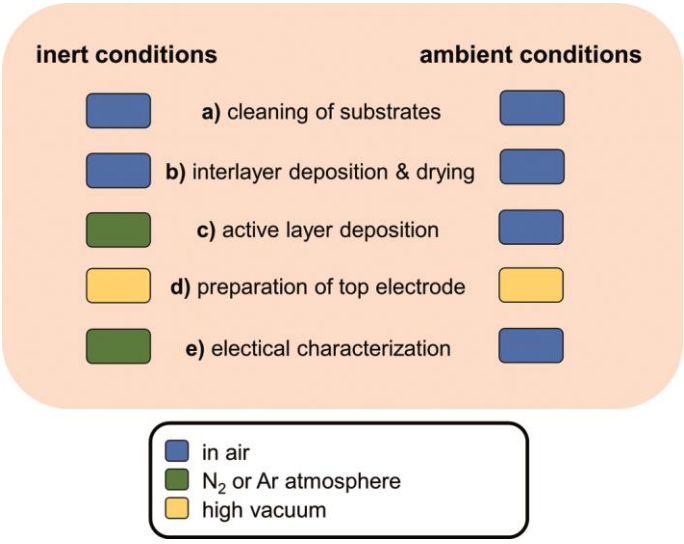

Figure 22. Different steps (a-e) performed during preparation and characterization of an organic solar cell in a glass/ITO/PEDOT:PSS/BHJ/top electrode architecture, as well as conditions being present during the single steps under inert or ambient conditions (colored boxes).

electrical characterization (e) has to be performed. Steps a) to e) can be performed in air, where the devices are stressed by oxygen and moisture, or under protective conditions, like nitrogen/argon atmosphere or high vacuum. For the latter conditions a well-equipped glove box system is required. The devices are well protected at least during steps c) to e), when working under inert conditions. It is worth noticing that it would not be reasonable to perform steps a) and b) under inert conditions, because cleaning and the preparation of PEDOT:PSS involve water. When working under ambient conditions, the devices are stressed with water and oxygen all the time. Only during electrode deposition, they are protected by high vacuum.

In conclusion, when devices are fabricated under ambient conditions the active layer deposition as well as the electrical characterization have to be performed under the presence of oxygen and moisture. Thus, oxygen and water molecules are further embedded within the device, where they can reduce the device's performance and stability, e.g. due to chemical reactions. Fabrication under inert conditions can prevent this, but requires an expensive and specialized equipment.

3.1.1.2 Comparison of Different DA Dyes

To test our fabrication and characterization tools and to find out whether it is possible to fabricate DA dye-based solar cells under ambient conditions a series of merocyanine donor $PC_{61}BM$ acceptor solar cells was chosen that had been investigated under inert conditions beforehand by the research group of Prof. Dr. K. Meerholz (Cologne).[196] The chemical structures of the investigated compounds are shown in Figure 23. The DA dyes

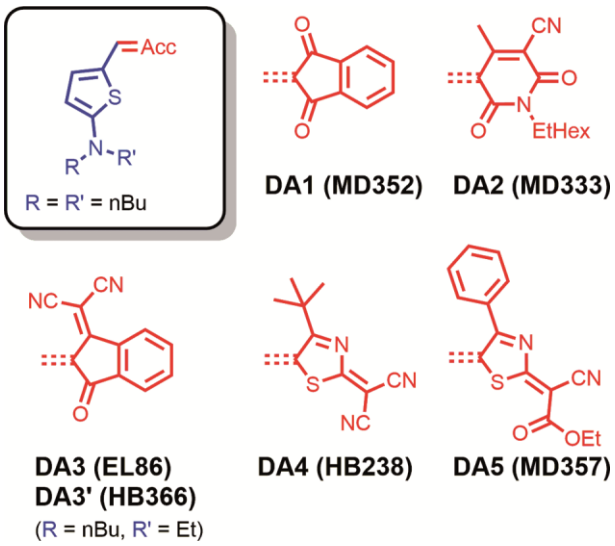

Figure 23. Chemical structures of DA dyes consisting of an electron-rich aminothiophene donor (blue) and an electron poor acceptor moiety (red).

consist of an electron-rich aminothiophene, which is attached to different electron accepting moieties via a methine bridge. The solar cells were built identical to the devices from literature[196] in a glass/ITO/PEDOT:PSS/**active layer**/Al architecture. The active layer of DA dye and $PC_{61}BM$ was spin coated from chlorobenzene in a concentration of 20 mg ml^{-1}, except for **DA3'** which was cast at a concentration of 10 mg ml^{-1} from $CHCl_3$ due to solubility problems. Optimized donor to acceptor ratios were chosen according to literature, being 30:70 for **DA1**, **DA2** and **DA5**, 40:60 for **DA3**, 45:55 for **DA3'** and 25:75 for **DA4**, respectively.[196] The obtained current-voltage characteristics of devices fabricated and measured under ambient conditions are shown in Figure 24. The characteristic device parameters are collected in Table 2, where they are compared to the ones from literature (fabricated and measured under inert conditions).[196]

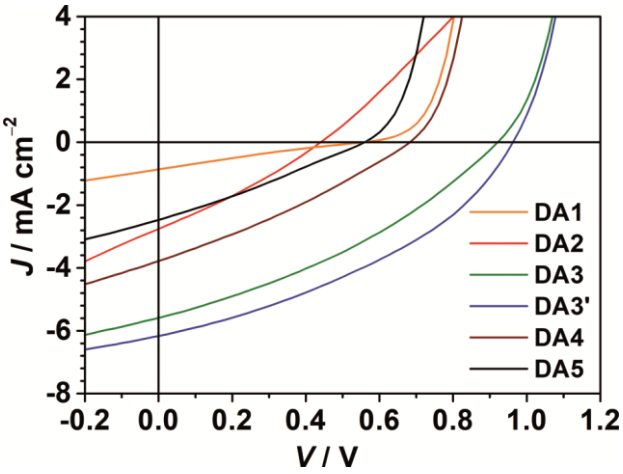

Figure 24. *J-V* characteristics of BHJ solar cells of **DA1** (orange), **DA2** (red), **DA3** (green), **DA3'** (blue), **DA4** (brown) and **DA5** (black) in a glass/ITO/PEDOT:PSS/**active layer**/Al architecture. Curves were measured under simulated AM1.5 G illumination, with 100 mW cm^{-2} and under ambient conditions.

All six investigated DA dyes yielded operating devices under ambient conditions. However, a rather linear voltage response can be found for the device with **DA2** and the typical diode characteristics are hardly visible. The short circuit current density shows a large variation under ambient conditions (0.9 to 6.2 mA cm^{-2}), which was also observed under inert conditions (2.9 to 8.3 mA cm^{-2}). In the former case the short circuit current densities are typically lower by 0.7 – 2.0 mA cm^{-2}, except for **DA3**, where the same value is measured under inert conditions (ca. 5.8 mA cm^{-2}). The fill factors of compounds **DA1** (28 %) and **DA3'** (38 %) coincide under ambient and inert conditions, while they are lower by 10 to 15 % under ambient conditions for all other dyes. This indicates a more pronounced charge recombination or a more hindered charge extraction under ambient conditions, when **DA2**, **DA3**, **DA4** or **DA5** are used. The open circuit voltages are in

Table 2. Solar cell characteristics of glass/ITO/PEDOT:PSS/**active layer**/Al devices under ambient conditions. Procedure based on literature.[196]

donor [a]	solvent	conditions	*PCE* [b] [%]	J_{SC} [mA cm^{-2}]	*FF* [%]	V_{OC} [V]
DA1	CB	ambient	0.10 (0.10)	0.9	28	0.56
	CB	inert [d]	0.5	2.9	27	0.63
DA2	CB	ambient	0.35 (0.33)	2.7	29	0.44
	CB	inert [d]	0.9	4.0	32	0.73
DA3	CB	ambient	1.82 (1.76)	5.7	34	0.92
	CB	inert [d]	2.3	5.8	41	0.96
DA3'	$CHCl_3$ [c]	ambient	2.20 (2.06)	6.2	38	0.94
	$CHCl_3$ [c]	inert [d]	3.0	8.3	38	0.94
DA4	CB	ambient	0.77 (0.71)	3.8	30	0.68
	CB	inert [d]	1.1	4.5	35	0.72
DA5	CB	ambient	0.38 (0.35)	2.5	27	0.56
	CB	inert [d]	0.5	4.0	27	0.47

[a] $PC_{61}BM$ was used as acceptor. [b] Value in brackets is the average over up to seven devices. [c] Solubility problems in CB. [d] Values from reference.[196]

good agreement under ambient as well as under inert conditions. Deviations are below 0.1 V, except for **DA2**, which is probably related to the unusual *J-V* curve progression found for this compound. Furthermore, it is worth mentioning that a slightly higher voltage (+0.09 V) was obtained under ambient conditions for **DA5**. As discussed in literature,[196] the highest open circuit voltages (> 0.92 V) can be found for the dyes with the lowest HOMO levels (**DA3**, **DA3'**), which is again true under ambient conditions. Consequently, the power conversion efficiencies measured under ambient conditions (0.10 – 2.20 %) are lower by 20 – 40 % compared to inert conditions (0.5 – 3.0 %), mainly due to inferior short circuit current densities and/or decreased fill factors. The spectrally resolved external quantum efficiencies of devices measured under ambient conditions are shown in Figure 25a. The *EQE* spectra for the BHJ solar cells in this device architecture that were fabricated under inert conditions, are not reported in reference[196]. It was not possible to obtain an *EQE* spectrum of **DA4**, due to fast degradation. However, the *EQE* spectra of the other dyes revealed that the relative contribution of DA dye and fullerene to the photocurrent varies with utilized compound. While fullerene and DA dye proportion both show a maximum at around 40 % in case of **DA3'**, the *EQE* is typically lower in the DA dye region for the other compounds. The shape of the *EQE* spectra is in good agreement with the UV/vis absorption spectra (Figure 25b). The optical density is between 0.28 and 0.43 in the fullerene and between 0.12 and 0.33 in the DA dye region, which is a result of different donor to acceptor ratios.

The active layer thickness of the devices was measured by AFM, where values of 47, 52, 58, 62, 54 and 52 nm were obtained for **DA1**, **DA2**, **DA3**, **DA3'**, **DA4** and **DA6**. This is in good agreement with the device thickness reported in reference[196] (50 – 60 nm).

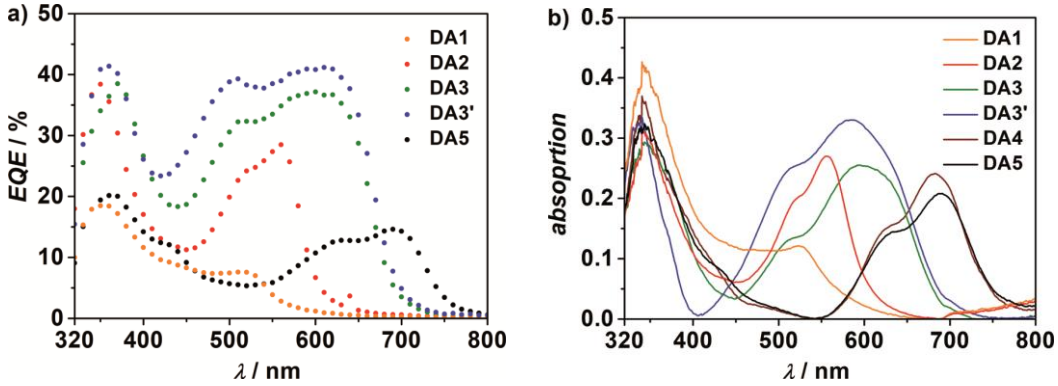

Figure 25. a) Spectrally resolved *EQE* and b) UV/vis absorption spectra of BHJ solar cells in glass/ITO/PEDOT:PSS/**active layer**/Al architecture of DA dyes **DA1** (orange), **DA2** (red), **DA3** (green), **DA3'** (blue), **DA4** (brown) and **DA5** (black).

3.1.1.3 Stability and Reproducibility

Solar cell stability is required for real-life application. To this end, a good understanding of the degradation phenomena is necessary.[104,172] Therefore, many studies can be found in literature where e.g. the influence of illumination and electrical stresses,[197] water and oxygen[198] or various exciton blocking layers[199] on the device's stability have been tested. As shown in the chapter above, DA dye based solar cells work when fabricated and characterized under ambient conditions. However, a decrease in short circuit current density and fill factor was often observed, so that two questions arise: 1. How good is the reproducibility under ambient conditions? 2. How good is the stability of these devices under ambient conditions? In order to find answers to these questions, devices of the best performing compound **DA3'** were fabricated using the same conditions described in the former section. Furthermore, the fabrication was conducted on two different days, where every time six substrates (each containing 7 sub cells) from separately weighed blends (of fullerene and **DA3'**; two substrates per blend) were prepared. This way three independent experiments could be performed on each of these days (Exceptions are e.g. aluminum deposition procedure or work flow and timing). The results of these experiments are collected in Table 3. When comparing the characteristic device parameters of the investigated solar cells to the ones measured under inert conditions, the same conclusion as in the former section can be drawn: The open circuit voltages and the fill factors correspond to those of the solar cells fabricated under inert conditions, while

Table 3. Solar cell characteristics of glass/ITO/PEDOT:PSS/**active layer**/Al devices under ambient conditions. Procedure based on literature.[196]

donor [a]	rel. humidity [%]	day	conditions	blend	*PCE* [b] [%]	J_{SC} [mA cm^{-2}]	*FF* [%]	V_{OC} [V]
DA3'	60 %	A	ambient	1	1.86 ± 0.11	5.65 ± 0.19	34 ± 1	0.96 ± 0.01
				2	1.86 ± 0.17	5.65 ± 0.40	34 ± 1	0.96 ± 0.02
				3	1.88 ± 0.15	5.46 ± 0.39	36 ± 1	0.96 ± 0.02
	46 %	B	ambient	1	2.15 ± 0.12	6.04 ± 0.17	38 ± 1	0.93 ± 0.02
				2	2.14 ± 0.08	5.89 ± 0.11	38 ± 1	0.95 ± 0.02
				3	2.11 ± 0.07	6.18 ± 0.10	37 ± 1	0.92 ± 0.01
	–	–	inert[196]	–	3.0	8.3	38	0.94

[a] $PC_{61}BM$ was used as acceptor (donor:acceptor ratio = 45:55 w/w). [b] Average value over fourteen devices.

a large deviation can be found for the short circuit current densities. All device parameters, and therefore the power conversion efficiencies, match very well for all cells that were prepared on the same day, regardless of each blend. However, when the device parameters of the two different processing days are compared, more deviation becomes apparent. Devices prepared on day A (60 % rel. humidity) show larger open circuit voltages (0.96 V), but lower fill factors (ca. 34 %) and short circuit current densities (ca. 5.65 mA cm^{-2}) than devices processed on day B (46 % rel. humidity), where open circuit voltages of ca. 0.93 V, fill factors of 38 % and short circuit current densities of ca. 6.04 mA cm^{-2} were measured. Consequently, the power conversion efficiency obtained on day A (ca. 1.87 %) is significantly lower than on day B (ca. 2.13 %). It was assumed that the natural variation of ambient conditions is probably the reason for this day to day dependence. To find out whether this assumption is correct, solar cells of **DA3'** were fabricated (like before) on 22 different days, while monitoring the relative humidity. In Figure 26 the power conversion efficiency is plotted against the relative humidity of air that was measured on the day the experiment was performed. Even though, the data pointes do not show a very strong correlation, a clear trend can be observed: Power conversion efficiencies were more likely to be above the average (1.83 %; green dashed line), when the relative humidity was low. These results prove our assumption that the humidity is indeed a crucial point for device stability and operation. Some degradation pathways are e.g. segregation of the hygroscopic PEDOT:PSS layer, oxidation and introduction of trapping sites in the active layer or oxidation of aluminum electrodes (see section 2.1.4). Moisture intrusion is also known to weaken the contact between electrodes and the solar cell or between various layers of device and can also increase the leakage

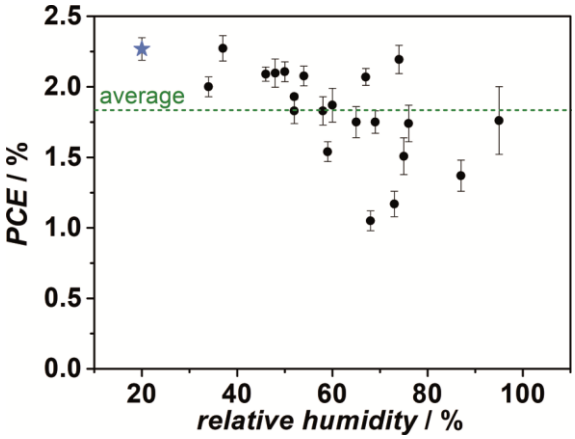

Figure 26. Power conversion efficiencies of solar cells in a glass/ITO/PEDOT:PSS/**active layer**/Al architecture, where each data point represents the average efficiency of seven sub cells on one substrate. The blue star corresponds to an experiment at 20 % rel. humidity, where fabrication of the devices was performed in a climate controlled room. All other experiments were performed under ambient rel. humidity (depending on the weather). The green dashed line represents the average power conversion efficiency (1.83 %) over all experiments.

current, resulting in a reduced performance.[200] The average device parameters as well as the values for the best and the worst device can be found in Table 4. The best device showed an efficiency of 2.40 % (37 % rel. humidity), while the worst device showed a *PCE* of 1.00 % (68 % rel. humidity). Short circuit current density and open circuit voltage of the best device are above the average, while the fill factor is only average. The worst performing device is below average in all device parameters. However, especially at higher relative humidity values the device performance becomes more random. Therefore, the observation of high power conversion efficiencies (> 2.0 %) of devices processed at high relative humidity (up to 74 %) are most surprising. Thus, another question arises: How strong is the influence of the time the devices spends under ambient conditions until it is fabricated and measured? This question was also studied on the same type of devices. For this purpose, three solar cells of **DA3'** were prepared like before. Then measurements were performed on the devices every 30 minutes, in air. Between each measurement the solar cells were stored differently. One device was stored under

Table 4. Average solar cell parameters of devices in glass/ITO/PEDOT:PSS/**active layer**/Al architecture.

donor	device	*PCE* [%]	J_{SC} [mA cm^{-2}]	*FF* [%]	V_{OC} [V]
DA3' [a]	average [b]	1.83 ± 0.40	5.9 ± 0.81	36 ± 4	0.85 ± 0.07
	best [c]	2.40	7.41	36	0.90
	worst	1.00	5.08	27	0.74

[a] $PC_{61}BM$ was used as acceptor. [b] Average value over 21 substrates with seven devices each. [c] Climate controlled with 20 % rel. humidity.

argon atmosphere (low oxygen level and low humidity), a second device was stored in a desiccator, which was filled with phosphorus pentoxide (low humidity; going down from 50 % to about 20 – 30 % within 10 minutes) and a third device was stored under ambient conditions (rel. humidity = 50 %). The initial device parameters can be found in Table 5. They are all quite similar and accordingly do not reveal a specific effect of the storage conditions. Next, the corresponding device parameters (relative values) were measured as a function of time (Figure 27). Here significant changes are observed for ΔPCE and ΔJ_{SC} (Figure 27a), whereas ΔFF and ΔV_{OC} only show a moderate decrease (Figure 27b). The latter parameters drop by around 10 to 15 %, during the first 10 hours of measurement. This might also be related to measurement stresses or morphological changes within the active layer of the device. While *FF* and V_{OC} behave very similarly for devices stored under argon and dry air and still show 90 % of their initial performance after 24 h, a large scattering can be observed for these device parameters, when the device is stored under ambient conditions. Furthermore, the devices completely fail after 24 h, when stored under ambient conditions.

Table 5. Initial device parameters of devices with **DA3'** in a glass/ITO/PEDOT:PSS/**active layer**/Al devices under ambient conditions. Procedure based on literature.[196]

active layer	storage conditions	*PCE* [%]	J_{SC} [mA cm^{-2}]	*FF* [%]	V_{OC} [V]
DA3'	argon	2.09 ± 0.05	6.10 ± 0.11	37 ± 1	0.93 ± 0.02
	dry air	2.10 ± 0.08	6.03 ± 0.15	38 ± 1	0.92 ± 0.01
	ambient conditions	2.11 ± 0.06	6.19 ± 0.10	37 ± 1	0.92 ± 0.01

The relative changes of short circuit current density and power conversion efficiency almost overlap for the particular devices (Figure 27a), showing that the former parameter dominates over the relatively small changes in fill factor and open circuit voltage. During the first minutes and hours of measurements a strong drop in short circuit current density and accordingly in power conversion efficiency can be observed and degradation slows down over time. The degradation process in *PCE* and short circuit current density cannot be described with a monoexponential decay but rather with a bi- or triexponential one, indicating that several processes happen in parallel. The time dependence of short circuit current density and power conversion efficiency is highly dependent on the storage conditions. While devices stored under argon atmosphere still possess around 75 % of

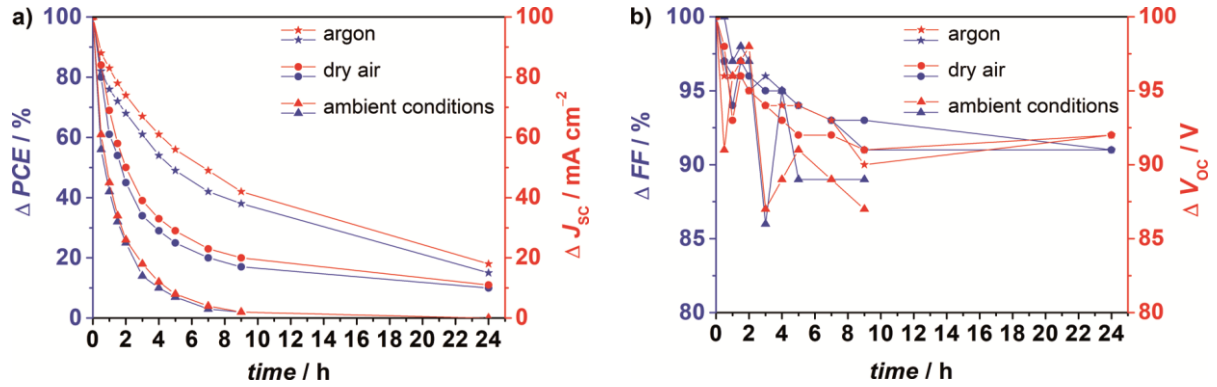

Figure 27. Relative changes in a) power conversion efficiency (blue), short circuit current density (red) and b) fill factor (blue) and open circuit voltage (red), of solar cells when stored under argon atmosphere (star), under dry air (circle) or under ambient conditions (triangle). Devices were of glass/ITO/PEDOT:PSS/**active layer**/Al architecture. Average values over 6 – 7 sub cells are given.

the initial efficiency after one hour and still 15 % after 1 d, devices stored under dry air or under ambient conditions possess only 60 and 40 % of the initial efficiency after one hour and 10 % or cease to operate after 1 d, respectively. This experiment shows that the storage conditions strongly affect the solar cell device parameters, mainly J_{SC} and *PCE*, and the solar cell stability. Furthermore, it demonstrates that humidity dominates the device's degradation rather than the oxygen that is present under ambient conditions. K. Kawano *et. al.* studied a very similar system, utilizing only poly[2-methoxy-5-(3',7'-dimethyloctyloxy)-1,4-phenylenevinylene] (MDMO-PPV) instead of a merocyanine as donor in the active layer.[201] Thus, they were able to measure very similar temporal changes in device parameters.

The very fast device degradation during the initial minutes and hours after fabrication shown here requires a fast characterization and proper storage (ideally inert conditions) in order not to underestimate the device's efficiency. This is especially true if one considers that it takes at least six minutes to measure the *J*-*V* curves of one substrate and that it is possible to fabricate up to 9 substrates at a time. Thus, it might take up to around 1 h until the last solar cell is characterized, which might have up to 40 % reduced efficiency compared to the first cell measured, if the device is stored under ambient conditions. Therefore, it is highly recommended to store the devices under argon atmosphere until all of them are completely characterized.

To assess which element of the solar cell is degraded by water, the active layer was probed by AFM (Figure 28). The device measured directly after fabrication serves as

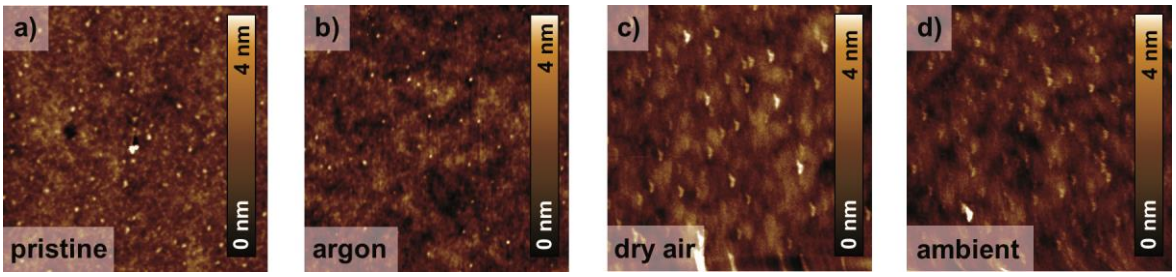

Figure 28. Active layer morphology of **DA3'**:$PC_{61}BM$ after fabrication (a) and after storage for 24 h under argon atmosphere (b), under dry air (c) or under ambient conditions (d). Layers were prepared by spin-coating on glass/ITO/PEDOT:PSS substrates (10 mg ml^{-1} in $CHCl_3$; 1000 rpm, 1000 rpm s^{-1}, 60 s). Size of AFM images is 5 × 5 μm^2.

reference. It shows a smooth film surface with height differences of only 4 nm. While some tiny particles are visible, thorough mixing can be observed for the predominant part of the film. Regardless of storage conditions (argon, dry air or ambient conditions), the AFM images barely change (Figure 28b-d). However, this does not necessarily mean that no changes occur in the BHJ of the device. It is possible that some changes in morphology happen at a length scale which cannot be resolved by AFM. For example it is known from literature that PEDOT:PSS is hygroscopic, so that swelling and demixing of PEDOT and PSS is expected upon contact with moisture.[202] Furthermore, it is possible that the active layer components undergo photo-degradation, e.g. oxidation processes, which will lead to device degradation.[203] However, UV/vis measurements revealed no significant bleaching of the devices after this experiment, so that the active layer components seem to be rather stable.

Even though the AFM measurements were inconspicuous, it was possible to generate huge morphological changes, when the devices were stored under saturated water vapor for 2 minutes (worst case scenario). Figure 29 shows light microscope images of a solar cell, which was freshly prepared (a,b) and after storage under saturated water vapor (c,d). When looking at the device from the bottom (Figure 29a,c) the purple color of the active layer is visible, where light is reflected by the aluminum electrode. Viewed from the top (Figure 29b,d) the light is directly reflected by the aluminum electrode, giving it a white appearance. Two things can be observed after stressing the device with humidity. First, the moisture penetrates into the solar cell from the edges, where protection by the top electrode is the weakest. This is visible with the bare eye due to a darker appearance of the device in the regions with moisture. The moisture front is rather sharp and extends mostly uniform, which is marked by a red line for better visibility (Figure 29c). Second,

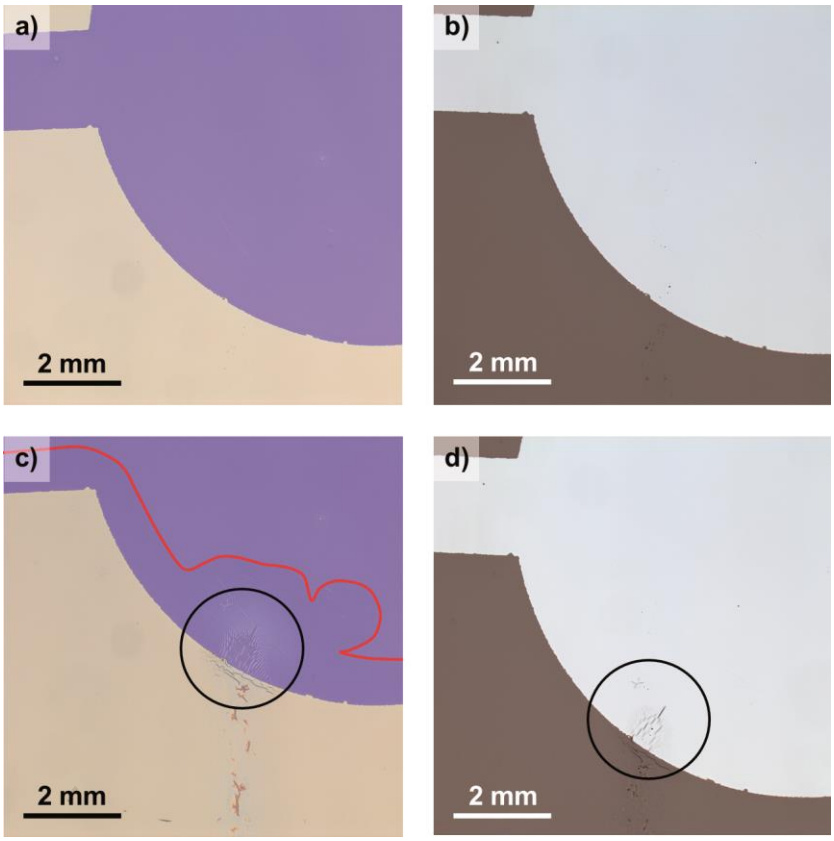

Figure 29. Optical microscope images of a solar cell of **DA3'** in a glass/ITO/PEDOT:PSS/**active layer** /Al architecture. (a,b) Freshly prepared and (c,d) after contact with high humidity for 1 min viewed from the bottom (a,c) and viewed from the top (b,d).

the device starts curling (Figure 29c; black circle), where the PEDOT:PSS layer expands by soaking in the moisture. Next to the waves, cracks become visible that go even through the electrode layer (Figure 29d), resulting in an even faster expansion of the moisture front in this area and therefore in a faster overall device degradation. So like in the studies of K. Kawano *et. al.*, we were able to attribute the degradation of the solar cells to the absorption of water into the PEDOT:PSS layer.[201]

3.1.1.4 Conclusion

DA dye-based solar cells were successfully manufactured under ambient conditions. Their power conversion efficiencies were typically lower by 20 to 40 % compared to reported devices characterized under inert conditions. Furthermore, it was found that the reproducibility of devices manufactured on the same day is good, but significant deviations result depending on the processing day. Further investigations revealed that the device's performance is highly affected by the relative humidity, where processing under low humidity conditions more reliably leads to highly efficient devices. Depending on relative humidity devices could be obtained of **DA3'** with power conversion

efficiencies in the range of 1.00 to 2.40 %. The stability of the solar cells significantly decreased under ambient conditions and the device's degradation was shown to be fast during the first few hours after fabrication. Swelling and segregation of the hygroscopic PEDOT:PSS layer seems to dominate the solar cell degradation of investigated devices under ambient conditions. These processes might further induce a mechanical degradation of the top electrodes, as shown by optical microscopy. In contrast, the negative influence of oxygen and the photo-degradation of active layer components seem to be much weaker than the influence of water.

3.1.2 DA Dye-Fullerene Dyads for Single Component Organic Solar Cells*

3.1.2.1 Design of DA Dye-Fullerene Dyads

The active layer in conventional organic solar cells consists of a mixture of p- and n-type semiconductors. However, it is possible to build up single component solar cells, where the active layer is formed by only one material. This can be done by utilizing dyad molecules. These molecules consist of p- and n-type semiconducting moieties that are covalently bound to each other. The use of such dyads does not only simplify and speed up the processing procedure of organic solar cells – which is very beneficial under ambient conditions – but it can also have further advantages. For instance, the exciton migration should not be limiting in single component solar cells.

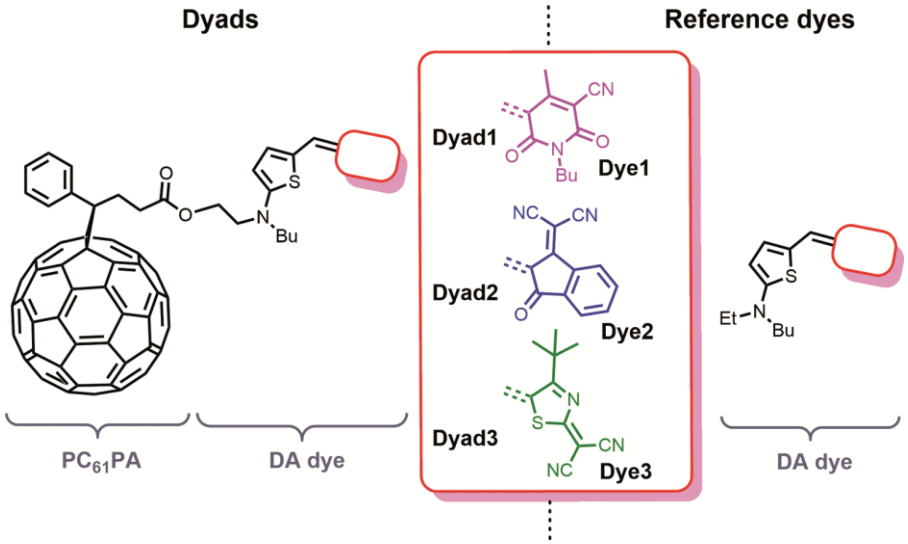

Figure 30. Chemical structures of **Dyad1**, **Dyad2**, **Dyad3** and of the corresponding reference dyes **Dye1**, **Dye2** (formerly **DA3'**) and **Dye3**.

In this study a set of three different DA dye-fullerene dyads were investigated. They were designed based on the n-type semiconducting [6,6]-phenyl-C_{61}-propionic acid ($PC_{61}PA$) and a selection of three different p-type semiconducting DA dyes. The latter themselves consist of an electron-rich donor (D) and an electron poor acceptor (A) moiety. The covalent connection between $PC_{61}PA$ and DA dye was formed via an ethyl chain at DA dyes' amine moieties (Figure 30). This breaks the conjugation between DA dye and C_{60} moiety. However, the linker is short in this set of dyad molecules so that some communication between these might be possible. The DA dyes attached to the fullerene

* The dyads where synthesized by L. Otter & Dr. D. Bialas. The characterization in solution was performed by Dr. D. Bialas.

were built up of an electron-rich aminothiophene connected with an electron poor acceptor moiety, which is either an dioxocyano-pyridine (DOCP), a dicyanomethylene indanone (DCIND) or a thiazol moiety (THZL). The corresponding DA reference dyes **Dye1**, **Dye2** (formerly **DA3'**) and **Dye3** where already introduced in the literature (Figure 30).[196,204–207] In these DA dyes a neutral polyene-like as well as a zwitterionic resonance structure exist. If the charge is perfectly delocalized over the conjugated double bonds, the push-pull chromophore is in the cyanine limit where the bond length alternation is zero. Exemplarily, these three resonance structures are given in Figure 31 for **Dye2**.

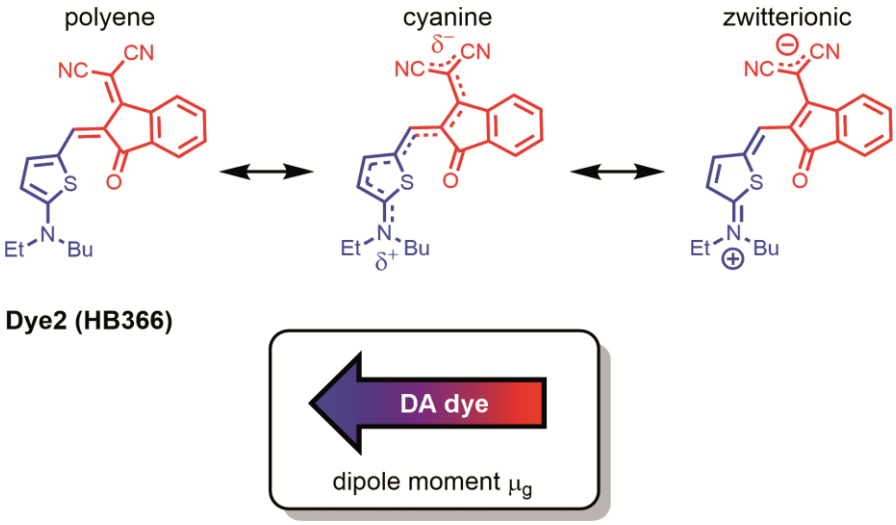

Figure 31. DA dye **Dye2** (donor = blue; acceptor = red) in its polyene like structure (left), in the cyanine limit (middle; *BLA* = 0) and in its zwitterionic form (right). The blue-red arrow symbolizes this kind of dye, while showing the direction of the ground state dipole moment μ_g.

In general, the properties of DA dyes depend on the number of conjugated double bonds, as well as on the strength of the individual donor and acceptor unit. DA dyes utilized in the dyad molecules are made from strong electron-donating and electron-accepting subunits. This leads to the formation of a large ground state dipole moment μ_g, in the range of 5.7 – 13.1 D.[208] To indicate this, an arrow is often used to symbolize these kind of dyes (Figure 31). Furthermore, the bond length alternation is often low in these dyes, so that typically an intense and sharp absorption band can be observed.[209] This is especially true if the DA dye is in the cyanine limit, where the *BLA* is minimized (Figure 31, middle).[208] According to the Gaussian Disorder Model[210] highly dipolar dyes induce a broad density of states in disordered films, which is highly unfavorable for efficient charge transport and application in organic electronics. However, if the dipole moments annihilate in the solid state, due to the dimerization of two dipolar dyes sufficient charge transport properties can be found.[211–213] When the DA dyes are utilized in DA dye-fullerene dyads, dimer formation might still be possible and

if afterwards further aggregation occurred, it would be possible to take control over the active layer morphology. An example for a possible interaction of two dyad molecules via dimer formation is shown in Figure 32.

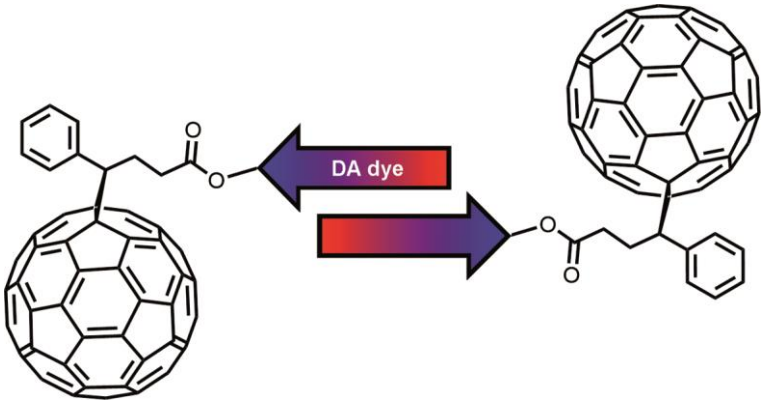

Figure 32. Example for the interaction of two dyad molecules by antiparallel alignment of the highly dipolar DA push-pull chromophores.

3.1.2.2 Absorption and Redox Properties

Absorption spectra of the dyads in comparison to those of the DA dyes are depicted in Figure 33 and the optical properties are given in Table 6. According to the expectations, the differences in acceptor strength and conjugation length have a strong influence on the absorption properties of the reference dyes. A red-shift of the absorption maximum λ_{max} can be observed for **Dye3** (650 nm) and **Dye2** (579 nm) in comparison to **Dye1** (537 nm). The absorption band of **Dye1** is sharp and intense (ε_{max} = 158 × 10^3 M^{-1} cm^{-1}), while it is slightly weaker and broadened for **Dye3** (ε_{max} = 136 × 10^3 M^{-1} cm^{-1}). In **Dye2**, the main absorption band is much broader and its molar extinction coefficient ε_{max} of 65 × 10^3 M^{-1} cm^{-1} is significantly lower than for the other dyes. Thus, it appears that **Dye1** and **Dye3** are much closer to the cyanine limit than **Dye2**, which is reasonable in comparison to similar dyes in literature.[196] All dyes show apparent vibronic progressions at shorter wavelengths, which are most pronounced in **Dye3**. With regard to position and shape, the absorption of all dyads is very similar to the corresponding DA dye absorption. This is because the covalently bound DA dye, which is not in conjugation with the fullerene, dominates the dyads' absorption in the visible range. However, the molar extinction coefficients are decreased in all dyad systems (59 – 153 × 10^3 M^{-1} cm^{-1}). While the decrease is rather small for **Dyad1** and **Dyad2** ($\Delta\varepsilon_{max}$ ~5 × 10^3 M^{-1} cm^{-1}), it becomes much larger for and **Dyad3** ($\Delta\varepsilon_{max}$ = 38 × 10^3 M^{-1} cm^{-1}). This indicates an electronic communication between fullerene and DA dye in the interlinked systems, being most pronounced in **Dyad3**.

Another difference in absorption between dyads and DA dyes can be found at wavelengths below 400 nm. There the $S_0 \rightarrow S_2$ transition of the DA dyes overlaps the absorption of the fullerene in the dyad molecules, giving rise to increased molar extinction coefficients of about 40×10^3 M^{-1} cm^{-1}.

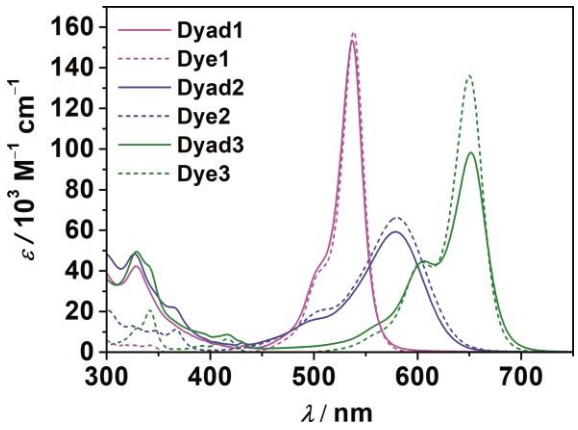

Figure 33. Absorption spectra of **Dyad1** (magenta, bold), **Dyad2** (blue, bold), **Dyad3** (green, bold) and of merocyanine reference dyes **Dye1** (magenta, dashed), **Dye2** (blue, dashed), **Dye3** (green, dashed) in CH_2Cl_2 ($c \sim 10^{-5}$ K).

To determine the energetic position of the frontier molecular orbitals, cyclic voltammetry measurements were performed in CH_2Cl_2 (Figure 34). The oxidation and reduction half wave potentials $E_{1/2}$ as well as the electrochemical E_{gap}^{CV} and optical band gaps E_{gap}^{opt} are given in Table 6. For all dyad molecules reversible oxidation and reduction potentials were found, which are located at similar potentials as the oxidation potentials of the corresponding reference dyes. Nevertheless, the oxidation of the dyads seems to be shifted by around 50 mV, compared to the corresponding reversible oxidation of the reference compound. Consequently, there has to be a slight interaction between fullerene and DA dye building block. The reduction potentials of the dyad molecules occur in a close range of 1.09 – 1.14 V as it known for $PC_{61}BM$, indicating that the reduction indeed takes place at the fullerene moieties. As expected, the irreversible reduction potentials (peak potentials) of **Dye1**, **Dye2**, and **Dye3** are located at −1.74, −1.52 and −1.43 V, respectively, showing that it is much more difficult to form stable radical anions for these compounds than for the dyads. As already seen from UV/vis absorption measurements the different acceptor strengths the heterocyclic acceptors lead to a variation in the optical band gap (Table 6), which is 2.30, 2.14 and 1.91 eV for **Dye1**, **Dye2** and **Dye3**, respectively. The dyad molecules possess the same optical band gap as their reference

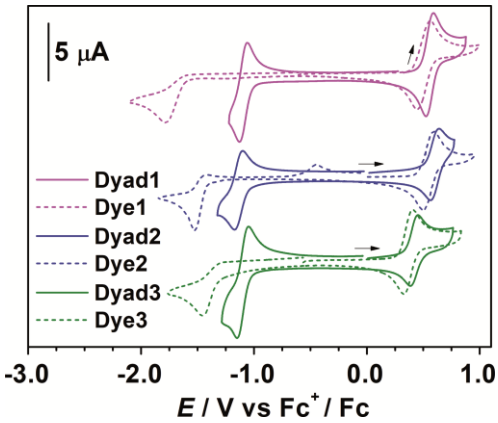

Figure 34. Cyclic voltammograms of **Dyad1** (magenta, bold), **Dyad2** (blue, bold), and **Dyad3** (green, bold) and of corresponding DA dyes **Dye1** (magenta, dashed), **Dye2** (blue, dashed) and **Dye3** (green, dashed). Measurement conditions: CH_2Cl_2, c ~10^{-4} M, 298 K (scan rate: 100 mV s^{-1}; supporting electrolyte: Bu_4NPF_6 (0.1 M); Pt-disc electrode (Ø 3mm); calibrated vs. Fc^+/Fc as an internal standard).

dyes. While the electrochemical band gap (Table 6) fits very well to the optical band gap of the reference dyes, this is not the case for the dyad molecules. In the latter the electrochemical band gaps are much smaller (1.74 – 1.52 eV) than the optical band gaps. Therefore, the optical transition still seems to be located on the DA-dye, while the LUMO is now located on the fullerene. This confirms that the already observed interaction between DA-dye and fullerene is rather small.

Table 6. Optical and electrochemical properties of dyads and DA reference dyes.

dye	λ_{max} [a] [nm]	ε_{max} [a] [10^3 M^{-1} cm^{-1}]	μ^2_{eg} [b] [D^2]	$E_{1/2}^{red}$ [c] [V]	$E_{1/2}^{ox}$ [c] [V]	E_{gap}^{opt} [eV]	E_{gap}^{CV} [eV]
Dyad1	537	153	100	–1.09	+0.56	2.31	1.65
Dye1	539	158	94	–1.74 [d]	+0.51	2.30	2.25
Dyad2	579	59	87	–1.14	+0.60	2.14	1.74
Dye2	578	65	94	–1.52 [d]	+0.54	2.14	2.06
Dyad3	651	98	96	–1.10	+0.42	1.90	1.52
Dye3	650	136	99	–1.43 [d]	+0.37	1.91	1.80

[a] CH_2Cl_2 (c ~ 10^{-5} M, 298 K). [b] Square transition dipole moments. [c] Measurements were carried out in dry CH_2Cl_2, c ~10^{-4} – 10^{-5} M. scan rate 100 mV s^{-1}; supporting electrolyte Bu_4NPF_6 (c = 0.1 M); Pt-disc electrode (Ø 3mm); calibrated vs. ferrocenium/ferrocene (Fc^+/Fc; −5.15 eV vs. vacuum) as an internal standard. [d] Peak potential of irreversible reduction.

The HOMO and LUMO levels of the compounds calculated from the optical or the electrochemical band gap are shown in Figure 35. The LUMO levels determined from the optical band gap are effectively reduced when going from **Dye1** over **Dye2** to **Dye3**, being in the range of 3.36 – 3.67 eV. This trend is lost in the dyad molecules, when the electrochemical band gap is used for LUMO calculation. In this case, all dyads

show LUMO levels in the range of −4.01 to −4.06 eV, which fits well to the LUMO level of $PC_{61}BM$ of −3.9 eV. The HOMO levels of **Dyad1** and **Dyad2** or **Dye1** and **Dye2** are very similar (−5.71 and −5.75 eV or −5.66 and −5.69 eV). The HOMO levels of **Dyad3** and **Dye3** are located around 0.2 eV higher than the HOMO levels of the other molecules.

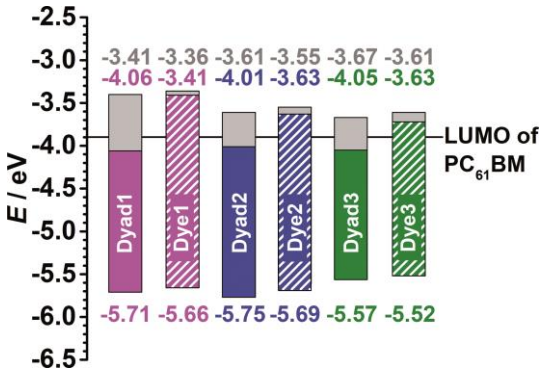

Figure 35. Frontier molecular Orbitals of dyads (filled) and of corresponding DA reference dyes (dashed) and LUMO level of $PC_{61}BM$.

The optical and electrochemical studies show that the DA dye dominates the absorption of the dyad molecules. Thus, by variation of DA dye subunit the dyads' absorption occurs at a different spectral range. Small differences in molar extinction coefficients and oxidation potentials between dyads and corresponding DA dyes indicate interaction between the two subunits of the dyad molecules. The fact that oxidation and reduction are located on the DA dye and the fullerene, respectively, indicates that this interaction is rather small. Furthermore, the dyad molecules enable independent tuning of HOMO and LUMO levels, which can be a big advantage.

3.1.2.3 Single Component Solar Cells of Dyads measured under Ambient Conditions

To investigate the performance of the three different dyad molecules **Dyad1**, **Dyad2** and **Dyad3** as an active layer in single component organic solar cells, devices were prepared in a simple glass/ITO/PEDOT:PSS/**Dyad**/Al architecture. The active layer, consisting of only one component, was spin coated from a 10 mg ml^{-1} solution in $CHCl_3$. For comparison, devices were fabricated from the corresponding reference dyes in the same architecture, but a BHJ of DA dye and $PC_{61}BM$ was used as active layer. The ratio of DA dye to $PC_{61}BM$ was chosen to match the DA dye to fullerene ratio within the dyad molecules, meaning a molar ratio of 1:1. The *J-V* characteristics and corresponding solar cell parameters of the best devices are depicted in Figure 36 and in Table 7.

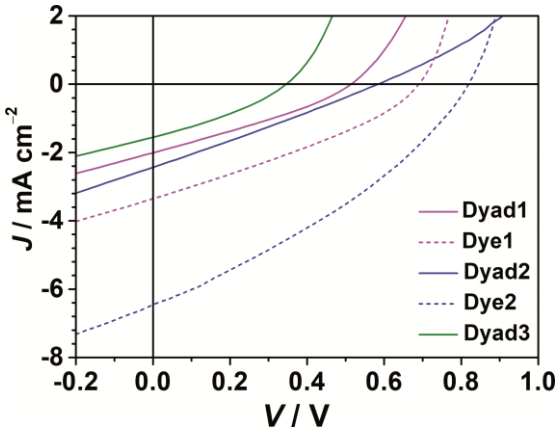

Figure 36. *J-V* characteristics of solar cells of **Dyad1** (magenta, bold), **Dyad2** (blue, bold), **Dyad3** (green, bold) and of reference BHJ solar cells (molar ratio of DA dye:$PC_{61}BM$ was 1:1) of **Dye1** (magenta, dashed) and **Dye2** (blue, dashed) all in a glass/ITO/PEDOT:PSS/**active layer**/Al architecture. Curves were measured under simulated AM1.5 G illumination, with 100 mW cm^{-2}.

Surprisingly, devices of **Dye3** did not show any reproducible performance in BHJ solar cells and were therefore omitted from further experiments. All single component devices, containing dyad molecules as active layer material, showed a moderate solar cell performance. Efficiencies were the highest for **Dyad2** and **Dyad1** with 0.37 and 0.31 %, respectively, while **Dyad 3** showed a lower performance of only 0.17 %. This trend resembles the difference in open circuit voltage of 0.58 V (**Dyad2**), 0.52 V (**Dyad1**) and 0.34 V (**Dyad3**), which again correlates with the electrochemical band gap of the dyad molecules. Additionally, the same order can be observed in the short circuit current density, which is 2.43, 2.00 and 1.55 mA cm^{-2} for **Dyad2**, **Dyad1** and **Dyad3**, respectively. The variation in short circuit current density in turn cannot be solely explained by the difference in optical density of the solar cells, which is the highest for **Dyad1** and much lower for **Dyad2** and **Dyad3** (Figure 37a). The BHJ devices based on a mixture of DA dye and $PC_{61}BM$ in a molar ratio of 1:1, clearly outperform the

Table 7. Solar cell characteristics of glass/ITO/PEDOT:PSS/**active layer**/Al devices under simulated AM 1.5 illumination (100 mW cm^{-2}) in air. Additionally, the molar donor to acceptor ratio (D:A) is given.

active layer	D:A [n:n]	*PCE* [a] [%]	J_{SC} [mA cm^{-2}]	*FF* [%]	V_{OC} [V]
Dyad1	–	0.31 (0.30)	2.00	30	0.52
Dye1:PC$_{61}$BM	1:1	0.73 (0.68)	3.34	32	0.68
Dyad2	–	0.37 (0.35)	2.43	27	0.58
Dye2:PC$_{61}$BM	1:1	1.76 (1.70)	6.45	33	0.82
Dyad3	–	0.17 (0.16)	1.55	32	0.34
Dye3:PC$_{61}$BM	1:1	–	–	–	–

[a] Value in brackets is the average over 7 devices.

corresponding single component solar cells with power conversion efficiencies of 0.73 (**Dye1**) and 1.76 % (**Dye2**), respectively. This is due to the improved fill factors (32 – 33 %), much higher open circuit voltages of 0.68 (**Dye1**) and 0.82 V (**Dye2)** as well as higher short circuit current densities of 3.34 mA cm^{-2} (**Dye1**) and 6.45 mA cm^{-2} (**Dye2**). Most probably, charge separation and charge transport are much better in the BHJ devices and less recombination processes occur. If the 1:1 devices based on **Dye1** and **Dye2** are compared with each other, the latter show a superior open circuit voltage and short circuit current density. This difference is even more pronounced than in the case of **Dyad1** and **Dyad2**. While the absorption of the dyad-based solar cells and of the reference solar cells is similar with regard to shape and strength, the external quantum efficiency is much higher in the reference devices. This confirms the trend observed in short circuit current density derived from *J-V* measurements. Devices based on **Dye1** and **Dye2** yielded a maximum *EQE* of 32 and 43 % at 540 and 580 nm, respectively. In contrast, the maximum *EQE* of **Dyad1** and **Dyad2** was only 21 and 16 % at 520 and 610 nm, respectively.

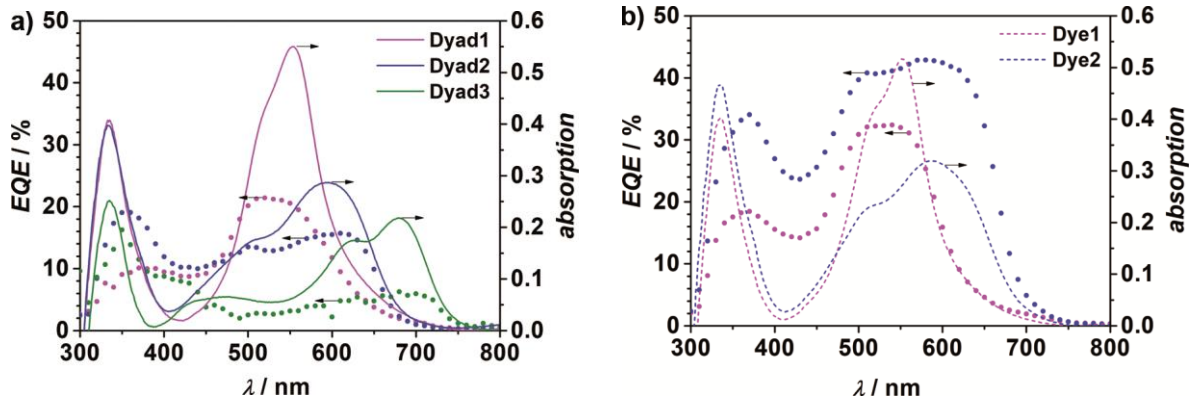

Figure 37. Spectrally resolved *EQE* (dotted lines) and absorption spectra (bold lines) of a) single component solar cells utilizing **Dyad1** (magenta), **Dyad2** (blue), **Dyad3** (green) and b) BHJ solar cells with **Dye1**:$PC_{61}BM$ (magenta; molar D:A ratio of 1:1) and **Dye2**:$PC_{61}BM$ (blue; molar D:A ratio of 1:1) as active layer. The devices were fabricated in a glass/ITO/PEDOT:PSS/**active layer**/Al architecture.

To optimize the performance of the dyad based devices, solar cells with thermally annealed active layers were fabricated next. This gives the molecules the possibility to rearrange and pack in a more efficient and ordered structure, so that the devices' performance might improve. The dyads were again spin coated from a 10 mg ml^{-1} solution in $CHCl_3$ on transparent glass/ITO substrates, covered with a PEDOT:PSS interlayer. Before back contact preparation (aluminum), thermal annealing was performed for 1 min at 150 °C. At this temperature decomposition of the active layer materials should not occur to a large extent, especially not for this short annealing time.

Indeed, the performance of the devices was slightly increased by thermal annealing as shown in Figure 38 and Table 8.

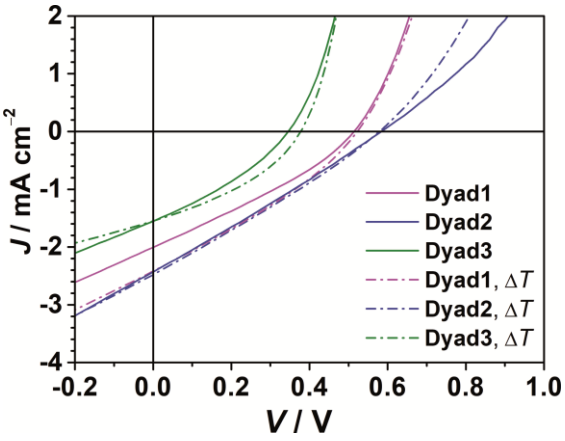

Figure 38. *J-V* characteristics of solar cells with glass/ITO/PEDOT:PSS/**dyad**/Al architecture of **Dyad1** (magenta), **Dyad2** (blue) and **Dyad3** (green), before (bold lines) and after (dot-dashed lines) thermal annealing ΔT (1 min, 150 °C). Curves were measured under simulated AM1.5 G illumination, with 100 mW cm^{-2}.

The power conversion efficiencies rose from 0.31 to 0.38 %, from 0.37 to 0.39 % and from 0.17 to 0.22 % for **Dyad1**, **Dyad2** and **Dyad3**, respectively. The main reason for the improvement was an increase in short circuit current density for **Dyad1** and **Dyad2** by 0.41 and 0.04 mA cm^{-2}, respectively. In case of **Dyad3**, the fill factor and the open circuit voltage were increased from 32 to 36 % and from 0.34 to 0.38 V, respectively.

Table 8. Comparison of device parameters of thermally annealed (ΔT; 1 min, 150 °C) and pristine single component organic solar cells in glass/ITO/PEDOT:PSS/**dyad**/Al architecture.

active layer	ΔT	*PCE* [a] [%]	J_{SC} [mA cm^{-2}]	*FF* [%]	V_{OC} [V]
Dyad1	−	0.31 (0.30)	2.00	30	0.52
	+	0.38 (0.31)	2.41	30	0.52
Dyad2	−	0.37 (0.35)	2.43	27	0.58
	+	0.39 (0.36)	2.47	27	0.58
Dyad3	−	0.17 (0.16)	1.55	32	0.34
	+	0.22 (0.21)	1.55	36	0.38

[a] Value in brackets is the average over 7 devices.

To find an answer to the questions why a) the reference devices made from DA dye and $PC_{61}BM$ in a molar ratio of 1:1 perform much better than the single component devices based on **Dyad1-3** and b) which effect the thermal annealing has on the active layer morphology, AFM images were measured of the corresponding devices (Figure 39). The surfaces of the active layers of **Dyad1-3** were found to be quite homogeneous in the

pristine devices (Figure 39a-c), showing a root mean square roughness R_{rms} of around 1nm. This is indicative for intimate phase segregation. However, it was observed that the spin coating procedure creates many small, distinct pinholes of up to 200 nm in diameter, which might affect the performance as well as the stability of the devices. Similar observations were made in the literature,[214,215] where in one case the problem was overcome by vacuum sublimation of the corresponding layer.[215] Due to the fact that **Dyad1-3** are not sufficiently stable for vacuum sublimation at high temperatures, this was not an option.

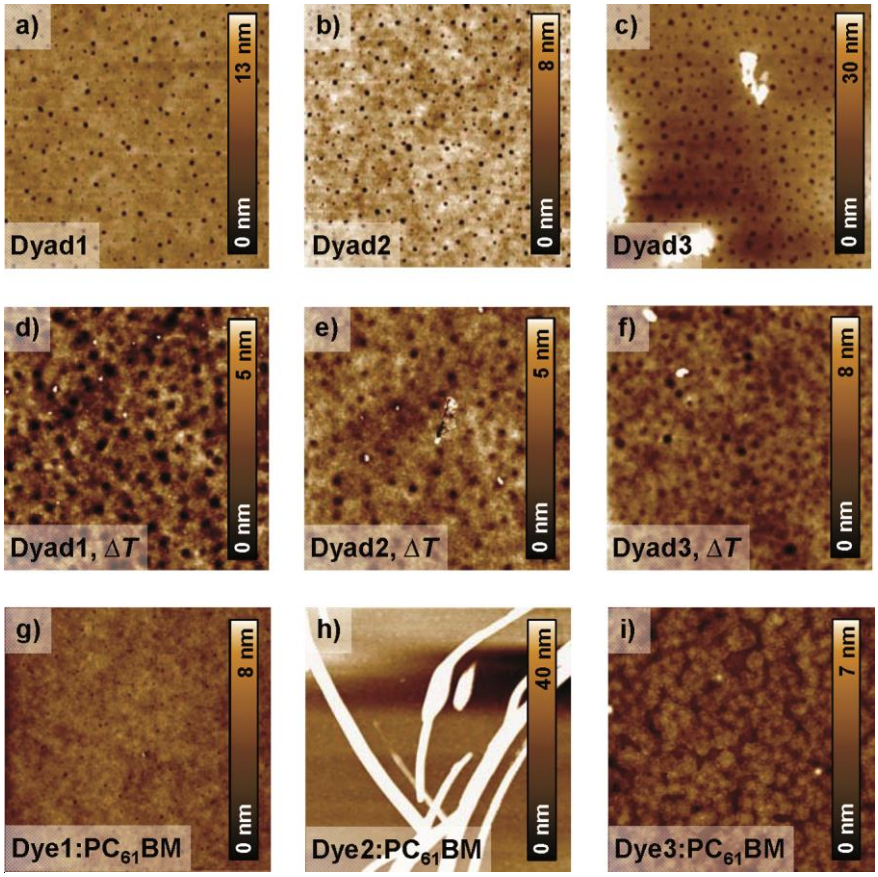

Figure 39. Active layer morphology of a) **Dyad1**, b) **Dyad2**, c) **Dyad3** as single components, of d) **Dyad1**, e) **Dyad2**, f) **Dyad3** after thermal annealing (150 °C, 1 min) and of g) **Dye1**, h) **Dye2**, i) **Dye3** in a BHJ structure with $PC_{61}BM$ (molar ratio = 1:1). Layers were prepared by spin-coating on glass/ITO/PEDOT:PSS substrates (10 mg ml^{-1} in $CHCl_3$; 1000 rpm, 1000 rpm s^{-1}, 60 s). Size of AFM images is 5 × 5 μm^2.

In contrast, the reference devices based on **Dye1-3** (Figure 39g-i) all behaved differently. **Dye1** in combination with $PC_{61}BM$ formed a smooth active layer, with very tiny pinholes. The active layer of **Dye2** and $PC_{61}BM$ was again smooth, but on top large fibers of 40 – 120 nm in height and several micrometers in length could be observed. These were probably formed by the DA dye. When **Dye3** was used as donor component,

segregation into small domains of **Dye3** and $PC_{61}BM$ could be observed, while the root mean square roughness of the film stayed below 1 nm. These differences in active layer morphology give a possible explanation for the better performance of the BHJ devices in comparison to the single component devices. In the former ones the active layer components can undergo phase separation, to form domains or even strands of the single components, which is favorable e.g. for charge transport. This is almost impossible in the dyad based devices, due to the covalent linkage between donor and acceptor moieties. Consequently, the BHJ devices outperform the single component solar cells. The active layers of **Dyad1**, **Dyad2** and **Dyad3** (Figure 39d-f) undergo some changes upon thermal annealing, too. The pin holes observed in the pristine devices increase in diameter (up to 350 nm), but due to the fact that the layer looks washed out, it is assumed that they are filled up with material. Thus, these small morphological changes in the structure of the active layer have to be the reason for the beneficial effects of the thermal annealing procedure.

A more impressive improvement than by thermal annealing of dyad based solar cell was achieved by using a MoO_3 instead of an PEDOT:PSS interlayer. The high work function of MoO_3 is known to cause a pinning of the deep HOMO levels and by that enhancing the obtained open circuit voltage in merocyanine based solar cells.[196,216,217] The dyad based devices were prepared as before, but instead of PEDOT:PSS, a vacuum deposited interlayer of MoO_3 (10 nm) was utilized, which was thermally evaporated. The current voltage curves as well as the *EQE* and solar cell absorption spectra of devices with MoO_3 interlayer are shown in Figure 40. Parameters for devices on both interlayers are displayed in Table 9.

Table 9. Comparison of device parameters of single component organic solar cells on PEDOT:PSS and MoO_3 interlayer. **Dyad1**, **Dyad2** and **Dyad3** were investigated in a glass/ITO/interlayer/**dyad**/Al architecture.

active layer	interlayer	*PCE* [a] [%]	J_{SC} [mA cm^{-2}]	*FF* [%]	V_{OC} [V]
Dyad1	PEDOT:PSS	0.31 (0.30)	2.00	30	0.52
	MoO_3	0.99 (0.98)	3.59	34	0.82
Dyad2	PEDOT:PSS	0.37 (0.35)	2.43	27	0.58
	MoO_3	1.14 (1.10)	4.36	31	0.86
Dyad3	PEDOT:PSS	0.17 (0.16)	1.55	32	0.34
	MoO_3	0.50 (0.49)	2.04	39	0.62

[a] Value in brackets is the average over 7 devices.

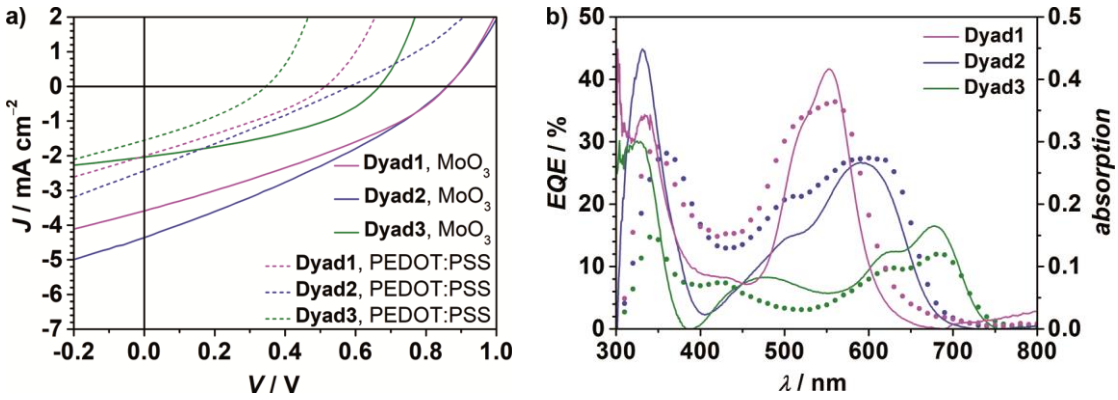

Figure 40. a) *J-V* characteristics of solar cells with **Dyad1** (magenta), **Dyad2** (blue), **Dyad3** (green) in a glass/ITO/interlayer/**dyad**/Al architecture, utilizing PEDOT:PSS (dotted lines) or MoO_3 (bold lines) as interlayer. *J-V* curves were measured under simulated AM1.5 G illumination with 100 mW cm^{-2}. b) Corresponding *EQE* and absorption spectra of solar cells on MoO_3 interlayer.

As expected for the solar cells on MoO_3, the open circuit voltage was increased by around 0.3 V for devices with all dyads. Additionally, an increase in short circuit current density of up to 1.93 mA cm^{-2} and in fill factor by 4 to 7 % could be obtained. Consequently, the device performance was increased for **Dyad1-3** from 0.31 – 0.99 %, 0.37 – 1.14 % and from 0.17 – 0.50 %. This clearly shows that MoO_3 is the superior interlayer for devices based on DA dye-fullerene dyads, like it is for other BHJ solar cell of the merocyanine material class.[196,217]

Conclusively, it could be shown that all three dyad molecules yield functioning solar cells devices, with efficiencies in the following order: **Dyad2** > **Dyad1** > **Dyad3**. The comparison of dyad based solar cells and their corresponding reference devices (**Dye1-3** in combination with $PC_{61}BM$ in a molar ratio of 1:1) revealed that phase segregation seems to be very important for efficient solar cells, which is one drawback of the dyad molecules. However, by utilization of MoO_3 interlayers the single component solar cell efficiency could be increased up to 1.14 % (**Dyad2**) under ambient conditions.

3.1.2.4 Optimization of Single Component Solar Cells under Inert Conditions[†]

To further optimize the single component solar cells and to utilize the advantage of inert conditions,[104] a collaboration with the working group of Prof. Dr. K. Meerholz was started. During a stay at the Universität zu Köln two of the three introduced dyad compounds could be tested, namely **Dyad1** and **Dyad2**. These were choosen because

[†] During a guest stay **Dyad1** and **Dyad2** were optimized and investigated under inert conditions (Spin coating & measurements under N_2; Top contact preparation under Ar and high vacuum ~ 2×10^{-6} mbar; O_2 and H_2O < 0.1ppm) in collaboration with the research group of Prof. Dr. K. Meerholz under supervision of Dr. M. R. Lenze at the Institut für Physikalische Chemie of the Universität zu Köln.

promising efficiencies of 0.99 % and 1.14 % could already be measured for them under ambient conditions.

The device architecture we used during the collaboration was a little different compared to the architecture investigated in Würzburg. Instead of an aluminim top contact a combination of calcium interlayer (1 nm) combined with silver electrode (150 nm) was used (architecture: glass/ITO/interlayer/**dyad**/Ca/Ag). This combination is advantageous under inert conditions, because the low work function of the calcium (~3 eV)[218] ensures an ohmic contac to the n-type semiconductor and increases the charge carrier selectivity.[30] It is well known that due to the high reactivity of calcium, the device's stability is decreased significantly under ambient conditions. Therefore, electrodes from calcium and silver were not utilized in Würzburg.

At first the active layer thickness of the organic solar cells was optimized, because it is of high importance for the device performance.[219–221] Its influence was studied in detail for devices with **Dyad2**. This experiment was not performed on MoO_3, because scratching on this interlayer does not work sufficiently, so that thickness measurements with a profilometer or AFM did not yield reliable results. The active layer thickness was controlled by different spin speeds (400 – 4000 rpm), while spin coating from a 10 mg ml^{-1} solution in $CHCl_3$. This procedure led to a thickness variation from 92 to 35 nm, measured with a profilometer. The resulting solar cell parameters can be found in Table 10. The influence of active layer thickness on the different device parameters is shown in Figure 41. The power conversion efficiency of the devices indeed changes dramatically upon variation of active layer thickness, covering values of 0.37 – 0.74 %. The fill factor decreases steadily upon increasing the film thickness, which is common in

Table 10. Device characteristics of **Dyad2** solar cells (glass/ITO/PEDOT:PSS/**Dyad2**/Ca/Ag) with different active layer thickness.

active layer	spin speed [rpm]	d [a] [nm]	PCE [b] [%]	J_{SC} [b] [mA cm^{-2}]	FF [b] [%]	V_{OC} [b] [V]
Dyad2	400	92	0.44	2.30	27	0.72
	550	77	0.60	2.95	28	0.72
	700	75	0.56	3.01	28	0.67
	850	68	0.63	3.28	28	0.67
	1000	59	0.68	3.43	29	0.68
	1250	**54**	**0.73**	3.49	31	0.67
	1600	**51**	**0.74**	3.37	33	0.66
	2200	42	0.67	2.91	36	0.64
	3000	38	0.56	2.38	39	0.61
	4000	35	0.37	1.69	40	0.55

[a] Deviation is ±5 %. [b] Average value over 7 devices on the same subtrate.

organic solar cells, e.g. due to increased transport resistance and stronger charge accumulation.[222–224] The V_{OC} increases by around 20 %, when the film thickness is increased and a saturation is reached at a thickness of about 50 nm. The short circuit current density (Figure 41a) reaches a maximum of 3.49 mA cm^{-2} at about 55 nm. Very thin layers do not absorb much light so the J_{SC} first rose with increasing layer thickness until the negative effects dominated, like hindered charge transport. Mainly as a result of change of *FF* and J_{SC}, the power conversion efficiency reaches a maximum of around 0.74 % at an active layer thickness of 50 − 55 nm.

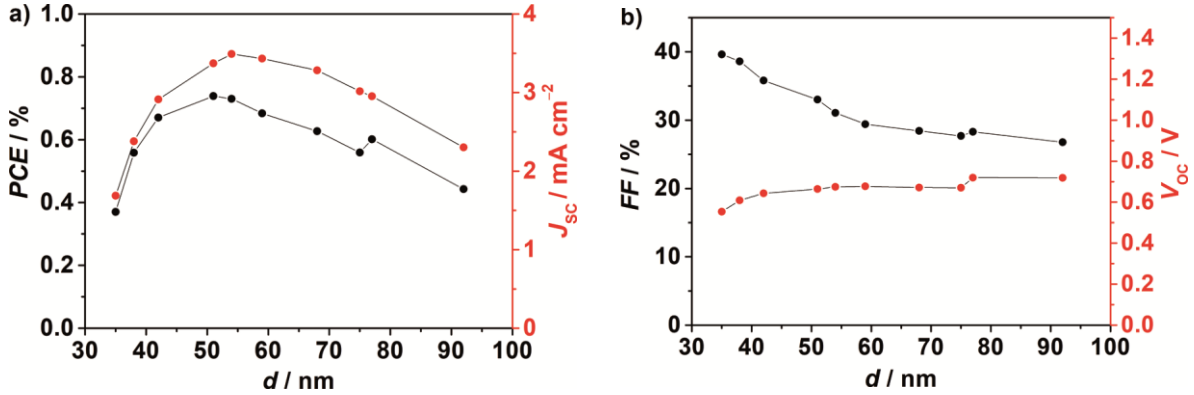

Figure 41. a) Change of power conversion efficiency *PCE* (black) and short circuit current density J_{SC} (red) and b) variation of fill factor *FF* (black) and open circuit voltage V_{OC} (red), with variation of active layer thickness *d* in glass/ITO/PEDOT:PSS/**Dyad2**/Ca/Al single component solar cells.

Finally, optimized devices of **Dyad1** and **Dyad2** of glass/ITO/MoO_3/**dyad**/Ca/Ag were prepared, where the active layer was spin coated from chloroform solution with a rotation speed of 1500 and 1300 rpm, respectively. For ideal performance MoO_3 was used instead of PEDOT:PSS as interlayer: The device performance is superior with this material (see Section 3.1.2.3). The *J-V* characteristics of the optimized devices, corresponding *EQE* spectra as well as the absorption of the device can be found in Figure 42. When the optimized devices are compared to the ones produced under ambient conditions, an increase in *PCE* for **Dyad1** from 0.99 to 1.18 % and for **Dyad2** from 1.14 to 1.59 % can be observed, respectively. This is the result of an increase in *FF* as well as V_{OC}. Due to the use of the optimized, increased spin speeds, the active layer thickness is most probably decreased in devices that were produced under inert conditions. Consequently, this leads to a reduced short circuit current density, but is probably one reason for increased fill factors, too. The fact that **Dyad2** showed superior performance in non-optimized devices, is maintained after optimization. Interestingly, both optimized

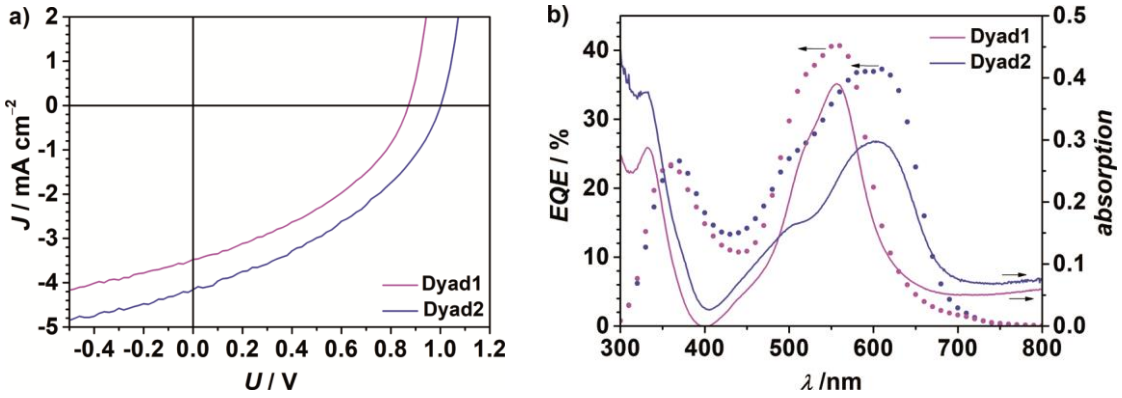

Figure 42. a) *J-V* curves of optimized glass/ITO/MoO_3/**dyad**/Ca/Ag devices of **Dyad1** (magenta) and **Dyad2** (blue) under simulated AM1.5 G irradiation (100 mW cm^{-2}). b) Corresponding *EQE* (dotted) and absorption spectra (bold; measured in transmission). The absorption spectra do not fall down to zero at long wavelengths, most probably because of an imperfect glass/ITO/MoO_3 reference.

devices possess a fill factor of 39 %, while J_{SC} and V_{OC} are increased in devices with **Dyad2**. The *EQE* of the two dyad molecules covers the whole range from 300 to 700 nm, showing that charges are generated, whether absorption takes place at the fullerene or at the DA dye. The maximum *EQE* of the optimized devices is measured at 560 and 610 nm with 41 and 37 % for **Dyad1** and **Dyad2**, respectively. This fits quite well to the absorption maximum of the solar cells, which is at 556 and 603 nm for **Dyad1** and **Dyad2**, respectively.

Table 11. Device parameters of solar cells fabricated under optimized conditions in a glass/ITO/MoO_3/**dyad**/Al (ambient) or glass/ITO/MoO_3/**dyad**/Ca/Ag (inert) architecture.

active layer	conditions	spin speed [rpm]	*PCE* [a] [%]	J_{SC} [mA cm^{-2}]	*FF* [%]	V_{OC} [V]	EQE_{max} [%]
Dyad1	ambient	1000	0.99 (0.98)	3.59	34	0.82	36
	inert [b]	1500	1.18 (1.16)	3.45	39	0.88	41
Dyad2	ambient	1000	1.14 (1.10)	4.36	31	0.86	27
	inert [b]	1300	1.59 (1.60)	4.13	39	1.00	37

[a] Value in brackets is the average over 7 devices. [b] Glove Box (N_2; O_2 and H_2O < 0.1ppm).

Compared to other dyad molecules that can be found in literature (see Figure 18), **Dyad1** and **Dyad2** perform very well after careful optimization under inert conditions. Their efficiencies of 1.18 and 1.59 % are among the highest currently reported for single component solar cells (see Chapter 2.3.2).

3.1.2.5 Conclusion

Comparison of dyad based solar cells with the corresponding BHJ devices of free donor and acceptor units reveals that the active layer morphology is most probably one limiting factor for the device performance, because no phase segregation is possible in the case of dyad molecules. In contrast to most dyad molecules, **Dyad1-3** possesses a short linking unit between donor and fullerene and are much smaller. The best performing dyad (PCE_{max} ~2.2 %)[151] utilizes a short aliphatic linking unit, too, indicating that this approach might be advantageous in general. Possibly, a better communication between donor and acceptor is the reason for this. It is known that the high dipolarity of the DA dyes was not problematic for good charge transport behavior due to the formation of centrosymmetric dimers, as shown in recent work.[212,213] The good device performance of our dyad molecules indicates that this still might be valid, even though single crystals could not be grown for a dyad molecule. Finally, optimized devices showed power conversion efficiencies of up to 1.59 % under inert conditions, being among the highest values reported to date.

3.2 ADA and AπA Molecules as New Electron Acceptors in Organic Electronics

3.2.1 ADA Dyes Tailored by Core and Acceptor Group Variation‡

3.2.1.1 Design and Synthesis

In the field of organic photovoltaics, there is a large demand for new electron acceptor materials that outperform fullerenes, e.g. with regard to absorption and tunability, to further improve device performance (*PCE* >10 – 15 %). As described above the design of small molecules with alternating donor and acceptor units is a very appealing strategy to create such tailored materials with desired properties, like low lying LUMO levels, sufficient electron transport behavior as well as strong absorption in the visible range of light. This concept was followed, when ADA systems flanked either by two 1,3-indandione (IND) or 1,1-dicyanomethylene-3-indanone (DCIND)[211,196,226–229] acceptor units were designed and synthesized. Systematic variation of donor and acceptor moieties were performed, to investigate the influence on photophysical and electrochemical properties of the series of the ADA dyes. Therefore, two sets of ADA compounds were designed, distinguishable by two different acceptor units (Figure 43). As donor core, four different types of electron-donating moieties were chosen, consisting of a central five-membered ring, which is surrounded by two five- or six-membered aromatic rings. One half of these donors contains two bithienyl units (compounds **ADA1** and **ADA2**), while the other half bears two biphenyl moieties (compounds **ADA3** and **ADA4**).

Another possibility to classify the series of molecules is by type of their central (hetero-)cycle in the donor core. Two compounds possess a central ring containing nitrogen as heteroatom (compounds **ADA1** and **ADA3**), the other two cores are built up of a carbocyclic central ring (compounds **ADA2** and **ADA4**). Solubilizing side chains are attached to the molecules. To choose the right length of the alkyl chains was highly important. They have to be long enough to ensure reasonable solubility to simplify synthesis, work-up and purification without being too long to hinder the self-assembly of the dyes in the solid, which would have been detrimental for device operation.[230]

‡ Adopted from reference[225] with permission from the Chinese Chemical Society (CCS), Shanghai Institute of Organic Chemistry (SIOC), and the Royal Society of Chemistry. Dr. A. Nowak-Król contributed greatly to the syntheses and performed all quantum chemical calculations.

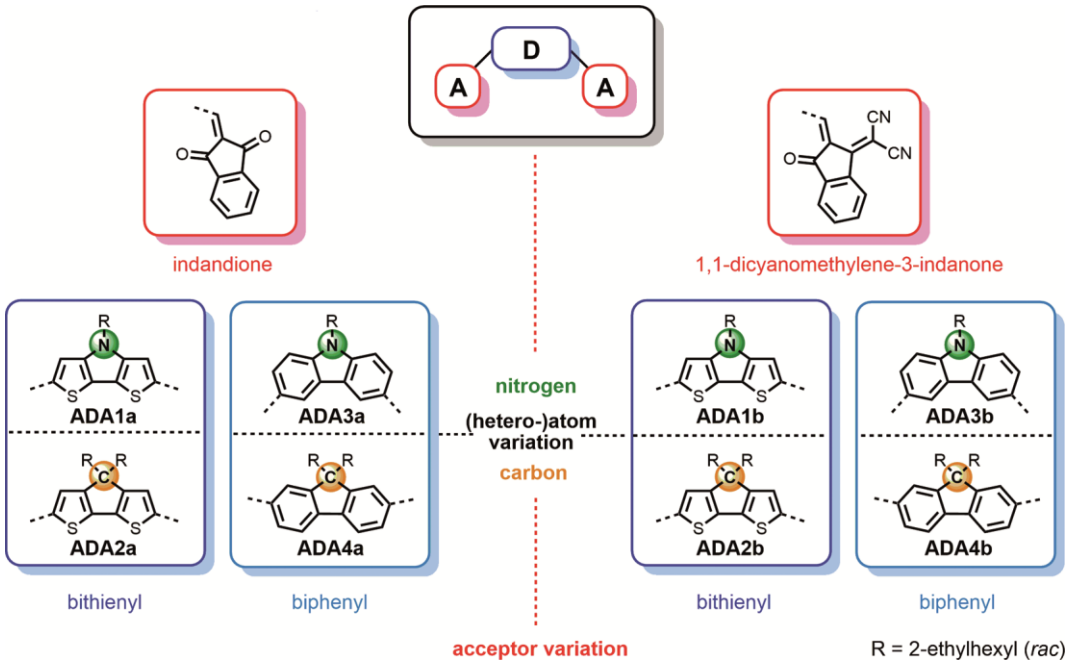

Figure 43. Structures of ADA molecules **ADA1a – 4a** with 1,3-indandione and **ADA1b – 4b** with 1,1-dicyanomethylene-3-indanone acceptors (red). The central donor cores contain bithienyl (dark blue) and biphenyl units (light blue) and their (hetero-)atom varies (nitrogen = green; carbon = orange).

In the ideal case, the processability should not be limited to either vacuum sublimation (very short/no side chains; low solubility) or solution processing (very large side chains; high molar mass; not sublimable). Thus, racemic ethylhexyl chains were selected for the studies. The proposed synthetic route was based on a Knoevenagel condensation between electron-rich dialdehydes and electron-poor CH-acids in the key step (Figure 44). For active methylene compounds indandione IND and DCIND were chosen. Both compounds possess a rigid framework with an additional benzene ring, which was supposed to further shift the absorption towards lower energies. Donor cores, symmetrically functionalized with aldehyde moieties, as well as the DCIND acceptor were synthesized according to the literature-known procedures (see Chapter 6). With all building blocks in hand, Knoevenagel condensation reactions between donor components and active methylene compounds were performed. The conditions of selected experiments and the yields of the main products are shown in Table 12. First, CH-acids **A1** and **A2** were reacted with the dithienopyrrole (DTP) core **Ald1** utilizing pyridine as a base. Both reactions were carried out overnight and at RT, producing corresponding dyes **ADA1a** and **ADA1b** in satisfactory yields of around 50 %. The condensation between the structurally similar cyclopentadithiophene (CPDT) core **Ald2** and acceptor **A1** was initially carried out under analog conditions, but during the first

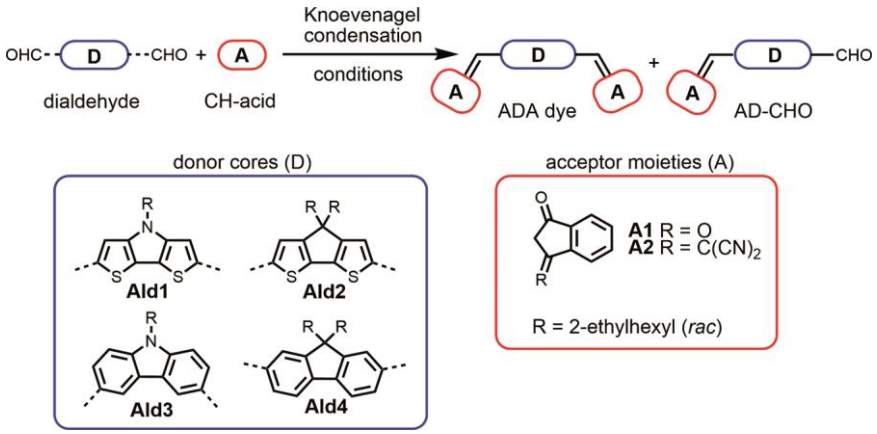

Figure 44. Synthesis of ADA dyes and AD-CHO molecules via Knoevenagel condensation. Reproduced from reference[225] with permission from the Chinese Chemical Society (CCS), Shanghai Institute of Organic Chemistry (SIOC), and the Royal Society of Chemistry.

hour the reaction was unsatisfactorily slow. Additionally, the formation of unidentified side- and/or by-products in significant amounts was observed. After 50 min, compound **ADA2a** was isolated with low yield (14 %), together with a small amount of mono-product **AD2a** (11 %). The yields of **ADA2a** and **AD2a** could be improved to 67 % and 32 %, respectively, when acidic conditions were applied. Additionally, the reaction proceeded cleaner, which simplified isolation of the target molecules. In striking contrast to the synthesis of **ADA2a**, the condensation between **Ald2** and **A2** proceeded smoothly, with pyridine as a base. During the first five minutes of the reaction **ADA2b** was formed as a major product and significant amounts of mono-product **AD2b** were obtained as well. If the reaction proceeded for only 1 h, the starting material was fully converted and **ADA2b** was obtained in a quantitative yield. The synthesis of the dyes consisting of a

Table 12. Yields and reaction conditions for the synthesis of ADA and AD-CHO molecules.

dialdehyde	CH-acid	ADA	Y [a] [%]	AD-CHO [b]	Y [a] [%]	conditions [c]
Ald1	**A1**	**ADA1a**	52	–	–	pyridine, DCE, RT, 18 h
Ald1	**A2**	**ADA1b**	50	–	–	pyridine, DCE, RT, 20 h
Ald2	**A1**	**ADA2a**	67	**AD2a**	32	Ac_2O, NaOAc, 60 °C, 2 h
Ald2	**A1**	**ADA2a**	11	**AD2a**	14	pyridine, DCE, 60 °C, 50 min
Ald2	**A2**	**ADA2b**	99	–	–	pyridine, DCE, 60 °C, 1 h
Ald3	**A1**	**ADA3a**	52	**AD3a**	17	Ac_2O, NaOAc, 80 °C, 7 h
Ald3	**A2**	**ADA3b**	38	**AD3b**	40	pyridine, DCE, 60 °C, 75 min
Ald3	**A2**	**ADA3b**	20	**AD3b**	56	pyridine, DCE, 60 °C, 30 min
Ald4	**A1**	**ADA4a**	34	**AD4a**	8	piperidine, EtOH, 60 °C, 1.5 h
Ald4	**A1**	**ADA4a**	6	**AD4a**	11	Ac_2O, NaOAc, 80 °C, 8 h
Ald4	**A2**	**ADA4b**	– [d]	**AD4b**	– [d]	pyridine, DCE, 60 °C, 50 min

[a] Isolated yield. [b] mono-condensation product. [c] Conditions of selected reactions. [d] Product decomposed. Reproduced from reference[225] with permission from the Chinese Chemical Society (CCS), Shanghai Institute of Organic Chemistry (SIOC), and the Royal Society of Chemistry.

biphenyl unit in donor scaffolds (**ADA3** and **ADA4**) was challenging. The condensation reaction of **Ald3** and indandione (**A1**) in Ac_2O gave the stable bis-product **ADA3a** in 52 % yield. Even though **ADA3b** was formed under various basic reaction conditions (solvent:base = dichloromethane (DCM)/pyridine; dichloroethane (DCE)/ pyridine or ethanol (EtOH)/piperidine) at RT as well as under elevated temperatures, the isolation of the target molecule was difficult. This was because decomposition occurred in all the cases when the product had extensive contact with a stationary phase (silica gel, alumina or Bio-Beads) and/or when chlorinated solvents were applied. Decomposition was suppressed when the crude product was purified by flash chromatography using a mixture of ethyl acetate (EtOAc) and pentane, followed by recrystallization. In doing so, **ADA3b** and **AD3b** were observed after 0.5 h reaction time in isolated yields of 20 % and 56 %, respectively. By increasing the reaction times up to 1¼ h, almost twofold increased yields were achieved for **ADA3b**. It was assumed that decomposition takes place by a retro-Knoevenagel reaction, which is rather scarce in literature. An interesting report was published by Lambert and co-workers[231] who investigated a reversible aminolysis of electron-poor fulvene derivatives to cyclopentadienes and imines. To prove the assumption of a retro-Knoevenagel reaction, column chromatography on silica gel in CH_2Cl_2 was performed on a highly pure sample of **ADA3b**. Within a short time, a gradual conversion of a purple band of **ADA3b** into a red band was observed, which in turn partially transformed into a yellow one. All fractions were collected and the identities of the compounds were ultimately confirmed by ^{1}H NMR. Thus, **AD3b** was found to be the major decomposition product of **ADA3b**, which gives concrete evidence for the correctness of our assumption of a retro-Knoevenagel reaction. Nevertheless, **ADA3b** shows a decent stability in solution as well as in the solid state even upon heating to high temperatures (Figure 45).

The syntheses of the fluorine (FL) derivatives were even more demanding. **ADA4a** was formed, when dialdehyde **Ald4** was reacted at 80 °C with an excess of CH-acid **A1** in Ac_2O and in the presence of sodium acetate. After 4 h, another portion of IND was added and the stirring was continued overnight, due to a low conversion of the starting material. Because the prolonged heating only resulted in decomposition of the bis-product **ADA4a**, the reaction was repeated. This time it was quenched after 8 h to give **ADA4a** and **AD4a** in low yields of 6 and 11 %, respectively. To improve the yields, basic conditions were used during the next attempt. And indeed, by utilizing piperidine in dry

ethanol, **ADA4a** could be isolated in yields of 34 %, after reacting for 1.5 h at 60 °C. The analogous reaction as well as reactions employing pyridine as a base were performed for the DCIND acceptor. During these syntheses of **ADA4b** and **AD4b** the formation of an orange-colored dye, accompanied by a less polar yellow compound and unreacted starting material was observed. By high resolution mass spectrometry the orange-colored dye could be identified as **ADA4b** (*m/z* for $[M+K]^+$ = 837.3565) and the yellow compound was found to be the mono-product **AD4b** (*m/z* for $[M+H]^+$ = 623.36). As for **ADA3b**, decomposition of **ADA4b** into the corresponding mono-product and other compounds could be observed upon column chromatography on silica gel. Product **AD4b** could not be isolated either. All attempts to purify this molecule for analyses resulted in further decomposition, showing that the retro-Knoevenagel reaction in this case is much more pronounced than for the carbazole (CAR) derivative **ADA3b**.

With regard to stability it can be concluded that the ADA dyes based on DTP and CPDT are much more stable than the dyes based on CAR and FL core. Additionally, the ADA dyes with DCIND moieties are more prone to decomposition than dyes bearing IND acceptors. The reason for this is most probably the stronger electron-withdrawing nature of DCIND. The high polarization of the exocyclic double bond, facilitated by the stabilization of the negative charge by dicyanomethylidene and carbonyl groups, favors the nucleophilic attack on the vinyl carbon atom. Consequently, the donor acceptor bond is already cleaved under the mild conditions provided by a stationary phase. The inferior stability of CAR and FL to the bithienyl based compounds can be explained by the lower sterical demands (enabling a fully planar π-scaffold)[196] of the latter and a lower resonance energy of thiophene comparing to benzene. For these reasons, conjugation and charge delocalization are less pronounced in the CAR and FL based systems and as a consequence the positive charge is more localized on the vinyl carbon atom and the molecules are more susceptible to nucleophilic attack.[124,232] However, all the molecules display high stability at least in the solid state. The stability upon heating to 250 – 300 °C was proven by differential scanning calorimetry (DSC; Figure 45).

All synthesized compounds containing only one 2-ethylhexyl chain (DTP, CAR) were obtained as racemic mixtures, whereas diastereomeric mixtures were found for compounds with two 2-ethylhexyl chains (CPDT, FL). As a result, the ^{1}H and ^{13}C NMR

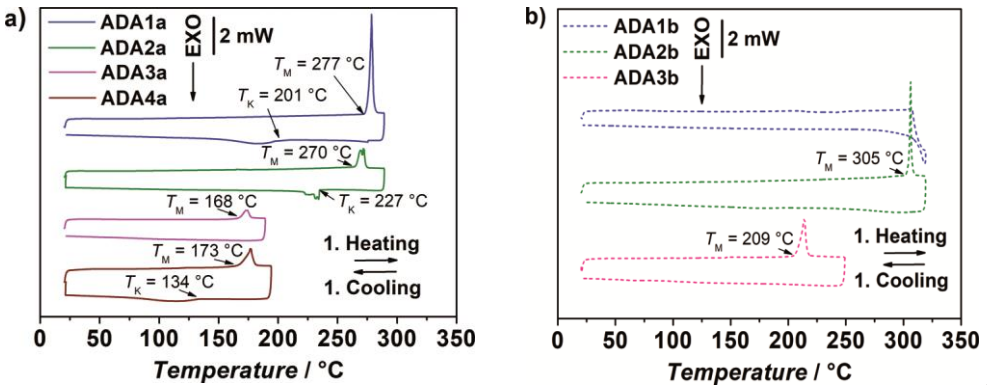

Figure 45. First heating and cooling curves for a) **ADA1a** (blue), **ADA2a** (green), **ADA3a** (pink) and **ADA4a** (brown) with IND acceptors (bold) and b) **ADA1b** (blue), **ADA2b** (green) and **ADA3b** (pink) with DCNID acceptors (dashed). The DSC measurements were performed under N_2 with a heating/cooling rate of 10 K min^{-1}. Reproduced from reference[225] with permission from the Chinese Chemical Society (CCS), Shanghai Institute of Organic Chemistry (SIOC), and the Royal Society of Chemistry.

spectra were more complex for the latter ones and showed more than one set of signals in both aliphatic and aromatic regions. Compounds with DCIND acceptors could be isolated as single geometrical isomers, which was proven by combined NMR techniques. This can be rationalized for **ADA1b** and **ADA2b** by a sterical hindrance around the thiophene ring and by stabilization via sulfur-oxygen interactions, so that the formation of *Z*,*Z*-isomers is favored.[196,205,227–229] In the case of **ADA3b** and **ADA4b**, again a preference towards the *Z*,*Z*-isomer was expected due to the lower steric hindrance than in the *E*,*E*-isomer. This is in consistence with the structure of a CAR-DCIND DA dye published elsewhere.[233] As expected, the solubility of derivatives with CPDT and FL core are much better soluble, due to the presence of two alkyl chains, than derivatives based on CAR or DTP. The latter feature a relatively poor solubility in many different solvents, being the lowest in compound **ADA1b** (<0.2 mg ml^{-1} in $CHCl_3$).

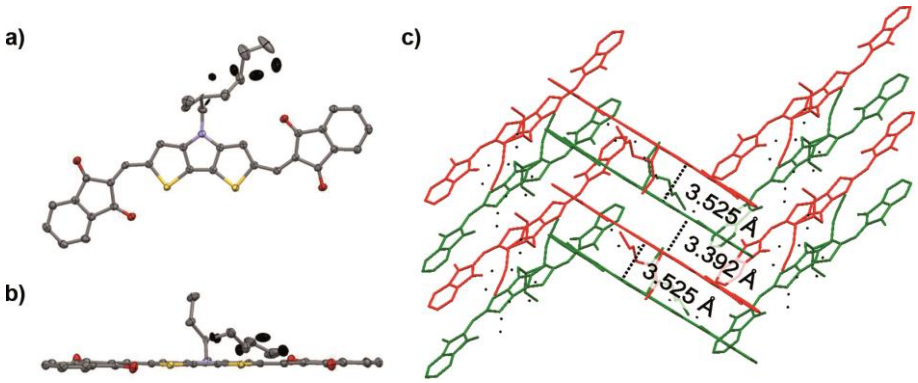

Figure 46. a) top view, b) side view of solvent free single crystal structure of **ADA1a**, determined by X-ray diffraction. Ellipsoids were set to 50 % probability and the black ellipsoids indicate disorder in the 2-ethylhexyl (*rac*) side chains. c) Superordinate packing motive. Hydrogen atoms are omitted for clarity.

Solvent free single crystals of **ADA1a** were obtained by vacuum sublimation. The top view (Figure 46a) reveals that there is disorder in the side chains, because they were used in a racemic mixture. Furthermore, the IND groups are not facing into the same direction. In advance, it was predicted by NMR spectroscopy that the IND residues are likely to face in the same direction, forming the *Z,Z*-isomer. Therefore, it is assumed that the molecules have more energy during sublimation at 210 to 230 °C, so that a different conformation is favored as in solution. For other ADA compounds it was not possible to obtain crystals of sufficient quality for single X-ray diffraction measurements, mainly due to disorder induced by the racemic 2-ethylhexyl chains. Sill, partially solved structures of **ADA2a** and **ADA4a** indicate a symmetric arrangement of the acceptor units. However, the side view (Figure 46b) shows that the thiophene subunits of the DTP are effectively planarized by the bridging nitrogen atom, with corresponding C-C-C-C and S-C-C-S torsion angles of 0.05 and 1.12°. The whole molecule is very planar, which is evident by small angles between the mean planes of the DTP and the IND units of around 1.40 and 3.10°. The superordinate packing motive (Figure 46c) shows that the molecules are arranged in antiparallel piles with alternating π-π stacking distances of around 3.525 and 3.392 Å. Unfortunately, it was not possible to correlate this single crystal structure to the transistor device (see section below).

3.2.1.2 Optical and Electrochemical Properties

The optical properties of molecules **ADA1-4** were investigated in solution by steady-state absorption and fluorescence spectroscopy. Figure 47 shows the absorption spectra of the ADA dyes, measured in CH_2Cl_2, in comparison to the photon flux density coming from the sun. The optical properties of the ADA dyes are summarized in Table 13. The absorption behavior of **ADA1a** and **ADA2a** is very similar. Both dyes possess absorption maxima λ_{max} located at around 583 nm, characterized by high molar absorption coefficients (ε_{max} above $122 \times 10^3\ M^{-1}\ cm^{-1}$). As other dyes based on DTP or CPDT core,[234] they show additional vibronic shoulders at shorter wavelengths at around 543 nm. If the DTP and CPDT donors are flanked by DCIND instead of IND moieties, the absorption is red-shifted by about 80 nm (~ 2100 cm^{-1}), keeping a similar spectral shape. The large bathochromic shifts observed in **ADA1b** and **ADA2b** reveal that electronic interactions are strong between the electron-rich cores of DTP and DTCP and the electron-withdrawing DCIND substituents. The absorption maxima of **ADA3a** and

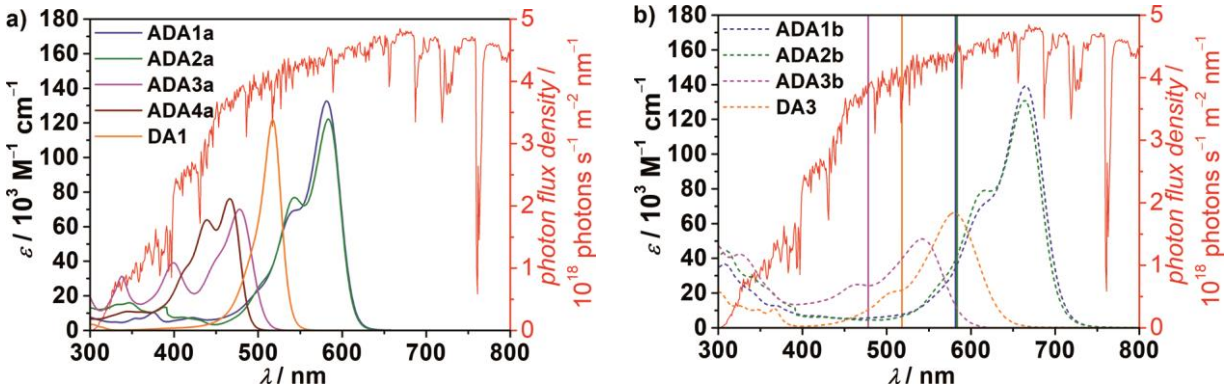

Figure 47. a) Photon flux density of the sun (red) and absorption spectra of IND derivatives (bold) **ADA1a** (blue), **ADA2a** (green), **ADA3a** (pink), **ADA4a** (brown) and of DA dye **DA1** (orange). b) Photon flux density and absorption spectra of DCIND derivatives (dashed) **ADA1b** (blue), **ADA2b** (green), **ADA3b** (pink) and of DA dye **DA3** (orange). Absorption maxima of IND derivatives are given as straight lines. All spectra were measured in CH_2Cl_2 at RT ($c = 10^{-5}$ M).

ADA4a are located at 478 nm and 466 nm, respectively. So they are hypsochromically shifted against the ones of **ADA1a** and **ADA2a**, showing that CAR and FL are weaker donors than DTP and CPDT. Additionally, **ADA3a** and **ADA4a** are weaker absorbers than the latter dyes, which is expressed in lower ε_{max} values (70×10^3 – 76×10^3 M^{-1} cm^{-1}). The absorption maximum of compound **ADA3b** is bathochromically shifted by 64 nm (~ 2500 cm^{-1}) compared to **ADA3a**, which bears the weaker IND acceptors.

In general, all dyes with DCIND acceptors are stronger absorbers than the corresponding dyes with IND acceptors. An exception is the IND based dye **ADA3a**, which has a higher

Table 13. Optical and electrochemical properties of ADA systems.

dye	λ_{max} [a] [nm]	ε_{max} [a] [10^3 M^{-1} cm^{-1}]	μ^2_{eg} [D^2]	λ_{em} [a] [nm]	$\Delta\tilde{\nu}$ [cm^{-1}]	$E_{1/2}^{red}$ [b] [V]	$E_{1/2}^{ox}$ [b] [V]	E_g^{opt} [c] [V]	E_g^{CV} [d] [V]
ADA1a	582	133	147	611	800	–1.52 [e]	+0.49	2.13	2.01
ADA1b	665	139	175	697	700	–0.96 [e]	+0.83 [e]	1.86	1.79
ADA2a	584	122	138	610	700	–1.30	+0.84	2.12	2.14
ADA2b	664	131	167	693	600	–0.84 [e]	+1.08	1.87	1.92
ADA3a	478	70	75	518	1600	–1.76 [e]	+0.97 [e]	2.59	2.73
ADA3b	542	51	89	582	1300	–1.25 [e]	+0.93	2.29	2.18
ADA4a	466	76	102	497	1300	–1.51 [e]	+1.26 [e]	2.66	2.77
DA1[196]	517	144	82	–	–	–1.86 [e]	+0.41 [e]	2.39	2.27
DA3[196]	577	78	97	–	–	–1.53	+0.55	2.14	2.08

[a] CH_2Cl_2. [b] Redox potentials. Measurements were carried out in dry CH_2Cl_2; c ~10^{-4} – 10^{-5} M; Scan rate 100 mV s^{-1}; Supporting electrolyte Bu_4NPF_6 (c = 0.1 M); Pt-disc electrode (Ø 3mm); Calibrated vs. ferrocenium/ferrocene (Fc^+/Fc; −5.15 eV vs. vacuum) as an internal standard. [c] $E_g^{opt} = E_{HOMO} - E_{LUMO}$. [d] $E_g^{CV} = E_{1/2}^{ox} - E_{1/2}^{red}$. [e] Peak potential of irreversible redox processes. Reproduced from reference[225] with permission from the Chinese Chemical Society (CCS), Shanghai Institute of Organic Chemistry (SIOC), and the Royal Society of Chemistry.

ε_{max} value than **ADA3b** due to a broadened absorption. Nevertheless, the square transition dipole moment μ^2_{eg} of **ADA3b** (89 D^2) is higher than for **ADA3a** (75 D^2), which resembles the situation between **ADA1b** and **ADA1a** (175 vs. 147 D^2) or **ADA2b** and **ADA2a** (167 vs. 138 D^2). Vibronic progressions can be observed for all of these ADA dyes at shorter wavelengths. The absorption properties of these ADA dyes are similar to the ones of DA dyes. For the latter it is known that absorption bands are sharp and molar extinction coefficients are maximized at the cyanine limit. At this limit the π-system is most delocalized over the whole chromophore, due to equal contributions of two resonance structure (Figure 48). The narrow and intense absorption bands of the ADA dyes indicate that a similar cyanine limit seems to be present in these dyes, too. This is especially true for the bithienyl dyes (**ADA1a**, **ADA1b**, **ADA2a**, **ADA2b**), however, the limit does not seem to be completely reached in these molecules.

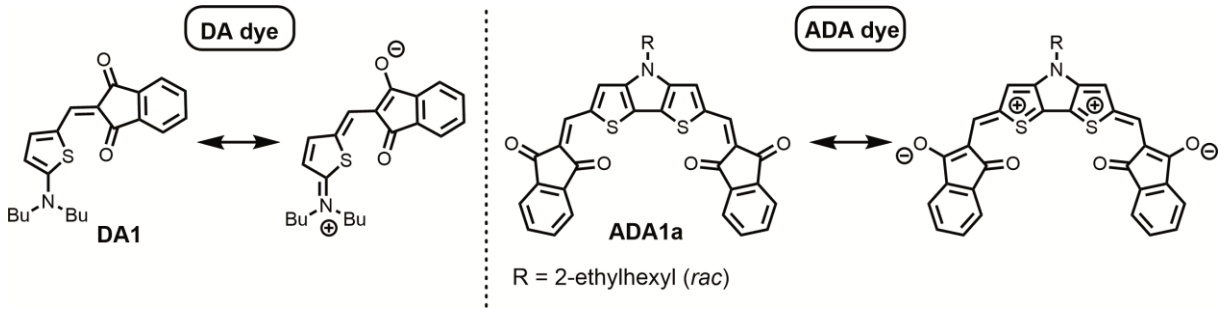

Figure 48. Resonance structures of DA dye **DA1** and of ADA dye **ADA1a**. Reproduced from reference[225] with permission from the Chinese Chemical Society (CCS), Shanghai Institute of Organic Chemistry (SIOC), and the Royal Society of Chemistry.

Two merocyanine dyes **DA1** and **DA3**, introduced in Section 3.1.1, were chosen for comparison (Figure 49).[196,235] It is worth mentioning that **DA3** is one of the best performing merocyanine dyes in bulk heterojunction solar cells.[196] In analogy to the ADA dyes, the DA dyes are made of a 2-aminothiophene donor and IND or DCIND acceptor units. The absorption spectrum of **DA1** is very sharp and shows no vibronic progression. The one of compound **DA3** is similar to the absorption of ADA dye **ADA3b**. Absorption maxima of **DA1** and **DA3** are positioned at 517 and 577 nm, respectively. Therefore, they are located in between the absorption bands of dithienyl and biphenyl based ADA compounds, bearing the same acceptor units. The two DA dyes possess square transition dipole moments of 82 and 97 D^2, being comparable to those of **ADA3a**, **ADA3b** and **ADA4a**. They feature a comparable absorption strength but lower optical band gaps, while possessing only one acceptor moiety. The ADA dyes based on a

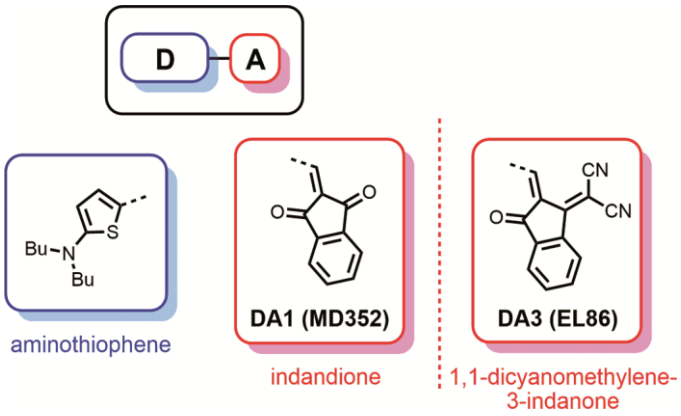

Figure 49. Structures of the reference DA dyes **DA1** and **DA3** bearing IND and DCIND acceptors, respectively.[196]

biphenyl donor (**ADA3a**, **ADA3b**, **ADA4a**) possess an inferior absorption strength and lower optical band gaps than dyes based on a stronger dithienyl donor (**ADA1a**, **ADA1b**, **ADA2a**, **ADA2b**). Thus, the latter dyes are very promising for application in organic solar cells. Furthermore, the results show that it is highly important to choose the right donor and acceptor combination to ensure an effective π-conjugation.

As the reference DA dyes,[196,235] the ADA dyes show weak emission and fluorescence quantum yields Φ_{fl} below 5 % were measured. Like the absorption maxima, the emission maxima λ_{em} of the ADA dyes cover a wide range from 497 nm (**ADA4a**) to 697 nm (**ADA1b**). No vibronic progressions can be found in the fluorescence spectra of the ADA dyes. The normalized absorption and emission spectra are depicted in Figure 50. The Stokes shifts $\Delta\tilde{\nu}$ of the chromophores are moderate, which indicates a relatively small reorganization in the excited state as expected for dyes with a cyanine-type electronic structure. When going from dyes with IND to dyes with the stronger DCIND acceptors, the Stokes shifts are decreased by 100 – 300 cm^{-1}. Furthermore, the Stokes shifts are significantly larger for ADA dyes with CAR or FL cores (1300 – 1600 cm^{-1}) as for dyes with DTP or CPDT cores (600 – 800 cm^{-1}). This can be rationalized by the better delocalization and a more cyanine-type character of the latter dyes.

Cyclic voltammetry measurements were performed in CH_2Cl_2 for all ADA dyes, to gain more information on the position of the frontier molecular orbitals (Figure 51). The measured redox potentials as well as the calculated electrochemical and optical band gaps are in shown in Table 13. A reversible oxidation behavior can be observed for dyes **ADA1a**, **ADA2a**, **ADA2b**, and **ADA3b**. In contrast, the reduction is irreversible or quasi-reversible for most of the dyes. One exception is **ADA2a**, which shows a well-resolved

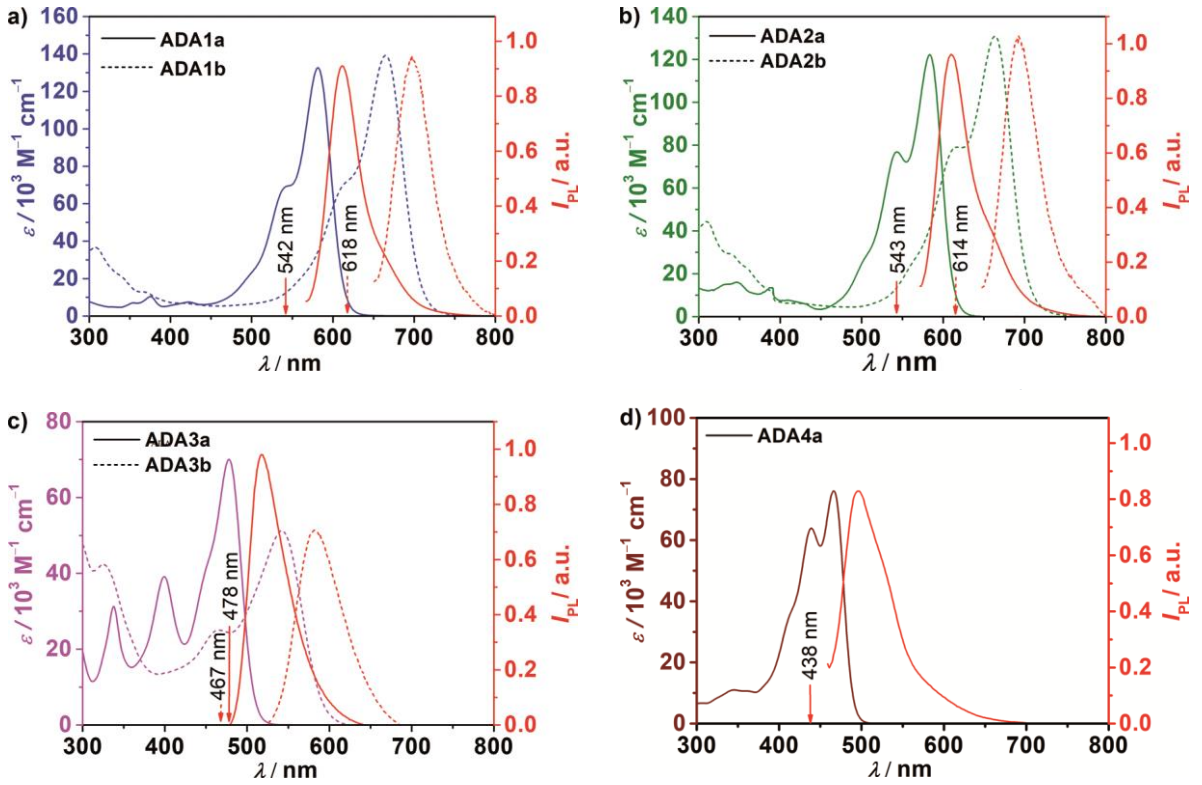

Figure 50. Absorption spectra of a) **ADA1a**, **ADA1b** (blue), b) **ADA2a**, **ADA2b** (green), c) **ADA3a**, **ADA3b** (pink), and d) **ADA4a** (brown) as well as corresponding photoluminescence spectra (red lines). UV/vis: CH_2Cl_2, ~10^{-5} M, 298 K. Photoluminescence: CH_2Cl_2, ~10^{-7} M, 298 K. Solid lines represent the spectra of compounds with IND acceptors, whereas dotted lines correspond to the spectra of DCIND derivatives. Reproduced from reference[225] with permission from the Chinese Chemical Society (CCS), Shanghai Institute of Organic Chemistry (SIOC), and the Royal Society of Chemistry.

reduction wave at –1.30 V and forms a rather stable radical anion. The dyes **ADA3a** and **ADA4a** show a second reduction process, which is correlated with the formation of dianions. The reduction potentials of compounds bearing IND acceptors are negatively shifted by about 0.5 V against their DCIND counterparts (see Table 13). Additionally,

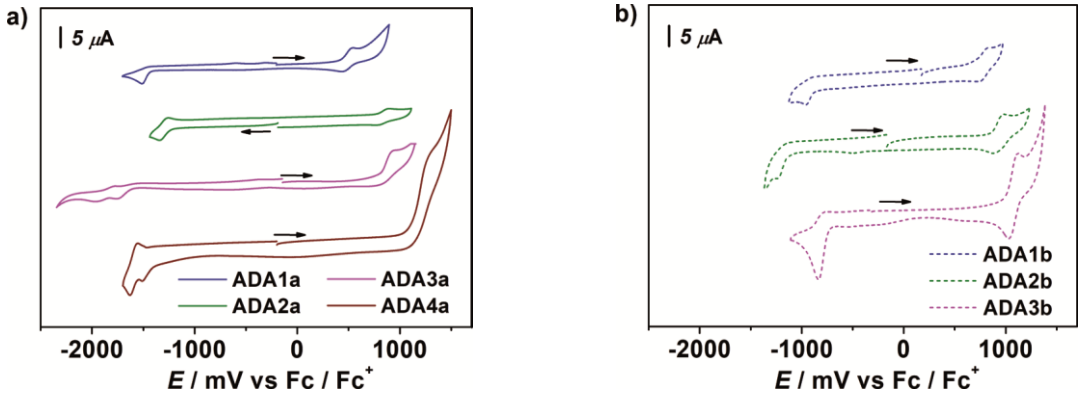

Figure 51. Cyclic voltammograms of a) compounds **ADA1a** (blue), **ADA2a** (green), **ADA3a** (pink) and **ADA4a** (brown) with IND acceptors (bold) and of b) compounds **ADA1b** (blue), **ADA2b** (green) and **ADA3b** (pink) with DCIND acceptors (dashed). Measurements conditions: CH_2Cl_2; c ~ 10^{-4} – 10^{-5} M, 298 K; Scan rate: 100 mV s^{-1}; Supporting electrolyte: Bu_4NPF_6 (0.1 M); Calibrated vs. Fc^+/Fc as an internal standard. Reproduced from reference[225] with permission from the Chinese Chemical Society (CCS), Shanghai Institute of Organic Chemistry (SIOC), and the Royal Society of Chemistry.

the oxidation potentials are shifted by around 0.3 V when going from dyes with IND (**ADA1a**, **ADA2a**) to dyes with DCIND acceptors (**ADA1b**, **ADA2b**). These observations are in agreement with the stronger electron-withdrawing nature of the DCIND substituents.

The measured oxidation potentials were used to calculate the HOMO energy levels of all ADA dyes, assuming a value for the Fc^+/Fc redox pair of −5.15 eV below vacuum.[206–208] The frontier molecular orbitals (FMOs) of the ADA dyes are shown in Figure 52. The LUMO level of $PC_{61}BM$ is given for comparison, too. The HOMOs vary between −5.64 and −6.41 eV (ΔE_{HOMO} = 0.85 eV) and the LUMO levels between −3.51 and −4.36 eV (ΔE_{LUMO} = 0.77 eV) among the ADA dyes. The optical band gaps of most ADA dyes are small and below 2.29 eV. Higher band gaps of 2.59 and 2.66 eV can be found in **ADA3a** and **ADA4a**, respectively. Thus, they are able to absorb solar irradiation in the most important photon-rich range of the sun spectrum (compare Figure 47). The HOMO and LUMO levels of the ADA compounds are located at low energies, indicating high electron affinities. The HOMO and LUMO levels of the carbocyclic compounds **ADA2a** and **ADA4a** are decreased by around 0.3 eV in comparison to the ones of their nitrogen containing analogues (**ADA1a**, **ADA3a**). Apparently, the nitrogen acts as electron donor and makes the central core more electron-rich. So if donor components for organic solar cells are desired, it is helpful to replace the bridging methylene unit by a nitrogen atom.[234,239] The substitution of IND by DCIND moieties mainly influences the LUMO levels, which are decreased by up to 0.6 eV. Consequently, the band gaps are smaller by about 0.3 eV in compounds bearing DCIND. By combining dithienyl cores and DCIND acceptors, compounds with low lying LUMO levels are obtained (**ADA1b**, **ADA2b**).

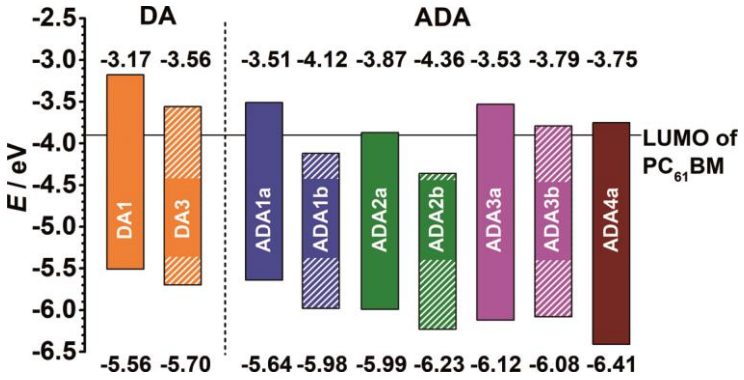

Figure 52. HOMO and LUMO levels derived from the optical band gap of dyes **ADA1a** (blue), **ADA1b** (blue; dashed), **ADA2a** (green), **ADA2b** (green; dashed), **ADA3a** (pink), **ADA3b** (pink; dashed), **ADA4a** (brown), and DA dyes **DA1** (orange), and **DA3** (orange, dashed). The solid black line represents the LUMO energy level of $PC_{61}BM$ (−3.9 eV).[155]

With values of −4.12 eV (**ADA1b**) and −4.36 eV (**ADA2b**), these LUMO levels lie even below the LUMO level of $PC_{61}BM$, which is commonly used as an acceptor in BHJ solar cells.[155] Due to the fact that fullerenes like $PC_{61}BM$ possess several deficiencies, e.g. limited tunability and weak absorption,[210–212] alternative acceptor dyes are of high interest. Some of the ADA dyes studied here (e.g. **ADA1b** and **ADA2b**) are good candidates to replace fullerenes, because they show intense absorption and suitable LUMO levels.

The optical band gaps of the reference DA dyes **DA1** (2.39 eV) and **DA3** (2.14 eV) are relatively low. Their LUMO levels are high and do not meet criteria for efficient acceptor materials in solar cells. However, both DA dyes could be utilized successfully as donor components in combination with $PC_{61}BM$.[196] The LUMO level of **DA3** at −3.56 eV corresponds well to the LUMO level of **ADA1a** and **ADA3a**, so that these molecules are expected to behave similarly. Thus, they are more suitable as donor than acceptor components. In conclusion, by variation of donor as well as acceptor strength in ADA compounds, the optical and electrochemical properties could be tuned effectively. Combination of only moderately electron-releasing donor cores with very strong acceptors provided dyes with strong absorption in the most important spectral range of sunlight combined with small band gaps and low lying FMOs. This makes these molecules promising candidates to substitute fullerene acceptors in organic solar cells.

3.2.1.3 Quantum Chemical Calculations

Density functional theory (DFT) calculations were performed on all ADA dyes at the B3LYP/def2-SVP level and for the gas phase, to gain insight into their electronic structures and to verify the measured molecular energy levels. To simplify the quantum chemical calculations, the branched alkyl chains at the ADA dyes were replaced with methyl moieties. The geometry optimized structures of the ADA dyes, as well as the orbital contour plots of HOMO and LUMO are shown in Figure 53. The optimized molecular geometries show that the molecules are highly planar, which is beneficial for close π-π interactions in the solid state. In all ADA compounds, the electron densities of the HOMOs are mainly located at the central donor cores as well as on the conjugated carbonyl and dicyanomethylidene functionalities. For the LUMOs, electron densities are spread over the whole molecules, including both acceptor moieties. This indicates the presence of charge transfer between the central donor core and the acceptor moieties. The orbital contour plots of HOMO and LUMO of compounds **ADA1a** and **ADA1b** closely

resemble the ones of their DCIND substituted counterparts **ADA2a** and **ADA2b**, which are based on a carbocyclic donor core.

The calculated molecular orbital energy levels are listed in Table 14. The calculated HOMO energy levels correlate well with the ones obtained from cyclic voltammetry measurements. The calculated LUMO energies are higher than the measured ones, so that differences in energy gaps of 0.34 – 0.65 eV can be observed. The experimental as well as the theoretical data suggest that the investigated molecules are suitable for application in photovoltaics/organic electronics.

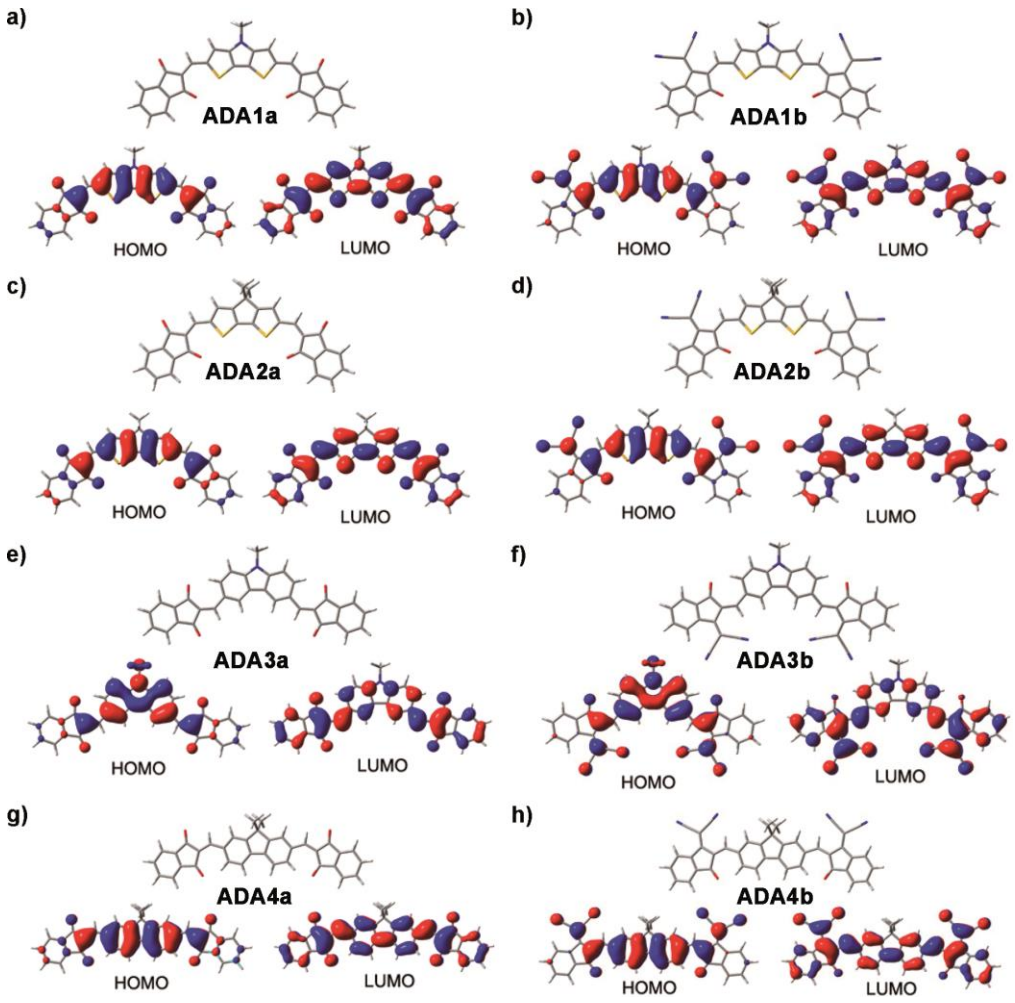

Figure 53. Geometry-optimized structures (with B3LYP/def2-SVP) as well as orbital contour plots of HOMO and LUMO orbitals for model compounds a) **ADA1a**, b) **ADA1b**, c) **ADA2a**, d) **ADA2b**, e) **ADA3a**, f) **ADA3b**, g) **ADA4a**, h) **ADA4b** (ethylhexyl substituents are replaced with methyl groups to simplify the calculations). Reproduced from reference[225] with permission from the Chinese Chemical Society (CCS), Shanghai Institute of Organic Chemistry (SIOC), and the Royal Society of Chemistry.

Table 14. HOMO/LUMO levels and energy gaps (E_g) derived from quantum chemical calculations.

dye	E_{HOMO} [eV]	E_{LUMO} [eV]	E_g [eV]
ADA1a	−5.75	−3.21	2.54
ADA1b	−6.07	−3.84	2.23
ADA2a	−5.79	−3.29	2.50
ADA2b	−6.10	−3.89	2.21
ADA3a	−6.02	−2.78	3.24
ADA3b	−6.25	−3.39	2.86
ADA4a	−6.19	−3.15	3.04
ADA4b [a]	−6.44	−3.74	2.70

[a] Could not be isolated. Reproduced from reference[225] with permission from the Chinese Chemical Society (CCS), Shanghai Institute of Organic Chemistry (SIOC), and the Royal Society of Chemistry.

3.2.1.4 Organic Thin Film Transistors and Solar Cell

To test the charge transport properties of the series of ADA molecules, transistor devices of dyes **ADA1a**, **ADA2a** and **ADA2b** were prepared. The organic thin film transistors were fabricated on *n*-tetradecylphosphonic acid (TPA) modified $Si/SiO_2/AlO_x$ substrates via vacuum deposition (nominal thickness of 30 nm). Characterization was performed under ambient conditions, by measuring transfer and corresponding output curves (Figure 54 and Figure 55). The mobilities were obtained in the saturation regime. For **ADA1a** moderate hole mobilities of 1.85×10^{-3} $cm^2\ V^{-1}\ s^{-1}$ a current on/off ratio of 3×10^3 and a threshold voltage of −5 V could be measured. Much higher hole mobilities of 0.12 $cm^2\ V^{-1}\ s^{-1}$, a current on/off ratio of 4×10^4 and a threshold voltage of about −1 V were obtained for **ADA2a**. At a gate voltage of about −10 V, the device showed decreasing slope in the square root plot of the I_{DS} current, which yields a reduced mobility (0.002 $cm^2\ V^{-1}\ s^{-1}$). However, the higher mobility value is of importance, because the device already switches almost completely between on and off state, when a gate voltage of only −10 V is applied. In contrast to the other two molecules, **ADA2b** showed electron mobilities of 0.07 $cm^2\ V^{-1}\ s^{-1}$, a current on/off ratio of 3×10^4 and a threshold voltage of 4 V. The corresponding output curves of devices with **ADA1a**, **ADA2a** and **ADA2b** are shown in Figure 55.

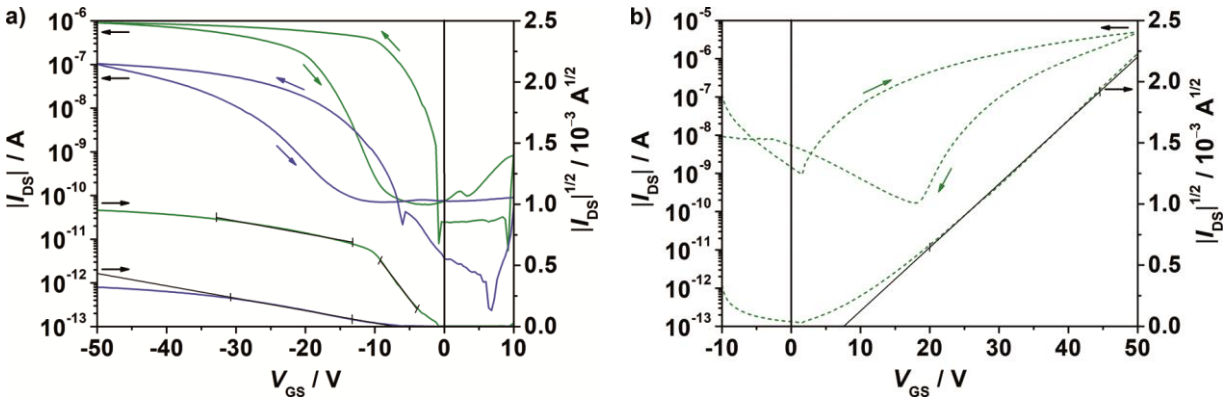

Figure 54. Transfer curves of organic thin film transistors in $Si/SiO_2/AlO_x$/TPA/**ADA dye**/gold architecture, utilizing the dyes a) **ADA1a** (blue, bold), **ADA2a** (green, bold) and b) of **ADA2b** (green, dashed).

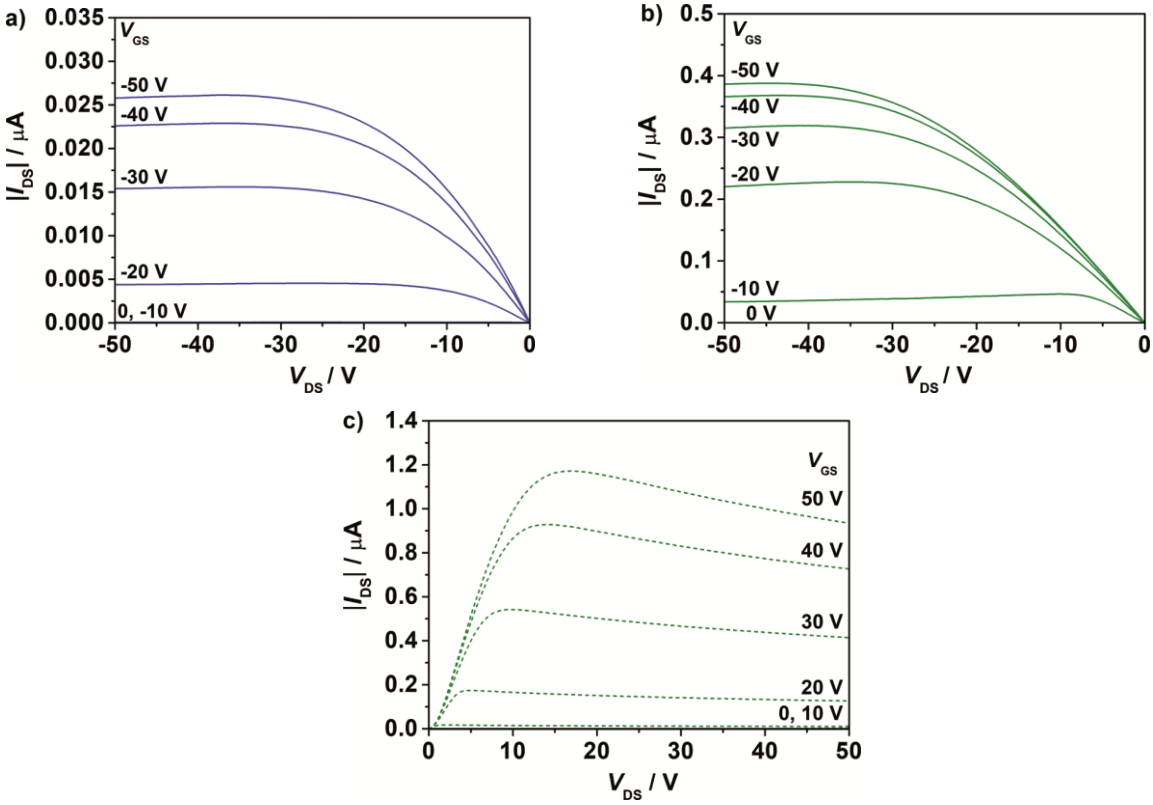

Figure 55. Output curves of organic thin film transistors in $Si/SiO_2/AlO_x$/TPA/**ADA dye**/gold architecture of p-type semiconductors a) **ADA1a**, b) **ADA2a** and of n-type semiconductor c) **ADA2b**.

The morphology of the organic layers was investigated by AFM While the thin films of **ADA2a** and **ADA2b** (Figure 56b,c) appear crystalline, with domains of rod-like and terrace-like shape, respectively, the film of **ADA1a** seems to be less ordered. This might be one reason for the inferior charge carrier mobility of the latter dye.

In conclusion, the functioning transistor devices proved that the ADA dyes are able to transport charges efficiently. To demonstrate that these molecules are even more versatile and able to convert sunlight into electrical energy, organic solar cells were fabricated in

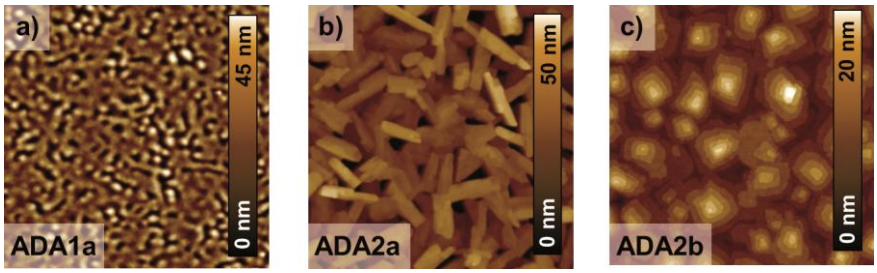

Figure 56. AFM images of a) **ADA1a**, b) **ADA2a** and c) **ADA2b** thin films (5 × 5 µm^2). Measurements were performed between the two top electrodes of the corresponding transistor devices in Si/SiO_2/AlO_x/TPA/**ADA dye**/gold architecture.

Würzburg, utilizing the hole transport materials **ADA1a** and **ADA2a** in combination with fullerene acceptors. While devices with **ADA2a** did not work at all, **ADA1a** resulted in functioning PHJ devices in combination with C_{60} as electron acceptor. Prefabricated ITO substrates with PEDOT:PSS interlayer (~40 nm) were used and **ADA1a** was spin coated from $CHCl_3$ in a concentration of 2 mg ml^{-1}. Processing at higher concentrations was not possible due to moderate solubility in $CHCl_3$, which was even worse in chlorobenzene and *o*-dichlorobenzene (<0.2 mg ml^{-1}). Before preparation of aluminum contacts, a layer of C_{60} was sublimed on top of the donor layer (**ADA1a**) at an optimized thickness of 30 nm. The *J-V* characteristics, the spectrally resolved *EQE* measurements as well as the solar cell absorption of the best device are depicted in Figure 57. The best device showed a power conversion efficiency of 1.67 %, with a J_{SC} of 3.8 mA cm^{-2}, fill factor of 54 % and an open circuit voltage of 0.80 V. The average over seven devices yielded a *PCE* of 1.44 %. The photoconversion efficiency was above 17 % in the spectral range from 350 to 630 nm, being maximized at 390 nm with 26 %. This correlates to the thin film absorption of the corresponding solar cell (Figure 57b).

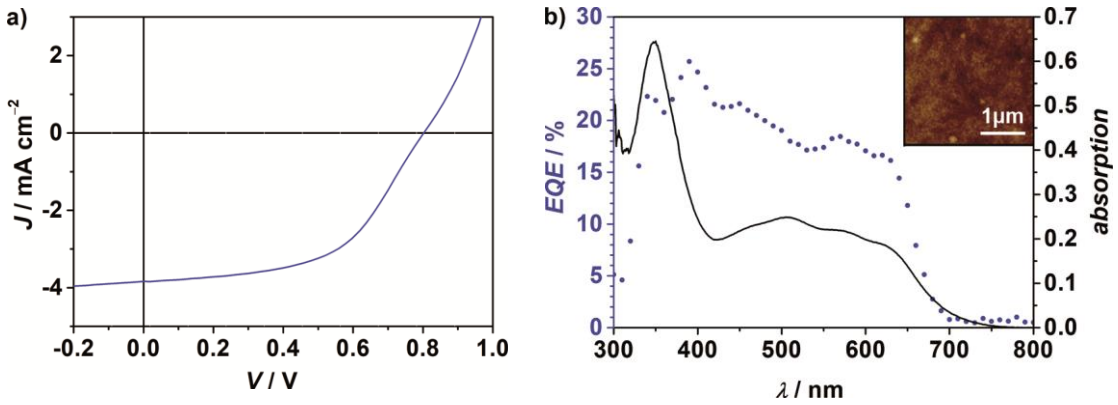

Figure 57. a) *J-V* curve, b) spectrally resolved external quantum efficiency and solar cell absorption (measured in transmission) of PHJ devices of glass/ITO/PEDOT:PSS/**ADA1a**/C_{60}/Al architecture, the inset shows the AFM morphology of the active layer before aluminum deposition.

3.2.1.5 Conclusion

Seven different ADA dyes derived from four different donor cores and two electron acceptors were successfully synthesized via Knoevenagel condensation. The variation of the electron-releasing and electron-accepting character of the central donor cores and surrounding acceptor moieties, respectively, the frontier molecular orbitals and optical band gaps were modulated systematically. The absorption spectra of the dyes cover a broad range of the visible spectrum and the absorption bands are sharp and intense, especially when bithieyl based donor cores are used. Most interestingly, the combination of bithienyl cores and DCIND acceptors gave molecules (**ADA1b**, **ADA2b**) with low band gaps (E_g^{opt} ~ 1.86 eV) and deep lying LUMO levels, which even fall below the LUMO level of $PC_{61}BM$. Investigation of **ADA2a** and **ADA2b** in organic thin film transistors showed that the alternation of the acceptor changed their semiconducting properties. While hole transport was observed in **ADA2a** (μ = 0.12 $cm^2\ V^{-1}\ s^{-1}$), **ADA2b** showed electron-transport properties with an electron mobility of 0.073 $cm^2\ V^{-1}\ s^{-1}$. Additionally, it was shown that **ADA1a** could be used as electron donor in combination with C_{60}, to give functional PHJ solar cells with a power conversion efficiency of up to 1.67 %. This gives rise to the assumption that compounds **ADA2a** and **ADA3a** bear the same potential, while **ADA2b** and **ADA1b** are potent candidates for electron acceptors in organic solar cells. Altogether, the potential of this set of ADA dyes for organic electronic applications was shown.

3.2.2 Donor Polymer ADA Acceptor Organic Solar Cells[§]

3.2.2.1 Optical and Electrochemical Properties of Polymers and ADA Dyes

The concept using small molecule acceptors in combination with donor polymers already yielded solar cells with high power conversion efficiencies of up to 12 % (as shown in section 2.4).[26] Therefore, the highly promising electron transport material **ADA2b** (introduced in Section 3.2.1) and the derivative **ADA2b'** were investigated in donor polymer small molecule acceptor BHJ solar cells, during a guest stay in the research group of Prof. Dr. R. A. J. Janssen at the Technische Universiteit Eindhoven. Thus, four different donor polymers were selected for the studies (**PPDTNBT**,[243] **BDT-FBT-C32**,[244] **PDPP3T**[245–248] and **PCDTBT**[249,250], see Figure 58), which proved to be useful in combination with $PC_{61}BM$ or $PC_{71}BM$ acceptors (Table 15).[243–245,250]

Table 15. Photovoltaic characteristics of optimized donor polymer-fullerene acceptor BHJ solar cells derived from ref.[243–245,250]

donor	acceptor	*PCE* [%]	J_{SC} [mA cm^{-2}]	*FF* [%]	V_{OC} [V]
PPDTNBT[243]	$PC_{71}BM$	1.8	4.3	42	0.98
BDT-FBT-C32[244]	$PC_{61}BM$	2.1	4.4	54	0.98
PDPP3T[245]	$PC_{71}BM$	7.1	15.4	69	0.67
PCDTBT[250]	$PC_{71}BM$	7.0	17.8	66	0.60

PPDTNBT and **BDT-FBT-C32** were able to yield solar cell efficiencies of around 2 %, being the result of low short circuit current densities (~4 mA cm^{-2}), but high open circuit voltages (~0.98 V). **PDPP3T** and **PCDTBT** even showed power conversion efficiencies of around 7 %, because of much higher short circuit current densities (>15 mA cm^{-2}) and fill factors (>66 %), but lower open circuit voltages (>0.67 V). Further reasons for the selection of the polymers were: Their absorption spectra cover different parts of the visible spectrum, offering a good chance for complementarity to the absorption spectra of the ADA dyes; Their HOMO and LUMO levels show good variation. This is favorable to tune ΔE_{LUMO}, which is necessary to overcome the exciton binding energy,[78] as well as the $\Delta E_{HOMO\text{-}LUMO}$, which is related to the open circuit voltage of the device;[112] They offer chemical diversity with regard to the building blocks they consist of, e.g.

[§] The investigation of the ADA acceptor molecules in combination with donor polymers was performed during a guest stay in the Molecular Materials and Nanosystems group of Prof. Dr. R. A. J. Janssen under supervision of Dr. K. Hendriks at the Department of Applied Physics of the Technische Universiteit Eindhoven.

thiophenes, benzothiadiazoles and benzodithiophenes. This might have an influence on packing and mixing of donor and acceptor in the solid state, which is crucial for good device performance.

The molecular structures of the donor polymers and small ADA acceptors are depicted in Figure 58. In contrast to **ADA2b** the derivative **ADA2b'** bears elongated, branched alkyl chains. It was assumed that this modification would only slightly affect the electronic nature of the chromophore, to result in similar optical and electrochemical properties but improved solubility, which is a very important parameter for device manufacturing. Additionally, differences in packing behavior of molecules in the solid state were expected, due to the variation of the sterically demand of the side chains.

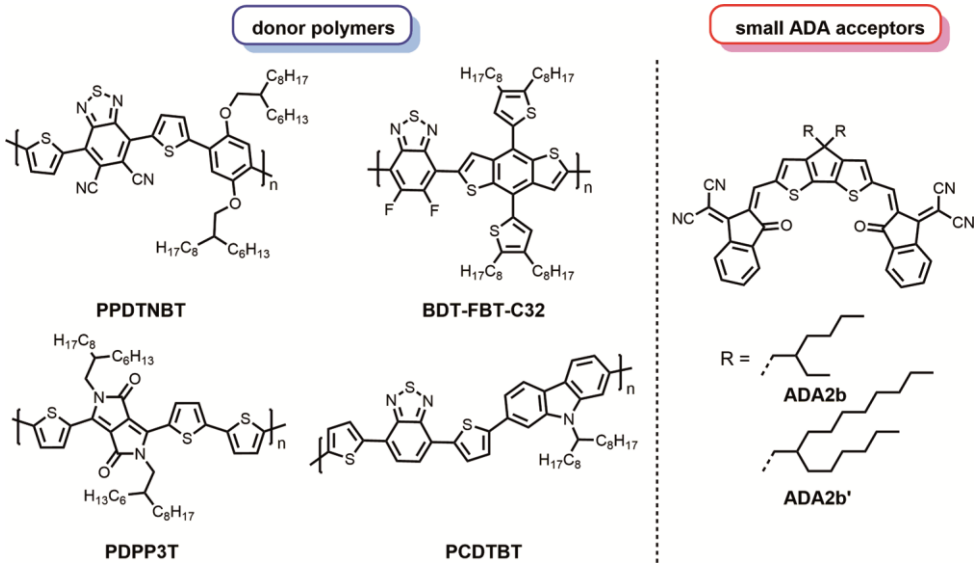

Figure 58. Chemical structures of hole transporting donor polymers **PPDTNBT**, **BDT-FBT-C32**, **PDPP3T**, and **PCDTBT** (left), as well as chemical structures of electron transporting small ADA acceptors **ADA2b** and **ADA2b'** (right).

The UV/vis absorption properties of implemented materials are compared in Table 16 and Figure 59. The absorption properties of **ADA2b** and **ADA2b'**, measured in CH_2Cl_2, are almost identical. Both dyes show sharp absorption bands with apparent vibronic progressions at shorter wavelengths. The absorption maxima are located at around 665 nm, with high molar extinction coefficients of around 135×10^3 M^{-1} cm^{-1} for **ADA2b** and slightly higher for **ADA2b'** (138×10^3 M^{-1} cm^{-1}). As mentioned before, the absorption of the different polymers in solution is spread over the whole spectral range. **PCDTBT** absorbs at short wavelengths of up to 650 nm, being maximized at 546 nm (measured in $CHCl_3$). The absorption spectra of **BDT-FBT-C32** and **PPDTNBT** lie at higher wavelengths (measured in *o*-dichlorobenzene). Their main absorption bands cover

Table 16. Optical and electrochemical properties of acceptor dyes (**ADA2b**, **ADA2b'**) and of the donor polymers **PPDTNBT**, **BDT-FBT-C32**, **PDPP3T**, **PCDTBT**.

compound	λ_{max}^{sol} [nm]	λ_{max}^{film} [nm]	$E_{1/2}^{red}$ [V]	$E_{1/2}^{ox}$ [V]	E_{gap}^{opt} [eV]	E_{gap}^{CV} [eV]	E_{HOMO} [eV]	E_{LUMO} [eV]
ADA2b	664	748	−0.84	+1.08	1.87	1.92	−6.23	−4.36
ADA2b'	665	645, 702	−0.85	+1.07	1.87	1.92	−6.22	−4.35
PPDTNBT[243]	655	737	−1.11	+0.64	1.47	1.75	−5.64	−3.89
BDT-FBT-C32[244]	649	669	−1.47	+0.72	1.70	2.19	−5.95	−3.76
PDPP3T[245,246]	830	828	−1.49	+0.07	1.33	1.56	−5.30	−3.74
PCDTBT[249]	546	576	−1.90	+0.27	1.88	2.17	−5.5	−3.3

the range from around 500 to 700 nm (**BDT-FBT-C32**) or even up to 800 nm (**PPDTNBT**). Their absorption maxima are both located at around 650 nm. **PDPP3T** shows the most red-shifted absorption (measured in *o*-dichlorobenzene), which mainly covers wavelengths from 600 to 900 nm. The absorption maximum can be found at 830 nm. Accordingly, complementarity with the ADA acceptor components in solution is excellent for **PCDTBT** as well as for **PDPP3T**, while the absorption of the other two polymers is to a large extent redundant to the absorption of **ADA2b** and **ADA2b'**. Complementarity in absorption is an important parameter to maximize the amount of absorbed sunlight in organic BHJ solar cells, which again leads to increased power conversion efficiencies.

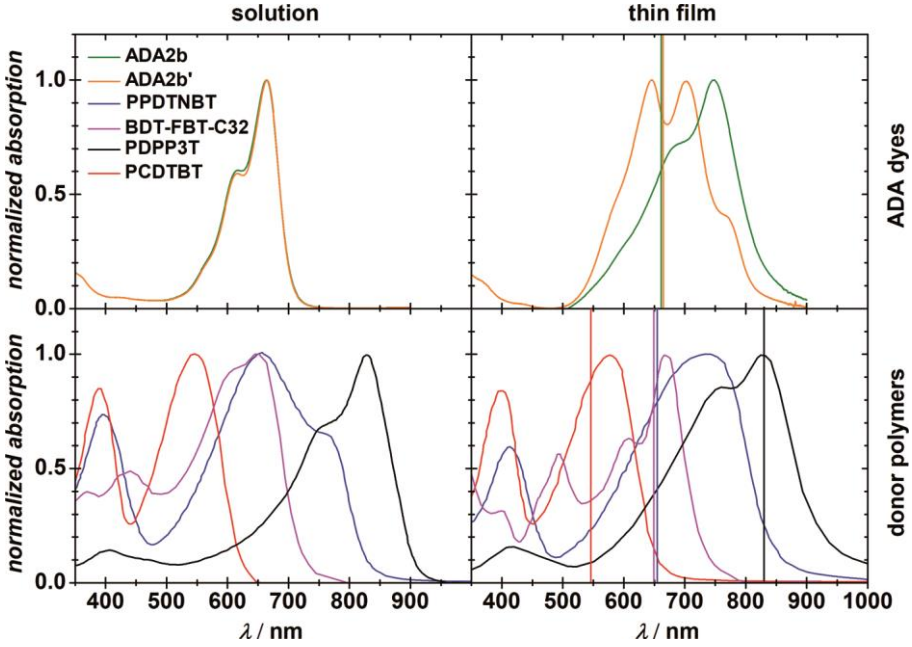

Figure 59. UV/Vis absorption spectra of ADA dyes (top) **ADA2b** (green) and **ADA2b'** (orange) and of donor polymers (bottom) **PPDTNBT** (blue),[243] **BDT-FBT-C32** (magenta),[244] **PDPP3T** (black)[245] and **PCDTBT** (red).[249] In the thin film spectra, the absorption maxima of the corresponding compounds in solution are indicated by vertical lines in the respective color. Original data for polymers can be found in references[243–245,250].

While taking a look on absorption spectra in solution is a good starting point, it is more important to study the absorption spectra of the compounds in the solid state (Figure 59). The thin film absorption spectra of **ADA2b** and **ADA2b'** are both red-shifted and broadened, in compared to the monomers in solution. The most red-shifted absorption maxima are located at 748 and 702 nm for **ADA2b** and **ADA2b'**, showing that the two dyes behave differently. While **ADA2b'** mainly covers wavelengths from ~550 to 800 nm, **ADA2b** strongly absorbs between 500 and 850 nm. The shape of the absorption of compound **ADA2b'** is different form the absorption in solution and from the absorption of dye **ADA2b**, indicating a different packing in the solid, due to the elongated and sterically more demanding alkyl chains. The thin film absorption of the polymers **PCDTBT**, **PPDTNBT** as well as **BDT-FBT-C32** is red-shifted by around 20 – 80 nm. While the absorption broadens for the former compounds, **BDT-FBT-C32** shows distinct vibronic progressions. The absorption of **PDPP3T** undergoes a broadening and barely shows a red-shift compared to the one in solution. These results show that some complementarity is lost between the ADA dyes and all polymers in the solid state. And even in the case of **PCDTBT** or **PDPP3T**, where the complementarity appeared to be ideal in solution, it is reduced to some extent.

In addition to the optical data, the electrochemical properties of the compounds are of interest, when solar cells are to be fabricated. Thus, cyclic voltammetry measurements were performed on **ADA2b** and **ADA2b'**. In Figure 60, the cyclic voltammograms of the ADA dyes are compared to the ones of the donor polymers (taken from literature).

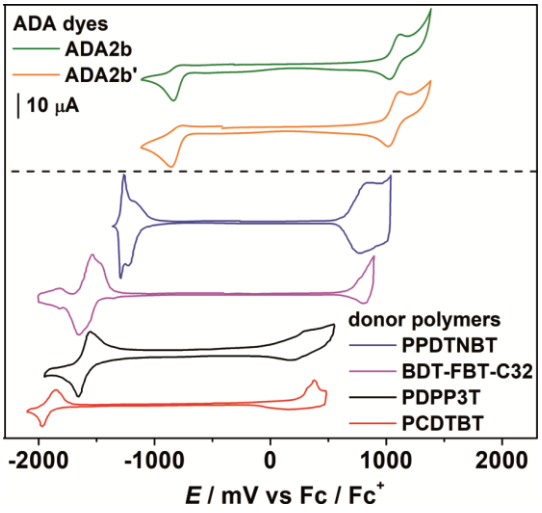

Figure 60. Cyclic voltammograms of ADA dyes **ADA2b** (green), **ADA2b'** (orange) and of donor polymers **PPDTNBT** (blue),[243] **BDT-FBT-C32** (magenta),[244] **PDPP3T** (black)[245] and **PCDTBT** (red).[249]

As expected both ADA dyes possess identical reduction and oxidation potentials of −0.84 and 1.08 V, respectively. From that HOMO and LUMO levels of −6.23 and −4.36 eV could be derived. The oxidation and reduction potentials of the polymers are all shifted to more negative potentials, showing that these compounds are more electron-rich than the ADA dyes. The derived LUMO levels are −3.89, −3.76, −3.74 and −3.3 eV for **PPDTNBT**, **BDT-FBT-C32**, **PDPP3T** and **PCDTBT**, respectively. The calculated LUMO offset (ΔE_{LUMO}) between donor polymers and ADA acceptors are all above 0.4 eV, being the highest for **PCDTBT**, which is above 1 eV. Therefore, the offset energy always exceeds the typical value of the exciton binding energy of 0.3 eV, which has to be overcome during the exciton dissociation process. Next to ΔE_{LUMO}, the HOMO-LUMO difference between polymer donor and ADA acceptor ($\Delta E_{HOMO\text{-}LUMO}$) is of interest, because it is typically related to the open circuit voltage in the corresponding devices (Figure 61). According to $\Delta E_{HOMO\text{-}LUMO}$, quite some variation in the open circuit voltage can be expected for the different ADA dye-donor polymer combinations. However, it is worth noticing that the open circuit voltage is affected by several other factors than this, e.g. charge generation and recombination, energetic disorder, charge transport layers or morphology and crystallinity of the active layer.[244] Therefore, $\Delta E_{HOMO\text{-}LUMO}$ can only indicate a certain trend and the measured open circuit voltages are typically at least 0.3 eV below it (Equation 2.8). The highest $\Delta E_{HOMO\text{-}LUMO}$ can be calculated for **BDT-FBT-C32** (~1.60 eV) followed by **PPDTNBT** (~1.29 eV), **PCDTBT** (~1.15 eV) and **PDPP3T** (~0.95 eV), when combined with **ADA2b** or **ADA2b'**, resulting in maximum open circuit voltages of around 1.30, 0.99, 0.85 and

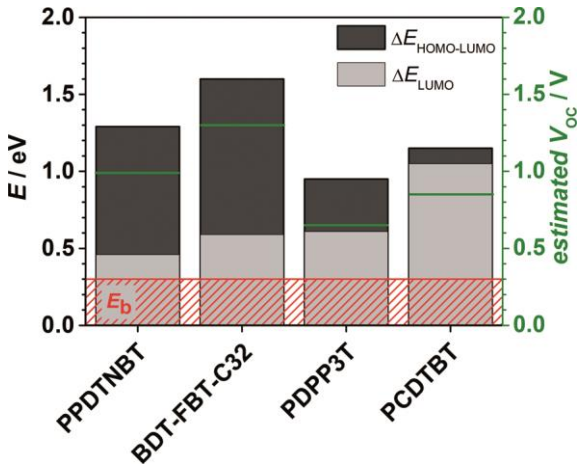

Figure 61. Calculated LUMO offset (light grey) between the LUMOs of polymer donor and ADA acceptor (ΔE_{LUMO}), exceeding the typical value for the exciton binding energy E_b (red; 0.3 eV) for all polymer ADA dye combinations. Calculated HOMO-LUMO gaps (dark grey) between donor and acceptor component ($\Delta E_{HOMO\text{-}LUMO}$) as well as derived open circuit voltages (green).

0.65 V, respectively (Figure 61). Altogether, **ADA2b** and **ADA2b'** possess a low lying LUMO level (~ –4.4 eV), which is even below the LUMO level of $PC_{61}BM$ (−3.9 eV)[155] and they show a strong absorption (> 130 × 10^3 $M^{-1}cm^{-1}$) in the visible range.[225] Thus, they might be possible alternatives for fullerene acceptors in organic solar cells.

3.2.2.2 BHJ Solar Cells of Donor Polymers and ADA acceptors

The compounds **ADA2b** and **ADA2b'** match well to all selected donor polymers with regard to energetics. Therefore, organic solar cells of glass/ITO/PEDOT:PSS(~40 nm) /**BHJ**/LiF(1 nm)/Al(100 nm) architecture were fabricated for all eight polymer-acceptor combinations. The donor to acceptor ratio was chosen to be 1:2 for this experiment, based on the experience that all used donor polymers show their maximum performance in combination with fullerenes when the latter one is used in excess.[243–245,250] The measured current voltage characteristics of the devices can be found in Figure 62. The device parameters for the cells with **PPDTNBT**, **BDT-FBT-C32, PDPP3T** and **PCDTBT** are given in Table 17 and are visualized in Figure 63.

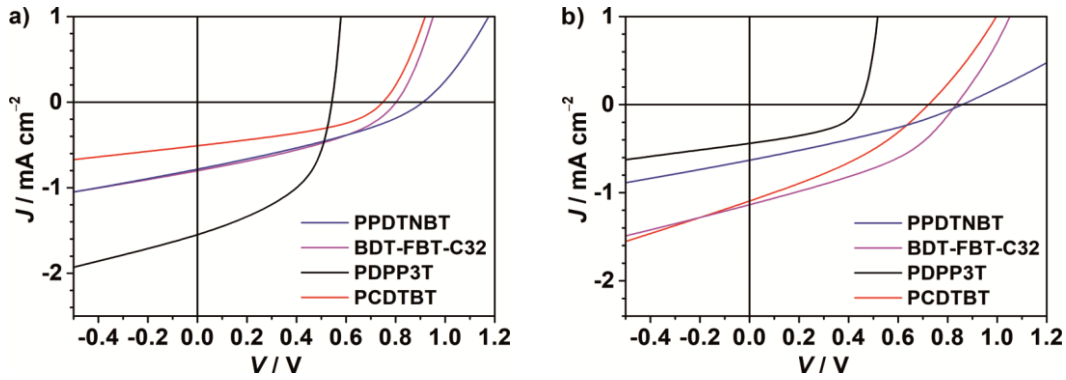

Figure 62. Current voltage characteristics of the solar cells with **PPDTNBT** (blue), **BDT-FBT-C32** (magenta), **PDPP3T** (black) and **PCDTBT** (red) donor and a) **ADA2b** or b) **ADA2b'** acceptor. Devices are of glass/ITO/PEDOT:PSS/**BHJ**/LiF/Al architecture. Curves were measured under simulated AM1.5 G illumination (100 mW cm^{-2}) and under inert conditions.

All polymers yielded functioning solar cells in combination with both acceptor dyes. The power conversion efficiencies, however, are rather low and in the range of 0.16 to 0.40 % for solar cells with **ADA2b** and between 0.09 to 0.37 % for solar cells with **ADA2b'**. The highest efficiency of all devices was found for **ADA2b** in combination with **PDPP3T**, because of a higher short circuit current density and fill factor compared to the other solar cells. In contrast, **ADA2b'** yielded the most efficient solar cells (0.37 %) in combination with **BDT-FBT-C32**.

Table 17. Solar cell parameters of devices with **PDPP3T**, **PPDTNBT**, **BDT-FBT-C32** or **PCDTBT** as donor and **ADA2b** or **ADA2b'** as acceptor. Devices with glass/ITO/PEDOT:PSS/**BHJ**/LiF/Al architecture were measured under simulated AM1.5 G irradiation with an intensity of 100 mW cm^{-2} and under inert conditions.

donor	acceptor	*PCE* [a] [%]	J_{SC} [mA cm^{-2}]	*FF* [%]	V_{OC} [V]
PPDTNBT	**ADA2b**	0.24 (0.24)	0.78	33	0.91
PPDTNBT	**ADA2b'**	0.17 (0.16)	0.63	31	0.86
BDT-FBT-C32	**ADA2b**	0.24 (0.22)	0.80	38	0.80
BDT-FBT-C32	**ADA2b'**	0.37 (0.36)	1.14	39	0.83
PDPP3T	**ADA2b**	0.40 (0.39)	1.55	48	0.54
PDPP3T	**ADA2b'**	0.09 (0.09)	0.44	44	0.45
PCDTBT	**ADA2b**	0.16 (0.16)	0.51	41	0.75
PCDTBT	**ADA2b'**	0.27 (0.27)	1.09	34	0.72

[a] Value in brackets gives the average efficiency over 4 devices.

While the trend observed in short circuit current densities of devices with **ADA2b** is similar to the one observed for the corresponding polymer-fullerene BHJ solar cells (Table 15), the J_{SC} of devices with **ADA2b'** behaves rather randomly (0.44 – 1.14 mA cm^{-2}). Therefore, identical low short circuit current densities can be found for devices with **PPDTNBT** and **BDT-FBT-C32** (0.24 mA cm^{-2}) while a higher value was observed for **PDPP3T** (0.40 mA cm^{-2}). Only **PCDTBT** shows a much lower J_{SC} as expected (0.16 mA cm^{-2}), compared to the other devices. Similar observations can be made for the fill factors in devices based on **ADA2b** as well as **ADA2b'**, which are in the range of 31 to 48 %. Like in the polymer-fullerene BHJ solar cells, the fill factors

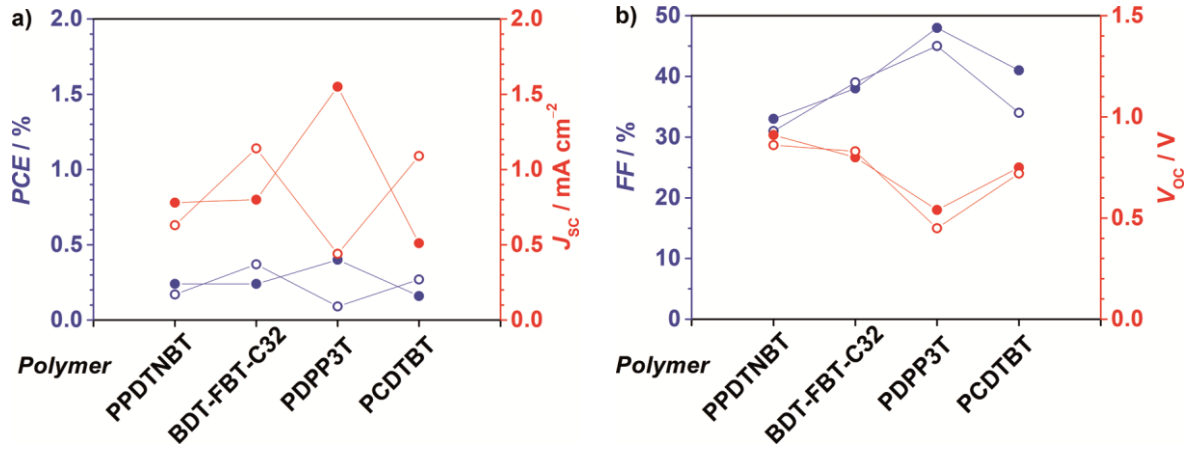

Figure 63. a) *PCE* (blue), J_{SC} (red) and b) *FF* (blue) and V_{OC} (red) of devices with **PPDTNBT**, **BDT-FBT-C32**, **PDPP3T** and **PCDTBT** as donor and **ADA2b** or **ADA2b'** as acceptor. Filled symbols denote devices with **ADA2b** and open symbols denote devices with **ADA2b'**. Devices are of glass/ITO/PEDOT:PSS/**BHJ**/LiF/ Al architecture. Curves were measured under simulated AM1.5 G illumination, with 100 mW cm^{-2} and under inert conditions. Lines serve as guide to the eye.

increase, when going from **PPDTNBT** (~32 %) over **BDT-FBT-C32** (~38 %) to **PDPP3T** (~46 %). Only the fill factors of **PCDTBT** are unexpectedly low in relation to the other polymers. As described above, changes in open circuit voltage are expected upon polymer variation. The voltages estimated from $\Delta E_{HOMO\text{-}LUMO}$ of ~1.0 and 0.65 V fit rather well to the V_{OC} of devices with **PPDTNBT** (~0.81 V) and **PDPP3T** (~0.50 V). Only for the devices with **BDT-FBT-C32** and **PCDTBT**, the measured open circuit voltages of ~0.81 and ~0.73 V do not reach the estimated values of 1.3 and 1.0 V. The UV/vis absorption spectra of all eight solar cells are shown in Figure 64. The solar cell absorption is a result of a combined donor and acceptor absorption (Figure 59). It is worth noticing that in all devices with **ADA2b'**, except the one with **PDPP3T**, the absorption is twice as high as for solar cells with **ADA2b**. The spectra of devices with **ADA2b** in combination with **BDT-FBT-C32** and **PPDTNBT** cover the spectral range of around 500 to 850 nm. Compared to that, the absorption spectrum of the **PCDTBT** device is increased in the range of 500 to 600 nm, while the device with **PDPP3T** extends the absorption to around 900 nm. So, as already derived from the thin film spectra of the pure components, devices with **BDT-FBT-C32** and **PPDTNBT** possess a redundant absorption to **ADA2b**. However, the other two polymers are able to increase (**PCDTBT**) or even extend (**PDPP3T**) the absorption properties of the solar cells. The absorption of **ADA2b'** is slightly blue-shifted and covers the range of 500 to 800 nm in the solid state. As a consequence, its absorption is rather redundant to **BDT-FBT-C32** as well as to **PCDTBT**, while being more complementary to **PPDTNBT** and **PDPP3T**. An appropriate complementarity can be observed in the solar cell spectra (Figure 64b). In the best case, the absorption of **ADA2b'** was complemented by the polymer's absorption,

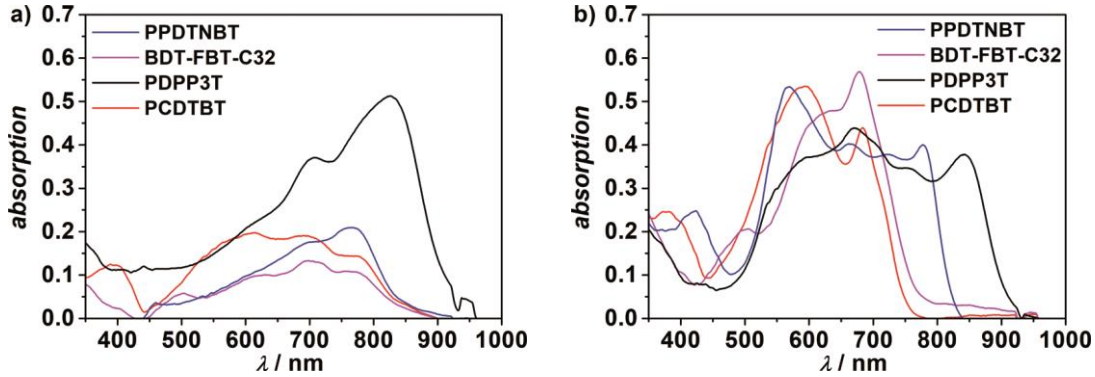

Figure 64. UV/vis spectra of solar cells in glass/ITO/PEDOT:PSS/**BHJ**/LiF/Al architecture, with **PPDTNBT** (blue), **BDT-FBT-C32** (green), **PDPP3T** (black) and **PCDTBT** (red) as donor and a) **ADA2b** or b) **ADA2b'** as acceptor. Artefacts at around 930 to 960 nm can be explained by scattering effects and detector change in this region.

to gain broader overall absorption, with a band edge at around 850 nm (**PPDTNBT**) or 940 nm (**PDPP3T**). It is worth noticing that extended or increased absorption does not necessarily lead to higher short circuit current densities or power conversion efficiencies.

In conclusion, functioning solar cells of all four donor polymers were fabricated in combination with the acceptor dyes **ADA2b** and **ADA2b'**, where the highest efficiencies were observed for **ADA2b** in combination with **PDPP3T** (0.40 %) and for **ADA2b'** in combination with **BDT-FBT-C32** (0.37 %). These efficiencies are much lower than in the corresponding polymer-fullerene solar cells, however, similar trends in J_{SC} and *FF* can be found for the investigated devices upon polymer variation. Furthermore, the estimation of the open circuit voltage via calculation of $\Delta E_{HOMO\text{-}LUMO}$ works well in the case of **PPDTNBT** and **PDPP3T**, for the other polymers the open circuit voltage is highly overestimated. Finally, investigation of solar cell absorption revealed some complementarity between ADA dyes with two polymers, in each case. Both ADA dyes exhibit the most prominent complementarity with **PDPP3T**.

3.2.2.3 Optimization of PDPP3T ADA dye BHJ Solar Cells

Variation of Donor to Acceptor Ratio

As can be seen from the former sections, **PDPP3T** shows the best complementarity in absorption to both acceptor dyes. Even though this polymer did not work so well with **ADA2b'**, it was chosen for further optimization, because it yielded the highest efficiencies of all devices in combination with **ADA2b** (0.40 %). Several techniques like thermal annealing,[251] solvent vapor annealing[252] or the utilization of additives[253] were applied, which commonly help to increase the efficiency of solar cell devices. Furthermore, by comparison of solar cells with **ADA2b** and **ADA2b'**, it was to be found out how the elongated side chains in **ADA2b'** influence processability, morphology and functionality of the devices.

First, the donor to acceptor ratio was varied in devices of glass/ITO/PEDOT:PSS (~40 nm)/**BHJ**/LiF(1 nm)/Al(100 nm) architecture. During fabrication of the solar cells, it was observed that the processability of **ADA2b'** was much better than of **ADA2b**. While the former dye readily dissolved in the processing solvent ($CHCl_3$), due to its elongated alkyl residues, excessive stirring was necessary to completely dissolve **ADA2b**. Furthermore, the spin cast layers of polymer and **ADA2b'** appeared to be much

more homogeneous and less scattering, which could already be observed with the bare eye. This indicates a better miscibility of polymer with **ADA2b'** than with **ADA2b**. As will be shown later, AFM images confirm this finding and show coarser and rougher structures as well as larger domains for the latter dye.

The current voltage characteristics of the devices are shown in Figure 65a and the extracted solar cell parameters are compiled in Table 18. Independent of the donor to acceptor ratio that was set, all devices with **ADA2b** and **ADA2b'** worked with power conversion efficiencies in the range of 0.28 to 0.40 % or 0.04 to 0.09 %, respectively. This shows that the power conversion efficiency is much lower for devices with **ADA2b'** than for devices based on **ADA2b**. Figure 65b clearly shows that the highest efficiencies for both acceptors can be found at a D:A ratio of 1:2. So an excess of electron acceptor is needed in devices with **PDPP3T** and the new ADA acceptors, like in **PDPP3T:PC$_{71}$BM** solar cells (ideal polymer:PC$_{71}$BM ratio = 1:2).[245]

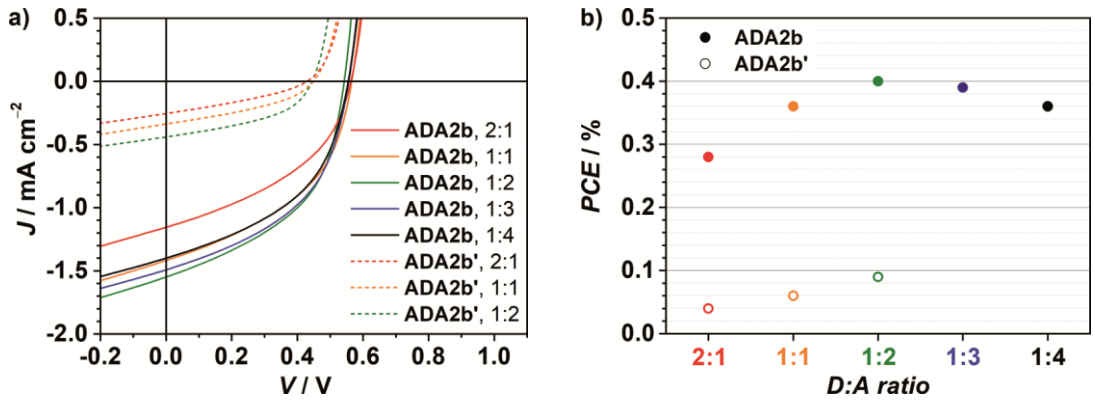

Figure 65. a) Current voltage characteristics of **PDPP3T**:**ADA2b** solar cells (bold) with a donor to acceptor ratio (D:A ratio) of 2:1 (red), 1:1 (orange), 1:2 (green), 1:3 (blue) and 1:4 (black) and of **PDPP3T**:**ADA2b'** solar cells (dashed) with a donor to acceptor ration of 2:1 (red), 1:1 (orange) and 1:2 (green). b) Dependence of power conversion efficiency on D:A ratio in **PDPP3T**:**ADA2b** (filled circles) and **PDPP3T**: **ADA2b'** (open circles) solar cells. Curves were measured under simulated AM1.5 G illumination (100 mW cm^{-2}) and under inert conditions.

All devices show appreciably high fill factors in the range of 43 to 48 % (Table 18). Similarly, the open circuit voltages do not show a strong dependence on the donor to acceptor ratio. However, they are quite different in devices with **ADA2b** vs. **ADA2b'**. When the former acceptor is used, values of around 0.56 V are the result, while devices based on **ADA2b'** yields much lower open circuit voltages of only about 0.45 V. This indicates that the energy of the LUMO levels of the two dyes might be different in the solid state. The different LUMO energies could be the result of a different packing behavior of **ADA2b** and **ADA2b'**, which is supported by the differences in the solid state

Table 18. Characteristic solar cell parameters in dependence of donor to acceptor ratio, for devices with glass/ITO/PEDOT:PSS/**PDPP3T**:**acceptor**/LiF/Al architecture. Measured under simulated AM1.5 G irradiation, with an intensity of 100 mW cm^{-2} and under inert conditions.

acceptor	donor:acceptor	*PCE* [a] [%]	J_{SC} [mA cm^{-2}]	*FF* [%]	V_{OC} [V]
ADA2b	2:1	0.28 (0.27)	1.16	43	0.56
	1:1	0.36 (0.35)	1.42	45	0.57
	1:2	**0.40** (0.39)	1.55	48	0.54
	1:3	0.39 (0.39)	1.49	47	0.56
	1:4	0.36 (0.36)	1.40	46	0.56
ADA2b'	2:1	0.04 (0.03)	0.26	43	0.26
	1:1	0.06 (0.05)	0.34	45	0.45
	1:2	**0.09** (0.09)	0.44	44	0.45

[a] Value in brackets gives the average over 4 devices.

absorption spectra of both dyes (Figure 59). As described above, the expected open circuit voltage for these devices amounts ~0.65 V (see Equation 2.8)[122]. This indeed fits well for devices with **ADA2b**, but it does not match as well for devices with **ADA2b'**. Similarly to the open circuit voltage the short circuit current density is much higher for the solar cells with **ADA2b** (1.16 to 1.55 mA cm^{-2}) than for solar cells with **ADA2b'**

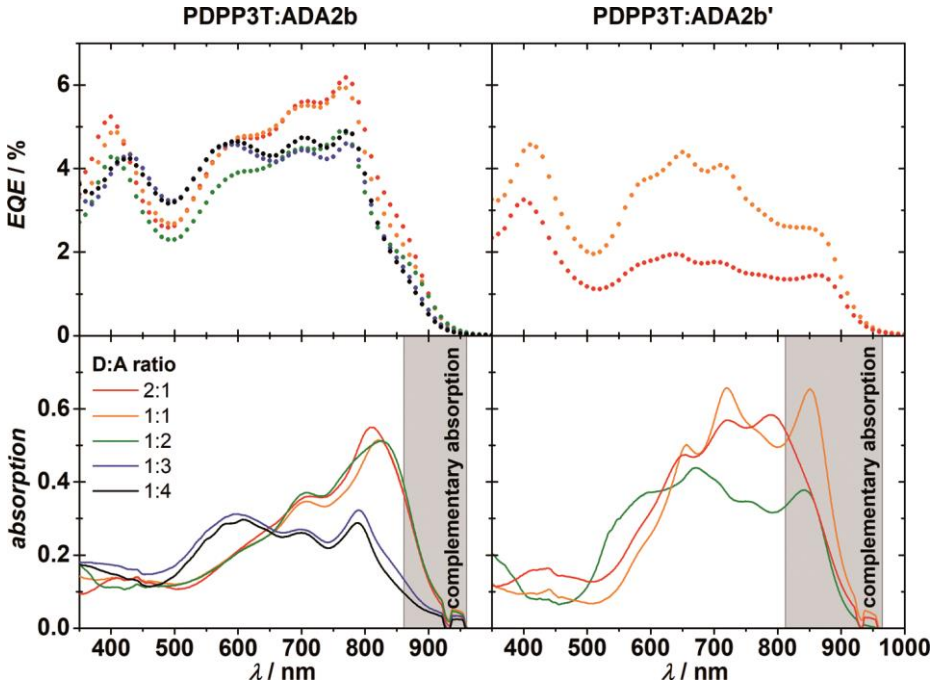

Figure 66. Spectrally resolved external quantum efficiencies of BHJ solar cells in glass/ITO/PEDOT:PSS/**BHJ**/LiF/Al architecture, with **PDPP3T:ADA2b** (top left) and **PDPP3T:ADA2b'** (top right) in ratios of 2:1 (red), 1:1 (orange), 1:2 (green), 1:3 (blue) and 1:4 (black). Absorption spectra of the same BHJ solar cells based on **PDPP3T:ADA2b** (bottom left) and **PDPP3T:ADA2b'** (bottom right), in ratios of 2:1 (red), 1:1 (orange), 1:2 (green), 1:3 (blue) and 1:4 (black). To show the complementarity in absorption between donor and acceptor compounds, the areas where the polymers absorption does not overlap with the acceptor absorption are highlighted in grey.

(0.26 to 0.44 mA cm^{-2}), even though the optical density of the devices is in the same range. However, the short circuit current density is the most sensitive parameter for changes in donor to acceptor ratio, and is therefore the reason for the observed differences in power conversion efficiency. Hence the photocurrent depends on the charge-carrier density and on the charge carrier mobility[254] where absorption, morphology and recombination processes come into play.

The respective *EQE* and absorption spectra of the solar cells with **ADA2b** and **ADA2b'** are depicted in Figure 66. The optical density of the solar cells with **ADA2b** and **ADA2b'** is in the range of 0.30 to 0.55 and 0.40 to 0.65, respectively. The overlap of the absorption of the pristine materials (Figure 59) corresponds to the absorption of the solar cell. Only at higher acceptor ratios, 1:3 and 1:4 for **ADA2b** and 1:2 in the case of **ADA2b'**, an unexpected blue-shifted absorption maximum/shoulder occurs probably due to acceptor aggregation. Areas where the **PDPP3T** absorption is complementary to the one of the ADA acceptors and therefore dominates the solar cell absorption are highlighted in grey. In all other parts of the spectra, polymer and ADA dye absorption overlap. The complementarity is superior in devices with **ADA2b'**, being a result of the different behavior of the two acceptor dyes in the solid state. The *EQE* is low at all wavelengths (< 7 %). The comparison between the *EQE* spectra and the thin film absorption of the donor and the acceptor dyes shows that higher *EQE* values can be found at wavelengths where the thin film absorption of the single components is high. This indicates that both components take part in the charge generation.

Figure 67 shows the AFM height images of the solar cells with **ADA2b** and **ADA2b'** that were measured on a glass/ITO/PEDOT:PSS substrate. While adding more **ADA2b** to the blend the photoactive layer forms a coarser structure and the root mean square roughness of the film increases from 4 to about 20 nm. For a certain degree this coarsening helps to improve the devices, but when huge domains are formed, like in the case of a donor to acceptor ratio of 1:4, the power conversion efficiency starts to drop again. When **ADA2b'** is used as acceptor in a ratio of 2:1, the active layer appears to be very smooth and flat, which is indicative for intimate mixing. The active layer structure becomes coarser, when higher amounts of acceptor are used. In contrast to **ADA2b** the roughness of the films with **ADA2b'** barely increases.

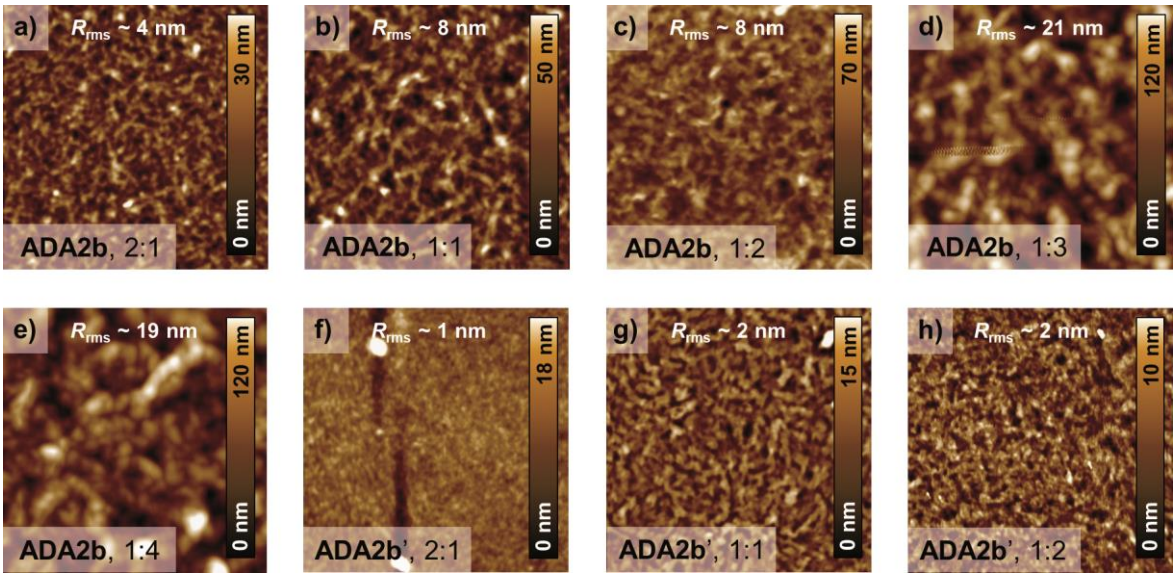

Figure 67. AFM images (5 × 5 µm^2; R_{rms} = root mean square roughness) of photoactive layers of **PDPP3T** with **ADA2b** in a donor to acceptor ratio of a) 2:1, b) 1:1, c) 1:2, d) 1:3, e) 1:4 and of photoactive layers of **PDPP3T** and **ADA2b'** in a donor to acceptor ratio of f) 2:1, g) 1:1 and h) 1:2. Samples were measured on glass/ITO/PEDOT:PSS substrates.

It could be demonstrated that an excess of acceptor compounds in a ratio of 1:2 yielded the highest solar cell efficiencies of 0.40 and 0.09 % for **ADA2b** and **ADA2b'**, respectively. The variation of donor to acceptor ratio changed short circuit current densities and therefore power conversion efficiencies of the devices. However, the solar cells yielded too little photocurrents to generate high efficiencies, although the absorption of the solar cells was high (OD ~ 0.30 to 0.65). A reason could be e.g. that polymer and acceptor did not intermix well enough to form a micro phase separated BHJ structure. Consequently, high exciton recombination rates and poor percolation pathways for charges are expected. This is supported by the AFM images especially for compound **ADA2b**, where rough and segregated structures can be observed. Interestingly, **ADA2b'** showed many differences to compound **ADA2b** just because of its slightly elongated alkyl chains:

(i) The processablility of **ADA2b'** is far superior to the one of **ADA2b**.

(ii) The absorption spectra of both compounds vary in the solid state. This affects the device absorption and gives rise to the assumption of different packing structures for **ADA2b** and **ADA2b'** in the solid state.

(iii) As a result of (ii), the complementarity between the absorption of polymer and **ADA2b'** is noticeably larger than for **ADA2b**.

(iv) Organic solar cells of compound **ADA2b** show significantly larger open circuit voltages (0.56 V) than devices of **ADA2b'** (0.45 V), which again is indicative for a difference in packing of the two dyes.

(v) AFM images reveal that intermixing of polymer and **ADA2b'** is much better than with **ADA2b**, which tends to segregate from the polymer.

Even though **ADA2b'** outperforms **ADA2b** with regard to processability, complementarity in absorption and active layer morphology, packing and energetics are presumably more ideal in the latter compound, indicated by higher power conversion efficiencies.

Morphology Control with Diiodooctane

After the ideal donor acceptor ratio of 1:2 was determined, the active layer morphology was optimized. As shown in the former section, **ADA2b** showed very strong segregation from the polymer while **ADA2b'** gave intimately mixed to slightly segregated active layer morphologies. However, the ideal morphology consists of structures of different length scales, e.g from micro-phase separated areas to larger domains of pure components.[255] To take influence on the morphology a number of solvent additives are frequently applied during active layer preparation.[253,255,256] The basic working principle is quite simple. The main solvent on the one hand dissolves donor and acceptor molecules very well, so that high concentrations (several mg ml^{-1}) for desired active layer thicknesses can be reached. The solvent additive on the other hand dissolves only donor or acceptor component sufficiently. Additionally, the boiling point of the additive is higher than the boiling point of the main solvent.[257] As a consequence, the main solvent evaporates fast during spin-coating, giving desired layer thicknesses, while the additive helps to keep one of the compounds slightly longer in solution, which in most cases will affect its domain size and the overall morphology. The amount of additive and the spin parameters further influence the active layer structure. It is worth mentioning that some additive molecules will probably remain within the active layer, if no heat or high vacuum is applied. In our studies, the frequently applied 1,8-diiodooctance (DIO)[258–260] was chosen as additive to influence the active layer morphology. In fullerene containing BHJ solar cells, diiodooctane with its high boiling point (167 – 169 °C), acts as selective solvent for the fullerene acceptor and thus prevents the formation of unfavorable, huge acceptor domains.[155] This is supported by B. A. Collins *et al.* who observed that DIO

had no effect on the domain composition and crystallinity in **PTB7**:$PC_{71}BM$ solar cells, while the domain size was strongly influenced by the additive, leading to big changes in cell performance.[261] Accordingly, solar cells of **PDPP3T** and **ADA2b** or **ADA2b'** were fabricated with and without addition of 2 vol% of DIO, in a glass/ITO/ PEDOT:PSS(~40 mn)/**BHJ**/LiF(1 nm) /Al(100 nm) architecture. The *J*-*V* characteristics and UV/vis absorption spectra of the corresponding devices are shown in Figure 68 and the device parameters are compiled in Table 19.

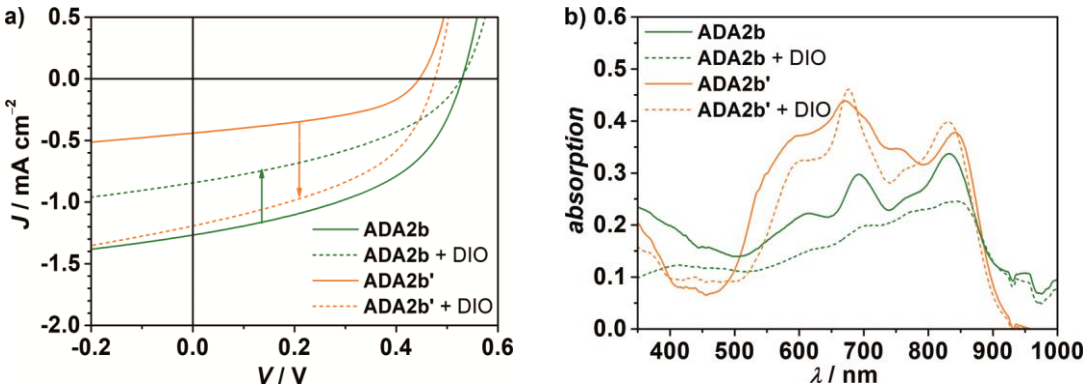

Figure 68. a) *J*-*V* curves of **PDPP3T**:**ADA2b** (green) and **PDPP3T**:**ADA2b'** (orange) BHJ solar cells in a donor to acceptor ratio of 2:1, with (dashed) and without DIO additive (bold). The arrows indicate the changes when DIO is used. The cells of glass/ITO/PEDOT:PSS(~40 mn)/**BHJ**/LiF(1 nm) /Al(100 nm) architecture were characterized under simulated AM1.5 G irradiation (100 mW cm^{-2}) and under inert conditions. b) UV/vis absorption of corresponding devices. Artefacts at around 930 and 980 nm can be explained by scattering effects due to large particle/domain size (AFM) and detector change in this region.

As can be seen from the deduced solar cell parameters, the device performance is highly influenced by DIO and different for both acceptor dyes. While the power conversion efficiency decreases from 0.32 to 0.18 % in devices with **ADA2b** acceptor, it increases from 0.09 to 0.26 % in solar cells with **ADA2b'**. In the case of **ADA2b** the fill factor and the short circuit current density are reduced upon addition of DIO. Solar cells with **ADA2b'** possess a much higher short circuit current density and slightly increased open

Table 19. Solar cell parameters of **PDPP3T**:**ADA2b** and **PDPP3T**:**ADA2b'** devices of glass/ITO/PEDOT:PSS (~40 mn)/**BHJ**/LiF(1 nm) /Al(100 nm) architecture, with and without diiodooctane as additive. Measured under simulated AM1.5 G irradiation (100 mW cm^{-2}) and under inert conditions.

acceptor	DIO (vol%)	*PCE* [a] [%]	J_{SC} [mA cm^{-2}]	*FF* [%]	V_{OC} [V]
ADA2b	–	0.32 (0.32)	1.27	47	0.53
	2	0.18 (0.18)	0.84	40	0.53
ADA2b'	–	0.09 (0.09)	0.44	44	0.45
	2	0.26 (0.24)	1.19	45	0.48

[a] Value in brackets is the average over 4 devices.

circuit voltage, when the blend was processed with these small amounts of additive. In this way they almost reach the performance of the pristine devices based on **ADA2b**. The UV/vis absorption spectra of the solar cells at least show four different absorption maxima in the range of 500 to 900 nm, as a result from combined polymer and acceptor absorption. Solar cells with **ADA2b** in the active layer show less pronounced absorption bands when DIO is used, while the opposite is true for the cells with **ADA2b'**. This indicates changes in the morphology of the active layer.

The AFM images of the photoactive layers of the solar cells are presented in Figure 69. When DIO is used in solar cells with **ADA2b'**, the active layer becomes coarser and more segregated. This leads to higher efficiencies in the corresponding solar cells. When DIO is used in solar cells containing **ADA2b**, a complete phase separation of the polymer and the acceptor molecules can be observed, where rosette shaped domains are formed, probably by **ADA2b**. This decreases the efficiency in these cells tremendously.

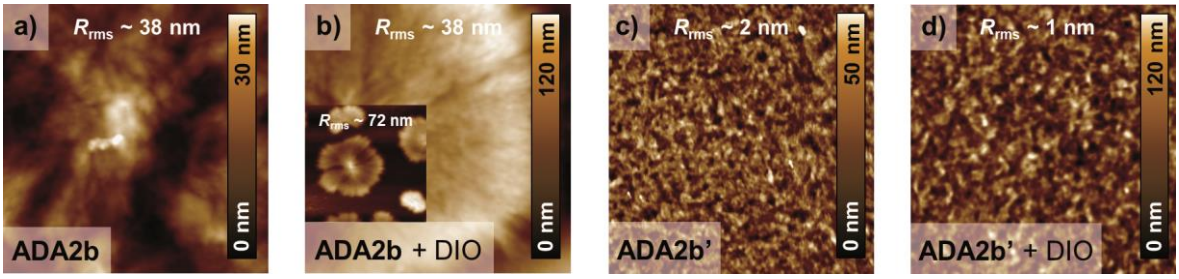

Figure 69. AFM images (5×5 μm^2; R_{rms} = root mean square roughness) of photoactive layers of **PDPP3T**:**ADA2b** a) without and b) with DIO additive and of **PDPP3T**:**ADA2b'** c) without and d) with DIO additive. The inset in b) shows an image of 20×20 μm^2. Samples were measured on glass/ITO/PEDOT:PSS substrates.

Morphology Control via Post Processing

While solvent additives influence the active layer morphology during its rapid formation, there are different techniques to modify the morphology after processing. Two important methods are thermal annealing (ΔT),[251,262–264] and solvent vapor annealing (SVA).[252,265–267] Both techniques allow for some molecular movement and rearrangement, often resulting in higher crystallinity of donor and acceptor molecules. Generally, short annealing times are ideal to reach an improved molecular arrangement, which is e.g. important for exciton and charge transport, without affecting the sensitive microphase-separation within the active layer of BHJ solar cell. K. Sun *et al.* nicely showed how powerful SVA can be. Their pristine devices composed of **DPP(TBFu)$_2$**

(a diketopyrrolopyrrole dye flanked symmetrically with two benzofuranyl groups that are bridged via thiophenes units) and $PC_{71}BM$ showed a power conversion efficiency of 0.55 %, which increased to >5 % under optimized SVA conditions.[252] Of course it can be advantageous to combine thermal and solvent vapor annealing to obtain the most favorable morphology.[266]

The great potential of ΔT and SVA procedures to boost the device performance was used for solar cells with **PDPP3T**:**ADA2b'**, too. Accordingly, three different post annealing techniques were tested on devices with ideal donor to acceptor ratio (1:2): firstly, solvent vapor annealing (SVA) with chloroform (1 min), secondly, solvent vapor annealing with chlorobenzene (1 min) and thirdly, thermal annealing at 100 °C (1 min). Because solar cells with **ADA2b** seem to be very crystalline and utilization of DIO only resulted in strong phase separation, SVA to increase the crystallinity was not performed with this molecule. The current voltage characteristics of the pristine devices with **ADA2b** and **ADA2b'** as well as the post annealed devices with **ADA2b'** are shown in Figure 70a and compiled in Table 20.

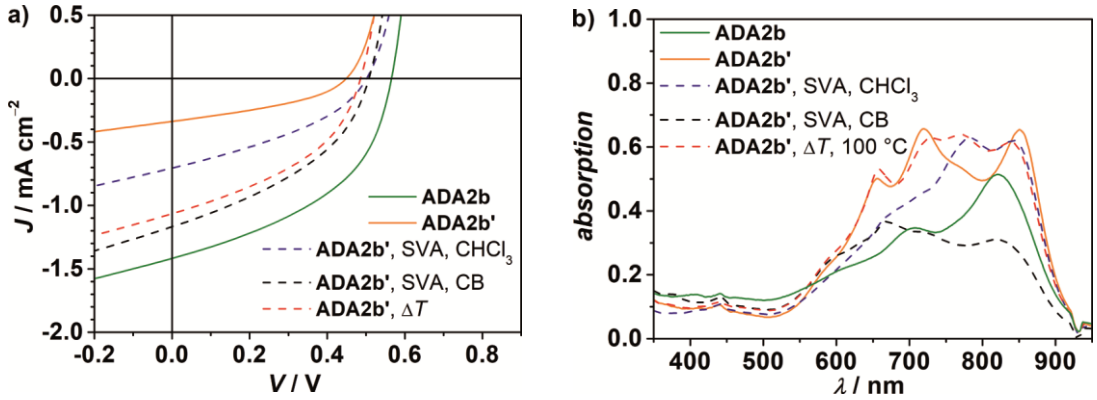

Figure 70. a) *J-V* characteristics of pristine devices (bold) with **ADA2b** (green), **ADA2b'** (orange) and of post treated devices (dashed) with **ADA2b'**. Post treatment was performed by either solvent vapor annealing (SVA) in $CHCl_3$ (blue), chlorobenzene (black) or by thermal annealing ΔT at 100 °C (red) for one minute each. The BHJ devices were of glass/ITO/PEDOT:PSS (~40 nm)/**BHJ**/LiF (1 nm)/Al (100 nm) architecture. They were characterized under simulated AM1.5 G irradiation (100 mW cm^{-2}) and under inert conditions. b) Thin film absorption spectra of corresponding devices. Artefacts at ~900 nm can be attributed to scattering and detector change.

The pristine **ADA2b'** device of glass/ITO/PEDOT:PSS (~40 nm)/**BHJ**/LiF(1 nm)/ Al (100 nm) architecture showed an efficiency of 0.06 %. After solvent vapor annealing with chloroform, the efficiency of the solar cell increased to 0.13 %. The fill factor was still around 38 % after SVA, the open circuit voltage rose from 0.45 to 0.50 V and the short circuit current density strongly increased from 0.34 to 0.71 mA cm^{-2}. When

Table 20. Solar cell parameters of **PDPP3T**:**ADA2b'** solar cells before and after post treatment and of a pristine **PDPP3T**:**ADA2b** solar cell. The devices with glass/ITO/PEDOT:PSS/**BHJ**/LiF/Al architecture were measured under simulated AM1.5 G irradiation with an intensity of 100 mW cm^{-2} and under inert conditions.

acceptor	annealing	*PCE* [a] [%]	J_{SC} [mA cm^{-2}]	*FF* [%]	V_{OC} [V]
ADA2b	–	0.36 (0.35)	1.42	45	0.57
ADA2b'	–	0.06 (0.05)	0.34	38	0.45
	SVA, $CHCl_3$, 1min [b]	0.13 (0.13)	0.71	37	0.50
	SVA, CB, 1min [b]	0.24 (0.23)	1.17	40	0.51
	ΔT, 100 °C, 1min [c]	0.22 (0.21)	1.07	41	0.49

[a] Value in brackets gives the average over 4 devices. [b] Solvent vapor annealing in a petri dish with 200 µl of CHCl3 or CB. [c] Thermal annealing was performed under inert gas atmosphere.

chlorobenzene was used for solvent vapor annealing, the performance grew even further to 0.24 %, mainly due to an improved J_{sc} (1.17 mA cm^{-2}) and fill factor (40 %). Interestingly, the increased J_{sc} was observed even though a huge decrease in absorption took place. Thermal annealing yields a performance of 0.22 %. In this much stronger absorbing solar cell, only the current density of 1.07 mA cm^{-2} lags behind the chlorobenzene treated device.

The absorption of the pristine solar cells (Figure 70b) is strong (0.70) in the range from 600 to 900 nm and four maxima can be observed here. The two low wavelength absorption maxima at 656 and 718 nm decrease, while a new absorption maximum arises at 784 nm, when SVA is performed with chloroform. After SVA with chlorobenzene, the absorption is decreased to 0.35. Thermal annealing of the devices causes a new maximum at 771 nm, while the rest of the spectrum hardly changes. All these changes indicate molecular rearrangement, so that higher crystallinity can be expected for active layers after annealing.

The AFM images of the active layers were measured of the pristine and the treated devices (Figure 71). In comparison to the pristine substrate, the surface of the active layer of the post treated devices does not change drastically. Among the treated devices, the AFM images do not differ either, even the surface roughness stays at 1 – 2 nm, indicating that the changes happen at another scale and cannot be monitored by AFM.

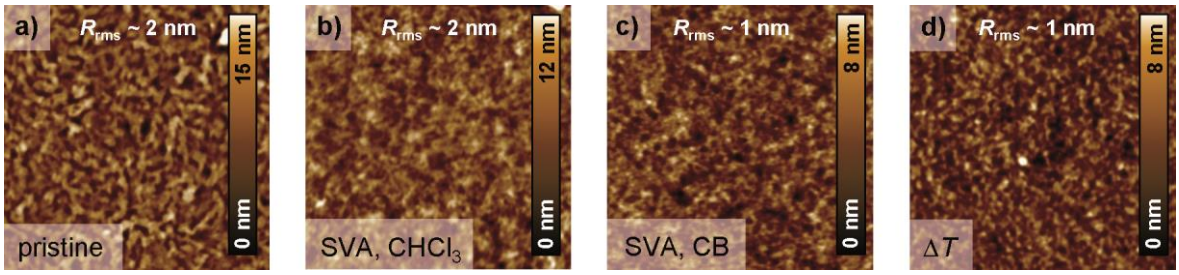

Figure 71. AFM images (5×5 µm^2; R_{rms} = root mean square roughness) of a) the pristine, b) the chloroform vapor annealed, c) the chlorobenzene vapor annealed and d) the thermally annealed (100 °C, 1min) photoactive layers, containing **ADA2b'**. Samples were measured on glass/ITO/PEDOT:PSS substrates.

3.2.2.4 Conclusion

Although, **ADA2b'** and **ADA2b** only deviate in the length of their alkyl chains, they show a different behavior in the solid state and within the organic solar cells. It could be demonstrated that the addition of 2 vol % diiodooctane had a strong impact on the domain size in the BHJ of **PDPP3T:ADA2b** or **ADA2b'** solar cells. In both cases, phase segregation was more pronounced when DIO was used. In the case of **ADA2b** AFM images displayed donor and acceptor domains of a few micrometers in size, which is much larger than the typical exciton diffusion length (~10 nm).[79,82,268,269] As expected, this led to a decrease in fill factor and short circuit current density in these cells. The solar cells with **ADA2b'** showed improved performance upon addition of DIO mainly due to increased short circuit current densities. In this case donor and acceptor were still separated in domains of a few tenth of a nanometer in size so that the interface where exciton separation takes place is small. Presumably, the formation of more crystalline pathways of donor or acceptor molecules, which is favorable for an efficient charge transport, is the reason for the improvement in these cells as absorbance and open circuit voltage remain nearly constant.[270]

Furthermore, devices of **ADA2b'** were improved by post treatment, i.e. SVA with chloroform or chlorobenzene as well as thermal annealing. In all cases the open circuit voltage was increased by 0.05 V, the fill factor changed slightly (37 - 41 %), while the short circuit current density was doubled or tripled in comparison to the pristine device. Thereby, the device performance of solar cells with **ADA2b'** approached the one of pristine **ADA2b**. The UV/vis absorption spectra of the annealed devices were different in comparison to the spectrum of the pristine device. The formation of new absorption bands (thermal annealing, SVA with $CHCl_3$) and a strong decrease of absorption bands (SVA with $CHCl_3$ or CB) were observed, indicating reorientation processes of the

molecules and phase reorganization. The AFM images did not show large differences between the pristine and the annealed devices, so that morphological changes have to happen at a scale below 100 nm. In principle dewetting could be a reason for the reduced absorption,[271] but this does not occur in the chlorobenzene treated devices (AFM). More likely, reorientation of the molecules was responsible.

Altogether it was determined that **ADA2b** seems to be the superior molecule, regardless of its low solubility. **ADA2b'** as well as **ADA2b** were not able to use the full potential of the polymers, e.g. **PDPP3T** results in *PCE*s of 7.1 % when it is combined with $PC_{71}BM$.[272] Even though good open circuit voltages and a nice absorption could be reached with the new dyes they were not able to afford high photocurrents. To this end further investigations and a deeper understanding of these molecules is necessary to improve power conversion efficiencies.

3.2.3 Electron Poor AπA Dyes Based on Four Coordinate Boron Complexes**

3.2.3.1 Design and Synthesis of Boron Bridged AπA Dyes

In section 3.2.1, ADA dyes based on biphenyl and bithienyl cores were investigated with the aim to find suitable electron transport materials for the application in organic electronics. It was observed that the HOMO and LUMO levels decreased by about 0.3 eV in bithienyl based compounds, when nitrogen was replaced with carbon as bridging atom in the central core. In this section a four-coordinate boron atom is utilized in the central moiety, to tune the molecule's photophysical and charge transport properties (Figure 72). Thus, a (3-boryl-2-thienyl)-2-thiazole (BTT) moiety was chosen as central core. This building block pairs the electron deficiency of the boron atom with the high electron affinity of N-heterocyclic aromatic compounds. Consequently, this central building block is now rather electron poor compared to the electron donating bithienyl units. Therefore, this building block is named π-bridge instead of donor.

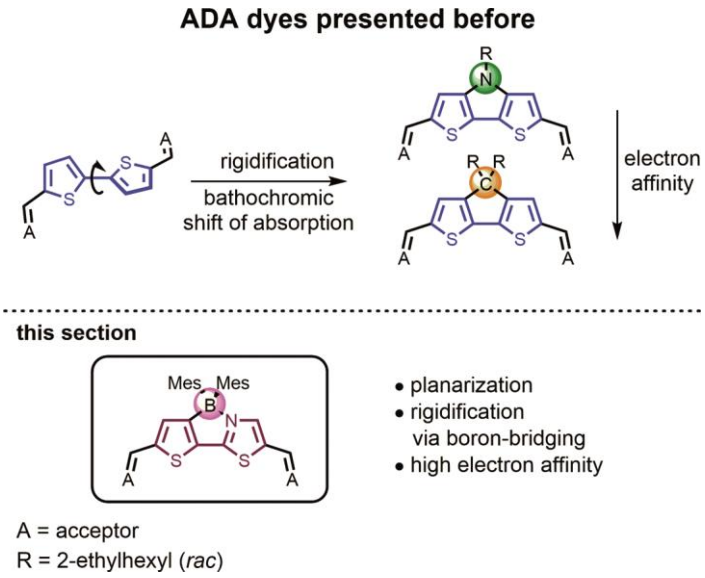

Figure 72. Design strategy towards electron-transport materials. Reproduced from reference[273] with permission from Wiley-VCH Verlag GmbH, Copyright 2017.

The BTT itself was introduced to literature by the group of Yamaguchi and its usefulness was demonstrated, when a dimeric BTT showed moderate electron mobilities of

** Large parts of the results presented in this chapter are reprinted from reference[273] with permission from Wiley-VCH Verlag GmbH, Copyright 2017. Dr. A. Nowak-Król and J. Kade performed the syntheses and quantum chemical calculations. Differential scanning calorimetry measurements were performed by Ana-Maria Krause.

1.5×10^{-4} cm^2 V^{-1} s^{-1}.[274] Furthermore, the BTT was studied as a building block in polymers, where it was utilized in alternation with different acceptor units.[275,276] Investigations on this moiety were performed by Yamaguchi in dimeric regioisomers,[274] and recently by Wakamiya in DπA systems.[277,278]

In this section, the BTT was utilized as central π-bridge in three different AπA dyes. As acceptor units either two malononitrile, indandione (IND) or 1,1-dicyanomethylene-3-indandione (DCIND) moieties were chosen. The latter acceptors are identical with the ones used in section 3.2.1, where they proved to tune the HOMO and LUMO levels effectively. Again, the Knoevenagel condensation reaction was used to link the dialdehydic BTT to the methylene activated acceptor components. The resulting ethylene linker between π-bridge and acceptors ensures full coplanarity and enhances the conjugation. To ensure a reasonable solubility and good stability of the AπA dyes, two mesityl (Mes) groups were introduced at the boron atoms, regardless of their bulkiness. As reference compounds, the most promising pair of the ADA molecules was chosen, **ADA2a** and **ADA2b** (section 3.2.1). These compounds, based on CDPT donor and IND or DCIND acceptor, showed very high molar extinction coefficients paired with low lying LUMO energies. Also n-channel semiconducting behavior (0.073 cm^2 V^{-1} s^{-1}) could be measured in OTFTs of **ADA2b**. Their chemical structure is shown in Figure 73.

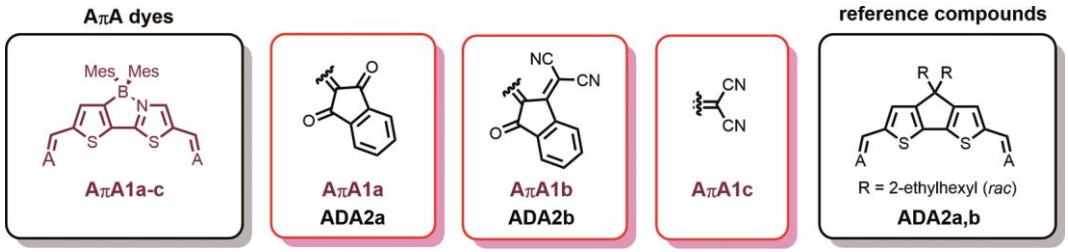

Figure 73. Chemical structure dyes **AπA1a-c** of reference compounds **ADA2a**,**b**.

The syntheses of **AπA1a-c** are described in Section 6.5.3. The stability of the synthesized compounds was investigated by DSC measurements (Figure 74). All compounds possess a good stability in the solid state upon heating under nitrogen atmosphere. Melting points were measured for **AπA1a** and **AπA1c** of 269 and 230 °C, respectively. The highest stability was observed for **AπA1b**, which decomposed without melting at around 350 °C. Furthermore, **AπA1a** and **AπA1c** show some crystal-to-crystal phase transitions before melting, observable by optical microscopy.

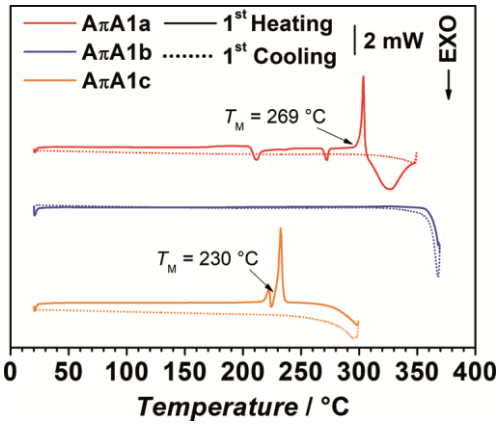

Figure 74. Differential scanning calorimetry measurements of **AπA1c** (orange), **AπA1a** (red) and **AπA1b** (blue). The DSC measurements were performed under N_2, with a heating/cooling rate of 10 K min^{-1}.

3.2.3.2 Solid State Packing of AπA Dyes

Single crystals of **AπA1a** and **AπA1c** were grown at room temperature by slow evaporation of CD_2Cl_2 or toluene, respectively. The crystal structures were obtained by X-ray diffraction measurements and their molecular structures are shown in Figure 76. Important bond lengths and angles of the molecules are compiled in Table 21. The characteristic (dihedral-)angles are explained in Figure 75. The dihedral angles between thiophene and thiazole rings (θ_{core}) in **AπA1a** and **AπA1c** are 3.3° and 4.4°, respectively, which shows the high planarity of the central moiety. The dihedral angles between π-bridge and the acceptor units ($\theta_{bridge\text{-}A}$) in **AπA1c** are 11.1° and 4.3°, on the side of the thiophene and thiazole, respectively. Even lower dihedral angles of around 2.0° were measured, when IND acceptors were utilized. The low dihedral angles show that the π-bridge is effectively conjugated to the flanking acceptor units in both compounds. The position of the boron atom in the central core is defined by the B-N and the B-$C_{thiophene}$ bond length. These distances amount 1.650 (B-N) and 1.645 Å (B-$C_{thiophene}$) in **AπA1a**

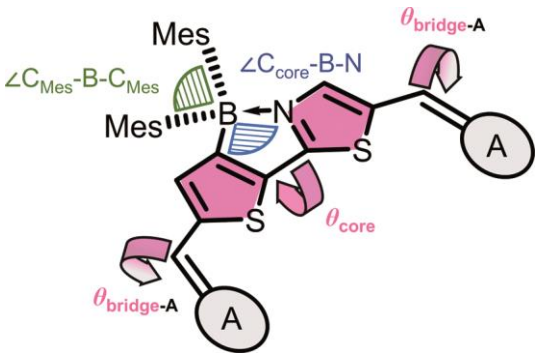

Figure 75. Important angles and dihedral angles in AπA compounds.

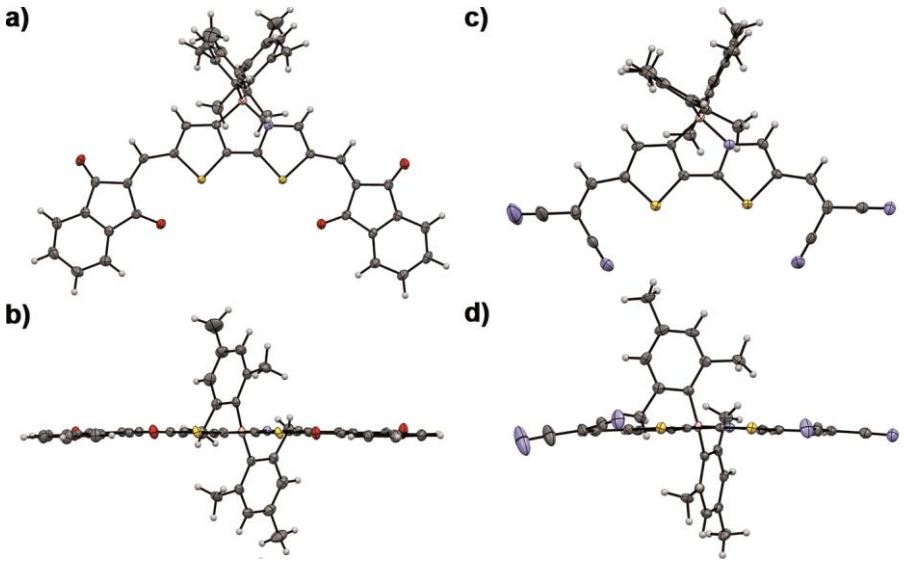

Figure 76. Molecular structures of **AπA1a** (grown from toluene) and **AπA1c** (grown from CD_2Cl_2) in the solid state, determined by single-crystal X-ray diffraction measurements. a) Front view and b) side view of **AπA1a**. c) front view, d) side view of **AπA1c**. The ellipsoids were set to 50 % probability. Solvent molecules embedded in the crystal structure of **AπA1a** are omitted for clarity. Reproduced from reference[273] with permission from Wiley-VCH Verlag GmbH, Copyright 2017.

and are identical in **AπA1c** (1.647 Å). In contrast, the two B-C_{Mes} bonds are almost identical in **AπA1a** (1.637 Å), while they vary in **AπA1c** (1.643 and 1.629 Å). The boron atom adopts a distorted tetrahedral geometry in both AπA dyes, to form N,C-chelate five membered rings. As a consequence, the ∠C_{core}-B-N angle is at around 94° in both dyes, which is much less than the ideal angle of 109.5°. Furthermore, the associated ∠C_{Mes}-B-C_{Mes} angles of 115 – 120° are larger than the ideal angle.

Table 21. Dihedral angles θ, bond lengths and tetraeder angles ∠ of **AπA1a** and **AπA1c**, derived from single crystal structures.

dye	solvent	θ_{core} [°]	$\theta_{bridge\text{-}A}$ [°]	B-N [Å]	B-$C_{thiophene}$ [Å]	B-C_{Mes} [Å]	∠C_{core}-B-N [°]	∠C_{Mes}-B-C_{Mes} [°]
AπA1a	toluene	3.3	2.1, 2.0	1.650	1.645	1.637, 1.638	94.2	115.4
AπA1c	CD_2Cl_2	4.4	11.1, 4.3	1.647	1.647	1.643, 1.629	93.7	120.2

3.2.3.3 Optical and Electrochemical Properties

Absorption spectra of compounds **AπA1a-c** were recorded in CH_2Cl_2 (Figure 77) and the optical data are listed in Table 22. Molar extinction coefficients between 35×10^3 to 67×10^3 M^{-1} cm^{-1} were measured for the AπA dyes, being inferior to the ones of the reference compounds. On the other hand, the absorption bands of the AπA dyes are

broader than for the reference dyes, so that their squared transition dipole moments μ^2_{eg} (**AπA1c** = 82 D^2, **AπA1a** = 118 D^2 and **AπA1b** = 140 D^2) approach the ones of the ADA dyes, being almost equal for **AπA1b** and **ADA2a** (138 D^2). The absorption maximum of **AπA1b** at 589 nm almost matches the one of reference **ADA2a**. Compared to this, **AπA1a** and **AπA1c** show red-shifted absorption maxima of 530 and 454 nm, respectively, due to a reduction of the conjugated π-system. Additionally, the larger shift observed for **AπA1b** can be attributed to the stronger electron accepting nature of the DCIND acceptors in comparison to the IND acceptors used in **AπA1a**. Vibronic progressions can be found for **AπA1a** and **AπA1b** at 499 and 554 nm, respectively. The emission was effectively quenched in this set of AπA compounds (CH_2Cl_2), so that charge transfer interactions (CT) might turn out to be one possible deactivation pathway.

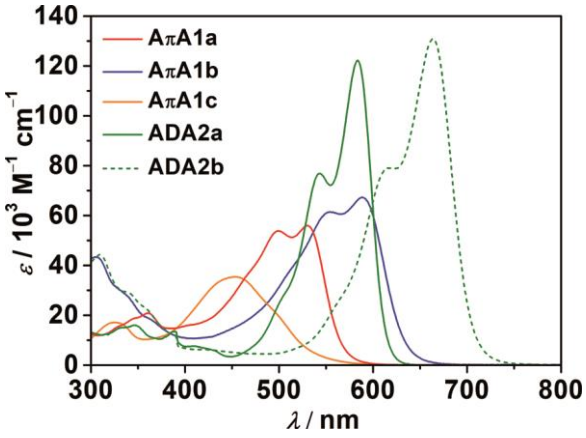

Figure 77. UV/vis absorption spectra of AπA dyes **AπA1a** (red), **AπA1b** (blue), **AπA1c** (orange) and of reference ADA dyes **ADA2a** (green, bold) and **ADA2b** (green, dashed). Measurements were performed in CH_2Cl_2 (c ~10^{-5} M, RT).

Table 22. Optical and electrochemical properties of AπA dyes **AπA1a**, **AπA1b**, **AπA1c** and of reference ADA dyes **ADA2a** and **ADA2b**.

dye	λ_{max} [a] [nm]	ε_{max} [a] [10^3 M^{-1} cm^{-1}]	μ^2_{eg} [D^2]	$E_{1/2}^{red}$ [b] [V]	$E_{1/2}^{ox}$ [b] [V]	E_g^{opt} [V]	E_g^{CV} [V]
AπA1a	530	56	118	–1.12, –1.49 [c]	+0.89, [c] +1.01, [c]	2.34	2.01
	499	54			+1.17 [c]		
AπA1b	589	67	140	–0.84 [c,d]	+0.90 [c]	2.10	1.74
	554	62					
AπA1c	454	35	82	–1.00, –1.25	+0.91 [c]	2.73	1.91
ADA2a	584	122	138	–1.30	+0.84	2.12	2.14
ADA2b	664	131	167	–0.84 [c]	+1.08 [c]	1.87	1.92

[a] CH_2Cl_2. [b] Measurements were carried out in dry CH_2Cl_2, c ~10^{-4} – 10^{-5} M. scan rate 100 mV s^{-1}; supporting electrolyte Bu_4NPF_6 (c = 0.1 M); Pt-disc electrode (Ø 3mm); calibrated vs. ferrocenium/ferrocene (Fc^+/Fc; −5.15 eV vs. vacuum) as an internal standard. [c] Peak potential for irreversible redox processes. [d] Further reaction potentials were observed but the peak potentials could not be resolved.

Cyclic voltammetry measurements were performed in CH_2Cl_2 to determine the energy levels of the frontier molecular orbitals from the measured redox potentials. The cyclic voltammograms are shown in Figure 78a and the electrochemical properties are summarized in Table 22.

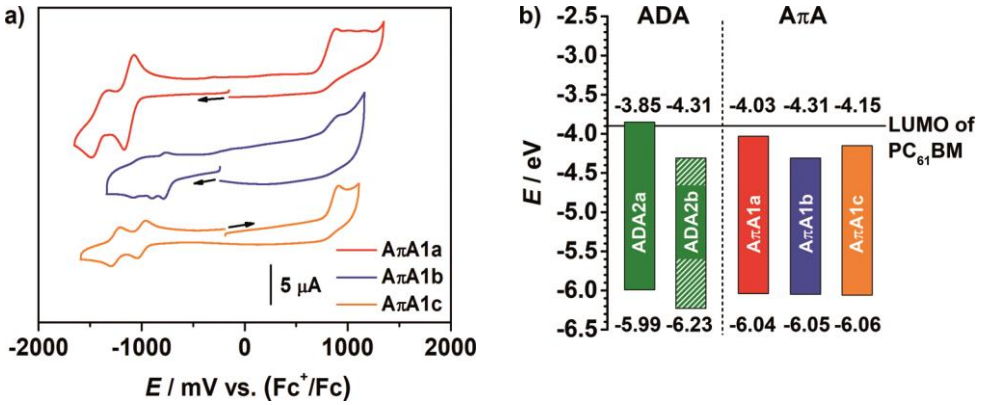

Figure 78. a) Cyclic voltammograms of compounds **AπA1a** (red), **AπA1b** (blue) and **AπA1c** (orange). Measurement conditions: CH_2Cl_2, c ~10^{-4} – 10^{-5} M, 298 K; Scan rate: 100 mV s^{-1}; Supporting electrolyte: Bu_4NPF_6 (0.1 M); Calibrated vs. Fc^+/Fc as an internal standard. b) HOMO and LUMO levels defining the electrochemical band gaps of the ADA reference dyes **ADA2a** (green, filled) and **ADA2b** (green, dashed) and of the AπA dyes **AπA1a** (red), **AπA1b** (blue), **AπA1c** (orange). The solid black line represents the LUMO energy level of $PC_{61}BM$ (−3.9 eV).[155] Reproduced from reference[273] with permission from Wiley-VCH Verlag GmbH, Copyright 2017.

Two reversible reduction potentials are measured at −1.00 and −1.25 V for **AπA1c**. These reduction potentials are similar to the ones of a core-unsubstituted perylene bisimide (−0.95, −1.15 V), which was successfully applied as an n-type semiconducting material.[279] The two reduction potentials observed for **AπA1a** occur at −1.12 and −1.49 V, showing that this compound is harder to reduce than the more electron-poor **AπA1c**. By utilizing AπA dyes with strong electron accepting DCIND acceptor moieties, a stronger modulation of the electron density was achieved. Accordingly, **AπA1b** shows a first irreversible reduction process at −0.84 V. Further reduction processes were observed in this dye, but could not be resolved satisfactorily due to the low solubility and concomitant low measured currents. The measurements of the reduction potentials reveal that **AπA1c** and **AπA1a** form rather stable radical anions, which is not the case in **AπA1b**. While the variation of acceptor units takes strong influence on the reduction processes of the AπA dyes, their oxidation processes are almost unaffected. Irreversible oxidations take place at comparable potentials of +0.89, +0.90 V and +0.91 for **AπA1a**, **AπA1b** and **AπA1c**, respectively. Further irreversible oxidation processes were observed for **AπA1a** (+1.01, +1.17 V). The frontier molecular orbitals as well as the LUMO level of $PC_{61}BM$ are shown in Figure 78. The HOMO levels of the AπA dyes are almost equal

(~ −6.05 eV) and correspond well to the HOMO of **ADA2a** (−5.99 eV). The HOMO level of **ADA2b** is even lower (−6.23 eV), because the acceptor variation has a stronger influence on the HOMO levels in the case of the ADA dyes. In contrast, the LUMO levels of the AπA dyes decrease in the following order: **AπA1a** (−4.03 eV) > **AπA1c** (−4.15 eV) > **AπA1b** (−4.31 eV). Thus, they show a good variation of around 0.30 eV, which is however not as high as for the ADA dyes.

Conclusively, by twofold acceptor functionalization of a (3-boryl-2-thienyl)-2-thiazole π-bridge, three molecules were obtained whose LUMO levels could be lowered effectively. That the LUMO levels fall even below the LUMO level of the well-known electron transport material $PC_{61}BM$ indicates the high electron affinity of the compounds. Electrochemical band gaps in the range of 1.74 − 2.01 eV were calculated for the AπA dyes, which is a good prerequisite to harvesting sunlight, if these dyes are applied in organic solar cells. The influence of the boron-bridging on the electrochemical properties of the dyes was evaluated by comparison with ADA dyes **ADA2a** and **ADA2b**. The first reduction potentials as well as the corresponding LUMO levels of the DCIND substituted dyes **AπA1b** and **ADA2b** are equal. In contrast, the reduction of IND substituted dyes **AπA1a** and **ADA2a** varies. The latter shows a reduction potential, which is cathodically shifted by 0.18 V with respect to the reduction potential of **AπA1a**. This moderate difference in reduction potentials and therefore in LUMO levels leads to the fact that **ADA2a** shows hole transport behavior in organic field-effect transistors, while electron transport behavior can be measured for **AπA1a** (see section 3.2.3.5).

3.2.3.4 Quantum Chemical Calculations

Quantum chemical calculations were performed for the AπA dyes using the B3LYP functional and def2-SVP basis set. CH_2Cl_2 was used as solvent in the polarizable continuum model (PCM). Like in ADA dyes, the geometry optimized structures of the AπA dyes (Figure 79) suggest a high planarity, favorable for close π-π contacts in the solid state. The electrostatic potential surfaces visualize the electron-rich and electron-poor sites of the molecules. The electron density appears not to be equally distributed over the π-bridge, showing that the thiophene is more electron-rich than the thiazole subunit. Furthermore, the electron density is the highest in **AπA1a** (IND acceptors) and the lowest in **AπA1c** (malononitrile acceptors). The calculated Kohn-Sham orbitals and their corresponding energies are shown in Figure 80. The calculations reveal that the HOMOs of all AπA dyes are located on one eletron rich mesityl group. The LUMOs of

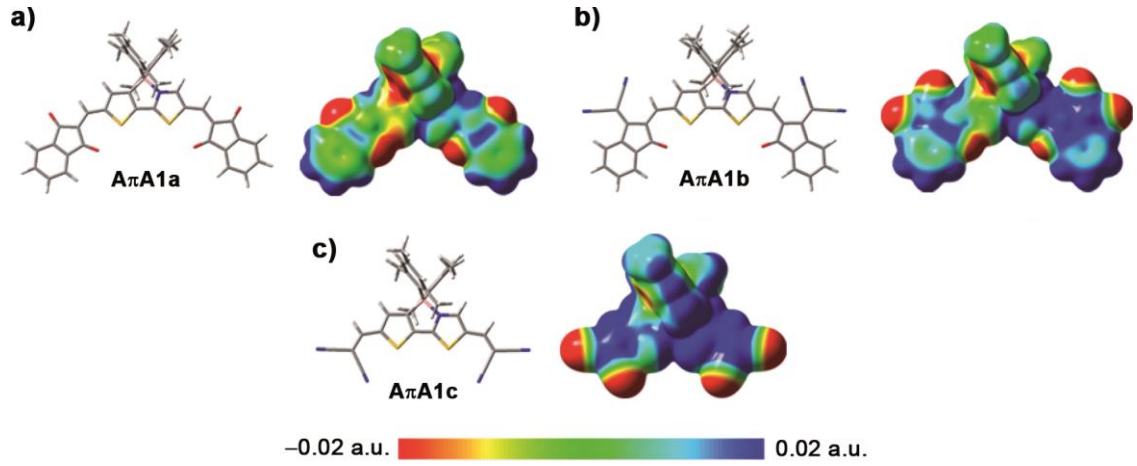

Figure 79. Geometrically optimized molecular structures (B3LYP/def2-SVP, solvent: CH_2Cl_2) and electrostatic potential surfaces (isovalue = 0.001 a.u.) calculated for **AπA1a-c**. Reprinted from reference[273] with permission from Wiley-VCH Verlag GmbH, Copyright 2017.

the compounds are distributed along the whole π-bridge including both acceptor units. The second highest occupied molecular orbitals (HOMO–1) of the AπA dyes are localized on the second mesityl moiety. Electronic absorption spectra were calculated for **AπA1a-c** using time-dependent DFT (CAM-B3LYP; def2-SVP). CH_2Cl_2 was used as a solvent for calculations (PCM model). Simulation of the spectra was performed with GaussView 5, and a half-width of 2000 cm^{-1} was assumed for proper simulation

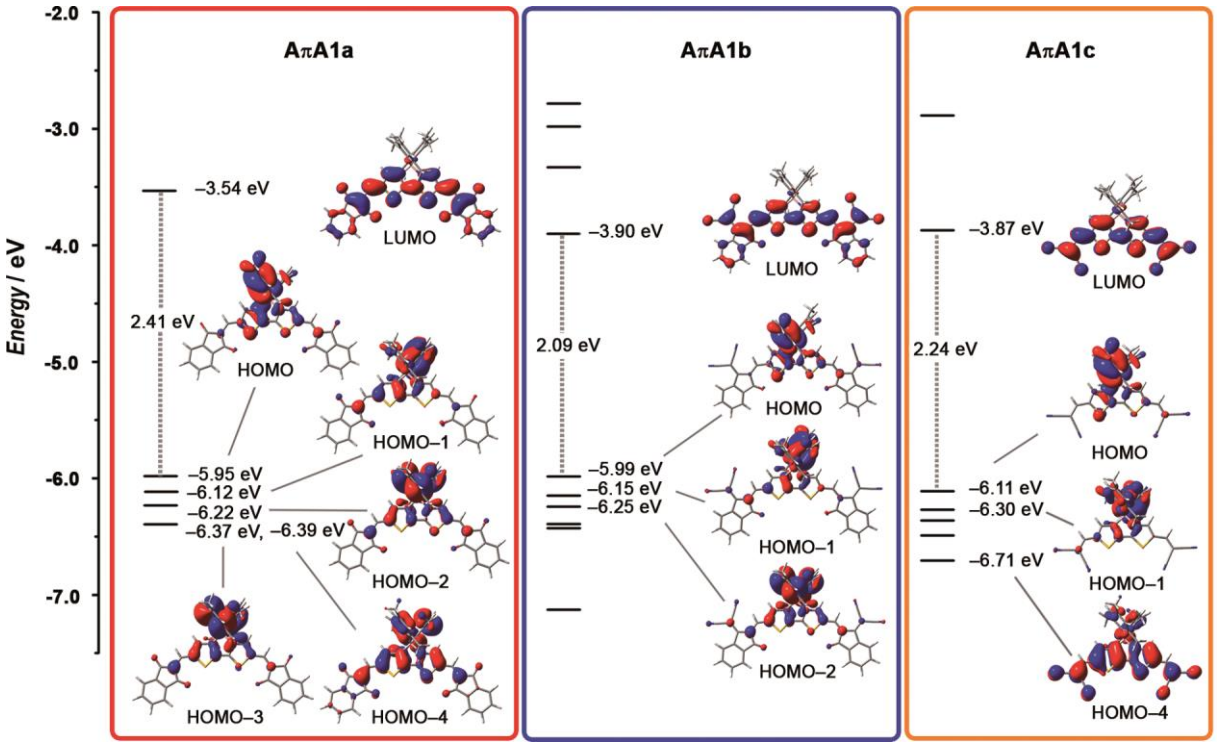

Figure 80. Calculated Kohn-Sham orbital energy level diagrams (B3LYP/def2-SVP; solvent: CH_2Cl_2; PCM model) and contour plots of selected orbitals (isovalue = 0.02 a.u.) of **AπA1a-c**. Reproduced from reference[273] with permission from Wiley-VCH Verlag GmbH, Copyright 2017.

(Figure 81). The calculations indicate that the $S_0 \rightarrow S_1$ transitions are a major result of HOMO to LUMO (60 – 67 %) and HOMO–1 to LUMO (18 – 21 %) transitions in **AπA1a** and **AπA1b**. Concomitant a charge is transferred from one of the two mesityl moieties to the rest of the molecules. The experimentally observed broad and irregular absorption band of **AπA1c** is the result of a superposition of three different transitions, as suggested by the calculations. It can be described as a mixture of HOMO to LUMO, HOMO−1 to LUMO, and HOMO−4 to LUMO transitions. The first transitions mentioned correspond to the charge transfer from mesityl moieties to the AπA scaffold of the molecule, the latter is a result of a π-π* transition of the AπA scaffold.

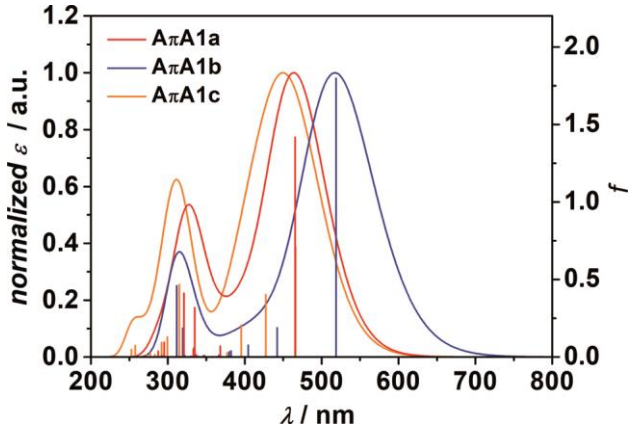

Figure 81. TD-DFT calculated absorption spectra of **AπA1a-c** (CAM-B3LYP/def2-SVP, solvent CH_2Cl_2, PCM model). A half-width of 2000 cm^{-1} was assumed for simulation (GaussView5). Reproduced from reference[273] with permission from Wiley-VCH Verlag GmbH, Copyright 2017.

3.2.3.5 Organic Thin Film Transistors

To gain insight into the charge transport properties of the molecules, organic thin film transistors (OTFTs) were fabricated via vacuum deposition of the compounds on *n*-tetradecylphosphonic acid (TPA) modified $Si/SiO_2/AlO_x$ substrates, in a bottom-gate, top-contact geometry. The mobilities were obtained in the saturation regime and measured under ambient conditions. When **AπA1c** with its small π-scaffold was used as active layer material, no functioning devices could be obtained. However, when the π-scaffold was extended with larger acceptor moieties, as in the case of **AπA1a** and **AπA1b**, the devices showed n-type semiconducting behavior. Devices based on **AπA1a** showed mobilities of 5.55×10^{-4} $cm^2\ V^{-1}\ s^{-1}$, a current on/off ratio of 4×10^3 and a threshold voltage of +1 V. Even better electron transport mobilities of 1.39×10^{-2} $cm^2\ V^{-1}\ s^{-1}$, an on/off ratio of 2×10^6 and a V_T of +6 V were measured for devices of **AπA1b**. The transfer curves and square root plots of the drain-source current of devices with **AπA1a** and **AπA1b** are depicted in Figure 82a. As an example the corresponding output

curve of the device with **AπA1b** is shown in Figure 82b. A large hysteresis can be observed in the transfer curves of both dyes. This could be due to the fact that their LUMO levels are close or even above −4.27 eV, which is claimed as the limit for air stability,[140] so that the radical anions of the dyes might not be perfectly stable.

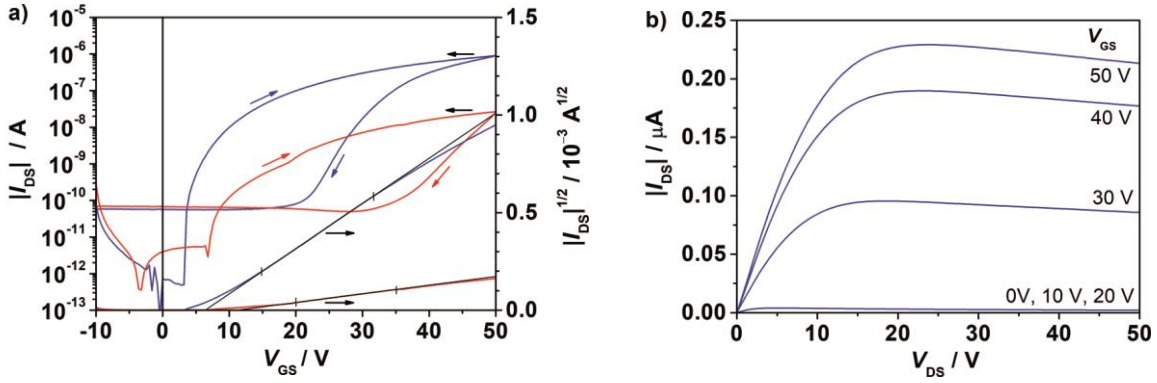

Figure 82. a) Transfer curves (left axis) and square root plots of the drain-source current (right axis) of organic thin film transistors of **AπA1a** (red) and **AπA1b** (blue) in Si/SiO_2/AlO_x/TPA/**AπA**/gold architecture. b) Exemplary output curve of the device with **AπA1b**.

To gain insight into the morphology of the thin films of **AπA1a** and **AπA1b** and its influence on the transistor performance AFM measurements were performed (Figure 83). While **AπA1a** possesses a densely packed and uniform surface morphology, the active layer of **AπA1b** shows a more needle-like structure, indicating higher crystallinity. This might be one reason for the superior mobility found for devices with **AπA1b**.

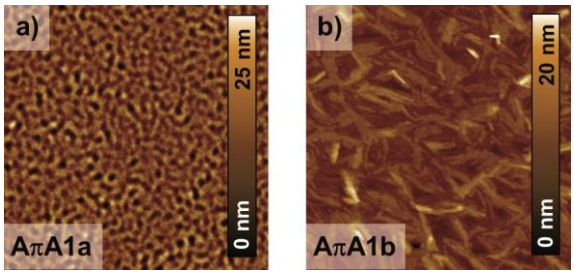

Figure 83. AFM images of a) **AπA1a** and b) **AπA1b** (5 × 5 µm²). Measurements were performed between the two top electrodes of the corresponding transistor devices in Si/SiO_2/AlO_x/TPA/**AπA**/gold architecture.

In addition to morphology charge transport is also influenced by electronic coupling (transfer integral) between two neighboring molecules as well as by reorganization energy (λ). Electronic coupling should be strong and the reorganization energy should be as small as possible to obtain efficient charge transport and high charge carrier mobilities. To reach a better understanding for the differences in electron mobility of the AπA dyes, the inner-sphere reorganization energy (λ_i) was calculated. Values for λ_i of 0.307, 0.235 and 0.266 eV were obtained for **AπA1a**, **AπA1b** and **AπA1c**, respectively. For

comparison, an inner-sphere reorganization energy of 0.276 eV was calculated for Alq_3, which is a common electron transport material. The DCIND substituted dye **AπA1b** has the smallest reorganization energy, which is in agreement with the high electron mobility that has been measured. Even though the reorganization energy of **AπA1c** is smaller than the one of **AπA1a**, no charge transport was observed for the former. These results indicate that the packing arrangement and interactions between adjacent molecules are very important. Thus, a deeper insight onto the crystal structures could be helpful. The relatively small AπA scaffold of **AπA1c** in combination with the bulky mesityl substituents, could prevent a close π-stacking and therefore a good orbital overlap between neighbouring molecules. Indeed, only one-dimensional stacks are observed in the crystal of **AπA1c** (Figure 84a). The molecules are stacked in a slipped fashion, with π-scaffolds being aligned in parallel at a distance of 3.52 Å. The bulkiness of the mesityl groups as well as electrostatic interactions between one acceptor moiety and the thiophene ring of the adjacent molecule (distance 3.41 Å) are the main driving forces for the packing. Even though the crystal of **AπA1a** contains solvent molecules (2.5 molecules toluene per **AπA1a**), it shows the clear tendency of the molecules to pack in a two-dimensional (2D) fashion. This 2D array is built from slipped stacks of parallel-oriented molecules (red; Figure 84b), which show interplanar packing distances of 3.27 Å. The π-π stacking distance between antiparallel-oriented molecules (red and green; Figure 84b) is a little larger (3.32 Å). A molecular overlap can be observed between an acceptor moiety of one molecule and a vinylene bridge with attached acceptor group of the adjacent molecule, resulting in short contacts of 3.34 – 3.39 Å. These stacks interact with neighboring arrays of antiparallel-orientedmolecules over C-H···π

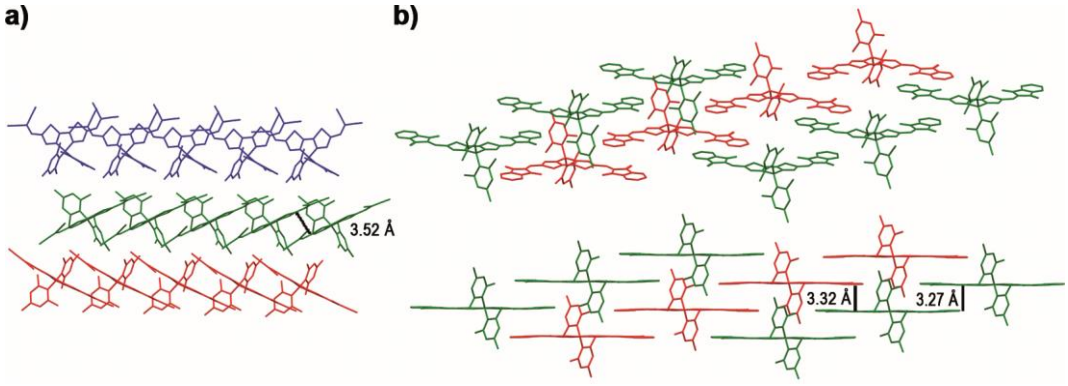

Figure 84. Superordinate packing motives and π-π stacking distances of a) **AπA1c** and b) **AπA1a**. Hydrogen atoms and solvent molecules are omitted for clarity. Reprinted from reference[273] with permission from Wiley-VCH Verlag GmbH, Copyright 2017.

interactions (between indandione C-H and mesityl π-surface) as well as over π-π interactions (between thiophene ring/vinylene bridge and acceptor moiety; short contacts of 3.34 – 3.38 Å). Furthermore, interactions over the acceptor units can be found with both antiparallel oriented molecules (short contacts of 3.36 Å). This indicates good communication between neighboring layers. Consequently, the extended π-surface of **AπA1a** induces a more favorable packing in the solid state, which allows for two-dimensional charge transport and moderate charge carrier mobilities. It is assumed that the same is valid for **AπA1b**, due to the even higher mobilities that were observed. In contrast, close π-π stacking distances in the crystal of **AπA1c** can only be observed in one dimension. This indicates that for films of **AπA1c** a good charge transport can only be expected, when a mono-domain with a suitable orientation between source and drain electrode is formed.

It is worth noticing that both AπA compounds (**AπA1a** and **AπA1b**) show n-type semiconducting behavior in OTFTs, while the charge transport properties of the reference ADA dyes (**ADA2a** and **ADA2b**) are dependent on the choice of acceptor unit (IND vs. DCIND). These results show that the strategy to a) extend the π-scaffold with larger acceptor units and b) to introduce a boron-bridge in the central core of the molecule works well to obtain n-type semiconducting materials. Furthermore, it appears that an extended π-surface in the molecules can compensate for sterically demanding substituents, enabling a good orbital overlap between adjacent molecules. The strategy especially worked out for compound **AπA1b**, which showed electron mobilities as high as 1.39×10^{-2} cm^2 V^{-1} s^{-1} and therefore seems to be a promising candidate for further applications, e.g. as replacement for fullerene acceptors in vacuum processed organic solar cells. Reported electron mobilities of small organoboron molecules, determined by OFET devices or obtained from time-of-flight (ToF) measurements, are typically one order of magnitude lower than the electron mobility observed for **AπA1b**.

3.2.3.6 Conclusion

A set of three AπA molecules was synthesized in appreciable yields via Knoevenagel condensation, which showed attractive properties and high stability. By introduction of a boron-bridge in the central core of the molecules and by variation of the acceptor strengths, the LUMO levels of the AπA dyes could be lowered systematically, falling below the LUMO level of $PC_{61}BM$. Organic thin film transistors were fabricated out of these three vacuum-sublimable molecules to prove the usefulness for application in

organic electronics. Devices based on **AπA1a** and **AπA1b** showed electron transport properties. For the latter compound, electron mobilities of 1.39×10^{-2} cm^2 V^{-1} s^{-1} were found under ambient conditions. This is the highest value for small organoboron compounds that can be found in literature to date. The superior electron transport properties of **AπA1a** and **AπA1b**, bearing π-surface increasing acceptors (IND and DCIND) was attributed to the formation of favorable 2D arrays in the solid state with stronger interchromophoric interactions. In contrast, the dysfunctional devices of **AπA1c** were rationalized by the one-dimensional packing arrangement in the solid state and by larger π-π distances (3.52 Å), being a result of bulky mesityl substituents combined with a small π-surface of the chromophore.

The AπA dyes were not yet investigated in organic solar cells, because they needed to be resynthesized in sufficient amounts and more importantly their solubility and their property to pack closely in the solid state have to be improved. This will be possible by careful fine-tuning of the solubilizing side chains at the boron atom, without weakening the favorable air stability of the dyes. Nevertheless, the comparison of boron-bridged AπA with carbon-bridged ADA dyes revealed that incorporation of a boron atom into the aromatic structure of the central core is a promising way to obtain electron transport materials.

Chapter 4

Summary

In the first part of this thesis known molecules were utilized to test the fabrication and characterization tools that were newly installed in the laboratories of the Center for Nanosystems Chemistry in Würzburg and to establish standard procedures. Furthermore, the influence of ambient conditions on device performance and stability had to be investigated (Figure 85), because our laboratory is technically limited to ambient conditions. The first investigations were performed on small merocyanine dyes, because these had proven to function as electron donors, in combination with $PC_{61}BM$ in organic bulk heterojunction solar cells, under inert conditions.[196] While all merocyanine dyes also yielded operating devices under ambient conditions, their power conversion efficiencies were reduced by about 20 – 40 %, compared to devices fabricated and characterized under inert conditions. This could be attributed to a decrease in short circuit current densities and/or in fill factors. The devicves' parameters could be reproduced reliably, when they were fabricated on the same day, but larger variations were found between different processing days. This was associated with the present relative humidity on the particular processing day. Furthermore, fast degradation of the devices was observed, especially during the initial hours after fabrication. Thus, only poor stability was achieved for the devices when stored under ambient conditions (devices failed completely after about 9 hours). The stability could be improved by storing the cells under dry or inert conditions, so that up to 40 % of initial efficiency could still be

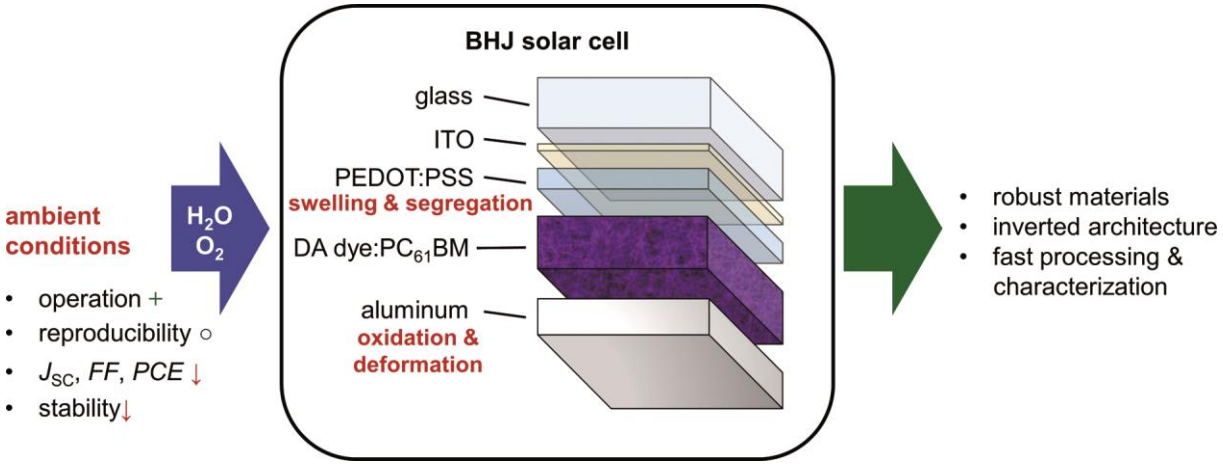

Figure 85. Effect of ambient conditions on DA dye:$PC_{61}BM$ BHJ solar cells.

measured after 9 hours. Again, stability problems were attributed to the presence of humidity, which causes swelling and segregation of the hygroscopic PEDOT:PSS interlayer. Furthermore, mechanical and chemical degradation of the aluminum electrodes was observed. Although the top electrode provides some protection and degradation mainly proceeds from its edges, the exchange of sensitive layers, the utilization of an inverted cell architecture or at least fast processing and characterization are recommended. Even though several drawbacks were observed under ambient conditions, it was possible to successfully establish a procedure for the fabrication and characterization of organic solar cells in our laboratory.

Next, experiments were performed on a system closely related to the initial one, to assure air stability. Instead of using a mixture of merocyanine dye and $PC_{61}BM$ as active layer, the subunits were covalently linked to form donor-acceptor dyads. Thus, only one component was necessary to form the active layer, which does not only simplify processing but also influences the device's function. Optical and electrochemical characterization of the dyads in comparison to the respective merocyanine dye revealed that the absorption is dominated by the latter and that some minor interactions between donor and fullerene acceptor occur. The independent tuning of HOMO and LUMO levels works for the dyads, even though the LUMO is rather fixed in its absolute position, because of the fullerene's modest tunability. Although the dyad molecules yielded functioning devices under ambient conditions, inferior power conversion efficiencies were determined in comparison to the reference devices based on DA dye and $PC_{61}BM$ in a molar ratio of 1:1. One reason for this is most probably a less efficient charge transport due to intimate mixing and the inability of the dyads to form domains of either donor or acceptor components. By thermal annealing or by utilizing a MoO_3 interlayer single component solar cells with power conversion efficiencies of 1.14 % (**Dyad2**) could be achieved in air (Figure 86). During a guest stay in the research group of Prof. Dr. K. Meerholz (Cologne) the single component solar cells were finally optimized under inert conditions. In this way, a power conversion efficiency of 1.59 % was accomplished for **Dyad2** in a glass/ITO/MoO_3/**Dyad2**/Ca/Ag architecture. This value is among the highest reported for single component solar cells to date.

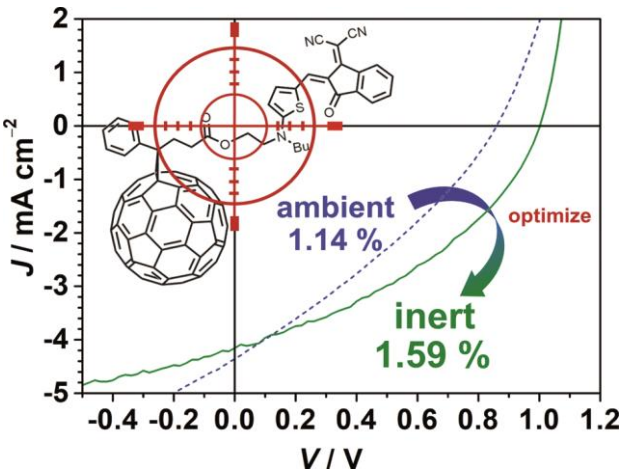

Figure 86. The crosshair was put on DA dye-fullerene dyads. Power conversion efficiencies of 1.14 % could be measured in air and improved to 1.59 % by careful optimization under inert conditions.

In Section 3.2 a series of seven different ADA dyes was successfully synthesized in order to obtain suitable electron acceptor materials that might in the future substitute fullerenes in organic solar cells. The molecules were devised according to the design rules presented in Section 2.3.1, i.e. the donor acceptor approach, the donor core planarization by a bridging atom and the inclusion of heteroatoms. The studied compounds showed strong absorption in the visible range (400 to 700 nm), with molar extinction coefficients of up to 139 × 10^3 M^{-1} cm^{-1}. Furthermore, the frontier molecular orbitals could be modulated systematically by donor and acceptor variation. The utilization of a stronger acceptor unit resulted in a decrease in HOMO and LUMO level of up to 0.3 eV and 0.5 eV, respectively (Figure 87). The most promising components were found when bithienyl donors and DCIND acceptors were combined (**ADA1b**, **ADA2b**). In this way, low band gaps (E_g^{opt} up to 1.86 eV) and low lying LUMO levels were obtained (< −4.10 eV). Additionally, by changing from compound **ADA2a** to **ADA2b** (acceptor group variation) a switching between p- and n-type semiconducting behavior was found. While the former showed hole mobilities in organic thin film transistors of 0.12 cm^2 V^{-1} s^{-1}, the latter compound yielded the desired n-type semiconducting behavior (μ_e = 0.073 cm^2 V^{-1} s^{-1}) under ambient conditions. The usefulness of these series of molecules for application in organic photovoltaics was further corroborated, when functioning PHJ devices of compound **ADA1a** were fabricated (*PCE* up to 1.67 %). Finally, the best performing ADA dye (**ADA2b**) and a better soluble derivative (**ADA2b'**) were investigated in organic solar cells in combination with donor polymers. Interestingly, the difference in solubilizing side chains of **ADA2b** and **ADA2b'** leads to huge differences in processing behavior and solid state packing. The utilization of different donor polymers resulted in

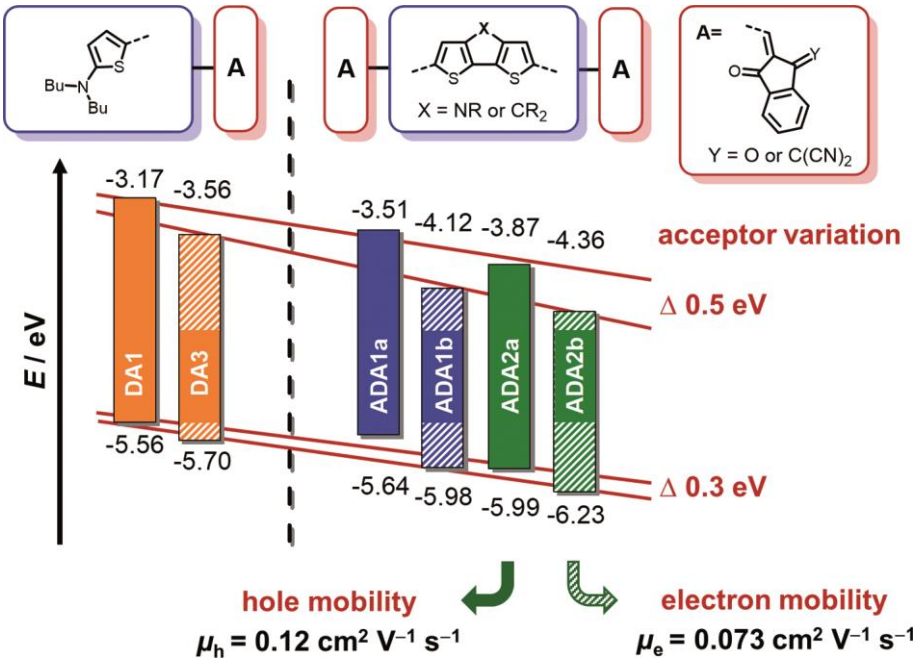

Figure 87. Illustration of the systematic variation of frontier molecular orbitals by acceptor group variation in a series of ADA dyes.

functioning devices with rather low power conversion efficiencies (<0.40 %), being mainly the result of insufficient short circuit current densities caused by strong phase separation. Altogether a series of compounds with very high extinction coefficients in the visible range and systematically tuned HOMO and LUMO levels could be successfully synthesized and investigated. Moreover, a material with sufficient electron transport properties as well as a derivative were found and investigated in organic solar cells, giving a proof of principle. Careful optimization of the molecules' processability will certainly yield highly efficient solar cells in the future.

In order to develop new electron transport materials a boron bridged thienylthiazole, mainly investigated as subunit in polymers, was to be utilized as a central π-bridge in a series of three acceptor-π-acceptor dyes (AπA dyes). The electron poor boron atom in these molecules was supposed to facilitate the electron transport of the dyes (Figure 88). UV/vis spectroscopy revealed that the molecules cover the range from about 400 to 650 nm with moderate extinction coefficients between 35×10^3 and 67×10^3 M^{-1} cm^{-1}. The electrochemical investigations showed that by introducing the boron in the central core and by variation of the acceptor units the LUMO levels of the molecules could be varied effectively. The charge transport behavior of the AπA dyes was probed in vacuum sublimed organic thin film transistor devices. Electron mobilities could be measured for

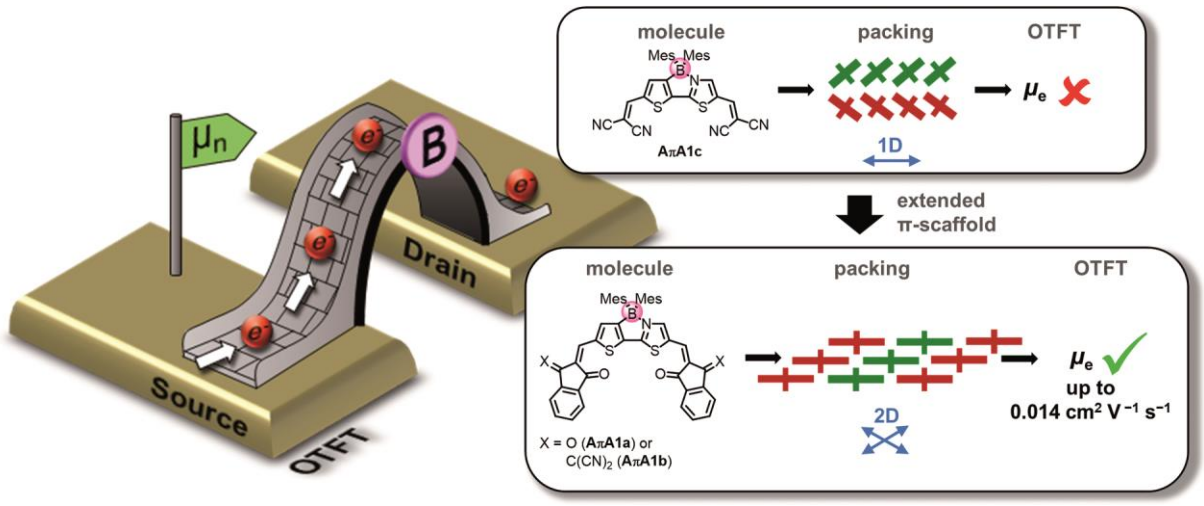

Figure 88. Illustration of the concept used to design the investigated AπA dyes. An electron deficient boron bridge in the central thienylthiazole core of acceptor flanked AπA dyes facilitated the electron transportin organic thin film transistors (OTFTs). Reproduced from reference[273] with permission from Wiley-VCH Verlag GmbH, Copyright 2017.

two of the three compounds in air, reaching values of up to 1.39×10^{-2} cm^2 V^{-1} s^{-1} (**AπA1b**), which is the highest value for small organoboron compounds found in literature to date.[273] The different electron transport propensity of the dyes was explained with the help of single crystal structures. While a larger acceptor unit like 1,3-indandione enables a packing in 2D arrays, a small malononitrile acceptor limits the packing to one dimension, because of the bulky mesityl substituents at the central core. Altogether, by utilizing of a boron bridge in the structure of AπA dyes it was possible to obtain promising and air stable electron transport materials. By variation of the substituents at the boron center that need to ensure stability in air without being too bulky, even higher mobilities will even be possible in the future.

Concluding, this thesis established the fabrication of organic solar cells of DA dye donors and fullerene acceptors under ambient conditions in our laboratory, however, with reduced power conversion efficiencies compared to inert conditions. It was shown that moisture had the strongest impact on the stability and reproducibility of the solar cells. Therefore, utilization of robust materials, inverted device architectures and fast fabrication/characterization are recommended if processing takes place in air. Furthermore, the dyad concept was successfully explored in merocyanine dye-fullerene dyads and power conversion efficiencies of up to 1.14 % and 1.59 % were measured under ambient and inert conditions, respectively. It was determined that the major drawback in comparison to comparable BHJ devices was the inability of the dyad

molecules to undergo phase separation. Finally, two series of small molecules were designed in order to obtain electron transport materials, using the acceptor-core-acceptor motive. By variation of the acceptor units especially the LUMO levels could be lowered effectively. Investigation of the compounds in organic thin film transistors helped to identify promising molecules with electron transport properties. Electron transport mobilities of up to 7.3×10^{-2} cm^2 V^{-1} s^{-1} (**ADA2b**) and 1.39×10^{-2} cm^2 V^{-1} s^{-1} (**AπA1b**) were measured in air for the ADA and AπA dyes, respectively. Investigation of selected molecules in organic solar cells proved that these molecules work as active layer components, even though power conversion efficiencies cannot compete with fullerene based devices yet. Thus, this thesis shows new possibilities that might help to develop and design small molecules as substitutes for fullerene acceptors.

Chapter 5

Zusammenfassung

Im ersten Teil der vorliegenden Dissertationsschrift wurden bereits bekannte Verbindungen genutzt, um neu installierte Geräte zur Herstellung und Charakterisierung von organischen Solarzellen in den Laboratorien des Zentrums für Nanosystemchemie in Würzburg zu testen und um Standardprozeduren zu etablieren. Aufgrund der Limitierung unseres Labors auf Umgebungsbedingen wurden die Experimente auch genutzt, um den Einfluss von Wasser und Sauerstoff auf die Leistungsfähigkeit und Haltbarkeit der organischen Solarzellen zu untersuchen (Abbildung 89). Für die Experimente wurden Merocyaninfarbstoffe in organischen BHJ Solarzellen verbaut, weil diese ihre Funktion als Donormaterialien in Kombination mit $PC_{61}BM$ unter inerten Bedingungen bereits bewiesen hatten.[196] Erfolgreich konnten funktionierende Bauteile von verschiedenen Merocyaninfarbstoffen unter Umgebungsbedingungen gefertigt werden, die allerdings nur verminderte Effizienzen (um ca. 20 bis 40 %) im Vergleich zu unter inerten Bedingungen hergestellten Solarzellen zeigten. Ursächlich dafür waren verminderte Kurzschlussstromdichten und/oder Füllfaktoren. Die auf Merocyaninfarbstoff-Absorbermaterialien basierten Bauteile zeigten eine gute Reproduzierbarkeit, wenn sie an ein und demselben Prozesstag gefertigt wurden. Größere Unterschiede waren zu beobachten, wenn die Herstellung an verschiedenen Prozesstagen stattfand. Dieses Verhalten wurde mit der relativen Luftfeuchtigkeit in Verbindung gebracht, die an dem jeweiligen Prozesstag vorherrschte. Zeitabhängige

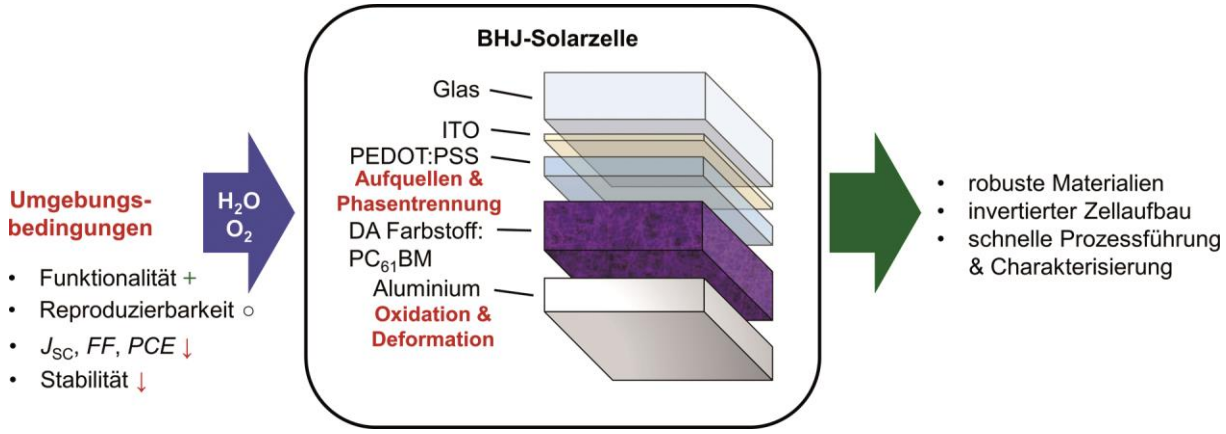

Abbildung 89. Einfluss von Umgebungsbedingungen auf DA-Farbstoff:$PC_{61}BM$ BHJ-Solarzellen.

Messungen der charakteristischen Solarzellenparameter zeigten, dass die Degradation der Solarzellen schnell vonstattengeht, insbesondere während der ersten Minuten nach ihrer Herstellung. Bei der Lagerung der Bauteile unter Umgebungsbedingungen waren die Bauteile nur wenig stabil und funktionierten nicht mehr nach 9 Stunden. Die Stabilität konnte wesentlich verbessert werden, wenn die Bauteile zwischen den Einzelmessungen unter inerten Bedingungen gelagert wurden. In diesem Falle zeigten die Zellen noch 40 % ihrer ursprünglichen Effizienz nach 9 Stunden. Hierbei wurde vor allem die vorherrschende Luftfeuchtigkeit für die verminderte Stabilität verantwortlich gemacht, die ein Aufquellen und Entmischen der hygroskopischen PEDOT:PSS Zwischenschicht verursacht. Außerdem konnte eine mechanische und chemische Alterung der unedlen Aluminiumelektrode beobachtet werden. Wenngleich die Top-Elektrode einen gewissen Schutz gegen Feuchtigkeit bietet, die vornehmlich vom Rand der Elektrode in das Bauteil eindringt, so ist es dennoch empfehlenswert, empfindliche Schichten der Solarzelle auszutauschen, invertierte Zellaufbauten zu nutzen oder zumindest die Bauteile schnell zu prozessieren und zu charakterisieren. Trotz diverser Nachteile unter Umgebungsbedingungen, konnte dennoch eine erfolgreiche Prozedur zur Herstellung und Charakterisierung organischer Solarzellen in unserem Labor etabliert werden.

Weitere Experimente wurden an sehr ähnlichen Systemen durchgeführt, um die Luftstabilität zu prüfen. Bei diesem wurde die aktive Schicht allerdings nicht aus einer Mischung von Merocyaninfarbstoff und $PC_{61}BM$ gebildet, sondern aus Donor-Akzeptor Dyaden, die aus kovalent verknüpftem Merocyaninfarbstoff und Fulleren bestehen. Das heißt, dass die aktive Schicht aus nur einer einzigen Komponente aufgebaut ist, was sowohl den Herstellungsprozess vereinfacht als auch die Funktion der Bauteile beeinflusst. Optische und elektrochemische Untersuchungen der Dyaden zeigten, dass deren Absorptionseigenschaften vom Merocyaninfarbstoff bestimmt werden und dass nur kleine Wechselwirkungen zwischen Fulleren und Farbstoff existieren. Die Untersuchungen zeigten, dass ein unabhängiges justieren der HOMO- und LUMO-Niveaus in den Dyaden möglich ist. Dabei ist zu berücksichtigen, dass das LUMO-Niveau durch die schlechte Modifizierbarkeit der Fullerens tendenziell eher in seiner absoluten Position fixiert ist. Funktionierende Solarzellen konnten mit allen untersuchten Dyaden gebaut werden, allerdings waren die Effizienzen geringer als für die Referenzbauteile bestehend aus DA-Farbstoff und $PC_{61}BM$ in einem molaren

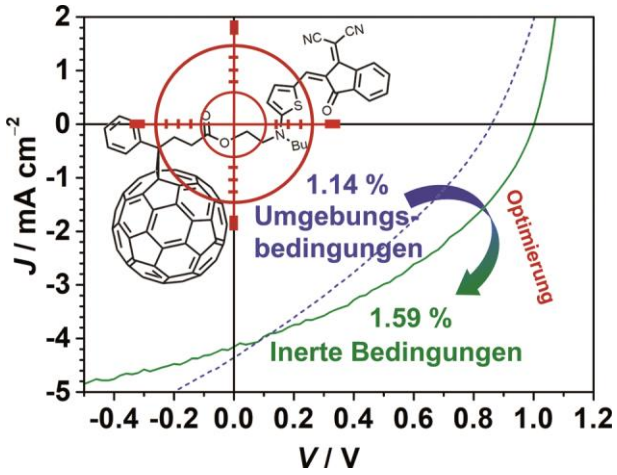

Abbildung 90. DA Farbstoff-Fulleren Dyaden wurden ins Fadenkreuz genommen. Bauteileffizienzen von bis zu 1.14 % wurden unter Umgebungsbedingungen gemessen. Durch sorgfältige Optimierung unter inerten Bedingungen konnte die Effizienz auf 1.59 % gesteigert werden.

Verhältnis von 1:1. Der Grund für diese verminderten Effizienzen ist vermutlich, dass die Dyaden durch die kovalente Verknüpfung von Donor und Akzeptor nicht im Stande sind, separate Domänen in erforderlicher Größe auszubilden. Durch thermische Behandlung der Solarzellen und durch Verwendung einer MoO_3-Zwischenschicht resultierten gesteigerte Effizienzen von 1.14 % (**Dyad2**) unter Umgebungsbedingungen (Abbildung 90). Schlussendlich wurden die Einkomponenten-Solarzellen im Rahmen eines Gastaufenthaltes im Arbeitskreis von Prof. Dr. K. Meerholz (Köln) weiter unter inerten Bedingungen optimiert. Dabei konnten Effizienzen für **Dyad2** von 1.59 % erzielt werden, bei Verwendung einer glass/ITO/MoO_3/**Dyad2**/Ca/Ag Architektur. Dieser Wert gehört zu den höchsten für Einkomponentensolarzellen publizierten.

Abschnitt 3.2 zeigt, wie eine Serie aus sieben verschiedenen ADA-Farbstoffen erfolgreich synthetisiert wurde, um so neue Akzeptormaterialien zu erhalten, die in der Zukunft Fullerene in organischen Solarzellen ersetzen könnten. Die Moleküle wurden mit Hilfe der in Abschnitt 2.3.1 vorgestellten Designregeln entworfen, d.h. sowohl der Donor-Akzeptor-Ansatz, die Planarisierung des zentralen Donorbausteins als auch Heteroatome wurden eingesetzt. Die untersuchten Verbindungen zeigten starke Absorptionskraft im sichtbaren Bereich (400 bis 700 nm) und molare Absorptionskoeffizienten von bis zu $139 \times 10^3\ M^{-1}\ cm^{-1}$ (**ADA1b**). Durch die Variation von Donor und Akzeptorgruppen war es möglich, die Grenzorbitale der Verbindungen systematisch zu variieren, sodass unter Einsatz besonders starker Akzeptoren die HOMO- und LUMO-Niveaus entsprechend um bis zu 0.3 und 0.5 eV gesenkt werden

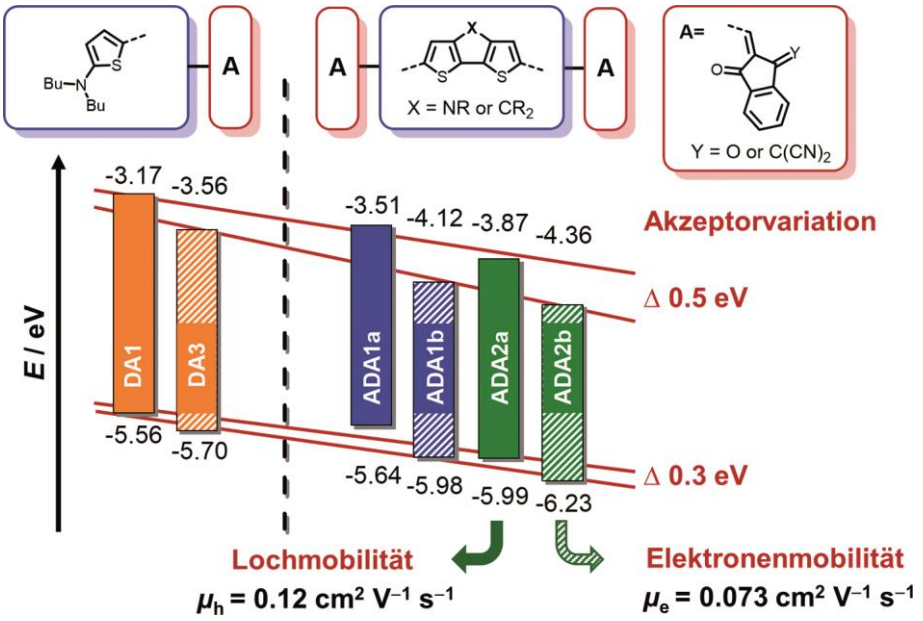

Abbildung 91. Systematische Erniedrigung von HOMO- und LUMO-Energien durch Variation der Akzeptoren in einer Serie von ADA Farbstoffen.

konnten (Abbildung 91). Besonders vielversprechende Moleküle wurden bei Verwendung von bithienylbasierten Donoren in Kombination mit DCIND-Akzeptoren erhalten (**ADA1b**, **ADA2b**), die sich durch geringe Bandlücken (E_g^{opt} bis zu 1.86 eV) und niedrige LUMO-Niveaus auszeichneten (< −4.10 eV). Außerdem konnten durch die Variation der Akzeptorgruppen die halbleitenden Eigenschaften der Moleküle so beeinflusst werden, dass sich ein Übergang von Loch- zu Elektronen-Transportverhalten zwischen Verbindung **ADA2a** und **ADA2b** finden ließ. So wurden in organischen Dünnfilmtransistoren für Verbindung **ADA2a** Lochmobilitäten von 0.12 $cm^2\ V^{-1}\ s^{-1}$ und für **ADA2b** Elektronenmobilitäten von 0.073 $cm^2\ V^{-1}\ s^{-1}$ gemessen. Darüber hinaus konnte die Nützlichkeit der neuen Verbindungen für den Einsatz in der organischen Elektronik weiter bekräftigt werden, indem funktionierende PHJ- Solarzellen von Verbindung **ADA1a** fabriziert wurden (PCE_{max} = 1.67 %). Abschließend wurden die Verbindung **ADA2b** und ein besser lösliches Derivat (**ADA2b'**) ausgewählt, um sie als Akzeptormaterialien kombiniert mit Donorpolymeren in organischen Solarzellen zu untersuchen. Interessanterweise konnte zwischen Verbindung **ADA2b** und **ADA2b'** ein großer Unterschied im Prozessierungsverhalten und in den Packungseigenschaften im Festkörper festgestellt werden, was an den unterschiedlich langen Löslichkeitsresten liegen muss. Durch die Kombination der neuen Akzeptoren mit verschiedenen Donorpolymeren konnten funktionierende Solarzellen hergestellt werden, die allerdings eher niedrige Effizienzen aufwiesen (<0.40 %). Das Hauptproblem lag dabei in einer

starken Phasenseparation, die vor allem geringe Kurzschlussstromdichten zur Folge hatte. Zusammengenommen konnte erfolgreich eine Molekülserie mit systematisch variierten HOMO- und LUMO-Niveaus synthetisiert werden, die sehr gute Lichtabsorption im sichtbaren Bereich zeigte. Darüber hinaus konnte ein vielversprechendes Material mit ausreichenden Elektronentransporteigenschaften identifiziert werden, welches zusammen mit einem besser löslichen Derivat in organischen Solarzellen untersucht werden konnte.

Mit dem Ziel, neue Elektronentransportmaterialien zu entwickeln, wurde ein borverbrücktes Thienylthiazol als zentraler Baustein in einer Serie aus drei Akzeptor-π-Akzeptor Farbstoffen (AπA Farbstoff) eingesetzt. Dieses wurde bisher hauptsächlich als konstitutionelle Repetiereinheit in Polymeren untersucht. Das elektronenarme Boratom in diesem Molekülbaustein sollte eingesetzt werden, um den Elektronentransport in den neuen AπA Materialien zu begünstigen (Abbildung 92).

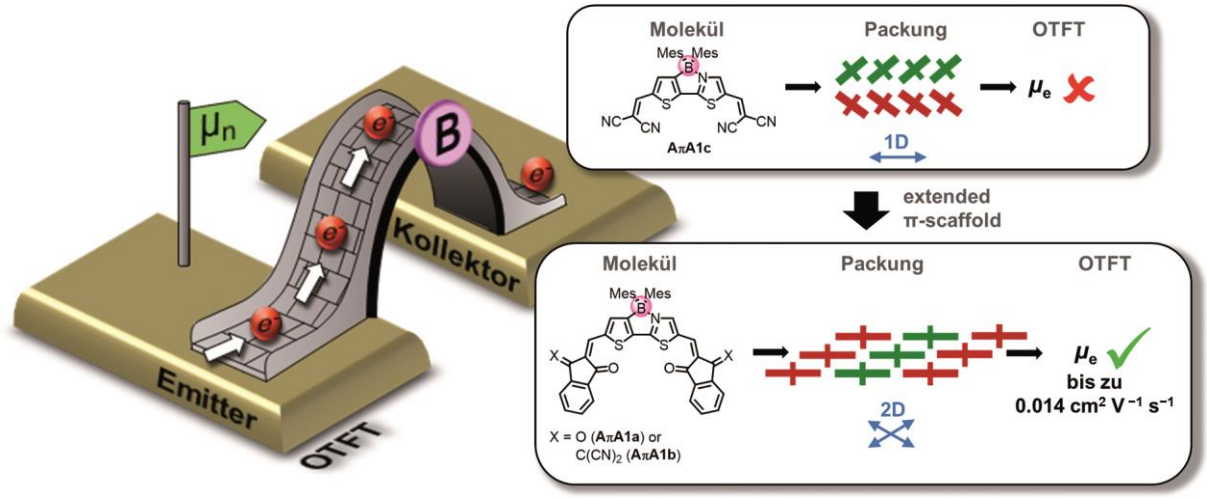

Abbildung 92. Verdeutlichung des Konzeptes zur Entwicklung der untersuchten AπA-Verbindungen. Durch die Verwendung einer elektronenarmen Borverbrückung in einer zentralen Thienylthiazoleinheit, die von Akzeptoren umgeben ist, konnte der Elektronentransport in organischen Dünnfilmtransistoren begünstigt werden.

UV/vis spektroskopische Untersuchungen an den neuen Verbindungen zeigten, dass diese hauptsächlich im Bereich von 400 bis 600 nm absorbieren und molare Extinktionskoeffizienten im Bereich von 35×10^3 bis $67 \times 10^3\,M^{-1}\,cm^{-1}$ aufweisen. Elektrochemische Untersuchungen zeigten, dass sich die LUMO-Niveaus der Moleküle effektiv senken lassen, indem die Akzeptoren variiert wurden und ein Boratom ins Molekülgerüst integriert wurde. Nach der grundlegenden Charakterisierung der Moleküle wurde das Ladungstransportverhalten der AπA-Verbindungen in sublimierten

organischen Dünnfilmtransistoren untersucht. Dabei konnten für zwei der drei Verbindungen Elektronenmobilitäten an Luft von bis zu 1.39×10^{-2} cm^2 V^{-1} s^{-1} (**AπA1b**) gemessen werden.[273] Das ist zur Zeit der höchste Wert, der für kleine bororganische Verbindungen in der Literatur gefunden werden kann. Mit Hilfe von Einkristall-Röntgenstrukturanalysen konnte die Packung im Festkörper für zwei der Verbindungen aufgeklärt werden. Dies erlaubte, die unterschiedlichen Ladungstransport-Eigenschaften der Materialien besser zu verstehen. So zeigte **AπA1c**, das kleine Malononitrilakzeptoren trägt, keinen Ladungstransport, weil der dieser durch das Packungsverhalten und die raumfüllenden Mesitlysubstituenten auf nur eine Dimension beschränkt ist. Die Verwendung von größeren Akzeptoren wie 1,3-Indandione ermöglichte hingegen die Packung in einer zweidimensionalen Anordnung, sodass relativ gute Elektronenmobilitäten gemessen werden konnten. Zusammenfassend konnten durch die Verwendung einer Borbrücke im Molekülgerüst von AπA Farbstoffen luftstabile Elektronentransportmaterialen erhalten werden. Wenn es in Zukunft gelingt die Substituenten am Boratom so zu variieren, dass sie die Stabilität der Verbindungen garantieren ohne sterisch zu anspruchsvoll zu sein, können die Elektronenmobilitäten sicherlich noch weiter verbessert werden.

Zusammenfassend wurde in dieser Arbeit gezeigt, dass die Herstellung und Charakterisierung von organischen Solarzellen auf Basis von kleinen DA-Farbstoffen in Kombination mit Fullerenakzeptoren unter Umgebungsbedingungen möglich ist. Außerdem konnte herausgefunden werden, dass die Luftfeuchtigkeit den größten Einfluss auf die Stabilität und die Reproduzierbarkeit der organischen Solarzellen hat. Aus diesem Grund sind der Austausch labiler Komponenten, die Verwendung von invertierten Bauteilarchitekturen sowie eine zügige Herstellung und Charakterisierung bei Prozessierung an Luft zu empfehlen. In weiteren Experimenten konnte das Dyadenkonzept erfolgreich angewendet werden, sodass sich Effizienzen von 1.14 und 1.59 % unter ambienten bzw. inerten Bedingungen messen ließen. Das Unvermögen der Dyaden, separate Phasen aus Donor- und Akzeptorverbindung zu bilden, konnte als größte Schwäche der Verbindungen ausgemacht werden. Schlussendlich wurden zwei Serien von Molekülen mit der Absicht Elektronentransportmaterialien zu generieren basierend auf einem Akzeptor-Kern-Akzeptor-Strukturmotiv entworfen. Die Variation der Akzeptoren ermöglichte in der Tat eine systematische Absenkung der Grenzorbitale und insbesondere der LUMO-Niveaus. Weiterhin wurden die Verbindungen in

organischen Dünnfilmtransistoren untersucht, um mehr über ihre Ladungstransporteigenschaften zu erfahren. Dabei konnten Moleküle ausgemacht werden, die zum Elektronentransport an Luft in der Lage sind. Für die besten ADA- und AπA-Farbstoffe konnten so jeweils Elektronenmobilitäten von 7.3×10^{-2} cm^2 V^{-1} s^{-1} (**ADA2b**) und 1.39×10^{-2} cm^2 V^{-1} s^{-1} (**AπA1b**) gemessen werden. Weitere Untersuchungen von ausgewählten Verbindungen in organischen Solarzellen, konnten beweisen, dass diese neu kreierten Moleküle im Prinzip als Aktivmaterialien funktionieren können, wenn auch die erzielten Effizienzen noch nicht mit denen von Fulleren-basierten Solarzellen konkurrieren konnten. Damit zeigt diese Arbeit neue Möglichkeiten auf, die bei der Entwicklung und dem Design von kleinen Molekülen als Alternativen zu Fullereneakzeptoren hilfreich sein können.

Chapter 6
Experimental Section

6.1 Methods

6.1.1 UV/vis/NIR Measurements

UV/vis/NIR absorption spectra in solution were recorded using a Lambda 950, Lambda 35 (Perkin-Elmer) or a V-670 (Jasco) spectrometer. Spectra were measured in quartz cuvettes with a thickness of 1 cm at room temperature. Spectroscopic grade solvents from Acros (Geel, Belgium) or Merck (Hohenbrunn, Germany) were used. Extinction coefficients were calculated according to Beer-Lambert law.

UV/vis/NIR spectra of organic solar cells and of thin films on quartz were measured in transmission mode with an integration sphere of a Lambda 950 spectrometer (Perkin-Elmer). Quartz substrates made of Suprasil® (Type: 202-QS) from Hellma Analytics were used.

The transition dipole moment μ_{eg} was calculated form the integral of an isolated absorption band I_{abs} according to Equation 6.1:

$$|\mu_{eg}| = \sqrt{\frac{3I_{abs}}{S}}, \tag{6.1}$$

where S equals:

$$S = \frac{2\pi^2 N_A}{\varepsilon_0 hc \ln 10} = 2.9356 \times 10^{60}\ \text{mol}^{-1}\,\text{C}^{-2}, \tag{6.2}$$

with N_A as Avogadro constant, h as Planck's constant and c as speed of light.

6.1.2 Photoluminescence Measurements

Photoluminescence spectra were recorded in quartz cuvettes with a thickness of 1 cm (Hellma Analytics), using a QM-4/2003 (PTI). Samples were measured under high dilution (OD < 0.05).[280]

6.1.3 Cyclic Voltammetry (CV)

Cyclic voltammograms were measured with an EC epsilon (BAS Instruments). In a three electrode setup an Ag/AgCl electrode was used as reference, a Pt wire was used as auxiliary electrode and a Pt disc electrode (diameter 3 mm) was used as working electrode. Measurements were performed under argon atmosphere in dry dichloromethane (HPLC grade), with NBu_4PF_6 as supporting electrolyte (0.1 M). Compounds were measured in concentrations of about 2.5×10^{-4} M. The ferrocenium/ferrocene redox couple (−5.15 eV vs. vacuum)[206–208] was used as internal standard for calibration of the potential. The internal resistance was compensated by 50 %.

6.1.4 Calculation of HOMO, LUMO and Band Gaps

The optical band gaps E_g^{opt} were calculated as follows:

$$E_g^{opt} = E_{HOMO} - E_{LUMO} = \frac{hc}{\lambda_{max}}. \quad (6.3)$$

The electrochemical band gaps E_g^{CV} were calculated as follows:

$$E_g^{CV} = E_{1/2}^{ox} - E_{1/2}^{red}, \quad (6.4)$$

for compounds showing irreversible oxidation or reduction processes, the appropriate peak potentials were used instead of the half wave potentials $E_{1/2}$.

The HOMO energy levels E_{HOMO} were calculated as follows:

$$E_{HOMO} = -eE_{1/2}^{ox} - 5.15 \text{ eV}. \quad (6.5)$$

The LUMO energy levels E_{LUMO} were calculated as follows:

$$E_{LUMO} = E_{HOMO} + (\frac{hc}{\lambda_{max}}) = E_{HOMO} + E_g^{opt}, \quad (6.6)$$

or

$$E_{LUMO} = E_{HOMO} + E_g^{CV}. \quad (6.7)$$

6.1.5 Differential Scanning Calorimetry (DSC)

Differential scanning calorimetry (DSC) measurements were carried out under nitrogen atmosphere using a DSC Q1000 (TA Instruments) at a heating rate/cooling rate of 10 K min^{-1}. At least two heating-cooling cycles were measured.

6.1.6 Atomic Force Microscopy (AFM)

AFM images were recorded in tapping mode wither with a AXS MultiMode™ Nanoscope IV System (Bruker) or with a SOLVER Next (NT-MDT). Silicon cantilevers OMCL-AC160TS (Olympus) with a resonance frequency of ~ 300 kHz and a spring constant of ~ 40 N m^{-1} were used. The roughness of the surface was characterized by its root-mean square roughness R_{rms} (Equation 6.8), where $N \times N$ is the pixel number, h_{mn} is the measured height of the pixel and $\bar{h}$ is the mean pixel height.

$$R_{rms} = \sqrt{\left[\frac{1}{N^2 - 1}\right] \sum_{mn-1}^{N \times N} \left(h_{mn} - \bar{h}\right)^2}. \tag{6.8}$$

6.1.7 Spin-coating

For cleaning of substrates (wafers, modified wafers & quartz plates) and deposition of PEDOT:PSS the spin 150 (APT) and for active layer preparation the spin 150i (APT GmbH) were used.

6.1.8 UV/ozon Cleaning

An UVO-Cleaner®-Ozone cleaning device $42A - 220$ (Jelight) was used to activate the surface and to remove remaining organic materials from pristine silicon wafers (5 min) and glass/ITO substrates (20 min).

6.1.9 Contact Angle Measurements

Contact angles θ of water on modified silicon wafers were measured with a Drop Shape Analysis System DSA25 (Krüss).

6.1.10 *I-V* Measurements on Organic Thin Film Transistors

OTFTs were characterized using a Micromanipulator 4060 (Micromanipulator) with a Semiconducter Parameter Analyzer 4155C (Agilent). Before contacting the transistor devices, they were electrically isolated by scratching with a needle. Transfer characteristics were measured in the saturation regime at a drain-source voltage of V_{DS} =

|50 V|. Afterwards, the corresponding output curves were measured. The mobility was determined according to the following equation:

$$|-I_{DS}|^{0.5} = \frac{\mu C_i W}{2L}(V_{GS} - V_T), \tag{6.9}$$

where I_{DS} is the drain-source current, μ is the charge carrier mobility, C_i the capacitance of the gate dielectric, W the width, L the length of the transistor channel and V_T the threshold voltage.

6.1.11 *I-V* Measurements on Organic Solar Cells

Laboratory in Würzburg

Current voltage characteristics were measured under ambient conditions using an Oriel Sol3A™ Class AAA Solar Simulator (Newport®) and a parameter analyzer by Botest Systems GmbH.

The basic measurement setup is depicted in Figure 93. The light, produced by a Xe-lamp (500 W), is bundled by a parabolic mirror. To ensure an evenly illuminated sample (100 × 100 mm^2) an integrator is included in the setup. Before the light is focused on the solar substrate, it is filtered by an AM1.5 filter, which basically cuts off the very intense peaks of the Xe-lamp (Figure 94). With the help of an unfiltered, encapsulated monocrystalline silicon solar cell (active area = 4.148 cm^2) the power of the solar simulator is adjusted to match 100 mW cm^{-2}. The solar cell itself was calibrated by the ISE CalLab giving a V_{OC} of 657.3 ± 3.3 mV, an I_{SC} of 144 ± 3.6 mA, a fill factor of 76.2 ± 0.8 % and a power conversion efficiency of 17.4 ± 0.5 %. It was placed at the same position as the test cells and the lamp power was adjusted for matching of measured short circuit current and the

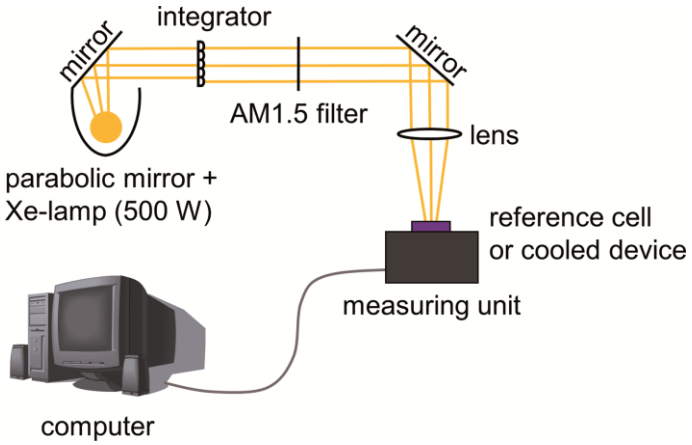

Figure 93. Measurement setup for characterization of organic solar cells.

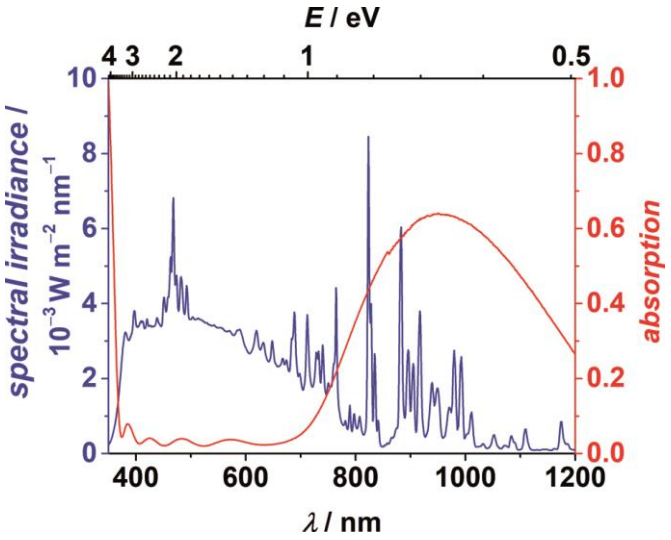

Figure 94. Spectral irradiance of a typical Xe-lamp (blue) and absorption of AM1.5 filter (red).

I_{SC} under calibration. Measurements were performed going from negative (−1.00 V) to positive voltages (−1.50 V) in steps of 20 mV and dark curves were measured first.

Laboratory in Cologne[196]

Current voltage characteristics of the solar cells were measured using a Keithley 2425 source measurement unit. The AM1.5 light was provided by a filtered Xe lamp. The intensity of 100 mW cm^{-2} of the simulated AM1.5 light was determined by using a calibrated inorganic solar cell from the Fraunhofer Institute for solar research (ISE) in Freiburg, Germany and a reference PCBM:P3HT cell measured by the same institute.

Laboratory in Eindhoven[245]

Current voltage characteristics were measured with a Keithley 2400 source meter under 100 mWcm^{-2} white-light illumination from a tungsten–halogen lamp filtered by a Schott GG385 UV filter and a Hoya LB120 daylight filter.

6.1.12 External quantum efficiency (*EQE*) Measurements

Laboratories in Würzburg and Cologne

Spectrally resolved *EQE* measurements were performed with a Quantum Efficiency/IPCE Measurement Kit (Newport®). A 300 W Xe lamp was taken as light source. Monochromatic light was generated by a Cornerstone monochromator. A Merlin Lock-In Amplifier was utilized for detection of the measurement signal, at a chopping frequency of 30 Hz. As reference a calibrated Si-detector was used.

The basic measurement setup is depicted in Figure 95. The generated light is guided to a filter wheel by the help of a lens. This is done because the spectral irradiance of the Xe lamp differs strongly with the wavelength (Figure 94). A monochromator is installed in the light path, which enables the measurement of spectrally resolved *EQE* curves. The monochromatic light is coupled into a fibre-optic cable. From there it either irradiates the calibrated silicon detector (reference scan) or the solar cell under test (*EQE* measurement). A Lock-In Amplifier is used for all measurements (chopper at 30 Hz). This is necessary because of the use of monochromatic light and concomitant low light intensities and measuring signals. Furthermore, due to the absence of bimolecular recombination at low light intensities (≠ *I-V* measurements), the *EQE* is likely to be overestimated.[216] Measurements in Würzburg were performed in air but under inert conditions in Cologne.

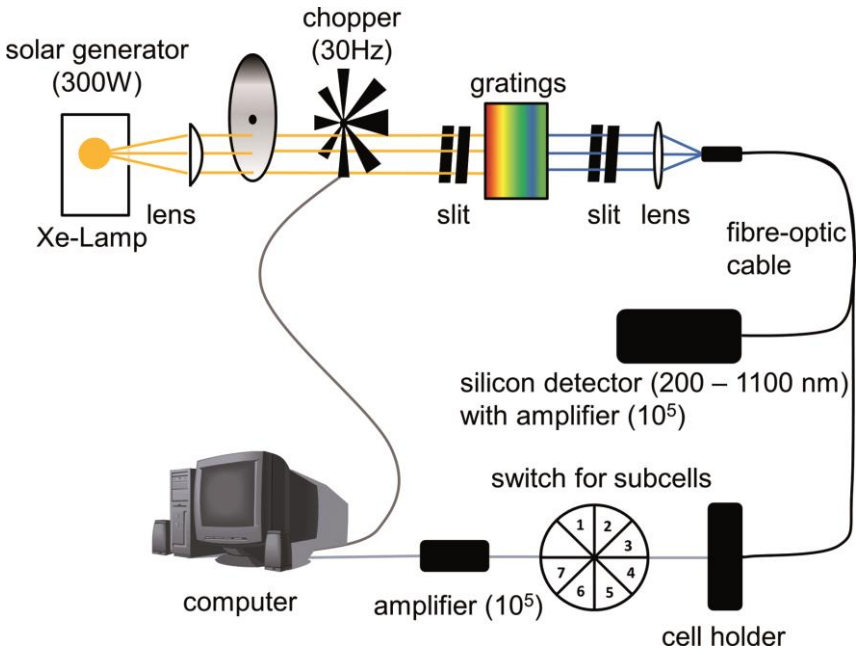

Figure 95. Schematic illustration of the *EQE* measurement setup.

Laboratory in Eindhoven[245]

Spectral response measurements were conducted under 1 sun operating conditions by using a 532 nm solid state laser (Edmund Optics) for bias illumination. The device was kept in a nitrogen filled box behind a quartz window and irradiated with modulated monochromatic light, from a 50 W tungsten-halogen lamp (Philips focusline) and monochromator (Oriel, Cornerstone 130) with the use of a mechanical chopper. The response was recorded as a voltage over a 50 Ω resistor using a lock-in amplifier (Stanford research Systems SR830). A calibrated silicon cell was used as reference.

6.2 Density Functional Theory (DFT) Based Calculations

Gaussian 09 program package[281] was used to perform DFT calculations. The B3LYP functional was utilized in combination with a def2-SVP[282] basis set. Chemical structures of the compounds were geometrically optimized and frequency calculation were performed to prove the existence of a minimum. Calculations were performed for the gas phase (ADA dyes; Section 3.2.1) or using the polarizable continuum model (PCM model; CH_2Cl_2; AπA dyes; Section 3.2.3). Time-dependent (TD)-DFT calculation were performed on the optimized structures of AπA dyes, using the coulomb-attenuating method (CAM)-B3LYP in combination with the def2-SVP basis set, to simulate the UV/vis absorption spectra of the AπA dyes. Spectra were simulated with the GaussView 5 visualization software package.[283] For proper simulation of the UV/vis spectra a half-width of 2000 cm^{-1} was assumed.

6.3 Single Crystal X-Ray Diffraction Experiments

Single crystal X-ray diffraction measurements of **1a** and **AπA1a** were measured on a D8 Quest Kappa Diffractometer (Bruker) with a Photon100 complementary metal-oxide-semiconductor (CMOS) detector at 100 K, working with Cu K_α radiation (0.15418 nm). Crystals of **AπA1c** were measured on X8APEX-II diffractometer (Bruker) with a charge-coupled device (CCD) area detector, using Mo K_α radiation (0.07107 nm). The obtained crystal structures were solved using direct methods, expanded by Fourier techniques and refined with the Shelx software package.[284] Anisotropical refinement was performed on non-hydrogen atoms, while hydrogen atoms were included in the structure factor calculation on geometrically idealized positions.

Crystal data for **1a** ($C_{36}H_{29}NO_4S_2$):
M = 603.72 g mol^{-1}, green needle, 0.460 × 0.070 × 0.066 mm^3, monoclinic space group $P2_1/n$, a = 15.7449(4) Å, α = 90 °, b = 8.5796(2) Å, β = 110.0330(1) °, c = 22.7812(6) Å, γ = 90 °, V = 2891.20(1) $Å^3$, Z = 4, $\rho(calcd.)$ = 1.387 g·cm^{-3}, μ = 2.018 mm^{-1}, $F_{(000)}$ = 1264, $GooF(F^2)$ = 1.034, R_1 = 0.0386, wR^2 = 0.0963, for I > 2σ(I), R_1 = 0.0429, wR^2 = 0.0989 for all data, 5709 unique reflections [$\theta \leq 67.679°$] with a completeness of 99.8 % and 425 parameters, 25 restraints.

Crystal data for **AπA1a** (2 $C_{45}H_{34}BNO_4S_2 \cdot 5\ C_7H_8$):
M = 1915.99 g mol^{-1}, orange block, 0.50 × 0.46 × 0.44 mm^3, triclinic space group $P\bar{1}$, a = 13.0930(7) Å, α = 73.1250(10) °, b = 14.3404(7) Å, β = 70.3680(10) °, c = 15.8959(8) Å, γ = 67.0580(10) °, V = 2544.7(2) Å^3, Z = 1, ρ(*calcd.)* = 1.250 g·cm^{-3}, μ = 1.338 mm^{-1}, $F_{(000)}$ = 1010, *GooF*(F^2) = 1.056, R_1 = 0.0392, wR^2 = 0.0999 for I > 2σ(I), R_1 = 0.0404, wR^2 = 0.1009 for all data, 10015 unique reflections [θ ≤ 72.481°] with a completeness of 99.2 % and 749 parameters, 151 restraints.

Crystal data for **AπA1c** ($C_{33}H_{26}BN_5S_2$):
M = 567.52 g mol^{-1}, orange block, 0.148 × 0.143 × 0.095 mm^3, tetragonal space group $P\bar{4}2_1c$, a = 26.5145(7) Å, α = 90 °, b = 26.5145(7) Å, β = 90 °, c = 7.9461(2) Å, γ = 90 °, V = 5586.3(3) Å^3, Z = 8, $\rho(calcd.)$ = 1.350 g·cm^{-3}, μ = 0.224 mm^{-1}, $F_{(000)}$ = 2368, *GooF*(F^2) = 1.039, R_1 = 0.0404, wR^2 = 0.0941 for I > 2σ(I), R_1 = 0.0506, wR^2 = 0.0993 for all data, 5507 unique reflections [θ ≤ 26.036°] with a completeness of 99.9 % and 376 parameters, 0 restraints.

6.4 Sample Preparation

6.4.1 Preparation of Organic Solar Cells

6.4.1.1 General Procedures (Laboratory in Würzburg)

Cell Geometry

Figure 96 illustrates the solar cell geometry used in Würzburg. A continuous ITO pattern

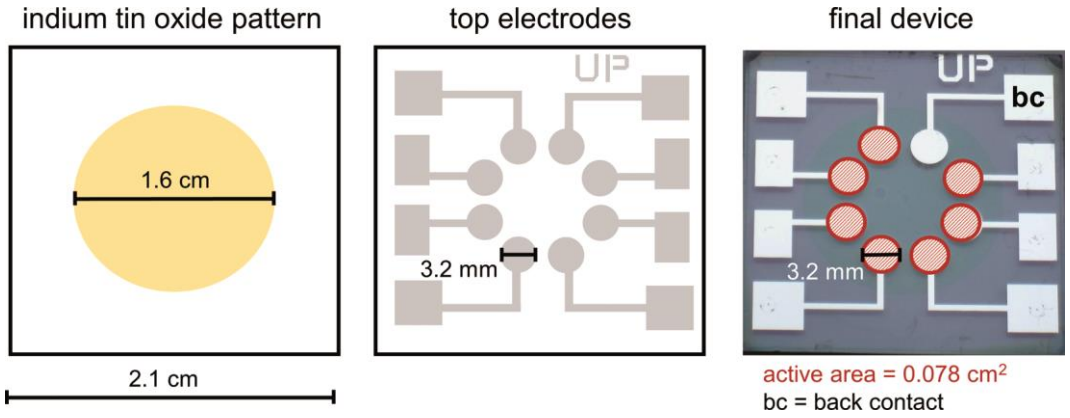

Figure 96. Solar cell geometry of devices prepared in this thesis. a) Pattern of ITO electrodes, b) shape of top electrodes and c) final device consisting of seven sub cells with active area size of 0.078 cm^2. One sub cell is used to realize a connection to the ITO back contact.

and round top electrodes were used, defining round solar cells. The active layer as well as the interlayers were positioned in between the ITO and the top electrodes. The final device contains eight sub cells with active layer sizes of 0.078 cm^2. However, one sub cell was used as back contact to the ITO.

Cleaning Procedure of ITO Substrates

The purchased glass/ITO substrates (sheet resistance of ~15 Ω sq^{-1}) were washed with detergent and DI-water. Then they were put in an ultrasonic bath with *i*PrOH (5 min) and then with acetone (5 min). Additional washing with *i*PrOH and acetone was performed, using the spin coater (30s, 3000 rpm, 3000 rpm s^{-1}). Finally, the substrates were treated in the UVO cleaner for 10 minutes.

Preparation of PEDOT:PSS Interlayers

A cleaned ITO substrate was used. PEDOT:PSS solution (Heraeus) was warmed to RT and filtrated through a 45 μm polyvinylidene difluoride (PVDF) syringe filter. The layer was spin coated with 2000 rpm, 4000 rpm s^{-1} for 30 s. Finally, the PEDOT:PSS layer (~ 40 nm) was annealed for 10 minutes at 150 °C under argon atmosphere.

Preparation of MoO_3 Interlayers

10 nm of MoO_3 were evaporated on top of the ITO layer at a source temperature of 370 °C, a pressure of 10^{-6} mbar and with a rate of 0.8 – 1.2 Å s^{-1}.

Preparation of Top Contact

For the deposition of aluminum electrodes, the EVAP 300 (CreaPhys) was used. At a pressure of about 2×10^{-6} mbar, ~120 mg of aluminum were sublimed from a ceramic crucible. The first 10 nm were evaporated against the shutter, then the deposition onto the substrate was started. The evaporation rate was 0.3 Å s^{-1} for the first 10 nm, then it was increased to 0.5 Å s^{-1} for the next 15 nm. The final thickness of the electrodes (100 nm) was reached with a rate of 1 Å s^{-1}.

6.4.1.2 General Procedures (Laboratory in Cologne)

Cell geometry

Due to a long-term collaboration with the research group of Prof. Dr. K. Meerholz, the cell geometry in Würzburg could be adopted from them (see Figure 96).

Cleaning Procedure for ITO Substrates

The ITO substrates were cleaned using a UVO cleaner (10 min). Storage of the subtrates takes place under dust free conditions (Flow box).

Preparation of PEDOT:PSS Interlayers

The PEDOT:PSS layers (~ 45 nm) were prepared under ambient conditions, inside of the flow box. The PEDOT:PSS was filtrated (0.45 µm PVDF) before spin coating: (1) 2500 rpm, 4000 rpm s^{-1}, 25 s; (2) 4000 rpm, 4000 rpm s^{-1}, 5 s. The devices were dried (flow box) for 10 minutes at 150 °C. The warm substrates were brought into the glove box.

Preparation of MoO_3 Interlayers

15 nm of MoO_3 were evaporated on top of the ITO layer at a pressure of 10^{-6} mbar, with a rate of 0.5 Å s^{-1}.

Preparation of Ca Interlayers

5 nm of Ca were evaporated on top of the active layer at a pressure of 10^{-6} mbar, with a rate of 0.3 Å s^{-1}.

Preparation of Top Contact

Silver was used as electrode material and directly evaporated after Ca deposition. The first 10 nanometers were evaporated at a rate of 0.5 Å s^{-1}, then the rate was increased to 2 Å s^{-1} until a total thickness of 150 nm was reached. The pressure was 10^{-6} mbar.

6.4.1.3 General Procedures (Laboratory in Eindhoven)

Cell geometry

Figure 97 illustrates the solar cell geometry used in Eindhoven. The ITO pattern and the top electrodes define quadratic solar cells in two different sizes. The active layer as well

as possible interlayers are positioned in between the ITO and the top electrodes. The final device contains four sub cells with active layer sizes of 0.09 and 0.16 cm^2, respectively.

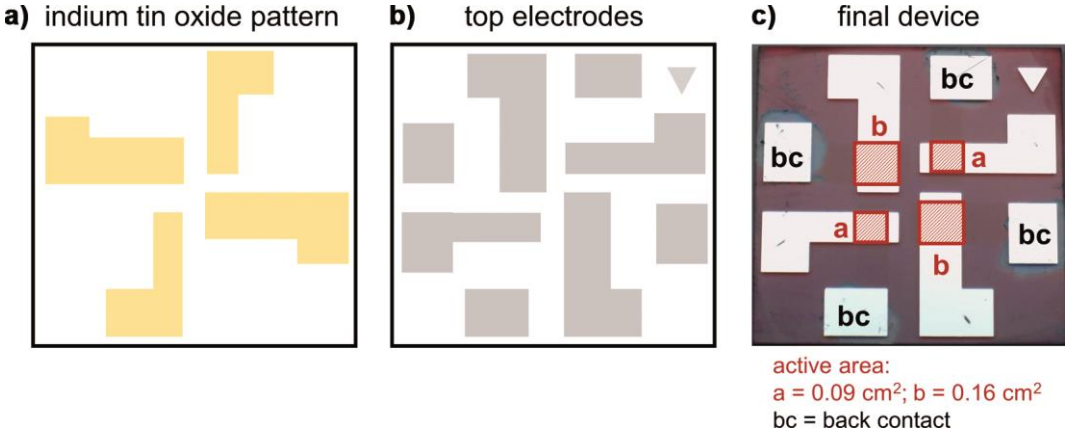

Figure 97. Solar cell geometry of devices prepared at the university of Eindhoven. a) Pattern of ITO electrodes, b) shape of top electrodes and c) final device consisting of four sub cells with active area size of 0.09 cm^2 (a) and 0.16 cm^2 (b).

Cleaning of ITO Substrates

The substrates were sonicated for 15 min in acetone. After manual cleaning with aqueous dodecyl sulfate solution (about 3 g in 300 ml water), the substrates were rinsed with DI-water for 15 min and afterwards sonicated for 15 min in *i*PrOH. After drying in nitrogen flux at RT, they were treated in an UVO cleaner for 30 minutes.

Preparation of Hole Collecting Contact

The PEDOT:PSS layers were prepared under ambient conditions at RT. Before spin coating at 3000 rpm for 60 s, the suspension was filtrated (0.45 µm PVDF).

Preparation of Electron Collecting Contact

1 nm of LiF was evaporated on top of the active layer at a pressure of 10^{-6} mbar, at a rate of 0.2 Å s^{-1}.

Preparation of Top Contact

Aluminum was used as electrode material and directly evaporated after LiF deposition. The first ten nanometers were evaporated at a rate of 2 Å s^{-1}, then the rate was increased to 5 Å s^{-1} until a total thickness of 100 nm was reached. The pressure was ~10^{-6} mbar.

Solvent Vapor Annealing

Solvent vapor annealing (SVA) was performed in a petri dish at RT. The substrates were placed on a screw cap, the active layer was facing upwards, and 200 µl of appropriate

solvent were evenly distributed in a circle around the sample. When the lid was closed the time measurement was started.

Thermal Annealing

Thermal annealing (ΔT) of the complete devices was performed on a hot plate, inside of a nitrogen filled glove box. Before measurement the devices were allowed to cool down on a metal plate.

6.4.1.4 Experimental Details for Active Layer Preparation

General

The blends were weighed in gravimetrically with the help of an analytical balance (Mettler Toledo), according to the given donor to acceptor ratio (±1 %). Vessels with teflon sealed caps were used. The appropriate solvent was added, using an Eppendorf pipette. The blend was stirred for 2 h at 50 °C (unless stated otherwise). Typically, the blends were filtrated using polytetrafluoroethylene (PTFE) syringe filters (0.22 μm) and cooled to RT before spin-coating (unless stated otherwise). The concentrations given represent the total concentration of donor and acceptor in mg ml^{-1}.

DA Dyes under Ambient Conditions (Section 3.1.1)

Table 23. Experimental parameters for DA dye-based solar cells of glass/ITO/PEDOT:PSS/**DA dye:PC_{61}BM**/Al architecture, based on literature.[196] Solar cells were fabricated under ambient conditions.

donor	acceptor	donor:acceptor	solvent	*c* [mg ml^{-1}]	spin speed [rpm]
DA1 (**MD352**)	PC_{61}BM	30:70	CB	20	1000
DA2 (**MD333**)	PC_{61}BM	30:70	CB	20	1000
DA3 (**EL86**)	PC_{61}BM	40:60	CB	20	1000
DA3' (**HB366**)	PC_{61}BM	45:55	$CHCl_3$ [a]	10	1000
DA4 (**HB238**)	PC_{61}BM	25:75	CB	20	1000
DA5 (**MD357**)	PC_{61}BM	30:70	CB	20	1000

[a] not enough soluble in chlorobenzene.

Table 24. Experimental parameters for all reproducibility and stability experiments. The devices were all prepared in a glass/ITO/PEDOT:PSS(35nm)/**blend/**Al(100nm) architecture using the same experimental parameters.

donor	acceptor	donor:acceptor	solvent	*c* [mg ml^{-1}]	spin speed [b, c] [rpm]
DA3' (HB366)	$PC_{61}BM$	45:55	$CHCl_3$	10	1000

DA Dye-Fullerene Dyad Solar Cells under Ambient Conditions (Section 3.1.2.3)

Table 25. Experimental parameters for dyad and DA dye:$PC_{61}BM$ based solar cells of glass/ITO/ PEDOT:PSS(~40nm)/**active layer**/Al(120nm) architecture. Thermally annealed devices of **Dyad1-3** were prepared accordingly. Thermal annealing was performed at 150°C for 1 min, before back contact preparation.

active layer	donor:acceptor [mol/mol]	solvent	*c* [mg ml^{-1}]	spin speed [rpm]
Dyad1	–	$CHCl_3$	10	1000
Dye1:$PC_{61}BM$	1:1	$CHCl_3$	10	1000
Dyad2	–	$CHCl_3$	10	1000
Dye2: $PC_{61}BM$	1:1	$CHCl_3$	10	1000
Dyad3	–	$CHCl_3$	10	1000
Dye3: $PC_{61}BM$	1:1	$CHCl_3$	10	1000

Table 26. Experimental parameters for dyad based solar cells of glass/ITO/MoO_3(10 nm)/**dyad**/ Al(120nm) architecture.

active layer	interlayer	solvent	*c* [mg ml^{-1}]	spin speed [rpm]
Dyad1	MoO_3	$CHCl_3$	10	1000
Dyad2	MoO_3	$CHCl_3$	10	1000
Dyad3	MoO_3	$CHCl_3$	10	1000

DA Dye-Fullerene Dyad Solar Cells under Inert Conditions (Section 3.1.2.4)[††]

Table 27. Experimental parameters of dyad based solar cells of glass/ITO/PEDOT:PSS(~45nm)/**dyad**/ Ca(5nm)/Ag(150nm) architecture, using different solvents for active layer preparation.

active layer	solvent	*c* [mg ml^{-1}]	spin speed [rpm]
Dyad1	$CHCl_3$	10	1000
	CB	20	1000
Dyad2	$CHCl_3$	10	1000
	CB	20	1000

Table 28. Experimental parameters of dyad based solar cells of glass/ITO/PEDOT:PSS(~45nm)/**Dyad2**/ Ca(5nm)/Ag(150nm) architecture, for variation of active layer thickness.

active layer	solvent	*c* [mg ml^{-1}]	spin speed [rpm]
Dyad2	$CHCl_3$	10	400
	$CHCl_3$	10	550
	$CHCl_3$	10	700
	$CHCl_3$	10	850
	$CHCl_3$	10	1000
	$CHCl_3$	10	1250
	$CHCl_3$	10	1600
	$CHCl_3$	10	2200
	$CHCl_3$	10	3000
	$CHCl_3$	10	4000

Table 29. Experimental parameters of optimized devices of glass/ITO/MoO_3(15nm)/**dyad**/ Ca(5nm)/Ag(150nm) architecture.

active layer [a]	solvent	*c* [mg ml^{-1}]	spin speed [rpm]
Dyad1	$CHCl_3$	10	1500
Dyad2	$CHCl_3$	10	1300

[a] The active layer was not thermally annealed, because degradation was observed in combination with MoO_3 interlayer.

[††] Investigation of dyad molecules under inert conditions was performed in collaboration with the research group of Prof. Dr. K. Meerholz under supervision of Dr. M. R. Lenze at the Institut für Physikalische Chemie of the Universität zu Köln.

ADA1a Donor C_{60} Acceptor PHJ Solar Cells (Section 3.2.1.4)

Table 30. Experimental parameters for glass/ITO/PEDOT:PSS(35nm)/**ADA1a**/C_{60}(30nm)/Al(100nm) PHJ devices.

donor	solvent	*c* [mg ml^{-1}]	spin speed [rpm]
ADA1a	$CHCl_3$	2	3000

Donor Polymer ADA Acceptor Solar Cells (Section 3.2.2)‡‡

Table 31. Experimental parameters for glass/ITO/PEDOT:PSS(~40nm)/**blend**/LiF(1nm)/Al(100nm) devices, utilizing different donor polymers.

donor	acceptor	donor:acceptor	solvent	*c* [mg ml^{-1}]	spin speed [a] [rpm]
PPDTNBT	**ADA2a**	1:2 [b]	$CHCl_3$	12	2000
PPDTNBT	**ADA2b'**	1:2 [b]	$CHCl_3$	12	2000
BDT-FBT-C32	**ADA2a**	1:2 [c]	CB	16	2000
BDT-FBT-C32	**ADA2b'**	1:2 [c]	CB	16	2000
PCDTBT	**ADA2a**	1:3 [c]	CB	18	2000 [d]
PCDTBT	**ADA2b'**	1:3 [c]	CB	18	2000 [d]

[a] No filtration of blend was performed. [b] Blend was stirred over night at 100 °C. [c] Blend was stirred over night at 70 °C. [d] The hot solution was spin coated.

Table 32. Experimental parameters for glass/ITO/PEDOT:PSS(~40nm)/**PDPP3T:acceptor**/LiF(1nm)/ Al(100nm) devices, with different donor to acceptor ratio.

donor	acceptor	donor:acceptor [a]	solvent	*c* [mg ml^{-1}]	spin speed [b, c] [rpm]
PDPP3T	**ADA2b**	2:1	$CHCl_3$	10	2000
		1:1	$CHCl_3$	10	2000
		1:2	$CHCl_3$	10	2000
		1:3	$CHCl_3$	14	2000
		1:4	$CHCl_3$	15	2000
PDPP3T	**ADA2b'**	2:1	$CHCl_3$	10	2000
		1:1	$CHCl_3$	10	2000
		1:2	$CHCl_3$	10	2000

[a] Blend was stirred for 1 h at 90 °C. [b] Cooling of blend for 2 min prior to spin-coating; spin-coating duration: 60 s. [c] No filtration of blend was performed.

‡‡ The investigation of the ADA acceptor molecules in combination with donor polymers was performed in collaboration with the Molecular Materials and Nanosystems group of Prof. Dr. R. A. J. Janssen under supervision of Dr. K. Hendriks at the Department of Applied Physics of the Technische Universiteit Eindhoven.

Table 33. Experimental parameters for glass/ITO/PEDOT:PSS(~40nm)/**PDPP3T:acceptor**/LiF(1nm)/ Al(100nm) devices, with and whithout diiodooctane (DIO) as additive.

donor	acceptor	additive	donor:acceptor [a]	solvent	*c* [mg ml^{-1}]	spin speed [b, c] [rpm]
PDPP3T	**ADA2b**	–	1:2	$CHCl_3$	12	2000
		2vol% DIO	1:2	$CHCl_3$	12	2000
PDPP3T	**ADA2b'**	–	1:2	$CHCl_3$	12	2000
		2vol% DIO	1:2	$CHCl_3$	12	2000

[a] Blend was stirred for 1 h at 90 °C. [b] Cooling of blend for 2 min prior to spin-coating; spin-coating duration: 60 s. [c] No filtration of blend was performed.

Table 34. Experimental parameters for glass/ITO/PEDOT:PSS(~40nm)/**PDPP3T:acceptor**/LiF(1nm)/ Al(100nm) devices, before and after post treatment.

donor	acceptor	annealing [a]	donor:acceptor [b]	solvent	*c* [mg ml^{-1}]	spin speed [c, d] [rpm]
PDPP3T	**ADA2b**	–	1:1	$CHCl_3$	10	2000
PDPP3T	**ADA2b'**	–	1:1	$CHCl_3$	10	2000
		SVA, $CHCl_3$, 1min	1:1	$CHCl_3$	10	2000
		SVA, CB, 1min	1:1	$CHCl_3$	10	2000
		Δ*T*, 100 °C, 1min	1:1	$CHCl_3$	10	2000

[a] Solvent vapor annealing (SVA); thermal annealing (Δ*T*). [b] Blend was stirred for 1 h at 90 °C. [c] Cooling of blend for 2 min prior to spin-coating; spin-coating duration: 60s. [d] No filtration of blend was performed.

6.4.2 Preparation of Organic Thin Film Transistors (OTFT)

6.4.2.1 General Procedures

All OTFTs were prepared in a bottom-gate, top-contact configuration by vacuum deposition of the organic materials (Figure 98). Si (100) wafers were used as substrates.

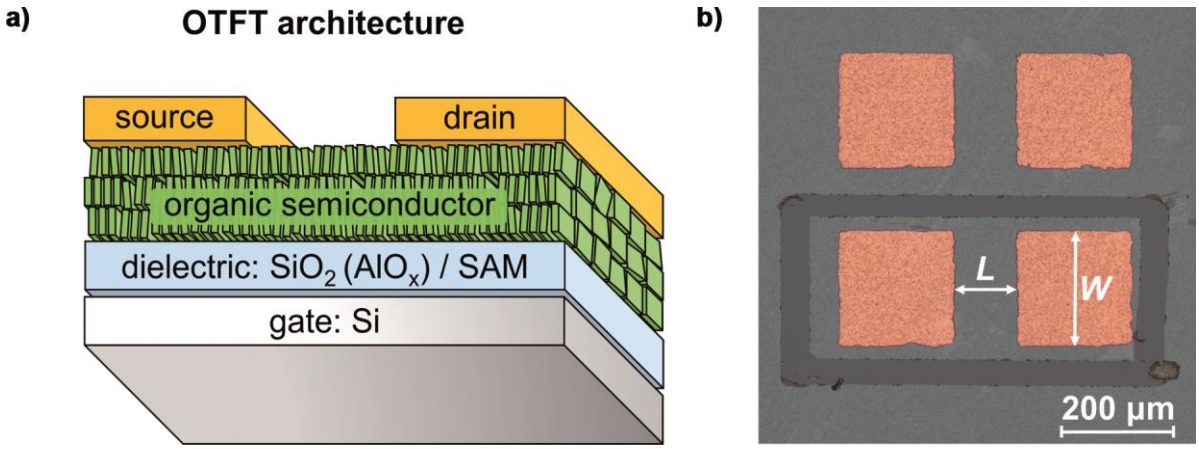

Figure 98. a) Illustration of the device architecture of an organic thin film transistor in bottom-gate, top-contact configuration. b) Light microscope image of two gold electrodes forming an organic thin film transistor. Uninsulated (top) and by scratching electrically insulated transistor device (bottom). *L* and *W* are the channel length *L* (100 µm) and channel width *W* (200 µm), respectively.

The dielectric is formed by SiO_2 (100 nm) and in some cases this surface was modified by a self-assembled mono layer (SAM). Source and drain contacts of gold were evaporated onto the organic thin films through a shadow mask. The channel length *L* and width *W* were 100 and 200 μm, respectively. More experimental details can be found below.

Substrates and Substrate Preparation

Heavily doped silicon (100) wafers (Si-Mat; σ = 0.01 – 0.02 Ω cm) with SiO_2 gate dielectric (100 nm; C_i = 34.0 nF cm^{-2}) were used as substrates. Based on these wafers modified substrates were fabricated:

- *n*-Octadecyltriethoxysilan (OTES) substrates:
  The pristine wafer substrates were cleaned and activated for 30 minutes in a freshly prepared piranha solution (sulfuric acid (95 %):hydrogen peroxide (30 %) = 7:3). The wafer was ultra-sonicated in demineralized water for five minutes and washed with water on a spin-coater (5000 rpm, 1 min). A solution of OTES in trichloroethylene (3 mM) was prepared and filtered twice (0.22 μm, PTFE). The wafer was covered with this solution for 10 s before spin-coating at 3000 rpm for 30 s. Afterwards, the wafers are stored for 12 h in a desiccator over ammonia solution. Finally, the excess of molecules is removed by sonication in toluene for six minutes.
- Hexamethyldisilazane (HMDS) substrates
  The pristine wafers were cleaned according to the standard procedure (see below). HMDS was filtered (0.22 μm, PTFE) and given on the substrate. After 10 s the spin-coater was started at 3000 rpm for 30 s to remove the excess of HMDS. The resultin monolayer is 2.1 nm thick.

Two additional monolayers were used frequently. These monolayers were produced at the Max Planck Insitut in Stuttgart and were kindly provided by Dr. Hagen Klauk. The preparation of these monolayers afforded additional modification of the Si/SiO_2 substrates. To this end, a layer of AlO_x (3.6 nm) was created by first applying a 20 nm thick aluminum layer on top of the substrate (atomic layer deposition) and secondly exposing the sample to an oxygen plasma. The monolayers themselves are based on tetradecylphosphonic acid (TPA) and 12,12,13,13,14,14,15,15,16,16,17,17,18,18, 18H-Pentadecylfluorooctadecylphos-phonic acid (FOPA). Preparation of the monolayers was

performed by spin-coating solutions of TPA or FOPA in isopropanol onto the $Si/SiO_2/AlO_x$ substrates. The chemical structures of the materials used for fabrication of the self-assembled monolayers are shown in Figure 99.

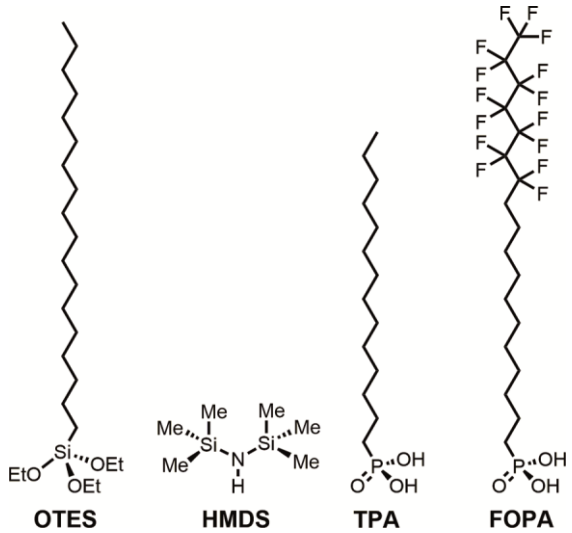

Figure 99. Chemical structures of materials used for fabrication of self-assembled monolayers on Si/SiO_2 and $Si/SiO_2/AlO_x$ substrates.

The different monolayers possess a different surface energy, which can strongly influence the morphology of the organic semiconductor during deposition process. To test if the monolayers are of good quality, contact angles for water were measured on these monolayers. Typical values are around 108, 97, 111 and 118 ° for OTES, HMDS, TPA and FOPA, respectively.

Cleaning Procedure for Si/SiO_2 Substrates

Rinsing with toluene, *i*PrOH and acetone, 30 s each, using the spin coater (3000 rpm, 3000 rpm s^{-1}). Afterwards using an UVO-cleaner for 5 min.

Cleaning Procedure for SAM Modified and Quartz Substrates

Rinsing with toluene, *i*PrOH and acetone, 30 s each, using the spin coater (3000 rpm, 3000 rpm s^{-1}).

Top Contact Preparation

Top electrodes were prepared by evaporation of gold (30 nm) on top of the organic thin film, using the EVAP300 (Creaphys). Shadow masks with a square shape (200 × 200 μm^2) were used, providing devices with a length *L* and width *W* of 100 µm

and 200 µm, respectively. The deposition rate was in the range of 0.2 – 0.6 Å s^{-1} at a pressure of around 2×10^{-6} mbar.

6.4.2.2 Experimental Details for Active Layer Preparation

General

Typically, thin layers of the molecules (30 nm) were sublimed using the EVAP300 (Creaphys, Germany). Sublimation took place at about 2×10^{-6} mbar. The sublimation rate was in the range of 0.2 – 1.0 nm min^{-1}.

Transistors of ADA Dyes (Section 3.2.1.4)

Table 35. Sublimation parameters of organic semiconductors for the preparation OTFT devices based on ADA dyes **ADA1a**, **ADA2a** and **ADA2b**.

dye	T_{sub} [a] [°C]	T_s [b] [°C]	p [c] [10^{-6} mbar]	r [d] [nm min^{-1}]
ADA1a	172	130	1.3	0.2–0.3
ADA2a	160	130	2.5	0.2–0.5
ADA2b	195	130	1.6	0.2–0.4

[a] Sublimation temperature. [b] Substrate temperature. [c] Pressure. [d] Sublimation rate.

Transistors of AπA Dyes (Section 3.2.3.5)

Table 36. Sublimation parameters of organic semiconductors for the preparation OTFT devices based on AπA dyes **AπA1a-c**.

dye	T_{sub} [a] [°C]	T_s [b] [°C]	p [c] [10^{-6} mbar]	r [d] [nm min^{-1}]
AπA1a	170	150	2.3	0.2–0.3
AπA1b	230	170	2.5	0.2–0.3
AπA1c	120	80	1.1	0.2–0.5

[a] Sublimation temperature. [b] Substrate temperature. [c] Pressure. [d] Sublimation rate.

6.4.3 Solvents and Chemicals for preparation of OSCs and OTFTs

Solvents and chemicals used for the preparation of organic solar cells or organic thin film transistors are compiled in Table 37.

Table 37. Solvents and other chemicals for device production.

compound	specification	supplier
acetone	semiconductor grade	Sigma Aldrich
aluminum	wire (99.999 %)	MaTecK
C_{60}	sublimed twice	Solenne
chloroform	water-free (≥ 99 %)	Sigma Aldrich
1,8-diiodooctane	copper stabilized (> 95 %)	TCI
gold	pellets (99.99 %)	Umicore
hexamethyldisilazane	electronic grade (99%)	ABCR
hydrogen peroxide	analytical reagent grade (30 %)	Merck
isopropanol	semiconductor grade	Sigma Aldrich
lithium fluoride	powder	Sigma Aldrich
molybdenum(VI) oxide	powder (99.99 %)	Sigma Aldrich
Mucasol®	–	Brand
n-octadecyltriethoxysilane	5–10 % branched C18-isomers (94 %)	Chemos
o-dichlorobenzene	water-free (≥ 99 %)	Sigma Aldrich
$PC_{61}BM$	> 99%	Solenne
PEDOT:PSS	CLEVIOSTM P VP AI 4083	Heraeus
silver	pellets (99.99 %)	Umicore
sulfuric acid	95 %	Fischer Scientific
toluene	analytical reagent grade	Fischer Scientific
trichloroethylene	water-free (≥ 99 %)	Sigma Aldrich
water	ultrapure water	TEP [a]

[a] Lehrstuhl für Technische Physik (Universität Würzburg)

6.5 Synthetic Procedures and Product Characterization

6.5.1 General

Reagents for synthesis were purchased from commercial sources and used as supplied. Reagent grade solvents were distilled before use. Column chromatography was performed on silica (silica gel, 230 – 400 mesh). ^{1}H and ^{13}C NMR spectra were recorded on a Avance III HD 400 or Avance III HD 600 spectrometer (Bruker) at room temperature, unless stated otherwise. NMR spectra were calibrated to the residual solvent signals or TMS. All chemical shifts δ are given in ppm. The following notation was used to designate multiplicities: s = singlet, d = doublet, t = triplet, m = multiplet. *J* values are given in Hz. Low resolution mass spectra were measured by matrix-assisted laser desorption/ionization (MALDI) on a Autoflex II MALDI-TOF mass spectrometer (Bruker). High resolution mass spectra were measured by electrospray ionization (ESI)

using an ESI micrOTOF Focus spectrometer (Bruker). Melting points are uncorrected and were determined on an BX41 optical microscope (Olympus) with heating stage.

6.5.2 Synthesis of ADA molecules

Synthesis of Acceptor and Donor Building Blocks

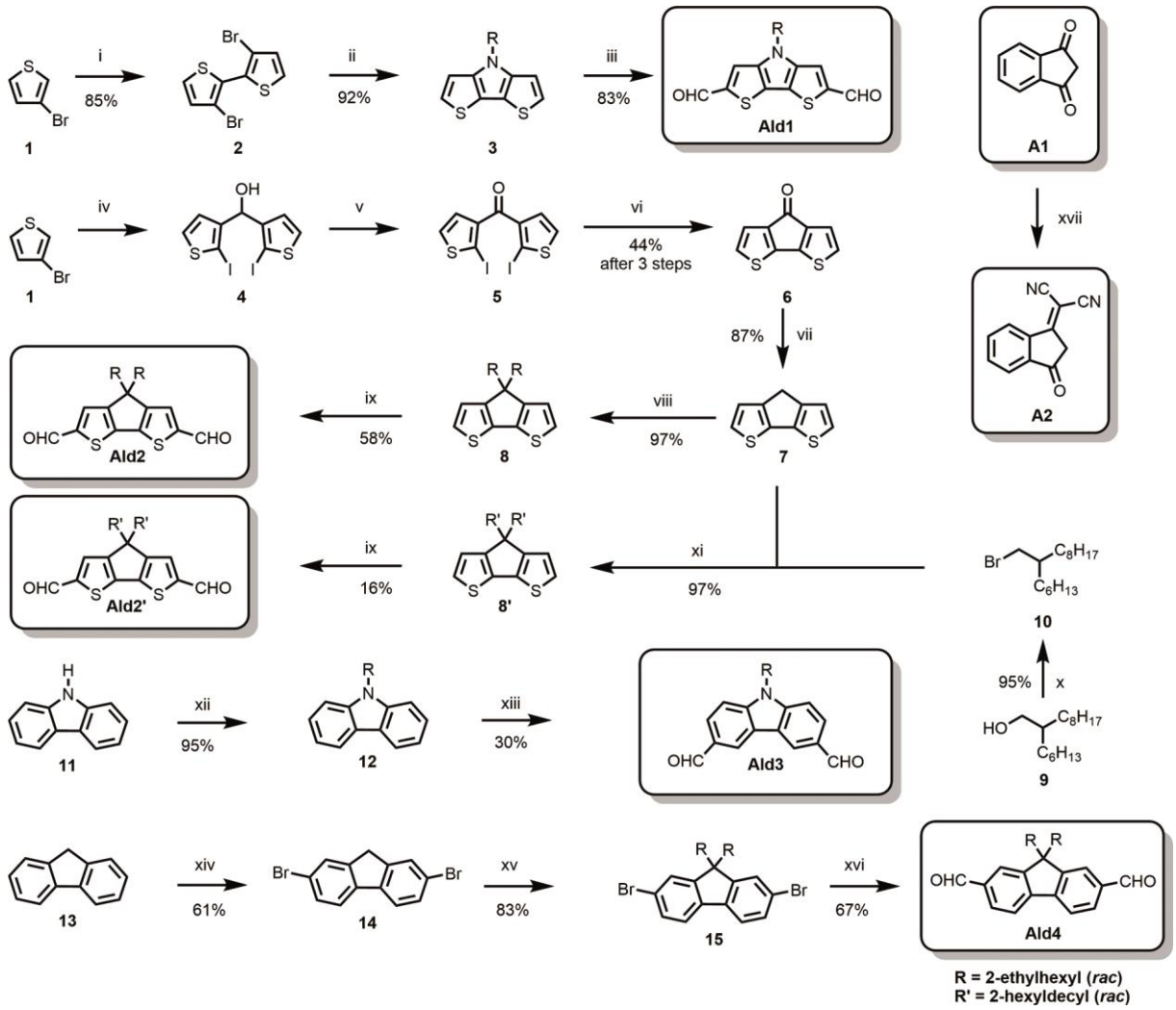

Figure 100. Synthesis of building blocks **Ald1**, **Ald2**, **Ald2'**, **Ald3**, **Ald4**, and **A2**. i) 1. LDA, 0 °C, 3.5 h; 2. $ZnCl_2$, 0 °C, 45 min; 3. $CuCl_2$, −78 °C to RT, 18 h. ii) RNH_2 (*rac*), $Pd_2(dba)_3$, BINAP, NaO*t*Bu, toluene, 110 °C, 25 h. iii) 1. $POCl_3$, DMF, 130 °C, 12 h; 2. 1 M NaOH (aq.), DCM, RT, 2 h. iv) 1. *n*BuLi, Et_2O, −78 °C, 1 h, then RT, 1 h. 2. 3-thiophenecarboxaldehyde (14), −78 °C, 30 min, then RT, 3 h; 3. *n*BuLi, −78 °C, 40 min, then RT, 2 h; 4. I_2, Et_2O, −20 °C, RT, 13.5 h. v) PCC, DCM, RT, 22 h. vi) Cu, DMF, 120 °C, 4 h. vii) 1. hydrazine hydrate, $OHCH_2CH_2OH$, 100 °C, 1 h; 2. KOH, H_2O, 180 °C, 3 h. viii) 1. 1.05 eq. *n*BuLi, THF, −78 °C, 1 h, then RT, 1 h; 2. 1.05 eq. RBr (*rac*), −78 °C, 30 min, then RT, 2 h; 3. 1.05 eq. *n*BuLi, THF, −78 °C, 1 h, then RT, 1 h; 4. 1.05 eq. RBr (r*ac*), −78 °C, 30 min, then RT, 2 h. ix) DMF, $POCl_3$, DCE, 90 °C, 2 d. x) PPh_3, DCM, 0 °C, NBS, then RT 24 h. xi) 1. 1.05 eq. *n*BuLi, THF, −78 °C, 1 h, then RT, 1 h; 2. 1.05 eq. **10** (*rac*), −78 °C, 30 min, then RT, 2 h; 3. 1.05 eq. *n*BuLi, THF, −78 °C, 1 h, then RT, 1 h; 4. 1.05 eq. **10** (r*ac*), −78 °C, 30 min, then RT, 2 h. xii) RBr (*rac*), NaOH (aq.), TBAB, toluene, reflux, 16 h. xiii) DMF, $POCl_3$, 100 °C, 16 h. xiv) Br_2, $CHCl_3$, RT, 20 h. xv) RBr (*rac*), NaO*t*Bu, THF, RT, 16 h. xvi) 1. *n*BuLi, THF, −78 °C, 40 min; DMF, −78 °C, 1 h, then RT, 1 h. xvii) malononitrile, NaOAc, EtOH, RT, 40 min.

The starting material for the preparation of both bithiophene-containing donor cores was 3-bromothiophene (**1**). The synthesis of dialdehyde **Ald1** contains three steps.[234,285–287] The first step is an oxidative aromatic coupling of **1**, which yielded 85 % of **2**.[285,286] Buchwald-Hartwig amination was performed in the second step.[287] The reaction employing Pd_2dba_3, 2,2'-bis(diphenylphosphino)-1,1'-binaphthyl (BINAP), and NaO^tBu produced DTP **3** in 92 %. Finally the donor buliding block **Ald1** was obtained by Vilsmeier-Haack formylation.[234]

Building blocks **Ald2** and **Ald2'** were obtained in a six-step synthesis. Compound **4** was prepared according to the reported procedure[288] in one pot procedure. **1** was lithiated, and then reacted with 3-thiophenecarboxaldehyde, followed by dilithiation and final reaction with iodine. The crude product was further oxidized by PCC to ketone **5**, which was finally converted into **6** *via* intramolecular Ullman reaction in 44 % overall yield of the three synthetic steps. [288] In the next, Wolff-Kishner reaction was performed on **6** to give **7** in 87 % yield. [288] Alkylation was performed with 2-ethylhexyl bromide (*rac*) or 2-hexyldecyl bromide (*rac*) (**10**) to yield 97 % of either **8** or **8'**, respectively. The dialdehydic CPDT donor cores **Ald2** and **Ald2'** were obtained by Vilsmeier-Haack formylation in yields of 58 and 16 %, respectively.[289]

The synthesis of the carbazole donor moiety was simple. The alkylated carbazole **12** was obtained from carbazole (**11**) by phase-transfer catalysis (PTC) methodology. In doing so, ethylhexyl bromide was used as an alkylating agent and tetrabutylammonium bromide (TBAB) as a PTC catalyst.[290] Subsequently, Vilsmeier-Haack formylation afforded compound **Ald3** in a moderate yield of 30 %.

Fluorene based donor core **Ald4** could be prepared easily. Bromination[291] was performed in the first step to give **14**. Then alkylation[292] was performed, which gave **15** in a yield of 83 %. **15** was then converted into dialdhyde **Ald4** by applying *n*BuLi and DMF.

Acceptor **A2** was prepared following the procedure by Robertson.[293]

3-bromothiophene (**1**), 3-thiophenecarboxaldehyde, 2-hexyldecanol (*rac*) (**9**), carbazole (**11**), 2-ethylhexyl bromide, fluorene (**13**) and 1,3-indandione (**A1**) were commercially available. Compounds **2**,[285,286] **3**,[287] **Ald1**,[234] **4**, [288] **5**,[288] **6**, [288] **7**,[288] **Ald2**,[289] **10**,[294] **14**,[291] **15**,[292] and **A2**[293] were prepared according to the procedures published in literature.

Synthesis of Compound 8

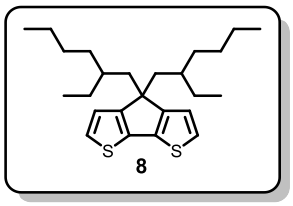

Compound **8** was synthesized by adopting the reported procedure.[288] A solution of compound **7** (1.65 g, 9.26 mmol) in THF (50 ml) was cooled to –78 °C under nitrogen. Then the following operations were conducted: a) *n*BuLi (2.5 M in hexane; 3.9 ml, 9.72 mmol) was added dropwise and the mixture was kept at –78 °C for 1 h, followed by 1 h at room temperature; b) the mixture was again cooled to –78 °C, 2-ethylhexyl bromide (1.74 ml, 9.72 mmol) was added and after 30 min the reaction was stirred at room temperature for 2 h. Next, steps a) and b) were repeated using the same amounts of reagents. Afterwards, the solution was extracted with diethyl ether, washed with water, brine, NH_4Cl (aq.) and dried over $MgSO_4$. The crude product was purified by column chromatography (silica, pentane) to obtain **8** (3.62 g, 97 %) as a light yellow oil. Compound **8** was obtained as a mixture of stereoisomers. ^{1}H NMR (400 MHz, CD_2Cl_2) δ 7.14 (d, *J* = 4.9 Hz, 2H), 6.99 – 6.94 (m, 2H), 2.00 – 1.75 (m, 4H), 1.44 – 1.17 (m, 2H), 1.07 – 0.83 (m, 16H), 0.83 – 0.69 (m, 6H), 0.64 – 0.54 (m, 8H). Analytical data are in accordance with the literature.[295]

Synthesis of Compound 8'

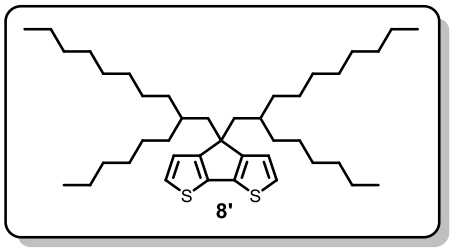

Compound **8'** was synthesized by adopting the reported procedure.[288] A solution of compound **7** (800 mg, 4.49 mmol) in THF (50 ml) was cooled to –78 °C under nitrogen. Then the following steps were followed: a) *n*BuLi (2.5 M in hexane; 1.88 ml, 4.712 mmol) was added dropwise to the reaction mixture, which was kept at –78 °C for 1 h, followed by 1 h at room temperature; b) the mixture was again cooled to –78 °C, 2-hexyldecyl bromide (1.44 ml, 4.712 mmol) was added and after 30 min the reaction was stirred at room temperature for 2 h. Next, steps a) and b) were repeated using the same amounts of reagents. Afterwards, the solution was extracted with diethyl ether, washed with water, brine, NH_4Cl (aq.) and dried over $MgSO_4$. The crude product was purified by column chromatography (silica, pentane) to obtain **8'** (2.75 g, 97 %) as a light yellow oil. Compound **8'** was obtained as a mixture of stereoisomers. ^{1}H NMR (400 MHz, $CDCl_3$) δ 7.10 (dt, *J* = 6.1, 0.7 Hz, 2 H), 6.91 (d, *J* = 6.1 Hz, 2 H), 1.88 (d, 6.2 H), 1.45 – 1.05 (m, 48 H), 0.79 (m, 12 H). Analytical data are in accordance with the literature.[296]

Synthesis of Compound Ald2'

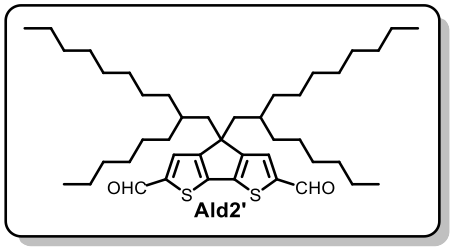

A Schlenk tube was charged with DMF (910 mg, 12.4 mmol) and cooled to 0 °C under nitrogen. Then phosphorus oxichloride (1.90 g, 12.4 mmol) was added dropwise over 10 minutes. A solution of **8'** (1.30 g, 2.07 mmol) in 10 ml of dry DCE was added slowly. Next, the solution was heated up to 90 °C and stirred for 24 h. Afterwards, the reaction was quenched with a saturated aqueous NaOAc solution. The reaction mixture was extracted with CH_2Cl_2, washed with water and dried over $MgSO_4$. Column chromatography (silica, pentane/etOAc 95:5) afforded **Ald2'** (220 mg, 16 %) as an orange oil. Compound **Ald2'** was obtained as a mixture of stereoisomers. ^{1}H NMR (400 MHz, CD_2Cl_2) δ 9.88 (s, 2H), 7.64 (m, 2H), 1.99 – 1.96 (m, 4 H), 1.30 – 1.03 (m, 30 H), 1.01 – 0.78 (m, 32 H). ^{13}C NMR (101 MHz, CD_2Cl_2) δ 182.4, 157.5, 136.8, 123.8, 122.3, 53.2, 43.9, 39.6, 36.5, 35.0, 33.4, 32.4, 31.9, 31.8, 29.7, 29.5, 29.4, 29.3, 26.3, 22.6, 14.10, 14.08. MS HR (ESI) *m/z* calcd. for $C_{43}H_{70}O_2S_2$ $[M]^+$ 682.4817, found 684.4812.

Synthesis of Compound 12

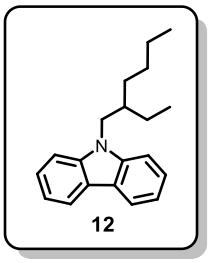

Compound **12** was synthesized by adopting the reported procedure.[297] To a solution of carbazole (**11**, 1.20 g, 7.16 mmol) and tetrabutylammonium bromide (46 mg, 0.14 mmol) in toluene (12 ml) NaOH (50 % w/w; 4.6 g, 57.3 mmol) was added. Next, 2-ethylhexyl bromide (1.60 g, 8.30 mmol) was added dropwise at RT to the mixture and the reaction was continued for 16 h under reflux. Afterwards, the layers were separated. The organic solvent was removed under reduced pressure and the residue was dissolved in CH_2Cl_2, washed with water and dried over $MgSO_4$. After filtration solvent was removed under reduced pressure and the crude product was purified by Kugelrohr distillation to afford **12** (1.90 g, 95 %) as a yellowish oil. ^{1}H NMR (400 MHz, $CDCl_3$) δ 8.14 – 8.07 (m, 2H), 7.50 – 7.36 (m, 4H), 7.25 – 7.19 (m, 2H), 4.26 – 4.07 (m, 2H), 2.15 – 1.99 (m, 1H), 1.47 – 1.18 (m, 8H), 0.92 (t, J = 7.4 Hz, 3H), 0.87 (t, J = 7.2 Hz, 3H). Analytical data are in accordance with the literature.[298]

Synthesis of Compound Ald3

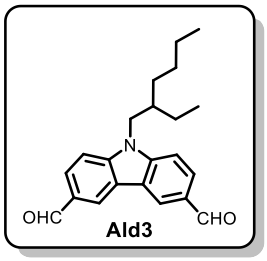

Compound **Ald3** was prepared by adopting the reported procedure.[299] A Schlenk tube was charged with dimethylformamide (24.20 g, 331 mmol) and the solvent was cooled to 0 °C. Then phosphorus oxichloride (50.76 g, 331 mmol) was added dropwise and the solution was stirred at 0 °C for 1 h. Next, compound **12** (5.00 g, 17.89 mmol) was added and the reaction mixture was strirred at 100 °C for 16 h. After cooling to 0 °C, the mixture was neutralized by adding NaOH solution (1 M). The product was extracted with CH_2Cl_2, washed with water and dried over Na_2SO_4. Column chromatography (silica, EtOAc/hexane 1:9 to 2:9) afforded **Ald3** (1.82 g, 30 %) as a colorless solid. ^{1}H NMR (400 MHz, $CDCl_3$) δ 10.14 (s, 2H), 8.67 (dd, *J* = 1.6, 0.5 Hz, 2H), 8.08 (dd, *J* = 8.6, 1.6 Hz, 2H), 7.54 (d, *J* = 8.6 Hz, 2H), 4.26 (d, *J* = 7.6 Hz, 2H), 2.14 – 2.00 (m, 1H), 1.49 – 1.20 (m, 8H), 0.94 (t, *J* = 7.4 Hz, 3H), 0.85 (t, *J* = 7.1 Hz, 3H). Analytical data are in accordance with the literature.[234]

Synthesis of Compound Ald4

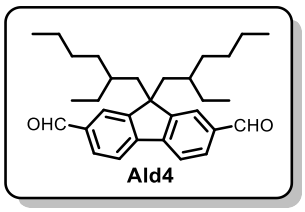

A dried flask was charged with dibromofluorene **14** (104 mg, 0.19 mmol). The vessel was purged with nitrogen and closed with a septum. Afterwards, anhydrous THF (0.79 ml) was added and the solution was cooled under nitrogen to –78 °C. Next, *n*BuLi (2.5 M in hexane; 0.23 ml, 0.58 mmol,) was added dropwise over 5 min and the mixture was stirred at –78 °C for ca. 40 min, followed by addition of anhydrous DMF (50 µL, 0.65 mmol) in THF (85 µL). The reaction was stirred at this temperature for 1 h. Then, the cooling bath was removed and the stirring was continued for 1 h. Afterwards, the reaction was quenched with a saturated aqueous NH_4Cl, and extracted with Et_2O. The combined organic extracts were dried over anhydrous Na_2SO_4, filtered, and evaporated. A crude product was purified by column chromatography (silica, hexane/EtOAc 19:1) to give **Ald4** (57 mg, 67 %) as a colorless solid. Compound **Ald4** was obtained as a mixture of stereoisomers. ^{1}H NMR (400 MHz, $CDCl_3$) δ 10.09 (s, 2H), 7.99 – 7.95 (m, 2H), 7.95 – 7.89 (m, 4H), 2.14 – 2.03 (m, 4H),

0.94 – 0.70 (m, 12H), 0.70 – 0.57 (m, 10H), 0.52 – 0.44 (m, 6H), 0.44 – 0.35 (m, 2H). Analytical data are in accordance with the literature.[300]

Synthesis of Compound ADA1a

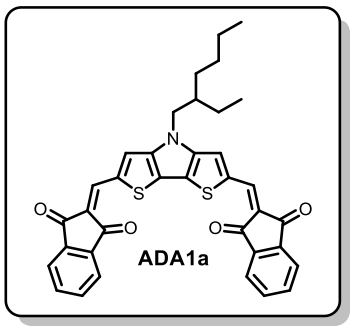

Aldehyde **Ald1** (200 mg, 0.58 mmol) and compound **A1** (336 mg, 2.30 mmol) were dissolved in dichloroethane (20 ml) and pyridine (0.50 ml, 6.21 mmol) was added. The reaction mixture was stirred at room temperature for 18 h. Then the solvents were removed *in vacuo* and the crude product was purified by column chromatography (silica, hexane:CH_2Cl_2, 1:4, then CH_2Cl_2 to CH_2Cl_2 + 5 % MeOH) and recrystallized (CH_2Cl_2/hexane) to give **ADA1a** (180 mg, 52 %) as green crystals. M.p. 278 – 280 °C (CH_2Cl_2/hexane). UV/vis (CH_2Cl_2, $c \sim 10^{-5}$ M): λ_{max} /nm 582 (ε/M^{-1} cm^{-1} 132 600), 544 (69 500), 422 (7 400), 376 (10 400), 354 (7 000). ^{1}H NMR (400 MHz, $CDCl_2CDCl_2$, 125 °C) δ 8.43 (s, 2H), 8.11 – 7.98 (m, 4H), 7.96 (s, 2H), 7.89 – 7.77 (m, 4H), 4.29 (d, J = 7.1 Hz, 2H), 2.26 – 2.06 (m, 1H), 1.61 – 1.34 (m, 8H), 1.08 (t, J = 7.4 Hz, 3H), 0.98 (t, J = 7.0 Hz, 3H). ^{13}C NMR (101 MHz, $CDCl_2CDCl_2$, 125 °C) δ 189.3, 188.5, 150.1, 142.4, 140.5, 140.1, 136.0, 134.6, 134.4, 126.1, 125.5, 122.7, 121.5, 51.9, 40.5, 31.1, 28.7, 24.5, 22.6, 13.4, 10.5. MS HR (ESI) *m/z* calcd. for $C_{36}H_{30}NO_4S_2$ $[M+H]^+$ 604.1616, found 604.1611. Anal. calcd. for $C_{36}H_{29}NO_4S_2$: C, 71.62; H, 4.84; N, 2.32; S, 10.62. Found: C, 71.51; H, 4.72; N, 2.48; S, 10.25.

Synthesis of Compound ADA1b

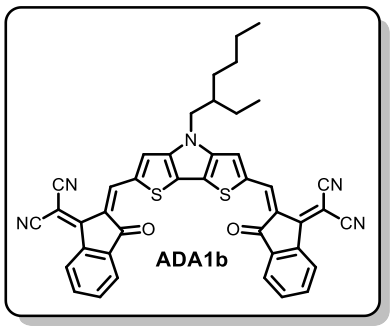

Aldehyde **Ald1** (200 mg, 0.58 mmol) and compound **A2** (450 mg, 2.32 mmol) were dissolved in dichloroethane (20 ml) and pyridine (0.50 ml, 6.21 mmol) was added. The reaction mixture was stirred at room temperature for 20 h. Then the solvents were removed *in vacuo* and the crude product was purified by column chromatography (silica, hexane:CH_2Cl_2, 1:4, then CH_2Cl_2 to CH_2Cl_2 + 10 % MeOH) and recrystallized (CH_2Cl_2/hexane) to give **ADA1b** (200 mg, 50 %) as green-golden crystals. M.p. 307 – 310 °C (CH_2Cl_2/hexane). UV/vis (CH_2Cl_2, $c \sim 10^{-5}$ M): λ_{max}/nm 665 (ε/M^{-1} cm^{-1} 139 300) with a shoulder at 367 (12 900), 308 (36 700). ^{1}H NMR (400 MHz, $CDCl_2CDCl_2$, 125 °C) δ 8.80 (s, 2H), 8.65 (d, J = 7.6 Hz, 2H), 7.96

– 7.94 (m, 4H), 7.81 – 7.68 (m, 4H), 4.15 (d, J = 7.0 Hz, 2H), 2.08 – 1.97 (m, 1H), 1.51 – 1.23 (m, 8H), 0.95 (t, J = 7.3 Hz, 3H), 0.91 – 0.82 (m, 3H). ^{13}C NMR (101 MHz, $CDCl_2CDCl_2$, 125 °C) δ 187.4, 160.4, 150.7, 141.1, 140.0, 137.8, 137.1, 135.3, 134.7, 128.9, 125.2, 124.8, 124.1, 123.7, 114.5, 70.2, 52.1, 40.4, 31.0, 28.7, 24.5, 22.9, 13.8, 10.7. MS HR (ESI) *m/z* calcd. for $C_{42}H_{29}N_5O_2S_2$ M^+ 699.1763, found 699.1757.

Synthesis of Compounds ADA2a and AD2a

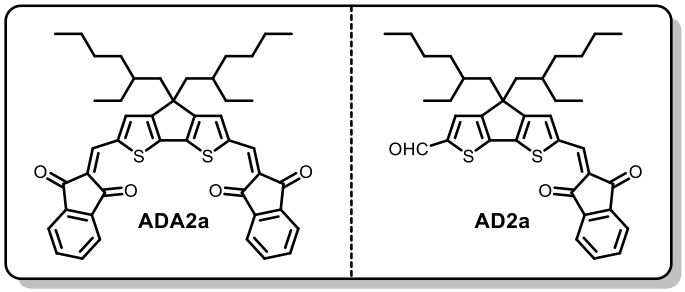

A flask was charged with aldehyde **Ald2** (100 mg, 0.22 mmol), indandione **A1** (129 mg, 0.88 mmol), anhydrous NaOAc (68 mg, 0.83 mmol), and Ac_2O (2 ml). The reaction mixture was stirred at 60 °C for 2 h. The crude product was chromatographed (silica, pentane/EtOAc 19:1) to obtaind pure **ADA2a** and a mixed fraction. Consecutive chromatography (silica, pentane/EtOAc 19:1) afforded additional portion of **ADA2a** and mono-product **AD2a**. Both products were recrystallized (CH_2Cl_2/pentane) to afford **ADA2a** (105 mg, 67 %) as green crystals and **AD2a** (41 mg, 32 %) as orange-red crystals. Compounds **ADA2a** and **AD2a** were obtained as mixtures of stereoisomers. Compound **ADA2a**: M.p. 270 – 272 °C (CH_2Cl_2/pentane). UV/vis (CH_2Cl_2, $c \sim 10^{-5}$ M): λ_{max} /nm 584 (ε/M^{-1} cm^{-1} 122 200), 544 (76 900), 411 (7 700), 387 (13 500), 346 (16 000), 333 (15 100). ^{1}H NMR (400 MHz, CD_2Cl_2) δ 8.06 – 7.89 (m, 8H), 7.85 – 7.74 (m, 4H), 2.12 – 1.97 (m, 4H), 1.08 – 0.84 (m, 16H), 0.77 – 0.55 (m, 14H). ^{13}C NMR (101 MHz, CD_2Cl_2) δ 190.48, 190.47, 190.46, 190.01, 189.96, 189.92, 163.0, 162.9, 162.8, 150.83, 150.77, 150.72, 142.73, 142.70, 142.66, 141.0, 136.5, 136.4, 136.3, 135.9, 135.6, 135.4, 124.94, 124.89, 124.83, 123.3, 43.6, 35.9, 34.8, 28.97, 28.96, 27.9, 23.3, 14.3, 10.9, signal of one carbon atom is overlapping with the solvent signal. MS HR (ESI) *m/z* calcd. for $C_{45}H_{47}O_4S_2$ [M+H]$^+$ 715.2916, found 715.2910. Anal. calcd. for $C_{45}H_{46}O_4S_2$: C, 75.60; H, 6.49; S, 8.97. Found: C, 75.23; H, 6.58; S, 8.91. Compound **AD2a**: M.p. 136 – 139 °C (CH_2Cl_2/pentane). UV/vis (CH_2Cl_2, $c \sim 10^{-5}$ M): λ_{max} /nm 507 (ε/M^{-1} cm^{-1} 70 100) with a shoulder, 324 (9 700), 312 (11 300). ^{1}H NMR (400 MHz, CD_2Cl_2) δ 9.91 (s, 1H), 8.07 – 7.87 (m, 4H), 7.86 – 7.75 (m, 2H), 7.68 – 7.67 (m, 1H), 2.17 – 1.88 (m, 4H), 1.16 – 0.82 (m, 16H), 0.81 – 0.66 (m, 6H), 0.66 – 0.53 (m, 8H). ^{13}C NMR (101 MHz, CD_2Cl_2) δ

190.48, 190.47, 190.46, 190.04, 190.00, 189.95, 183.53, 183.46, 183.39, 162.27, 162.22, 162.18, 150.38, 150.32, 150.26, 147.4, 146.05, 146.03, 146.00, 142.7, 141.89, 141.88, 141.85, 141.0, 136.7, 136.6, 136.5, 136.03, 136.00, 135.6, 135.4, 131.1, 131.03, 130.97, 124.81, 124.76, 124.72, 123.32, 123.28, 54.78, 43.5, 35.90, 35.87, 34.8, 34.7, 29.03, 29.02, 28.94, 28.92, 27.94, 27.86, 23.25, 23.24, 14.4, 14.3, 10.93, 10.89, 10.88. MS HR (ESI) *m/z* calcd. for $C_{36}H_{43}O_3S_2$ $[M+H]^+$ 587.2654, found 587.2648.

Synthesis of Compound ADA2b

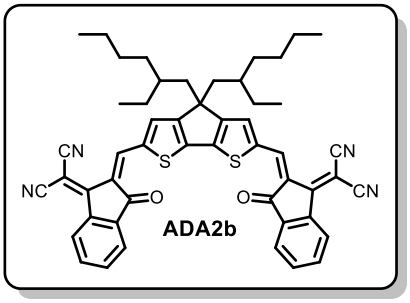

To dialdehyde **Ald2** (100 mg, 0.22 mmol) and compound **A2** (171 mg, 0.88 mmol) in dichloroethane (8 ml) dry pyridine (0.19 ml, 2.4 mmol) was added and the reaction mixture was stirred at 60 °C for 1 h. Then the solution was loaded on a column and chromatographed (silica, CH_2Cl_2) to obtain pure **ADA2b** (175 mg, 99 %), which was recrystallized (CH_2Cl_2/pentane) to give golden crystals. Compounds **ADA2b** was obtained as a mixture of stereoisomers. M.p. 305 – 307 °C (CH_2Cl_2/pentane). UV/vis (CH_2Cl_2, $c \sim 10^{-5}$ M): λ_{max} /nm 664 (ε/M^{-1} cm^{-1} 130 900), 617 (79 200), 337 (30 400), 310 (44 400). ^{1}H NMR (400 MHz, CD_2Cl_2) δ 8.92 (s, 2H), 8.74 – 8.67 (m, 2H), 8.01 – 7.94 (m, 2H), 7.86 – 7.73 (m, 6H), 2.13 – 1.96 (m, 4H), 1.11 – 0.85 (m, 16H), 0.81 – 0.67 (m, 8H), 0.67 – 0.58 (m, 6H). ^{13}C NMR (101 MHz, CD_2Cl_2) δ 188.77, 188.75, 188.72, 163.4, 163.34, 163.28, 160.65, 160.62, 160.60, 153.62, 153.60, 153.57, 143.3, 140.6, 138.2, 138.1, 138.0, 137.90, 137.85, 137.80, 137.5, 135.9, 135.2, 125.9, 124.4, 124.2, 115.2, 115.09, 115.06, 115.04, 70.68, 70.66, 70.64, 43.6, 36.1, 34.6, 28.91, 28.90, 27.91, 27.89, 23.3, 14.4, 10.88, 10.86, signal of one carbon atom is overlapping with the solvent signal. MS HR (ESI) *m/z* calcd. for $C_{51}H_{47}N_4O_2S_2$ $[M+H]^+$ 811.3140, found 811.3135. Anal. calcd. for $C_{51}H_{46}N_4O_2S_2$: C, 75.52; H, 5.72; N, 6.91; S, 7.91. Found: C, 75.77; H, 5.73; N, 7.06; S, 7.60.

Synthesis of Compound ADA2b'

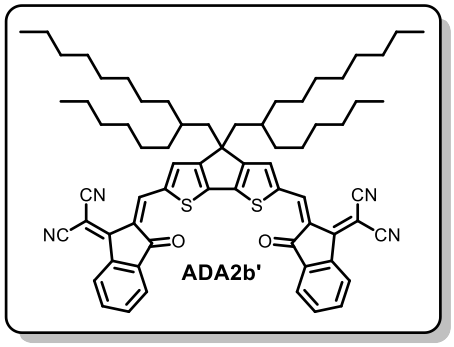

To compound **Ald2** (160 mg, 0.23 mmol) and compound **A2** (182 mg, 0.94 mmol) in dichloroethane (8.5 ml) dry pyridine (0.20 ml, 2.52 mmol) was added and the reaction mixture was stirred at 60 °C for 1 h. Then the solution was loaded on a column and chromatographed (silica, CH_2Cl_2) to obtain pure **ADA2b'** (188 mg, 76 %). The product was recrystallized in CH_2Cl_2/pentane to give golden crystals. Compounds **ADA2b'** was obtained as a mixture of stereoisomers. M.p. >300 °C (CH_2Cl_2/pentane). UV/vis (CH_2Cl_2, $c \sim 10^{-5}$ M): λ_{max} /nm 664 (ε/M^{-1} cm^{-1} 130 900), 617 (79 200), 337 (30 400), 310 (44 400). ^{1}H NMR (400 MHz, CD_2Cl_2) δ 8.95 – 8.91 (m, 2H), 8.73 – 8.69 (m, 2H), 8.00 – 7.95 (m, 2H), 7.86 – 7.75 (m, 6H), 2.00 – 1.99 (m, 4 H), 1.29 – 1.24 (m, 2H), 1.19 – 0.84 (m, 48 H), 0.78 – 0.70 (12H). ^{13}C NMR (101 MHz, CD_2Cl_2) δ 188.7, 163.3, 160.5, 153.7, 143.2, 140.6, 138.0, 137.5, 135.9, 135.2, 125.9, 124.25, 124.21, 124.18, 115.1, 115.0, 71.0, 44.15, 35.75, 35.67, 34.96, 32.5, 32.4, 30.3, 30.2, 30.0, 29.9, 28.90, 26.9, 26.8, 23.25, 23.23, 14.38. signal of one carbon atom is overlapping with the solvent signal. MS HR (ESI) *m/z* calcd. for $C_{67}H_{79}N_4O_2S_2$ $[M+H]^+$ 1035.5639, found 1035.5619.

Synthesis of Compounds ADA3a and AD3a

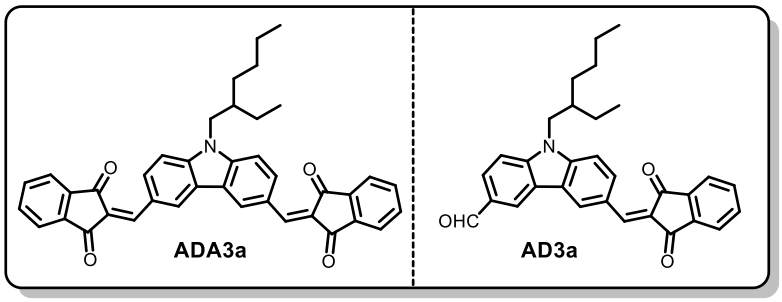

A flask was charged with carbazole **7** (150 mg, 0.45 mmol), indandione **A1** (229 mg, 1.57 mmol), anhydrous NaOAc (129 mg, 1.57 mmol), and Ac_2O (4 ml). The reaction mixture was stirred at 80 °C for 7 h, poured into water and extracted with CH_2Cl_2. Combined organic extracts were dried over anhydrous $MgSO_4$, filtered and evaporated. A crude product was chromatographed (silica, CH_2Cl_2, then CH_2Cl_2 + 1 % acetone). Consecutive chromatography (silica, EtOAc/pentane 1:4) provided mono-substituted **AD3a** and bis-substituted **ADA3a** that were recrystallized (CH_2Cl_2/pentane) to give **DA3a** (35 mg, 17 %) as yellow crystals and **ADA3a** (137 mg, 52 %) as orange crystals. Compound **ADA3a**: M.p. 168 – 170 °C (CH_2Cl_2/pentane). UV/vis (CH_2Cl_2, $c \sim$

10^{-5} M): λ_{max} /nm 478 (ε/M^{-1} cm^{-1} 70 100) with a shoulder, 399 (39 100), 338 (31 300). ^{1}H NMR (400 MHz, CD_2Cl_2) δ 9.35 (d, J = 1.6 Hz, 2H), 8.67 (dd, J = 8.8, 1.6 Hz, 2H), 8.04 – 7.98 (m, 2H), 7.96 (s, 2H), 7.95 – 7.90 (m, 2H), 7.84 – 7.74 (m, 4H), 7.45 (d, J = 8.7 Hz, 2H), 4.16 (d, J = 7.3 Hz, 2H), 2.08 – 1.99 (m, 1H), 1.50 – 1.17 (m, 8H), 0.92 (t, J = 7.4 Hz, 3H), 0.85 (t, J = 7.2 Hz, 3H). ^{13}C NMR (100 MHz, CD_2Cl_2) δ 190.9, 189.9, 147.9, 145.1, 143.0, 140.5, 135.5, 135.4, 134.1, 128.9, 127.1, 126.7, 124.1, 123.5, 123.3, 110.5, 48.5, 40.1, 31.5, 29.3, 24.9, 23.6, 14.3, 11.2. MS HR (ESI) *m/z* calcd. for $C_{40}H_{33}NNaO_4$ [*M*+Na]$^+$ 614.2307, found 614.2302. Compound **AD3a**: M.p. 99 – 102 °C (CH_2Cl_2/pentane). UV/vis (CH_2Cl_2, $c \sim 10^{-5}$ M): λ_{max} /nm 442 (ε/M^{-1} cm^{-1} 37 900) with a shoulder, 332 (16 000). ^{1}H NMR (400 MHz, CD_2Cl_2) δ 10.07 (s, 1H), 9.48 (d, J = 1.6 Hz, 1H), 8.65 (d, J = 1.1 Hz, 1H), 8.61 (dd, J = 8.8, 1.6 Hz, 1H), 8.03 – 7.97 (m, 2H), 7.97 – 7.87 (m, 2H), 7.79 – 7.71 (m, 2H), 7.50 (d, J = 8.7 Hz, 1H), 7.49 (d, J = 8.5 Hz, 1H), 4.19 (d, J = 7.4 Hz, 2H), 2.10-1.94 (m, 1H), 1.43 – 1.09 (m, 8H), 0.86 (t, J = 7.4 Hz, 3H), 0.77 (t, J = 7.2 Hz, 3H). ^{13}C NMR (101 MHz, CD_2Cl_2) δ 191.9, 191.1, 190.1, 148.0, 145.8, 145.3, 143.0, 140.6, 135.7, 135.5, 134.3, 130.4, 128.7, 128.0, 127.3, 126.5, 124.7, 124.0, 123.8, 123.5, 123.4, 110.8, 110.6, 48.6, 40.0, 31.5, 29.3, 24.9, 23.5, 14.3, 11.2. MS HR (ESI) *m/z* calcd. for $C_{31}H_{30}NO_3$ [*M*+H]$^+$ 464.2226, found 464.2220.

Synthesis of Compounds ADA3b and AD3b

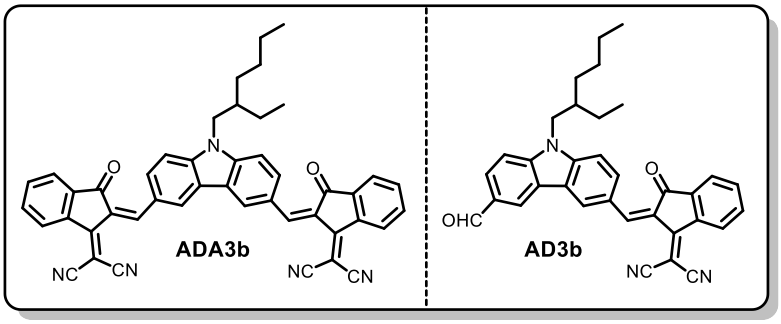

Carbazole **Ald3** (100 mg, 0.30 mmol) and CH-acid **A2** (233, 1.20 mmol) were placed in a flask. Then dichloroethane (10.5 ml) was added, followed by pyridine (0.26 ml, 3.23 mmol). The reaction mixture was stirred at 60 °C for 75 min. Then the solution was loaded on a column and purified (silica, EtOAc/pentane 1:4 to 3:7) to obtain pure fraction of **ADA3b** and a mixed fraction. Consecutive chromatography (silica, EtOAc/pentane 1:3) afforded pure products, which were recrystallized (CH_2Cl_2/pentane) to give **ADA3b** (78 mg, 38 %) and **AD3b** (61 mg, 40 %) as dark red and maroon crystals, respectively. Compound **ADA3b**: M.p. 210 – 211 °C (CH_2Cl_2/pentane). UV/vis (CH_2Cl_2, $c \sim 10^{-5}$ M): λ_{max} /nm 542 (ε/M^{-1} cm^{-1} 51 200), 466 (25 000), 327 (42 300). ^{1}H NMR (400 MHz, CD_2Cl_2) δ 9.28 (d, J = 1.6 Hz, 2H), 8.79 (s, 2H), 8.70 (dd, J = 7.0, 0.9 Hz,

2H), 8.47 (dd, *J* = 8.8, 1.6 Hz, 2H), 8.02 – 7.93 (m, 2H), 7.88 – 7.75 (m, 4H), 7.56 (d, *J* = 8.8 Hz, 2H), 4.26 (d, *J* = 7.2 Hz, 2H), 2.16 – 2.01 (m, 1H), 1.51 – 1.21 (m, 8H), 0.95 (t, *J* = 7.4 Hz, 3H), 0.87 (t, *J* = 7.2 Hz, 3H). ^{13}C NMR (101 MHz, CD_2Cl_2) δ 187.3, 163.1, 148.9, 145.5, 140.3, 138.0, 135.9, 135.3, 134.7, 129.2, 127.9, 126.3, 125.6, 124.6, 124.0, 115.2, 115.0, 110.6, 71.5, 48.7, 40.1, 31.5, 29.3, 24.9, 23.5, 14.3, 11.2. MS HR (ESI) *m/z* calcd. for $C_{46}H_{33}N_5NaO_2$ $[M+Na]^+$ 710.2532, found 710.2527. Anal. calcd. for $C_{46}H_{33}N_5O_2$: C, 80.33; H, 4.84; N, 10.18. Found: C, 79.98; H, 4.79; N, 10.06. Compound **AD3b**: M.p. 188 – 191 °C (CH_2Cl_2/pentane). UV/vis (CH_2Cl_2, $c \sim 10^{-5}$ M): λ_{max} /nm 502 (ε/M^{-1} cm^{-1} 27 100), 320 (28 300). ^{1}H NMR (400 MHz, CD_2Cl_2) δ 10.11 (s, 1H), 9.28 (d, *J* = 1.8 Hz, 1H), 8.75 (s, 1H), 8.68 – 8.63 (m, 2H), 8.42 (dd, *J* = 8.8, 1.8 Hz, 1H), 8.05 (dd, *J* = 8.5, 1.6 Hz, 1H), 7.97 – 7.90 (m, 1H), 7.84 – 7.73 (m, 2H), 7.54 (t, *J* = 8.9 Hz, 2H), 4.24 (d, *J* = 7.5 Hz, 2H), 2.17 – 1.98 (m, 1H), 1.51 – 1.17 (m, 8H), 0.93 (t, *J* = 7.4 Hz, 3H), 0.85 (t, *J* = 7.2 Hz, 3H). ^{13}C NMR (101 MHz, CD_2Cl_2) δ 191.8, 187.3, 163.0, 148.9, 145.8, 145.6, 140.2, 137.9, 135.8, 135.3, 134.6, 130.6, 129.2, 128.2, 127.6, 125.9, 125.6, 124.6, 124.5, 123.9, 123.8, 115.2, 115.0, 110.9, 110.5, 71.3, 48.6, 40.0, 31.4, 29.3, 24.9, 23.5, 14.3, 11.2. MS HR (ESI) *m/z* calcd. for $C_{34}H_{29}N_3NaO_2$ $[M+Na]^+$ 534.2157, found 534.2152. Anal. calcd. for $C_{34}H_{29}N_3O_2$: C, 79.82; H, 5.71; N, 8.21. Found: C, 79.70; H, 5.70; N, 8.21.

Synthesis of Compounds ADA4a and AD4a

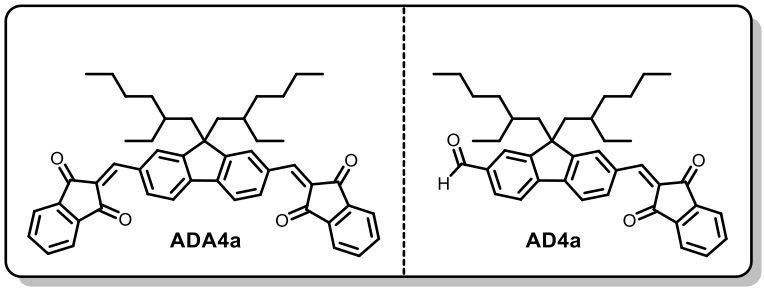

To a solution of fluorene **Ald4** (100 mg, 0.22 mmol) and indandione **A1** (120 mg, 0.82 mmol) in absolute EtOH (4.4 ml) dry piperidine (22 µL, 0.22 mmol) was added. The reaction mixture was heated at 60 °C for 1.5 h. Then solvents were evaporated and the crude product was chromatographed (silica, pentane/CH_2Cl_2 4:1, then CH_2Cl_2). Consecutive chromatography (silica, pentane/ CH_2Cl_2 4:1) afforded mono-product (10 mg, 8 %) as a light-yellow solid and bis-product (53 mg, 34 %) as a yellow solid. Compounds **ADA4a** and **AD4a** were obtained as mixtures of stereoisomers. Compound **ADA4a**: M.p. 169 – 171 °C. UV/vis (CH_2Cl_2, $c \sim 10^{-5}$ M): λ_{max} /nm 466 (ε/M^{-1} cm^{-1} 76 100), 439 (63 900) with a shoulder, 346 (11 000). ^{1}H NMR (400 MHz, CD_2Cl_2) δ

8.94-8.77 (m, 2H), 8.57 – 8.44 (m, 2H), 8.08 – 7.99 (m, 4H), 7.99 – 7.94 (m, 4H), 7.89 – 7.81 (m, 4H), 2.29 – 2.19 (m, 4H), 0.99 – 0.66 (m, 16H), 0.61 – 0.46 (m, 14H). ^{13}C NMR (101 MHz, CD_2Cl_2) δ 190.77, 190.75, 190.73, 189.55, 189.52, 189.49, 153.24, 153.18, 153.12, 147.13, 147.11, 145.73, 145.72, 145.71, 143.2, 140.6, 135.9, 135.7, 134.9, 134.8, 134.6, 133.65, 133.63, 133.60, 130.62, 130.57, 130.52, 129.46, 129.44, 129.42, 123.7, 123.6, 121.5, 56.0, 44.8, 35.4, 34.2, 28.47, 28.46, 27.7, 23.2, 14.3, 10.63, 10.62. MS HR (ESI) *m/z* calcd. for $C_{49}H_{50}NaO_4$ $[M+Na]^+$ 725.3607, found 725.3601. Anal. calcd. for $C_{49}H_{50}O_4$: C, 83.73; H, 7.17. Found: C, 83.83; H, 7.25. Compound **AD4a**: M.p. 91 – 95 °C. UV/vis (CH_2Cl_2, $c \sim 10^{-5}$ M): λ_{max} /nm 403 (ε/M^{-1} cm^{-1} 45 400) with a shoulder. ^{1}H NMR (400 MHz, CD_2Cl_2) δ 10.08 (s, 1H), 8.97 – 8.72 (m, 1H), 8.50 (m, 1H), 8.07 – 7.89 (m, 7H), 7.89 – 7.80 (m, 2H), 2.31 – 2.07 (m, 4H), 0.98-0.66 (m, 16H), 0.66 – 0.60 (m, 3H), 0.60 – 0.53 (m, 3H), 0.53 – 0.38 (m, 8H). ^{13}C NMR (101 MHz, CD_2Cl_2) δ 192.49, 192.42, 192.36, 190.71, 190.69, 190.68, 189.53, 189.50, 189.47, 153.49, 153.45, 153.40, 153.02, 152.95, 152.87, 147.05, 147.04, 147.03, 146.64, 146.63, 145.34, 145.33, 145.31, 143.2, 140.6, 136.5, 136.0, 135.8, 134.8, 134.7, 134.5, 133.64, 133.62, 133.60, 130.56, 130.51, 130.46, 130.25, 130.22, 130.20, 129.58, 129.55, 129.53, 125.5, 123.7, 123.6, 121.74, 121.72, 121.6, 55.9, 44.79, 44.75, 35.39, 35.36, 34.2, 34.13, 34.11, 28.54, 28.53, 28.43, 28.41, 27.6, 27.53, 27.50, 23.2, 14.3, 14.2, 10.63 (2 carbons), 10.55, 10.53. MS HR (ESI) *m/z* calcd. for $C_{40}H_{47}O_3$ $[M+H]^+$ 575.3525, found 575.3520.

6.5.3 Synthesis of AπA molecules

The reactants 3-bromo-2-iodothiophene (**16**) and 2-(tributhylstannyl) thiazole (**17**) were prepared according to published procedures.[301,302] These precursors were connected in a Stille coupling reaction, to obtain **18** in a very good yield of 98 %. Compound **19** was prepared in analogy to the group of Yamaguchi, by lithiation and subsequent conversion of **18** with Mes_2BF.[274] Formylation of **19** with *n*BuLi and dimethylformaide yielded 66 % of dialdehyde **Ald5**. During the last step of synthesis, Knoevenagel condensation reactions were performed between the dialdehyde **Ald5** and CH-acids **A1-3**. For high conversion rates, two equivalents of CH-acid were used per aldehyde functionality, so that the dyes **AπA1a**, **AπA1b** and **AπA1c** were obtained in yields of 53, 74 and 77 %, respectively.

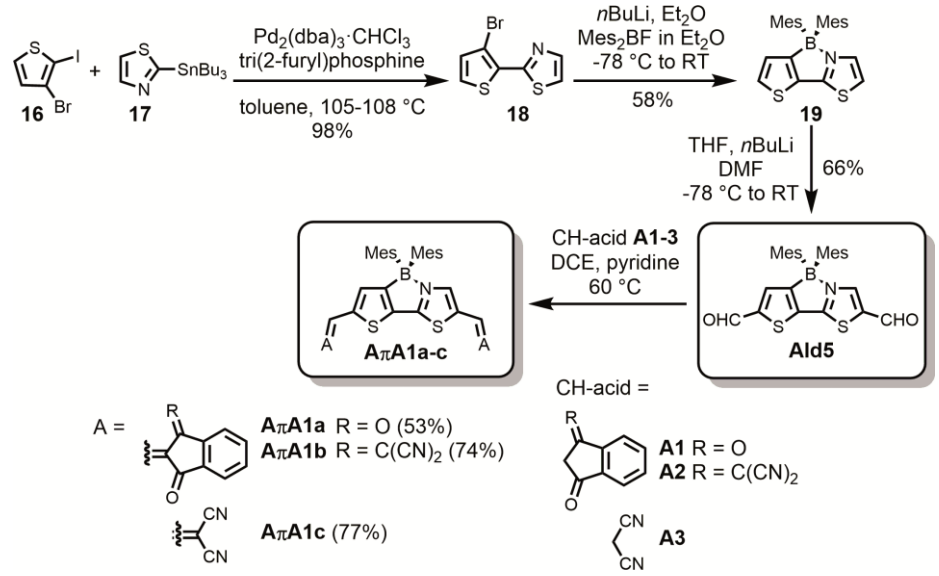

Figure 101. Synthesis of central building block **Ald5** and of AπA dyes **AπA1a-c.** Reproduced from reference[273] with permission from Wiley-VCH Verlag GmbH, Copyright 2017.

Synthesis of Compound 18

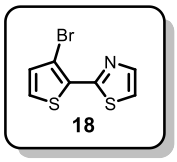

A dry Schlenk tube was charged with 1-bromo-2-iodothiophene (2.00 g; 6.92 mmol) and compound 2-tributylstannylthiazole (3.00 g; 8.02 mmol). Next, dry toluene (34 ml) was added, followed by tri(2-furyl)phosphine (140 mg; 0.60 mmol) and $Pd_2(dba)_3{\cdot}CHCl_3$ (72 mg; 0.070 mmol). The reaction mixture was stirred under nitrogen at 105 °C for 2 h. Then the temperature was increased to 108 °C and the stirring was continued for 19.5 h. Afterwards, the solvent was evaporated and the crude product was purified by column chromatography (silica; pentane/EtOAc 97:3) to obtain **18** (1.66 g, 98 %) as a yellow oil. ^{1}H NMR (400 MHz, $CDCl_3$, 25 °C) δ 7.86 (d, J = 3.3 Hz, 1H), 7.39 (d, J = 3.3 Hz, 1H), 7.34 (d, J = 5.3 Hz, 1H), 7.08 (d, J = 5.3 Hz, 1H). MS HR (ESI) m/z calcd. for $C_7H_5BrNS_2$ $[M+H]^+$ 245.9041, found 245.9043. Analytical data are in accordance with the literature.[274]

Synthesis of Compound 19

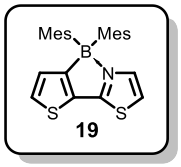

Compound **19** was prepared in a similar way to the procedure reported by Yamaguchi and co-workers.[274] To a solution of **18** (570 mg; 2.32 mmol) in Et_2O (12.9 ml), cooled under nitrogen atmosphere to –78 °C, *n*BuLi (2.5 M in hexane; 0.93 ml, 2.33 mmol) was added dropwise and the mixture was stirred at –78 °C for 1.5 h. In a separate vessel a stock solution of dimesitylfluoroborane (776 mg; 2.89 mmol) in Et_2O (5.40 ml) was prepared. Next, a solution of dimesitylfluoroborane (4.3 ml, 2.30 mmol) was added to the reaction mixture

and the temperature was kept at –78 °C for 25 min. Then the reaction mixture was gradually warmed to room temperature and stirred for 20 h. Afterwards, the solvent was removed and the crude product was purified by column chromatography (silica, pentane/CH_2Cl_2 4:1) to afford **19** (560 mg, 58 %) as a light yellow solid. M.p. 227 – 230 °C. ^{1}H NMR (400 MHz, CD_2Cl_2, 25 °C) δ 7.66 (d, *J* = 3.7 Hz, 1H), 7.53 (d, *J* = 4.7 Hz, 1H), 7.20 (d, *J* = 4.7 Hz, 1H), 7.12 (d, *J* = 3.7 Hz, 1H), 6.62 (s, 4H), 2.15 (s, 6H), 1.83 (s, 12H). ^{1}H NMR (400 MHz, $CDCl_3$, 25 °C) δ 7.70 (d, *J* = 3.7 Hz, 1H) 7.47 (d, *J* = 4.7 Hz, 1H), 7.23 (d, *J* = 4.7 Hz, 1H), 7.05 (d, *J* = 3.7 Hz, 1H), 6.65 (s, 4H), 2.17 (s, 6H), 1.85 (s, 12H). MS LR (MALDI) *m*/*z* calcd. for $C_{25}H_{26}BNS_2$ M^+ 415.2, found 415.2. MS HR (ESI) *m*/*z* calcd.. for $C_{16}H_{15}BNS_2$ [*M*–Mes]$^+$ (one mesityl group was cleaved) 296.0734, found 296.0738.

Synthesis of Compound Ald5

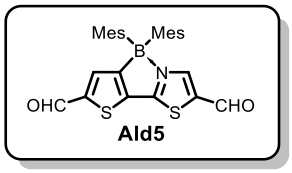

Ald5

A solution of compound **19** (300 mg; 0.72 mmol) in dry THF (7.2 ml) was cooled to –78 °C and *n*BuLi (2.5 M in hexane; 0.66 ml; 1.65 mmol) was added dropwise. The reaction mixture was stirred at –78 °C for 1 h. Then dry DMF (0.17 ml; 2.20 mmol) was added dropwise and the stirring was continued at –78 °C. After 40 min the mixture was allowed to warm to RT and stirred at this temperature for the next 1.5 h. Afterwards, the reaction was quenched with a saturated aqueous solution of NH_4Cl. A water layer was extracted with CH_2Cl_2, dried over Na_2SO_4, filtered and evaporated. The crude product was purified by column chromatography (silica; pentane/EtOAc 9:1) and crystallized (EtOAc/pentane) to give **Ald5** (225 mg, 66 %) as orange crystals. M.p. 215 – 218 °C (EtOAc/pentane). ^{1}H NMR (400 MHz, $CDCl_3$, 25 °C) δ 9.96 (s, 1H), 9.90 (s, 1H), 8.32 (s, 1H), 7.87 (s, 1H), 6.70 (s, 4H), 2.20 (s, 6H), 1.87 (s, 12H). ^{13}C NMR (100 MHz, $CDCl_3$, 25 °C) δ 184.4, 180.6, 170.2, 152.7, 145.2, 140.1, 138.8, 138.7, 135.8, 135.5, 130.1, 24.6, 20.9 (two carbon signals corresponding to the C atoms bound to the B atom are not visible due to the quadrupolar relaxation). MS HR (ESI) *m*/*z* calcd. for $C_{27}H_{26}BNNaO_2S_2$ [*M*+Na]$^+$ 494.1390, found 494.1386. Anal. calcd. for $C_{27}H_{26}BNO_2S_2$: C, 68.79, H, 5.56, N, 2.97, S, 13.60. Found: C, 68.71, H, 5.69, N, 2.92, S, 13.69.

Synthesis of Compound AπA1a

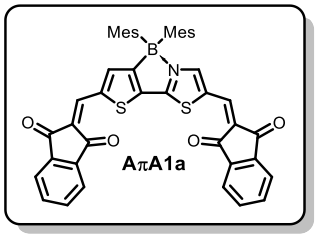

To dialdehyde **Ald5** (100 mg, 0.21 mmol) and compound **A1** (124 mg, 0.85 mmol) in dichloroethane (8 ml) dry pyridine (0.17 ml, 2.11 mmol) was added and the reaction mixture was stirred at 60 °C for 2.5 h. Then the solution was loaded on a column and chromatographed (silica, CH_2Cl_2). After recrystallization (CH_2Cl_2/pentane) pure **AπA1a** (81 mg, 53 %) was obtained as a dark red solid. ^{1}H NMR (400 MHz, CD_2Cl_2, 25 °C) δ 9.89 (s, 1H), 8.31 (s, 1H), 7.98 – 7.88 (m, 2H), 7.83 – 7.77 (m, 3H), 7.75 (s, 1H), 6.59 (s, 4H), 2.09 (s, 6H), 1.79 (s, 12H). ^{13}C NMR (101 MHz, CD_2Cl_2, 25 °C) δ 190.3, 189.83, 189.76, 188.8, 171.2, 149.0, 148.0, 144.3, 142.8, 142.4, 141.4, 141.2, 140.6, 140.4, 136.5, 136.4, 136.1, 136.0, 135.9, 135.1, 132.9, 131.5, 130.4, 128.1, 127.6, 124.99, 123.96, 123.7, 24.9, 21.0 (two carbon signals corresponding to the C atoms bound to the B atom are not visible due to the quadrupolar relaxation). ^{11}B NMR (128 MHz, CD_2Cl_2, 25 °C) δ 5.17. UV/vis (CH_2Cl_2, c = 1.02 × 10^{-5} M): λ_{max}/nm 530 (ε/M^{-1} cm^{-1} 55 900), 493 (53 800), 361 (20 800) with two shoulders. MS HR (ESI) m/z calcd. for $C_{45}H_{35}BNO_4S_2$ $[M+H]^+$ 728.2095, found 728.2086.

Synthesis of Compound AπA1b

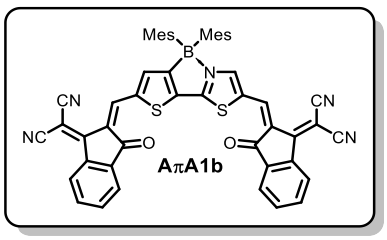

A flask was charged with compound **Ald5** (100.0 mg; 0.21 mmol) and CH-acid **A2** (165 mg; 0.85 mmol). Then DCE (8 ml) and pyridine (0.17 ml; 2.11 mmol) were added and the reaction mixture was stirred at 60 °C for 2 h. Afterwards, the reaction was cooled to RT and the precipitate was filtered and washed with acetone (150 ml). The resulting solid was suspended in the mixture of acetone and pentane and filtered to give **AπA1b** (130 mg, 74 %) as dark purple crystals. ^{1}H NMR (400 MHz, $C_2D_2Cl_4$, 125 °C) δ 8.86 (s, 1H), 8.83 – 8.74 (m, 2H), 8.72 (s, 1H), 8.37 (s, 1H), 8.07 (t, J = 5.9 Hz, 2H), 7.97 – 7.77 (m, 5H), 6.76 (s, 4H), 2.27 (s, 6H), 2.06 (s, 12H). ^{1}H NMR (600 MHz, $C_2D_2Cl_4$, 75 °C) δ 8.88 (s, 1H), 8.82 – 8.64 (m, 3H), 8.42 – 8.29 (m, 1H), 8.14 – 7.99 (m, 2H), 7.97 – 7.78 (m, 5H), 6.72 (s, 4H), 2.24 (s, 6H), 1.95 (s, 12H). ^{13}C NMR (151 MHz, CD_2Cl_2, 75 °C) δ 188.0, 187.5, 170.8, 159.5, 158.2, 151.4, 146.5, 145.4, 143.9, 141.0, 140.1, 137.2, 136.9, 136.5, 136.2, 135.5, 135.2, 134.9, 133.0, 132.4, 129.6, 126.5, 125.5, 125.3, 124.5, 124.2, 123.6,

120.2, 113.9, 113.4, 99.5, 79.7, 79.5, 79.4, 24.0, 20.7 (two carbon signals corresponding to the C atoms bound to the B atom are not visible due to the quadrupolar relaxation). Compound **AπA1b** features very low solubility. ^{1}H NMR spectra were measured at 125 °C and 75 °C. The measurement at 125 °C shows sharper proton signals. However, the ^{13}C NMR spectrum could not be collected at such a high temperature because a sample partially decomposed during the required long acquisition time. ^{11}B NMR (128 MHz, CD_2Cl_2, 25 °C) δ 3.89. UV/vis (CH_2Cl_2, c = 4.10 × 10^{-6} M): λ_{max}/nm 589 (ε/M^{-1} cm^{-1} 67 300), 554 (61 500), 305 (43 300) with two shoulders. MS LR (MALDI) *m*/*z* calcd. for $C_{51}H_{34}BN_5O_2S_2$ M^+ 823.2, found 823.2. MS HR (ESI) *m*/*z* calcd. for $C_{51}H_{35}BN_5O_2S_2$ $[M+H]^+$ 824.2320, found 824.2333.

Synthesis of Compound AπA1c

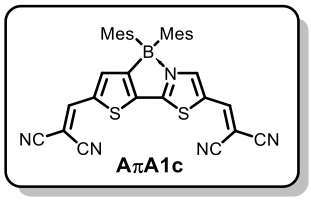

AπA1c

To dialdehyde **Ald5** (100 mg, 0.21 mmol) and compound **A3** (56 mg, 0.85 mmol) in dichloroethane (8 ml) dry pyridine (0.17 ml, 2.11 mmol) was added and the reaction mixture was stirred at 60 °C for 1 h 45 min. Then the solution was loaded on a column and chromatographed (silica, CH_2Cl_2). The consecutive chromatography (silica, CH_2Cl_2/pentane 4:1) afforded pure product, which was recrystallized (CH_2Cl_2/pentane), to give **AπA1c** (92 mg, 77 %) as a red solid. ^{1}H NMR (400 MHz, CD_2Cl_2, 25 °C) δ 8.23 (d, J = 0.5 Hz, 1H), 7.91 (d, J = 0.5 Hz, 1H), 7.86 (d, J = 0.5 Hz, 1H), 7.71 (d, J = 0.5 Hz, 1H), 6.69 (s, 4H), 2.18 (s, 6H), 1.86 (s, 12H). ^{13}C NMR (101 MHz, CD_2Cl_2, 25 °C) δ 168.6, 151.7, 148.2, 148.1, 144.6, 142.3, 140.6, 139.8, 136.8, 131.8, 130.4, 113.9, 113.4, 113.0, 112.8, 83.3, 81.9, 24.6, 21.1 (two carbon signals corresponding to the C atoms bound to the B atom are not visible due to the quadrupolar relaxation). ^{11}B NMR (128 MHz, CD_2Cl_2, 25 °C) δ 3.24. UV/vis (CH_2Cl_2, c = 6.89 × 10^{-5} M): λ_{max}/nm 454 (ε/M^{-1} cm^{-1} 35 400), 325 (17 100). MS HR (ESI) *m*/*z* calcd. for $C_{33}H_{26}BN_5NaS_2$ $[M+Na]^+$ 590.1615, found 590.1611.

References

[1] M. Grooten, R. Almond, R. McLellan, World Wide Fund for Nature, *Living Planet Report 2012: Biodiversity, Biocapacity and Better Choices*, World Wide Fund For Nature, Gland, Switzerland, **2012**.

[2] BP, "BP Statistical Review of World Energy," can be found under http://www.bp.com/content/dam/bp/pdf/energy-economics/statistical-review-2016/bp-statistical-review-of-world-energy-2016-full-report.pdf., **2016**.

[3] J. Martens, W. Obenland, *Die 2030-Agenda: globale Zukunftsziele für nachhaltige Entwicklung*, Global Policy Forum, Bonn, **2016**.

[4] M. Mungai, "World Energy Resources," can be found under https://www.worldenergy.org/wp-content/uploads/2016/10/World-Energy-Resources-Full-report-2016.10.03.pdf., **2016**.

[5] Enerdata, "Global Energy Statistical Yearbook," can be found under https://yearbook.enerdata.net/, **2016**.

[6] P. Würfel, *Physik der Solarzellen*, Spektrum, Akad. Verl, Heidelberg, **2000**.

[7] A. E. Becquerel, *Comptes Rendus Acad. Sci.* **1839**, *9*, 145–149.

[8] D. M. Chapin, C. S. Fuller, G. L. Pearson, *J. Appl. Phys.* **1954**, *25*, 676–677.

[9] C. Battaglia, A. Cuevas, S. D. Wolf, *Energy Environ. Sci.* **2016**, *9*, 1552–1576.

[10] K. Yoshikawa, H. Kawasaki, W. Yoshida, T. Irie, K. Konishi, K. Nakano, T. Uto, D. Adachi, M. Kanematsu, H. Uzu, et al., *Nat. Energy* **2017**, *2*, 17032.

[11] R. Frischknecht, "Life Cycle Inventories and Life Cycle Assessment of Photovoltaic Systems," can be found under www.seas.columbia.edu/clca/Task12_LCI_LCA_10_21_Final_Report.pdf., **2015**.

[12] N. Espinosa, M. Hösel, D. Angmo, F. C. Krebs, *Energy Environ. Sci.* **2012**, *5*, 5117–5132.

[13] K. A. Mazzio, C. K. Luscombe, *Chem. Soc. Rev.* **2014**, *44*, 78–90.

[14] National Renewable Energy Laboratory, "Best Research-Cell Efficiencies," can be found under https://www.nrel.gov/pv/, **2016**.

[15] C. J. Brabec, S. Gowrisanker, J. J. M. Halls, D. Laird, S. Jia, S. P. Williams, *Adv. Mater.* **2010**, *22*, 3839–3856.

[16] P. Sonar, J. P. F. Lim, K. Leok Chan, *Energy Environ. Sci.* **2011**, *4*, 1558–1574.

[17] Y. Lin, X. Zhan, *Mater. Horiz.* **2014**, *1*, 470–488.

[18] W. Kang, M. Kitamura, Y. Arakawa, *Appl. Phys. Express* **2011**, *4*, 121602.

[19] H. Li, B. C.-K. Tee, J. J. Cha, Y. Cui, J. W. Chung, S. Y. Lee, Z. Bao, *J. Am. Chem. Soc.* **2012**, *134*, 2760–2765.

[20] J. E. Anthony, *Chem. Mater.* **2011**, *23*, 583–590.

[21] G. Sauvé, R. Fernando, *J. Phys. Chem. Lett.* **2015**, *6*, 3770–3780.

[22] V. A. Trukhanov, D. Y. Paraschuk, *Polym. Sci. Ser. C* **2014**, *56*, 72–83.

[23] C. Zhan, X. Zhang, J. Yao, *RSC Adv.* **2015**, *5*, 93002–93026.

[24] W. Chen, Q. Zhang, *J. Mater. Chem. C* **2017**, *5*, 1275–1302.

[25] Y. Duan, X. Xu, Y. Li, Q. Peng, *Chin. Chem. Lett.* **2017**, *28*, 2105–2115.

[26] S. Li, L. Ye, W. Zhao, S. Zhang, S. Mukherjee, H. Ade, J. Hou, *Adv. Mater.* **2016**, *28*, 9423–9429.

[27] C. W. Tang, *Appl. Phys. Lett.* **1986**, *48*, 183–185.

[28] J. Roncali, *Adv. Energy Mater.* **2011**, *1*, 147–160.

[29] K. Nakano, K. Tajima, *Adv. Mater.* **2017**, *29*, DOI: 10.1002/adma.201603269.

[30] G. Yu, J. Gao, J. C. Hummelen, F. Wudl, A. J. Heeger, *Science* **1995**, *270*, 1789–1791.
[31] X. Liu, L. Nian, K. Gao, L. Zhang, L. Qing, Z. Wang, L. Ying, Z. Xie, Y. Ma, Y. Cao, et al., *J. Mater. Chem. A* **2017**, *5*, 17619–17631.
[32] K. Cnops, B. P. Rand, D. Cheyns, B. Verreet, M. A. Empl, P. Heremans, *Nat. Commun.* **2014**, *5*, 3406.
[33] U. Mehmood, A. Al-Ahmed, M. Afzaal, F. A. Al-Sulaiman, M. Daud, *Renew. Sustain. Energy Rev.* **2017**, *78*, 1–14.
[34] R. E. Haufler, J. Conceicao, L. P. F. Chibante, Y. Chai, N. E. Byrne, S. Flanagan, M. M. Haley, S. C. O'Brien, C. Pan, *J. Phys. Chem.* **1990**, *94*, 8634–8636.
[35] M. G. Debije, P. P. C. Verbunt, *Adv. Energy Mater.* **2012**, *2*, 12–35.
[36] M. Khamooshi, H. Salati, F. Egelioglu, A. Hooshyar Faghiri, J. Tarabishi, S. Babadi, *Int. J. Photoenergy* **2014**, 958521.
[37] O. Adebanjo, B. Vaagensmith, Q. Qiao, *J. Mater. Chem. A* **2014**, *2*, 10331–10349.
[38] O. Adebanjo, P. P. Maharjan, P. Adhikary, M. Wang, S. Yang, Q. Qiao, *Energy Environ. Sci.* **2013**, *6*, 3150–3170.
[39] L. Nian, Z. Chen, S. Herbst, Q. Li, C. Yu, X. Jiang, H. Dong, F. Li, L. Liu, F. Würthner, et al., *Adv. Mater.* **2016**, *28*, 7521–7526.
[40] Z. Xie, F. Würthner, *Adv. Energy Mater.* **2017**, *7*, 1602573.
[41] S. K. Hau, H.-L. Yip, A. K.-Y. Jen, *Polym. Rev.* **2010**, *50*, 474–510.
[42] Z. He, C. Zhong, S. Su, M. Xu, H. Wu, Y. Cao, *Nat. Photonics* **2012**, *6*, 591.
[43] R. Steim, F. R. Kogler, C. J. Brabec, *J. Mater. Chem.* **2010**, *20*, 2499–2512.
[44] R. T. Tung, *Mater. Sci. Eng. R Rep.* **2001**, *35*, 1–138.
[45] F. Jin, Z. Su, B. Chu, P. Cheng, J. Wang, H. Zhao, Y. Gao, X. Yan, W. Li, *Sci. Rep.* **2016**, *6*, 26262.
[46] H.-L. Yip, A. K.-Y. Jen, *Energy Environ. Sci.* **2012**, *5*, 5994–6011.
[47] H. Huang, W. Deng, *Organic and Hybrid Solar Cells*, Springer, New York, **2014**.
[48] S. B. Dkhil, D. Duché, M. Gaceur, A. K. Thakur, F. B. Aboura, L. Escoubas, J.-J. Simon, A. Guerrero, J. Bisquert, G. Garcia-Belmonte, et al., *Adv. Energy Mater.* **2014**, *4*, DOI: 10.1002/aenm.201400805.
[49] E. L. Ratcliff, B. Zacher, N. R. Armstrong, *J. Phys. Chem. Lett.* **2011**, *2*, 1337–1350.
[50] J. Hwang, F. Amy, A. Kahn, *Org. Electron.* **2006**, *7*, 387–396.
[51] M. Kemerink, S. Timpanaro, M. M. de Kok, E. A. Meulenkamp, F. J. Touwslager, *J. Phys. Chem. B* **2004**, *108*, 18820–18825.
[52] M. A. Leaf, M. Muthukumar, *Macromol.* **2016**, *49*, 4286–4294.
[53] L. S. C. Pingree, B. A. MacLeod, D. S. Ginger, *J. Phys. Chem. C* **2008**, *112*, 7922–7927.
[54] A. M. Nardes, M. Kemerink, R. A. J. Janssen, J. A. M. Bastiaansen, N. M. M. Kiggen, B. M. W. Langeveld, A. J. J. M. van Breemen, M. M. de Kok, *Adv. Mater.* **2007**, *19*, 1196–1200.
[55] A. M. Nardes, M. Kemerink, M. M. de Kok, E. Vinken, K. Maturova, R. A. J. Janssen, *Org. Electron.* **2008**, *9*, 727–734.
[56] Y. H. Kim, C. Sachse, M. L. Machala, C. May, L. Müller-Meskamp, K. Leo, *Adv. Funct. Mater.* **2011**, *21*, 1076–1081.
[57] S. Savagatrup, E. Chan, S. M. Renteria-Garcia, A. D. Printz, A. V. Zaretski, T. F. O'Connor, D. Rodriquez, E. Valle, D. J. Lipomi, *Adv. Funct. Mater.* **2015**, *25*, 427–436.

[58] S. D. Yambem, K.-S. Liao, N. J. Alley, S. A. Curran, *J. Mater. Chem.* **2012**, *22*, 6894–6898.
[59] E. Andreoli, K.-S. Liao, A. Haldar, N. J. Alley, S. A. Curran, *Synth. Met.* **2013**, *185–186*, 71–78.
[60] Z. Yin, J. Wei, Q. Zheng, *Adv. Sci.* **2016**, *3*, 1500362.
[61] J. Meyer, R. Khalandovsky, P. Görrn, A. Kahn, *Adv. Mater.* **2011**, *23*, 70–73.
[62] F. Xie, W. C. H. Choy, C. Wang, X. Li, S. Zhang, J. Hou, *Adv. Mater.* **2013**, *25*, 2051–2055.
[63] S. Chen, J. R. Manders, S.-W. Tsang, F. So, *J. Mater. Chem.* **2012**, *22*, 24202–24212.
[64] K. T. Butler, R. Crespo-Otero, J. Buckeridge, D. O. Scanlon, E. Bovill, D. Lidzey, A. Walsh, *Appl. Phys. Lett.* **2015**, *107*, 231605.
[65] H. Jin, M. Tuomikoski, J. Hiltunen, P. Kopola, A. Maaninen, F. Pino, *J. Phys. Chem. C* **2009**, *113*, 16807–16810.
[66] R. Po, C. Carbonera, A. Bernardi, N. Camaioni, *Energy Environ. Sci.* **2011**, *4*, 285–310.
[67] C. J. Brabec, S. E. Shaheen, C. Winder, N. S. Sariciftci, P. Denk, *Appl. Phys. Lett.* **2002**, *80*, 1288–1290.
[68] E. Ahlswede, J. Hanisch, M. Powalla, *Appl. Phys. Lett.* **2007**, *90*, 163504.
[69] T. M. Brown, R. H. Friend, I. S. Millard, D. J. Lacey, J. H. Burroughes, F. Cacialli, *Appl. Phys. Lett.* **2000**, *77*, 3096–3098.
[70] S. K. M. Jönsson, E. Carlegrim, F. Zhang, W. R. Salaneck, M. Fahlman, *Jpn. J. Appl. Phys.* **2005**, *44*, 3695–3701.
[71] B. N. Limketkai, M. A. Baldo, *Phys. Rev. B* **2005**, *71*, 085207.
[72] M. Klessinger, J. Michl, *Excited States and Photochemistry of Organic Molecules*, Wiley-VCH, New York, **1995**.
[73] V. Janković, N. Vukmirović, *Phys. Rev. B* **2015**, *92*, 235208.
[74] D. D. S. Fung, W. C. H. Choy, *Organic Solar Cells: Materials and Device Physics*, Springer, London, **2013**.
[75] T. Dittrich, *Materials Concepts for Solar Cells*, Imperial College Press, New Jersey, **2015**.
[76] I. G. Hill, A. Kahn, Z. G. Soos, J. Pascal R. A., *Chem. Phys. Lett.* **2000**, *327*, 181–188.
[77] P. I. Djurovich, E. I. Mayo, S. R. Forrest, M. E. Thompson, *Org. Electron.* **2009**, *10*, 515–520.
[78] B. A. Gregg, *J. Phys. Chem. B* **2003**, *107*, 4688–4698.
[79] O. V. Mikhnenko, H. Azimi, M. Scharber, M. Morana, P. W. M. Blom, M. Antonietta Loi, *Energy Environ. Sci.* **2012**, *5*, 6960–6965.
[80] O. V. Mikhnenko, P. W. M. Blom, T.-Q. Nguyen, *Energy Environ. Sci.* **2015**, *8*, 1867–1888.
[81] O. A. Abdulrazzaq, V. Saini, S. Bourdo, E. Dervishi, A. S. Biris, *Part. Sci. Technol.* **2013**, *31*, 427–442.
[82] Y. Tamai, H. Ohkita, H. Benten, S. Ito, *J. Phys. Chem. Lett.* **2015**, *6*, 3417–3428.
[83] B. A. Gregg, J. Sprague, M. W. Peterson, *J. Phys. Chem. B* **1997**, *101*, 5362–5369.
[84] N. S. Sariciftci, L. Smilowitz, A. J. Heeger, F. Wudl, *Science* **1992**, *258*, 1474–1476.
[85] Y. Moritomo, K. Yonezawa, T. Yasuda, *Int. J. Photoenergy* **2016**, 9105460.
[86] T. M. Clarke, J. R. Durrant, *Chem. Rev.* **2010**, *110*, 6736–6767.
[87] B. A. Gregg, M. A. Fox, A. J. Bard, *J. Phys. Chem.* **1990**, *94*, 1586–1598.

[88] N. Geacintov, M. Pope, H. Kallmann, *J. Chem. Phys.* **1966**, *45*, 2639–2649.
[89] A. Pivrikas, H. Neugebauer, N. S. Sariciftci, *IEEE J. Sel. Top. Quantum Electron.* **2010**, *16*, 1746–1758.
[90] H. Bässler, A. Köhler, in *Unimolecular Supramol. Electron. I*, Springer, Berlin, Heidelberg, **2011**.
[91] H. Sirringhaus, *Adv. Mater.* **2014**, *26*, 1319–1335.
[92] L. J. A. Koster, V. D. Mihailetchi, P. W. M. Blom, *Appl. Phys. Lett.* **2006**, *88*, 052104.
[93] M. Abbas, N. Tekin, *Appl. Phys. Lett.* **2012**, *101*, 073302.
[94] M. M. Mandoc, L. J. A. Koster, P. W. M. Blom, *Appl. Phys. Lett.* **2007**, *90*, 133504.
[95] W. Tress, Device Physics of Organic Solar Cells Drift-Diffusion Simulation in Comparison with Experimental Data of Solar Cells Based on Small Molecules, Technische Universität Dresden, **2011**.
[96] B. P. Rand, H. Richter, *Organic Solar Cells: Fundamentals, Devices, and Upscaling*, CRC Press, Miami, **2014**.
[97] F. C. Krebs, *Sol. Energy Mater. Sol. Cells* **2006**, *90*, 3633–3643.
[98] F. C. Krebs, J. E. Carlé, N. Cruys-Bagger, M. Andersen, M. R. Lilliedal, M. A. Hammond, S. Hvidt, *Sol. Energy Mater. Sol. Cells* **2005**, *86*, 499–516.
[99] M. P. de Jong, L. J. van IJzendoorn, M. J. A. de Voigt, *Appl. Phys. Lett.* **2000**, *77*, 2255–2257.
[100] F. C. Krebs, K. Norrman, *Prog. Photovolt. Res. Appl.* **2007**, *15*, 697–712.
[101] S. T. Lee, Z. Q. Gao, L. S. Hung, *Appl. Phys. Lett.* **1999**, *75*, 1404–1406.
[102] M. Lögdlund, J. L. Brédas, *J. Chem. Phys.* **1994**, *101*, 4357–4364.
[103] R. D. Scurlock, B. Wang, P. R. Ogilby, J. R. Sheats, R. L. Clough, *J. Am. Chem. Soc.* **1995**, *117*, 10194–10202.
[104] M. Jørgensen, K. Norrman, F. C. Krebs, *Sol. Energy Mater. Sol. Cells* **2008**, *92*, 686–714.
[105] J. Ajuria, I. Ugarte, W. Cambarau, I. Etxebarria, R. Tena-Zaera, R. Pacios, *Sol Energ Mat Sol C* **2012**, *102*, 148–152.
[106] S. K. Hau, H.-L. Yip, N. S. Baek, J. Zou, K. O'Malley, A. K.-Y. Jen, *Appl. Phys. Lett.* **2008**, *92*, 253301.
[107] J. D. Servaites, M. A. Ratner, T. J. Marks, *Energy Environ. Sci.* **2011**, *4*, 4410–4422.
[108] National Renewable Energy Laboratory, "Reference Solar Spectral Irradiance: Air Mass 1.5," can be found under http://rredc.nrel.gov/solar/spectra/am1.5/#refs, **2017**.
[109] A. Cheknane, H. S. Hilal, F. Djeffal, B. Benyoucef, J.-P. Charles, *Microelectron. J.* **2008**, *39*, 1173–1180.
[110] A. M. Humada, M. Hojabri, S. Mekhilef, H. M. Hamada, *Renew. Sustain. Energy Rev.* **2016**, *56*, 494–509.
[111] W. Shockley, H. J. Queisser, *J. Appl. Phys.* **1961**, *32*, 510–519.
[112] M. C. Scharber, N. S. Sariciftci, *Prog. Polym. Sci.* **2013**, *38*, 1929–1940.
[113] T. Ameri, G. Dennler, C. Lungenschmied, C. J. Brabec, *Energy Environ. Sci.* **2009**, *2*, 347–363.
[114] J. C. Bijleveld, M. Shahid, J. Gilot, M. M. Wienk, R. A. J. Janssen, *Adv. Funct. Mater.* **2009**, *19*, 3262–3270.
[115] A. De Vos, *J. Phys. Appl. Phys.* **1980**, *13*, 839–846.

[116] N. Khoshsirat, N. A. M. Yunus, *Nanoelectronics and Materials Development*, InTech, London, **2016**.
[117] Y.-W. Su, S.-C. Lan, K.-H. Wei, *Mater. Today* **2012**, *15*, 554–562.
[118] V. Shrotriya, G. Li, Y. Yao, T. Moriarty, K. Emery, Y. Yang, *Adv. Funct. Mater.* **2006**, *16*, 2016–2023.
[119] H. J. Snaith, *Energy Environ. Sci.* **2012**, *5*, 6513–6520.
[120] S. Ito, M. K. Nazeeruddin, P. Liska, P. Comte, R. Charvet, P. Péchy, M. Jirousek, A. Kay, S. M. Zakeeruddin, M. Grätzel, *Prog. Photovolt. Res. Appl.* **2006**, *14*, 589–601.
[121] R. E. Smallman, A. H. W. Ngan, *Physical Metallurgy and Advanced Materials*, Butterworth-Heinemann, Oxford, **2011**.
[122] M. C. Scharber, D. Mühlbacher, M. Koppe, P. Denk, C. Waldauf, A. J. Heeger, C. J. Brabec, *Adv. Mater.* **2006**, *18*, 789–794.
[123] Q. Wang, S. Zhang, B. Xu, L. Ye, H. Yao, Y. Cui, H. Zhang, W. Yuan, J. Hou, *Chem. – Asian J.* **2016**, *11*, 2650–2655.
[124] N. Kleinhenz, L. Yang, H. Zhou, S. C. Price, W. You, *Macromol.* **2011**, *44*, 872–877.
[125] S. A. Jenekhe, L. Lu, M. M. Alam, *Macromol.* **2001**, *34*, 7315–7324.
[126] A. D. Thilanga Liyanage, B. Milián-Medina, B. Zhang, J. Gierschner, M. D. Watson, *Macromol. Chem. Phys.* **2016**, *217*, 2068–2073.
[127] E. F. Oliveira, J. C. Roldao, B. Milián-Medina, F. C. Lavarda, J. Gierschner, *Chem. Phys. Lett.* **2016**, *645*, 169–173.
[128] M. Wykes, B. Milián-Medina, J. Gierschner, *Front. Chem.* **2013**, *1*, 1–12.
[129] T. Dutta, K. B. Woody, S. R. Parkin, M. D. Watson, J. Gierschner, *J. Am. Chem. Soc.* **2009**, *131*, 17321–17327.
[130] B. Milián-Medina, M. Wykes, Z. Chen, A. Facchetti, J. Gierschner, *J. Mater. Chem. C* **2016**, *4*, 9405–9410.
[131] R. D. McCullough, *Adv. Mater.* **1998**, *10*, 93–116.
[132] M.-H. Choi, K. Wook Song, D. Kyung Moon, *Polym. Chem.* **2015**, *6*, 2636–2646.
[133] W. Zhang, Z. Mao, N. Zheng, J. Zou, L. Wang, C. Wei, J. Huang, D. Gao, G. Yu, *J. Mater. Chem. C* **2016**, *4*, 9266–9275.
[134] M. Vetrichelvan, S. Valiyaveettil, *Chem Eur J* **2005**, *11*, 5889–5898.
[135] D. Chen, S.-J. Su, Y. Cao, *J. Mater. Chem. C* **2014**, *2*, 9565–9578.
[136] J. Gierschner, J. Cornil, H.-J. Egelhaaf, *Adv. Mater.* **2007**, *19*, 173–191.
[137] R. E. Peierls, *Quantum Theory of Solids*, Clarendon Press, Oxford, New York, **2001**.
[138] T. Izumi, S. Kobashi, K. Takimiya, Y. Aso, T. Otsubo, *J. Am. Chem. Soc.* **2003**, *125*, 5286–5287.
[139] S. Seki, A. Saeki, T. Sakurai, D. Sakamaki, *Phys. Chem. Chem. Phys.* **2014**, *16*, 11093–11113.
[140] B. Shan, Q. Miao, *Tetrahedron Lett.* **2017**, *58*, 1903–1911.
[141] W. Lin Leong, G. C. Welch, L. G. Kaake, C. J. Takacs, Y. Sun, G. C. Bazan, A. J. Heeger, *Chem. Sci.* **2012**, *3*, 2103–2109.
[142] K. T. Nielsen, K. Bechgaard, F. C. Krebs, *Macromol.* **2005**, *38*, 658–659.
[143] M. Wang, F. Wudl, *J. Mater. Chem.* **2012**, *22*, 24297–24314.
[144] C. B. Kc, G. N. Lim, V. N. Nesterov, P. A. Karr, F. D'Souza, *Chem. – Eur. J.* **2014**, *20*, 17100–17112.
[145] J. R. Pinzón, D. C. Gasca, S. G. Sankaranarayanan, G. Bottari, T. Torres, D. M. Guldi, L. Echegoyen, *J. Am. Chem. Soc.* **2009**, *131*, 7727–7734.

[146] G. Possamai, N. Camaioni, G. Ridolfi, L. Franco, M. Ruzzi, E. Menna, G. Casalbore-Miceli, A. M. Fichera, G. Scorrano, C. Corvaja, et al., *Synth. Met.* **2003**, *139*, 585–588.
[147] J. B. Kim, K. Allen, S. J. Oh, S. Lee, M. F. Toney, Y. S. Kim, C. R. Kagan, C. Nuckolls, Y.-L. Loo, *Chem. Mater.* **2010**, *22*, 5762–5773.
[148] T. Nishizawa, K. Tajima, K. Hashimoto, *J. Mater. Chem.* **2007**, *17*, 2440–2445.
[149] T. Nishizawa, H. K. Lim, K. Tajima, K. Hashimoto, *Chem. Commun.* **2009**, *0*, 2469–2471.
[150] S. Izawa, K. Hashimoto, K. Tajima, *Chem. Commun.* **2011**, *47*, 6365–6367.
[151] K. Narayanaswamy, A. Venkateswararao, P. Nagarjuna, S. Bishnoi, V. Gupta, S. Chand, S. P. Singh, *Angew. Chem. Int. Ed.* **2016**, *55*, 12334–12337.
[152] T. L. Chen, Y. Zhang, P. Smith, A. Tamayo, Y. Liu, B. Ma, *ACS Appl. Mater. Interfaces* **2011**, *3*, 2275–2280.
[153] W. Yan, S. M. Seifermann, P. Pierrat, S. Bräse, *Org. Biomol. Chem.* **2014**, *13*, 25–54.
[154] S. Kirner, M. Sekita, D. M. Guldi, *Adv. Mater.* **2014**, *26*, 1482–1493.
[155] C.-Z. Li, H.-L. Yip, A. K.-Y. Jen, *J. Mater. Chem.* **2012**, *22*, 4161–4177.
[156] W. Krätschmer, L. D. Lamb, K. Fostiropoulos, D. R. Huffman, *Nature* **1990**, *347*, 354–358.
[157] W. J. Anton, R. W. Stephen, I. S. David, *Biological Applications of Fullerenes*, Elsevier Science, New York, **1996**.
[158] B. C. Yadav, R. Kumar, *Int. J. Nanotechnol. Appl.* **2008**, *2*, 15–24.
[159] R. F. Verner, C. Benvegnu, *Handbook on Fullerene: Synthesis, Properties and Applications*, Nova Science Publishers, New York, **2012**.
[160] A. Mishra, P. Bäuerle, *Angew. Chem. Int. Ed.* **2012**, *51*, 2020–2067.
[161] Y. Lin, Y. Li, X. Zhan, *Chem Soc Rev* **2012**, *41*, 4245–4272.
[162] J. Roncali, P. Leriche, P. Blanchard, *Adv. Mater.* **2014**, *26*, 3821–3838.
[163] L. Lu, T. Zheng, Q. Wu, A. M. Schneider, D. Zhao, L. Yu, *Chem. Rev.* **2015**, *115*, 12666–12731.
[164] C. A. Reed, R. D. Bolskar, *Chem. Rev.* **2000**, *100*, 1075–1120.
[165] Y. Liu, C.-C. Chen, Z. Hong, J. Gao, Y. M. Yang, H. Zhou, L. Dou, G. Li, Y. Yang, *Sci. Rep.* **2013**, *3*, 3356.
[166] S. Zhang, L. Ye, J. Hou, *Adv. Energy Mater.* **2016**, *6*, 1502529.
[167] W. Yu, L. Huang, D. Yang, P. Fu, L. Zhou, J. Zhang, C. Li, *J. Mater. Chem. A* **2015**, *3*, 10660–10665.
[168] C. Liu, C. Yi, K. Wang, Y. Yang, R. S. Bhatta, M. Tsige, S. Xiao, X. Gong, *ACS Appl. Mater. Interfaces* **2015**, *7*, 4928–4935.
[169] R. Ganesamoorthy, G. Sathiyan, P. Sakthivel, *Sol Energ Mat Sol C* **2017**, *161*, 102–148.
[170] H. Kang, W. Lee, J. Oh, T. Kim, C. Lee, B. J. Kim, *Acc. Chem. Res.* **2016**, *49*, 2424–2434.
[171] Y. Lin, X. Zhan, *Adv. Energy Mater.* **2015**, *5*, DOI: 10.1002/aenm.201501063.
[172] M. Jørgensen, K. Norrman, S. A. Gevorgyan, T. Tromholt, B. Andreasen, F. C. Krebs, *Adv. Mater.* **2012**, *24*, 580–612.
[173] T. Heumueller, W. R. Mateker, A. Distler, U. F. Fritze, R. Cheacharoen, W. H. Nguyen, M. Biele, M. Salvador, M. von Delius, H.-J. Egelhaaf, et al., *Energy Environ. Sci.* **2016**, *9*, 247–256.
[174] G. Feng, Y. Xu, J. Zhang, Z. Wang, Y. Zhou, Y. Li, Z. Wei, C. Li, W. Li, *J. Mater. Chem. A* **2016**, *4*, 6056–6063.

[175] S. V. Dayneko, A. D. Hendsbee, G. C. Welch, *Chem. Commun.* **2017**, *53*, 1164–1167.
[176] X. Jiang, Y. Xu, X. Wang, Y. Wu, G. Feng, C. Li, W. Ma, W. Li, *Phys. Chem. Chem. Phys.* **2017**, *19*, 8069–8075.
[177] Y. Chen, X. Wan, G. Long, *Acc. Chem. Res.* **2013**, *46*, 2645–2655.
[178] H. Bai, Y. Wang, P. Cheng, Y. Li, D. Zhu, X. Zhan, *ACS Appl. Mater. Interfaces* **2014**, *6*, 8426–8433.
[179] X. Zhang, Z. Lu, L. Ye, C. Zhan, J. Hou, S. Zhang, B. Jiang, Y. Zhao, J. Huang, S. Zhang, et al., *Adv. Mater.* **2013**, *25*, 5791–5797.
[180] S. Li, Z. Zhang, M. Shi, C.-Z. Li, H. Chen, *Phys. Chem. Chem. Phys.* **2017**, *19*, 3440–3458.
[181] D. Meng, D. Sun, C. Zhong, T. Liu, B. Fan, L. Huo, Y. Li, W. Jiang, H. Choi, T. Kim, et al., *J. Am. Chem. Soc.* **2016**, *138*, 375–380.
[182] J. Liu, S. Chen, D. Qian, B. Gautam, G. Yang, J. Zhao, J. Bergqvist, F. Zhang, W. Ma, H. Ade, et al., *Nat. Energy* **2016**, *1*, 16089.
[183] H. Bin, Z.-G. Zhang, L. Gao, S. Chen, L. Zhong, L. Xue, C. Yang, Y. Li, *J. Am. Chem. Soc.* **2016**, *138*, 4657–4664.
[184] Y.-J. Hwang, H. Li, B. A. E. Courtright, S. Subramaniyan, S. A. Jenekhe, *Adv. Mater.* **2016**, *28*, 124–131.
[185] Y. Li, L. Zhong, F.-P. Wu, Y. Yuan, H.-J. Bin, Z.-Q. Jiang, Z. Zhang, Z.-G. Zhang, Y. Li, L.-S. Liao, *Energy Environ. Sci.* **2016**, *9*, 3429–3435.
[186] Y. Lin, Q. He, F. Zhao, L. Huo, J. Mai, X. Lu, C.-J. Su, T. Li, J. Wang, J. Zhu, et al., *J. Am. Chem. Soc.* **2016**, *138*, 2973–2976.
[187] Y. Lin, J. Wang, Z.-G. Zhang, H. Bai, Y. Li, D. Zhu, X. Zhan, *Adv. Mater.* **2015**, *27*, 1170–1174.
[188] Y. Lin, F. Zhao, Q. He, L. Huo, Y. Wu, T. C. Parker, W. Ma, Y. Sun, C. Wang, D. Zhu, et al., *J. Am. Chem. Soc.* **2016**, *138*, 4955–4961.
[189] D. Meng, H. Fu, C. Xiao, X. Meng, T. Winands, W. Ma, W. Wei, B. Fan, L. Huo, N. L. Doltsinis, et al., *J. Am. Chem. Soc.* **2016**, *138*, 10184–10190.
[190] Q. Wu, D. Zhao, A. M. Schneider, W. Chen, L. Yu, *J. Am. Chem. Soc.* **2016**, *138*, 7248–7251.
[191] Y. Yang, Z.-G. Zhang, H. Bin, S. Chen, L. Gao, L. Xue, C. Yang, Y. Li, *J. Am. Chem. Soc.* **2016**, *138*, 15011–15018.
[192] H. Yao, Y. Chen, Y. Qin, R. Yu, Y. Cui, B. Yang, S. Li, K. Zhang, J. Hou, *Adv. Mater.* **2016**, *28*, 8283–8287.
[193] W. Zhao, D. Qian, S. Zhang, S. Li, O. Inganäs, F. Gao, J. Hou, *Adv. Mater.* **2016**, *28*, 4734–4739.
[194] Y. Zhong, M. T. Trinh, R. Chen, G. E. Purdum, P. P. Khlyabich, M. Sezen, S. Oh, H. Zhu, B. Fowler, B. Zhang, et al., *Nat. Commun.* **2015**, *6*, 8242.
[195] B. Verreet, S. Schols, D. Cheyns, B. P. Rand, H. Gommans, T. Aernouts, P. Heremans, J. Genoe, *J. Mater. Chem.* **2009**, *19*, 5295–5297.
[196] H. Bürckstümmer, E. V. Tulyakova, M. Deppisch, M. R. Lenze, N. M. Kronenberg, M. Gsänger, M. Stolte, K. Meerholz, F. Würthner, *Angew. Chem. Int. Ed.* **2011**, *50*, 11628–11632.
[197] K. Harafuji, H. Sato, T. Matsuura, Y. Omoto, T. Kaji, M. Hiramoto, *Jpn. J. Appl. Phys.* **2014**, *53*, 122303.
[198] K. Norrman, M. V. Madsen, S. A. Gevorgyan, F. C. Krebs, *J. Am. Chem. Soc.* **2010**, *132*, 16883–16892.

[199] Y. Lare, B. Kouskoussa, K. Benchouk, S. Ouro Djobo, L. Cattin, M. Morsli, F. R. Diaz, M. Gacitua, T. Abachi, M. A. del Valle, et al., *J. Phys. Chem. Solids* **2011**, *72*, 97–103.
[200] V. Sharma, S. S. Chandel, *Renew. Sustain. Energy Rev.* **2013**, *27*, 753–767.
[201] K. Kawano, R. Pacios, D. Poplavskyy, J. Nelson, D. D. C. Bradley, J. R. Durrant, *Sol. Energy Mater. Sol. Cells* **2006**, *90*, 3520–3530.
[202] J. Huang, P. F. Miller, J. S. Wilson, A. J. de Mello, J. C. de Mello, D. D. C. Bradley, *Adv. Funct. Mater.* **2005**, *15*, 290–296.
[203] R. Hansson, C. Lindqvist, L. K. E. Ericsson, A. Opitz, E. Wang, E. Moons, *Phys. Chem. Chem. Phys.* **2016**, *18*, 11132–11138.
[204] E. Mecher, F. Gallego-Gomez, C. R. Braeuchle, K. Meerholz, R. W. Wortmann, S. Yao, A. Sautter, F. Würthner, **2000**, *4104*, 118–129.
[205] F. Würthner, S. Yao, J. Schilling, R. Wortmann, M. Redi-Abshiro, E. Mecher, F. Gallego-Gomez, K. Meerholz, *J. Am. Chem. Soc.* **2001**, *123*, 2810–2824.
[206] H. Bürckstümmer, Merocyanine Dyes for Solution-Processed Organic Bulk Heterojunction Solar Cells, Julius-Maximilians-Universität Würzburg, **2011**.
[207] A. Arjona-Esteban, Synthesis and Characterization of Dipolar Merocyanine Dyes for Organic Solar Cells and Transistor Devices, Julius-Maximilians-Universität Würzburg, **2015**.
[208] F. Würthner, R. Wortmann, K. Meerholz, *ChemPhysChem* **2002**, *3*, 17–31.
[209] F. Würthner, G. Archetti, R. Schmidt, H.-G. Kuball, *Angew. Chem. Int. Ed.* **2008**, *47*, 4529–4532.
[210] A. Dieckmann, H. Bässler, P. M. Borsenberger, *J. Chem. Phys.* **1993**, *99*, 8136–8141.
[211] A. Arjona-Esteban, J. Krumrain, A. Liess, M. Stolte, L. Huang, D. Schmidt, V. Stepanenko, M. Gsänger, D. Hertel, K. Meerholz, et al., *J. Am. Chem. Soc.* **2015**, *137*, 13524–13534.
[212] A. Liess, L. Huang, A. Arjona-Esteban, A. Lv, M. Gsänger, V. Stepanenko, M. Stolte, F. Würthner, *Adv. Funct. Mater.* **2015**, *25*, 44–57.
[213] A. Liess, M. Stolte, T. He, F. Würthner, *Mater. Horiz.* **2015**, *3*, 72–77.
[214] T.-W. Ha, Y.-B. Kim, G.-S. Heo, I. Hwang, H. G. Jeon, B. Park, *RSC Adv.* **2016**, *6*, 33063–33071.
[215] M.-C. Jung, S. R. Raga, L. K. Ono, Y. Qi, *Sci. Rep.* **2015**, *5*, 9863.
[216] M. R. Lenze, Advances in Understanding Merocyanine Based Organic Solar Cells – From the Molecular Level to the Device Level, Universität zu Köln, **2014**.
[217] V. Steinmann, N. M. Kronenberg, M. R. Lenze, S. M. Graf, D. Hertel, K. Meerholz, H. Bürckstümmer, E. V. Tulyakova, F. Würthner, *Adv. Energy Mater.* **2011**, *1*, 888–893.
[218] S. M. Sze, K. K. Ng, *Physics of Semiconductor Devices*, Wiley-Interscience, Hoboken, N.J, **2007**.
[219] D. W. Sievers, V. Shrotriya, Y. Yang, *J. Appl. Phys.* **2006**, *100*, 114509.
[220] Y. Min Nam, J. Huh, W. Ho Jo, *Sol. Energy Mater. Sol. Cells* **2010**, *94*, 1118–1124.
[221] D. Hazar Apaydın, D. Esra Yildiz, A. Cirpan, L. Toppare, *Sol. Energy Mater. Sol. Cells* **2013**, *113*, 100–105.
[222] Q. Zhang, B. Kan, X. Wan, H. Zhang, F. Liu, M. Li, X. Yang, Y. Wang, W. Ni, T. P. Russell, et al., *J Mater Chem A* **2015**, *3*, 22274–22279.
[223] D. Bartesaghi, I. del C. Pérez, J. Kniepert, S. Roland, M. Turbiez, D. Neher, L. J. A. Koster, *Nat. Commun.* **2015**, *6*, 7083.

[224] J. D. Kotlarski, D. J. D. Moet, P. W. M. Blom, *J. Polym. Sci. Part B Polym. Phys.* **2011**, *49*, 708–711.
[225] A. Nowak-Król, R. Hecht, F. Kraus, A. Mishra, P. Bäuerle, F. Würthner, *Org. Chem. Front.* **2016**, *3*, 545–555.
[226] N. M. Kronenberg, M. Deppisch, F. Würthner, H. W. A. Lademann, K. Deing, K. Meerholz, *Chem. Commun.* **2008**, 6489–6491.
[227] H. Bai, Y. Wang, P. Cheng, J. Wang, Y. Wu, J. Hou, X. Zhan, *J. Mater. Chem. A* **2015**, *3*, 1910–1914.
[228] Y. Lin, Z.-G. Zhang, H. Bai, J. Wang, Y. Yao, Y. Li, D. Zhu, X. Zhan, *Energy Environ. Sci.* **2015**, *8*, 610–616.
[229] Y. Lin, X. Zhan, *Acc. Chem. Res.* **2016**, *49*, 175–183.
[230] X. Guo, S. Wang, V. Enkelmann, M. Baumgarten, K. Müllen, *Org. Lett.* **2011**, *13*, 6062–6065.
[231] J. S. Bandar, R. W. Coscia, T. H. Lambert, *Tetrahedron* **2011**, *67*, 4364–4370.
[232] P. Coppo, M. L. Turner, *J. Mater. Chem.* **2005**, *15*, 1123–1133.
[233] A. Singh, C.-K. Lim, Y.-D. Lee, J. Maeng, S. Lee, J. Koh, S. Kim, *ACS Appl. Mater. Interfaces* **2013**, *5*, 8881–8888.
[234] A. Yassin, T. Rousseau, P. Leriche, A. Cravino, J. Roncali, *Sol. Energy Mater. Sol. Cells* **2011**, *95*, 462–468.
[235] A. Zitzler-Kunkel, M. R. Lenze, T. Schnier, K. Meerholz, F. Würthner, *Adv. Funct. Mater.* **2014**, *24*, 4645–4653.
[236] N. G. Connelly, W. E. Geiger, *Chem. Rev.* **1996**, *96*, 877–910.
[237] W. N. Hansen, G. J. Hansen, *Phys. Rev. A* **1987**, *36*, 1396–1402.
[238] C. M. Cardona, W. Li, A. E. Kaifer, D. Stockdale, G. C. Bazan, *Adv. Mater.* **2011**, *23*, 2367–2371.
[239] C. Wetzel, A. Mishra, E. Mena-Osteritz, A. Liess, M. Stolte, F. Würthner, P. Bäuerle, *Org. Lett.* **2014**, *16*, 362–365.
[240] S. M. McAfee, J. M. Topple, A.-J. Payne, J.-P. Sun, I. G. Hill, G. C. Welch, *ChemPhysChem* **2015**, *16*, 1190–1202.
[241] Y. Kim, C. E. Song, E.-J. Ko, D. Kim, S.-J. Moon, E. Lim, *RSC Adv.* **2014**, *5*, 4811–4821.
[242] H. Bai, Y. Wu, Y. Wang, Y. Wu, R. Li, P. Cheng, M. Zhang, J. Wang, W. Ma, X. Zhan, *J. Mater. Chem. A* **2015**, *3*, 20758–20766.
[243] R. Heuvel, J. J. van Franeker, R. A. J. Janssen, *Macromol. Chem. Phys.* **2017**, *218*, 1600502.
[244] C. Duan, R. E. M. Willems, J. J. van Franeker, B. J. Bruijnaers, M. M. Wienk, R. A. J. Janssen, *J. Mater. Chem. A* **2016**, *4*, 1855–1866.
[245] K. H. Hendriks, G. H. L. Heintges, V. S. Gevaerts, M. M. Wienk, R. A. J. Janssen, *Angew. Chem. Int. Ed.* **2013**, *52*, 8341–8344.
[246] J. C. Bijleveld, A. P. Zoombelt, S. G. J. Mathijssen, M. M. Wienk, M. Turbiez, D. M. de Leeuw, R. A. J. Janssen, *J. Am. Chem. Soc.* **2009**, *131*, 16616–16617.
[247] A. T. Yiu, P. M. Beaujuge, O. P. Lee, C. H. Woo, M. F. Toney, J. M. J. Fréchet, *J. Am. Chem. Soc.* **2012**, *134*, 2180–2185.
[248] W. Li, K. H. Hendriks, M. M. Wienk, R. A. J. Janssen, *Acc. Chem. Res.* **2016**, *49*, 78–85.
[249] N. Blouin, A. Michaud, M. Leclerc, *Adv. Mater.* **2007**, *19*, 2295–2300.
[250] W. Li, A. Furlan, K. H. Hendriks, M. M. Wienk, R. A. J. Janssen, *J. Am. Chem. Soc.* **2013**, *135*, 5529–5532.

[251] L. H. Nguyen, H. Hoppe, T. Erb, S. Günes, G. Gobsch, N. S. Sariciftci, *Adv. Funct. Mater.* **2007**, *17*, 1071–1078.
[252] K. Sun, Z. Xiao, E. Hanssen, M. F. G. Klein, H. H. Dam, M. Pfaff, D. Gerthsen, W. W. H. Wong, D. J. Jones, *J. Mater. Chem. A* **2014**, *2*, 9048–9054.
[253] C. Sprau, F. Buss, M. Wagner, D. Landerer, M. Koppitz, A. Schulz, D. Bahro, W. Schabel, P. Scharfer, A. Colsmann, *Energy Environ. Sci.* **2015**, *8*, 2744–2752.
[254] L. Zang, *Energy Efficiency and Renewable Energy through Nanotechnology*, Springer, London, **2011**.
[255] H.-C. Liao, C.-C. Ho, C.-Y. Chang, M.-H. Jao, S. B. Darling, W.-F. Su, *Mater. Today* **2013**, *16*, 326–336.
[256] J. Peet, J. Y. Kim, N. E. Coates, W. L. Ma, D. Moses, A. J. Heeger, G. C. Bazan, *Nat. Mater.* **2007**, *6*, 497–500.
[257] J. K. Lee, W. L. Ma, C. J. Brabec, J. Yuen, J. S. Moon, J. Y. Kim, K. Lee, G. C. Bazan, A. J. Heeger, *J. Am. Chem. Soc.* **2008**, *130*, 3619–3623.
[258] X. Guo, C. Cui, M. Zhang, L. Huo, Y. Huang, J. Hou, Y. Li, *Energy Environ. Sci.* **2012**, *5*, 7943–7949.
[259] Y. Gu, C. Wang, T. P. Russell, *Adv. Energy Mater.* **2012**, *2*, 683–690.
[260] L. Ye, S. Zhang, W. Ma, B. Fan, X. Guo, Y. Huang, H. Ade, J. Hou, *Adv. Mater.* **2012**, *24*, 6335–6341.
[261] B. A. Collins, Z. Li, J. R. Tumbleston, E. Gann, C. R. McNeill, H. Ade, *Adv. Energy Mater.* **2013**, *3*, 65–74.
[262] B. Walker, A. B. Tamayo, X.-D. Dang, P. Zalar, J. H. Seo, A. Garcia, M. Tantiwiwat, T.-Q. Nguyen, *Adv. Funct. Mater.* **2009**, *19*, 3063–3069.
[263] A. Tamayo, T. Kent, M. Tantitiwat, M. A. Dante, J. Rogers, T.-Q. Nguyen, *Energy Environ. Sci.* **2009**, *2*, 1180–1186.
[264] P. F. Xia, X. J. Feng, J. Lu, S.-W. Tsang, R. Movileanu, Y. Tao, M. S. Wong, *Adv. Mater.* **2008**, *20*, 4810–4815.
[265] S. Grob, A. N. Bartynski, A. Opitz, M. Gruber, F. Grassl, E. Meister, T. Linderl, U. Hörmann, C. Lorch, E. Moons, et al., *J. Mater. Chem. A* **2015**, *3*, 15700–15709.
[266] S.-X. Sun, Y. Huo, M.-M. Li, X. Hu, H.-J. Zhang, Y.-W. Zhang, Y.-D. Zhang, X.-L. Chen, Z.-F. Shi, X. Gong, et al., *ACS Appl. Mater. Interfaces* **2015**, *7*, 19914–19922.
[267] X. Gu, I. Gunkel, A. Hexemer, T. P. Russell, *Macromol.* **2016**, *49*, 3373–3381.
[268] C. Leow, T. Ohnishi, M. Matsumura, *J. Phys. Chem. C* **2014**, *118*, 71–76.
[269] R. R. Lunt, N. C. Giebink, A. A. Belak, J. B. Benziger, S. R. Forrest, *J. Appl. Phys.* **2009**, *105*, 053711.
[270] Y. Wang, H. Ohkita, H. Benten, S. Ito, *Phys. Chem. Chem. Phys.* **2015**, *17*, 27217–27224.
[271] K. Kim, S. Park, Y. Kim, J. Bang, C. Park, D. Y. Ryu, *Macromol.* **2016**, *49*, 1722–1730.
[272] K. H. Hendriks, G. H. L. Heintges, V. S. Gevaerts, M. M. Wienk, R. A. J. Janssen, *Angew. Chem. Int. Ed.* **2013**, *52*, 8341–8344.
[273] R. Hecht, J. Kade, D. Schmidt, A. Nowak-Król, *Chem. - Eur. J.* **2017**, *23*, 11620–11628.
[274] A. Wakamiya, T. Taniguchi, S. Yamaguchi, *Angew. Chem. Int. Ed.* **2006**, *45*, 3170–3173.
[275] C. Dou, Z. Ding, Z. Zhang, Z. Xie, J. Liu, L. Wang, *Angew. Chem. Int. Ed.* **2015**, *54*, 3648–3652.

[276] R. Zhao, C. Dou, Z. Xie, J. Liu, L. Wang, *Angew. Chem. Int. Ed.* **2016**, *55*, 5313–5317.
[277] H. Shimogawa, M. Endo, T. Taniguchi, Y. Nakaike, M. Kawaraya, H. Segawa, Y. Murata, A. Wakamiya, *Bull. Chem. Soc. Jpn.* **2017**, *90*, 441–450.
[278] H. Shimogawa, M. Endo, Y. Nakaike, Y. Murata, A. Wakamiya, *Chem. Lett.* **2017**, *46*, 715–718.
[279] R. Schmidt, J. H. Oh, Y.-S. Sun, M. Deppisch, A.-M. Krause, K. Radacki, H. Braunschweig, M. Könemann, P. Erk, Z. Bao, et al., *J. Am. Chem. Soc.* **2009**, *131*, 6215–6228.
[280] J. R. Lakowicz, *Principles of Fluorescence Spectroscopy*, Springer, New York, **2010**.
[281] M. J. Frisch, G. W. Trucks, H. B. Schlegel, G. E. Scuseria, M. A. Robb, J. R. Cheeseman, G. Scalmani, V. Barone, B. Mennucci, G. A. Petersson, H. Nakatsuji, M. Caricato, X. Li, H. P. Hratchian, A. F. Izmaylov, J. Bloino, G. Zheng, J. L. Sonnenberg, M. Hada, M. Ehara, K. Toyota, R. Fukuda, J. Hasegawa, M. Ishida, T. Nakajima, Y. Honda, O. Kitao, H. Nakai, T. Vreven, J. A. Jr. Montgomery, J. E. Peralta, F. Ogliaro, M. Bearpark, J. J. Heyd, E. Brothers, K. N. Kudin, V. N. Staroverov, T. Keith, R. Kobayashi, J. Normand, K. Raghavachari, A. Rendell, J. C. Burant, S. S. Iyengar, J. Tomasi, M. Cossi, N. Rega, J. M. Millam, M. Klene, J. E. Knox, J. B. Cross, V. Bakken, C. Adamo, J. Jaramillo, R. Gomperts, R. E. Stratmann, O. Yazyev, A. J. Austin, R. Cammi, C. Pomelli, J. W. Ochterski, R. L. Martin, K. Morokuma, V. G. Zakrzewski, G. A. Voth, P. Salvador, J. J. Dannenberg, S. Dapprich, A. D. Daniels, O. Farkas, J. B. Foresman, J. V. Ortiz, J. Cioslowski, D. J. Fox, Gaussian 09, Revision D.01, Gaussian Inc., Wallingford CT, **2013**.
[282] F. Weigend, R. Ahlrichs, *Phys. Chem. Chem. Phys.* **2005**, *7*, 3297–3305.
[283] R. Dennington, T. Keith, J. Millam, GaussView, Version 5, Semichem Inv., Shawnee Mission KS, **2009**.
[284] G. M. Sheldrick, *Acta Crystallogr. A* **2008**, *64*, 112–122.
[285] S. C. Rasmussen, S. J. Evenson, *Prog. Polym. Sci.* **2013**, *38*, 1773–1804.
[286] S. J. Evenson, S. C. Rasmussen, *Org. Lett.* **2010**, *12*, 4054–4057.
[287] X. Hu, M. Shi, L. Zuo, Y. Nan, Y. Liu, L. Fu, H. Chen, *Polymer* **2011**, *52*, 2559–2564.
[288] C.-Y. Yu, C.-Y. Wu, *Dyes Pigments* **2014**, *106*, 81–86.
[289] H. Padhy, D. Sahu, D. Patra, M. K. Pola, J.-H. Huang, C.-W. Chu, K.-H. Wei, H.-C. Lin, *J. Polym. Sci. Part Polym. Chem.* **2011**, *49*, 3417–3425.
[290] H.-Y. Wang, J.-J. Shi, G. Chen, X.-P. Xu, S.-J. Ji, *Synth. Met.* **2012**, *162*, 241–246.
[291] Q. Li, H. Guo, L. Ma, W. Wu, Y. Liu, J. Zhao, *J. Mater. Chem.* **2012**, *22*, 5319–5329.
[292] K. N. Winzenberg, P. Kemppinen, F. H. Scholes, G. E. Collis, Y. Shu, T. B. Singh, A. Bilic, C. M. Forsyth, S. E. Watkins, *Chem. Commun.* **2013**, *49*, 6307–6309.
[293] M. Planells, N. Robertson, *Eur. J. Org. Chem.* **2012**, *2012*, 4947–4953.
[294] M. A. Uddin, T. H. Lee, S. Xu, S. Y. Park, T. Kim, S. Song, T. L. Nguyen, S. Ko, S. Hwang, J. Y. Kim, et al., *Chem. Mater.* **2015**, *27*, 5997–6007.
[295] C.-H. Chen, C.-H. Hsieh, M. Dubosc, Y.-J. Cheng, C.-S. Hsu, *Macromol.* **2010**, *43*, 697–708.
[296] C. R. Bridges, M. J. Ford, B. C. Popere, G. C. Bazan, R. A. Segalman, *Macromol.* **2016**, *49*, 7220–7229.

[297] J.-H. Lee, J.-W. Park, S.-K. Choia, *Synth. Met.* **1997**, *88*, 31–35.
[298] H. Meng, Z.-K. Chen, X.-L. Liu, Y.-H. Lai, S.-J. Chua, W. Huang, *Phys. Chem. Chem. Phys.* **1999**, *1*, 3123–3127.
[299] Y. Song, C. Di, Z. Wei, T. Zhao, W. Xu, Y. Liu, D. Zhang, D. Zhu, *Chem Eur J* **2008**, *14*, 4731–4740.
[300] P. Auragudom, A. A. Tangonan, M. A. G. Namboothiry, D. L. Carroll, R. C. Advincula, S. Phanichphant, T. R. Lee, *J. Polym. Res.* **2010**, *17*, 347–353.
[301] A. C. J. Heinrich, B. Thiedemann, P. J. Gates, A. Staubitz, *Org. Lett.* **2013**, *15*, 4666–4669.
[302] S. Pu, C. Zheng, Q. Sun, G. Liu, C. Fan, *Chem. Commun.* **2013**, *49*, 8036–8038.

Acknowledgements

Many people have supported and encouraged me during the last years.

First, I am very grateful to my doctoral supervisor Prof. Dr. Frank Würthner, who was able to conjure an interesting topic as well as a PhD position out of his pocket in no time. His great interest in my work, his expertise and the opportunity to use his excellent research facilities was more than I could hope for. Furthermore, I am highly grateful that he made guest stays possible in Cologne and Eindhoven, which cannot be taken for granted.

Many thanks to Prof. Dr. Klaus Meerholz (University Cologne) and Prof. Dr. R. A. J. Janssen (University Eindhoven) for welcoming me in their working groups for guest stays, so that I could perform experiments that otherwise would not have been possible. Especially, I want to thank Dr. Martin R. Lenze (Cologne) and Dr. Koen Hendriks (Eindhoven) who helped me with my experiments and shared all their knowledge without hesitation. Special thanks also to Prof. Dr. P. Bäuerle, Dr. A. Mishra and Dr. Ibrahim Ata, who inspired me and my colleagues with regard to ADA dyes and helped us getting started in the area of organic photovoltaics.

I am grateful to Dr. Hagen Klauk and Dr. Ute Zschieschang (MPI Stuttgart) for providing TPA modified substrates.

I would like to thank Prof. Dr. Vladimir Dyakonov and Dr. A. Ziegler who also shared their knowledge and helped me to properly calibrate our solar simulator.

A big thanks to Dr. Matthias Stolte for his guidance and support. He never stopped encouraging me and always had an open door not only for technical discussions. I also want to thank him for proofreading so many documents including this thesis – his feedback was always full of good advice. Last but not least I want to thank him for all his great ideas (sunny greetings).

I want to thank Dr. Andreas Liess und Astrid Kudzus for being a great team to work with. Together we kept every instrument running, the lab clean and the working time fun. I further want to thank Astrid Kudzus for her support during device preparation, characterization and for all the thousand smaller things she did in the lab. Further thanks to Andreas Liess who co-reviewed this thesis.

I want to thank Dr. Agnieszka Nowak-Król, her bachelor students Felix Kraus and Juliane Kade and her lab technician Christian Simon for the joined synthesis of ADA and AπA compounds. Furthermore, I especially want to thank Dr. Agnieszka Nowak-Król for performing all quantum chemical calculations and for the hand in hand preparation of two joint manuscripts.

Thanks to Dr. David Bialas and his lab technician Lisa Otter, for the synthesis of the dyad compounds presented in this work. Also a big thanks to him for providing me with the basic characterization of the dyad molecules in solution.

I want to thank our bachelor student Julia R. Zillner and all practical students, Martin Mattenheimer, Niklas Noll and Julian Höcker, who all contributed to this work to some extent.

Many thanks to Dr. David Schmidt, Ana-Maria Krause and Dr. Christian Burschka who performed single crystal x-ray diffraction measurements for me, also many frustrating ones without losing their eagerness.

I would like to thank Dr. Vladimir Stepanenko for performing AFM measurements for me and for introducing me into this method.

I would also like to express my thanks to Christiana Toussaint and Eleonore Klaus who helped me with all administrative matters.

I am grateful to Dr. Matthias Grüne, Dr. Michael Büchner, Juliane Adelmann, Patricia Altenberger, Antje Heckmann and Fritz Dadrich of the NMR spectroscopy and mass spectrometry divisions for their measurements.

I am very grateful to the whole Würthner research group for the good working atmosphere, the funny evenings and lunch times we spent together and for the cooperativeness that all of them showed.

A special thanks goes to my wife and I want to express it with her own words, because I think you cannot do better: “You never failed to make me smile throughout the ups and downs of this work”. Finally, I want to thank my family who made all of this possible by their ongoing support.

List of Publications

- *A photoinduced mixed-valence state in an organic bis-triarylamine mixed-valence compound with an iridium-metal-bridge*, C. Lambert, R. Hecht, J. H. Klein, G. Grelaud, M. Moos, A. Schmiedel, M. Holzapfel, T. Bruhn, *Chem. Commun.* **2014**, *50*, 11350-11353.

- *Modulation of band gap and p- versus n-semiconductor character of ADA dyes by core and acceptor group variation*, A. Nowak-Król, R. Hecht, F. Kraus, A. Mishra, P. Bäuerle, F. Würthner, *Org. Chem. Front.* **2016**, *3*, 545-555.

- *n-Channel Organic Semiconductors Derived from Air-Stable Four-Coordinate Boron Complexes of Substituted Thienylthiazoles*, R. Hecht, J. Kade, D. Schmidt, A. Nowak-Król, *Chem. Eur. J.* **2017**, *23*, 11620-11628.

- *Temperature-Responsive Luminescent Solar Concentrators: Tuning Energy Transfer in a Liquid Crystalline Matrix*, J. A. H. P. Sol, V. Dehm, R. Hecht, F. Würthner, A. P. H. J. Schenning, M. G. Debije, *Angew. Chem. Int. Ed.* **2017**, *56*, 1-5.

List of Compounds

DA dyes:

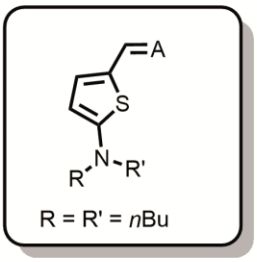

R = R' = *n*Bu

A =

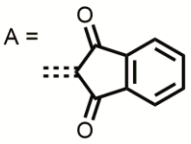

DA1 (**MD352**)

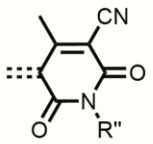

DA2 (**MD333**)
(R" = EtHex)

Dye1 (**MD302**)
(R' = R" = *n*Bu;
R = Et)

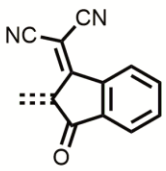

DA3 (**EL86**)

DA3'/Dye2 (**HB366**)
(R = Et; R' = *n*Bu)

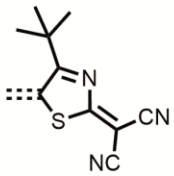

DA4 (**HB238**)

Dye3 (**CS254**)
(R' = R" = *n*Bu)

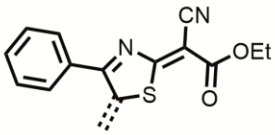

DA5 (**MD357**)

Dyads:

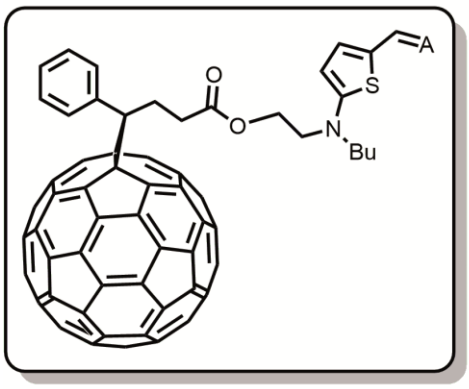

A =

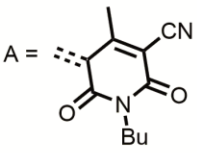

Dyad1 (**DBJ102**)

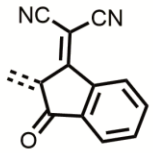

Dyad2 (**LO04**)

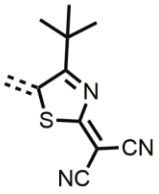

Dyad3 (**LO08**)

ADA and AπA dyes:

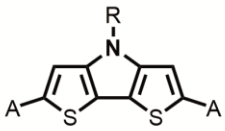

ADA1a
A = IND
ADA1b
A = DCIND

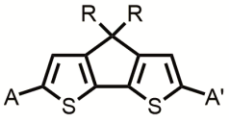

ADA2a
A = A' = IND
AD2a
A = IND; A' = CHO
ADA2b
A = A' = DCIND
ADA2b'
A = DCIND;
R = $CH_2CH(C_8H_{17})(C_6H_{13})$

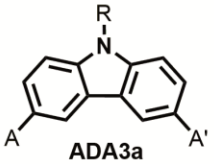

ADA3a
A = A' = IND
AD3a
A = IND; A' = CHO
ADA3b
A = A' = DCIND
AD3b
A = DCIND; A' = CHO

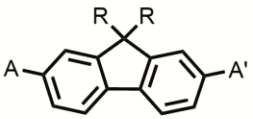

ADA4a
A = A' = IND
AD4a
A = IND; A' = CHO

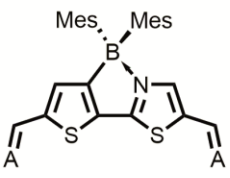

AπA1a
A = IND
AπA1b
A = DCIND
AπA1c
A = $C(CN)_2$

IND =

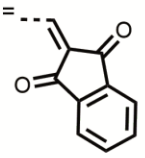

DCIND =

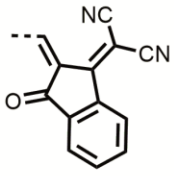

R = 2-ethylhexyl (*rac*)

Mes = mesityl

Polymers:

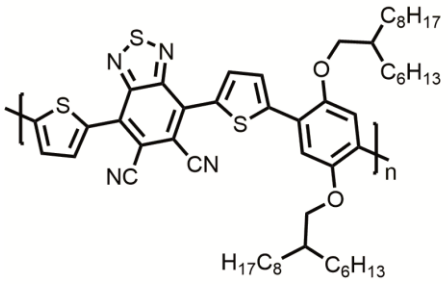

PPDTNBT

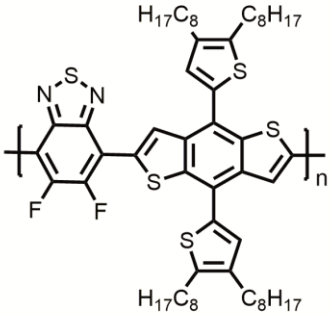

BDT-FBT-C32

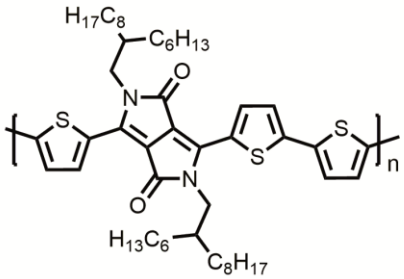

PDPP3T

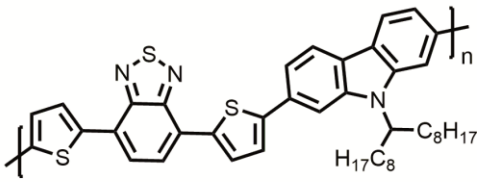

PCDTBT